LOCKHEED MARTIN ENERGY RESEARCH LIBRARIES
3 4456 0515590 7

CENTRAL RESEARCH LIBRARY
DOCUMENT COLLECTION

cy. 1

ORNL-4480
UC-25 – Metals, Ceramics, and Materials

FUELS AND MATERIALS DEVELOPMENT PROGRAM

QUARTERLY PROGRESS REPORT

FOR PERIOD ENDING SEPTEMBER 30, 1969

OAK RIDGE NATIONAL LABORATORY
CENTRAL RESEARCH LIBRARY
DOCUMENT COLLECTION
LIBRARY LOAN COPY
DO NOT TRANSFER TO ANOTHER PERSON
If you wish someone else to see this
document, send in name with document
and the library will arrange a loan.

OAK RIDGE NATIONAL LABORATORY
operated by
UNION CARBIDE CORPORATION
for the
U.S. ATOMIC ENERGY COMMISSION

Printed in the United States of America. Available from Clearinghouse for Federal Scientific and Technical Information, National Bureau of Standards, U.S. Department of Commerce, Springfield, Virginia 22151
Price: Printed Copy $3.00; Microfiche $0.65

LEGAL NOTICE

This report was prepared as an account of Government sponsored work. Neither the United States, nor the Commission, nor any person acting on behalf of the Commission:

A. Makes any warranty or representation, expressed or implied, with respect to the accuracy, completeness, or usefulness of the information contained in this report, or that the use of any information, apparatus, method, or process disclosed in this report may not infringe privately owned rights; or

B. Assumes any liabilities with respect to the use of, or for damages resulting from the use of any information, apparatus, method, or process disclosed in this report.

As used in the above, "person acting on behalf of the Commission" includes any employee or contractor of the Commission, or employee of such contractor, to the extent that such employee or contractor of the Commission, or employee of such contractor prepares, disseminates, or provides access to, any information pursuant to his employment or contract with the Commission, or his employment with such contractor.

ORNL-4480

Contract No. W-7405-eng-26

METALS AND CERAMICS DIVISION

FUELS AND MATERIALS DEVELOPMENT PROGRAM QUARTERLY PROGRESS REPORT FOR PERIOD ENDING SEPTEMBER 30, 1969

Compiled by

P. Patriarca

Edited by

D. J. Rucker

FEBRUARY 1970

OAK RIDGE NATIONAL LABORATORY
Oak Ridge, Tennessee
operated by
UNION CARBIDE CORPORATION
for the
U.S. ATOMIC ENERGY COMMISSION

LOCKHEED MARTIN ENERGY RESEARCH LIBRARIES

3 4456 0515590 7

FOREWORD

This quarterly progress report describes research and development on nuclear fuels and materials performed at the Oak Ridge National Laboratory for the U.S. Atomic Energy Commission. This work is either sponsored by or of particular interest to the Fuels and Materials Branch of the Division of Reactor Development and Technology.

Progress on these programs is reported for the three major divisions of the work — Fast Reactor Technology, Space Power Technology, and General Reactor Technology — under the appropriate AEC activity titles listed below.

AEC Activity Title	AEC Activity Number
PART I. FAST REACTOR TECHNOLOGY	
FUELS	
DEVELOPMENT OF LMFBR OXIDE FUELS	04 40 02 01 1
DEVELOPMENT OF HIGH-PERFORMANCE LMFBR FUELS	04 40 02 01 1
EFFECT OF POWER CYCLING ON LMFBR FUEL-CLADDING BEHAVIOR	04 40 02 01 1
LMFBR FUEL ELEMENT DESIGN AND MODEL DEVELOPMENT	04 40 02 01 1
CLADDING AND OTHER STRUCTURAL MATERIALS	
MECHANICAL PROPERTIES OF ALLOYS IN REACTOR ENVIRONMENTS	04 40 02 03 1
DEVELOPMENT OF LMFBR CLADDING AND STRUCTURAL MATERIALS	04 40 02 01 1
FABRICATION DEVELOPMENT FOR LMFBR STAINLESS STEEL TUBING	04 01 61 01 5
WELDING DEVELOPMENT FOR LMFBR VESSELS AND COMPONENTS	04 40 02 04 1
SHIELDED METAL-ARC WELDING FOR LMFBR COMPONENTS	04 01 61 01 5
NONDESTRUCTIVE TESTING TECHNIQUES FOR LMFBR	04 40 02 04 1
SODIUM CORROSION STUDIES	04 40 02 02 1
DEVELOPMENT OF FAST-REACTOR NEUTRON-ABSORBER MATERIALS	04 40 02 02 1

AEC Activity Title	AEC Activity Number
PART II. SPACE POWER TECHNOLOGY	
FUELS	
DEVELOPMENT OF URANIUM MONONITRIDE FUELS	04 40 02 01 1
CLADDING AND OTHER STRUCTURAL MATERIALS	
CLADDING MATERIALS FOR SPACE ISOTOPIC HEAT SOURCES*	04 30 05 04 1
PHYSICAL AND MECHANICAL METALLURGY OF REFRACTORY ALLOYS	04 40 02 05 1
TUNGSTEN METALLURGY	04 40 02 04 1
FAST-NEUTRON IRRADIATION EFFECTS ON ELECTRICAL INSULATORS*	04 30 02 02 1
CORROSION STUDIES OF ADVANCED REFRACTORY METALS	04 40 02 02 1
PART III. GENERAL REACTOR TECHNOLOGY	
FUELS	
RELEASE OF FISSION-GAS FROM FUEL MATERIALS DURING IRRADIATION	04 40 02 01 1
DEVELOPMENT OF FUEL ELEMENT FABRICATION	04 40 02 04 1
TECHNICAL ASSISTANCE IN PROCUREMENT OF FUEL ELEMENTS	04 40 02 01 1
CLADDING AND OTHER STRUCTURAL MATERIALS	
BEHAVIOR OF REFRACTORY MATERIALS UNDER IRRADIATION	04 40 02 03 1
JOINING RESEARCH ON NUCLEAR MATERIALS	04 40 02 04 1
NONDESTRUCTIVE TESTING	04 40 02 04 1
IMPROVEMENT OF HASTELLOY N AND RELATED COMPOSITIONS	04 40 02 03 1
ADVANCED MATERIALS FOR STEAM GENERATORS	04 40 02 02 1

*Research sponsored by Division of Space Nuclear Systems.

CONTENTS

Page

SUMMARY xiii

PART I. FAST REACTOR TECHNOLOGY

FUELS

1. DEVELOPMENT OF FAST-REACTOR OXIDE FUELS 3
   Preparation of $(U,Pu)O_2$ Fuel Materials 3
      Preparation of PuO_2 Sol 3
      Preparation of Microspheres 4
   Development of Fabrication Processes 4
      Sphere-Pac 4
      Pelletization of Sol-Gel $(U,Pu)O_2$ 6
      Capsule Fabrication 8
   Characterization of $(U,Pu)O_2$ Fuels 10
      Analytical Chemistry 11
      Analytical Characterization 15
      Behavior of Fission Products 16
      Thermal Conductivity of Lithium Fluoride 20
      Deformation of UO_2 21
   Irradiation Testing of $(U,Pu)O_2$ Fuels 23
      Uninstrumented Thermal-Flux Irradiation Tests 24
      ORR Instrumented Tests 26
      ETR Instrumented Tests 27
      Transient Testing 29
      Fast-Flux Irradiation Tests 29
      Irradiation Test Calculations 31
2. DEVELOPMENT OF HIGH-PERFORMANCE LMFBR FUELS 36
   Synthesis, Fabrication, and Characterization of Nitride Fuels 37
      Synthesis and Fabrication of Mixed Nitrides 37
   Synthesis, Fabrication, and Thermodynamic Properties of Carbonitride Fuels 42
      Manufacture of UC, UN, and U(C,N) From UO_2 42

Vacuum Conversion of UO_2-C Mixtures 42

Fabrication of (U,Pu)(C,N) 43

Compatibility of Mixed-Nitride and Carbonitride Fuels with LMFBR Cladding Alloys 44

Ternary U-V-N System 45

Ternary U-V-C System 46

Thermodynamic Investigations of High-Performance Fuel Systems 50

Thermodynamic Stability of UVC_2 50

Thermodynamic Stability of $UCrC_2$, $UMoC_2$, and UWC_2 51

Plutonium Nitride Thermodynamics 52

Measurements of the Physical Properties of (U,Pu)N Alloys . . 52

Irradiation Testing of Nitride Fuels for LMFBR Applications . 53

Thermal-Flux Irradiation Tests 53

Liquid-Metal Bonding of Fuel to Cladding 55

3. EFFECT OF POWER CYCLING ON LMFBR FUEL-CLADDING BEHAVIOR 58

Power Cycling of Mixed Oxide Fuel with Stainless Steel Cladding to Moderate Burnup 58

4. LMFBR FUEL ELEMENT DESIGN AND MODEL DEVELOPMENT 59

Model Integration 59

FMØDEL Computer Code 59

Fuel Performance 61

Heat Transfer 61

Distribution of Fission Gas 62

Fuel Restructuring 62

Swelling Caused by Fission Products 63

Cladding Performance 63

Mechanical Interaction 63

Swelling of the Cladding Due to Fast-Neutron Fluences 65

Cladding Failure Due to Crack Propagation and Grain-Boundary Cavitation 66

CLADDING AND OTHER STRUCTURAL MATERIALS

5. MECHANICAL PROPERTIES OF ALLOYS IN REACTOR ENVIRONMENTS AND DEVELOPMENT OF LMFBR CLADDING AND STRUCTURAL MATERIALS . 70

Austenitic Stainless Steels 70

Effects of Irradiation on Mechanical Properties of Type 316 Stainless Steel 70

Mechanical Properties of EBR-II Safety-Rod Thimble . . . 73

Effects of Irradiation Variables on Swelling and Formation of Voids 76

Comparison of Swelling and Formation of Voids Induced by Irradiation in Two Austenitic Stainless Steels . . . 85

Irregular Void Distributions 89

Incoloy 800 89

Aging Studies 89

6. FABRICATION DEVELOPMENT FOR LMFBR STAINLESS STEEL TUBING . . . 96

Fabrication Studies on Type 316 Stainless Steel 96

Melting, Extrusion, and Tube Reducing 96

Drawing of Type 316 Stainless Steel Tubing 99

Biaxial Stress-Rupture Testing of Stainless Steel Tubing . . . 103

Comparison of Tubing Produced by Mandrel Drawing and Planetary Swaging 103

7. WELDING DEVELOPMENT FOR LMFBR VESSELS AND COMPONENTS 105

Literature Search 105

Mechanical Properties of Austenitic Stainless Steel Weldments at Elevated Temperatures 105

Study of Submerged-Arc Process 108

Materials Procurement and Preliminary Welding Studies . . 108

Study of Gas Metal-Arc Process 109

Characterization of Welds 109

8. SHIELDED METAL-ARC WELDING FOR LMFBR COMPONENTS 111

Effect of Variations in Flux Coatings 111

Welding Studies 111

9. NONDESTRUCTIVE TESTING TECHNIQUES FOR LMFBR 114

Development of Advanced Nondestructive Testing 114

Development of Eddy-Current Instrument 114

Ultrasonic Schlieren Techniques for Evaluation of Welds 114

Measurement of Cold Work in Stainless Steel Tubing 115

Measurement of Changes in Magnetic Permeability 115

10. SODIUM CORROSION STUDIES 118

Comparative Corrosion Tests on Refractory Alloys 118

Effect of Oxygen on the Compatibility of Vanadium and Vanadium Alloys with Sodium 118

Mass Transport of Interstitial Impurities Between Vanadium Alloys and Type 300 Series Stainless Steels 119

Interstitial Contamination of Vanadium and Its Alloys 122

Interactions of Sodium with Nonmetallic Materials 124

Compatibility of Stainless Steel and Insulation for LMFBR Systems 124

11. DEVELOPMENT OF FAST-REACTOR NEUTRON-ABSORBER MATERIALS 129

Characterization of Boron Carbide 129

Powder Characterization 129

Chemical Composition and Density of Commercial Grades of Powder 133

Behavior of Boron Carbide Particles in Pressing and Sintering 133

Control of Polyhedral Voids 140

Some Observations on Boron Carbide Phase Equilibria . . . 142

Irradiation Behavior of Boron Carbide 145

Irradiation Tests 145

PART II. SPACE POWER TECHNOLOGY

FUELS

12. DEVELOPMENT OF URANIUM MONONITRIDE FUELS 149

Irradiation Testing 149

Capsules UN-1 and UN-2 149

Capsule UN-3 151

Capsules UN-4, UN-5, and UN-6 151

CLADDING AND OTHER STRUCTURAL MATERIALS

13. CLADDING MATERIALS FOR SPACE ISOTOPIC HEAT SOURCES 152

Creep Studies of Cobalt Superalloys 152

Interaction of Stress and Vacuum on the Creep Properties of Haynes Alloy No. 25 at Elevated Temperatures 152

Development of Improved Alloys 153
Creep Tests of Experimental Alloys 153
14. PHYSICAL AND MECHANICAL METALLURGY OF REFRACTORY ALLOYS . . . 157
Physical Metallurgy 157
Development of Age-Hardening Refractory Alloys 157
Mechanical Properties of Commercial Refractory Alloys 160
Molybdenum-Based Alloys 160
Welding and Brazing 163
Evaluation of the Weldability of Tantalum and Molybdenum Alloys 163
Physical Properties 164
Measurements of the Physical Properties of Tantalum . . . 164
15. TUNGSTEN METALLURGY 167
Primary and Secondary Working of Tungsten Alloys 167
Extrusion of Tungsten Tubing 167
Chemical Vapor Deposition of Tungsten Alloys 170
Chemical Vapor Deposition of W—5% Re Sheet and Tubing 170
Chemical Vapor Deposition of Vanadium 174
Metallurgical Properties of Tungsten Alloys 176
Effect of Low-Pressure Oxygen on the Creep Properties of Tungsten 176
Long-Time Creep Properties of Tungsten Alloys 180
Comparative Creep-Rupture Properties of W—25% Re Consolidated by Arc-Melting and Powder-Metallurgy Techniques 180
Long-Time Creep and Stress-Rupture Properties of Tungsten-Rhenium Alloys 181
Interrupted Creep Tests on Tungsten 181
Evaluation of Methods for Joining Tungsten Alloys 183
Development of Filler Metals with Low Melting Points . . 183
16. FAST-NEUTRON IRRADIATION EFFECTS ON ELECTRICAL INSULATORS . . 188
General Survey of Fast-Neutron Effects on Electrical Insulators 188
Silicon Oxynitride 188
Single-Crystal Materials and Other Advanced Materials . . 188

Irradiation of High-Density Commercial Al_2O_3 Products Considered for Thermionic Insulators 189

Metal-Clad Al_2O_3 Specimens 192

17. CORROSION STUDIES OF ADVANCED REFRACTORY METALS 196

Lithium Studies 196

Lithium Thermal-Convection Loop Experiments 196

Lithium Forced-Circulation Loop Experiments 196

Effect of Oxygen on Compatibility of Refractory Metals and Alkali Metals 201

Partitioning of Oxygen Between Potassium and Zirconium 201

Penetration of Refractory Metals by Alkali Metals 202

PART III. GENERAL REACTOR TECHNOLOGY

FUELS

18. FISSION-GAS RELEASE AND PHYSICAL PROPERTIES OF FUEL MATERIALS DURING IRRADIATION 209

Measurements of Thermal Diffusivity in UO_2 During Irradiation 209

Release of Fission Gas from UO_2 211

19. DEVELOPMENT OF FUEL ELEMENT FABRICATION 213

Irradiation Studies 213

Evaluation and Design of Cermet Fuel-Plate Irradiation Experiments 213

Status of Irradiation Experiments in ETR 214

Correlation of Cermet Swelling with Fabrication Voids . . 218

Refractory-Metal Cermet Fuels 219

HFIR Fuel Plates with Increased Fuel Loading 224

Technical Assistance for Commercial and Manufacturing Problems 228

Use of ZrO_2 to Generate Fabrication Voids in Composite Plates 228

Fabrication Behavior of Plates That Contain Shaped Cores 229

Susceptibility to Blistering of Fuel Plates That Contain Shaped Fuel Cores 230

Factors That Affect the Oakite Cleaning Process 231

Evaluation of Surface Chemistry on Some Chemically Cleaned Plates 232

Fabrication Development 233

Deformation Characteristics of U_3O_8-Al and UAl_x-Al Dispersion Fuel Plates with Increased Loadings 233

Development of Nondestructive Inspection Techniques 237

Radiographic Densitometry 237

Effect of Variations in Fuel Particle Size on X-Ray Attenuation 239

Studies of Joining and Assembly 241

Joining Fuel Plates to Side Plates 241

Construction of Prototype Element 241

20. TECHNICAL ASSISTANCE IN PROCUREMENT OF FUEL ELEMENTS 244

Technical Assistance in Solving Pressing Manufacturing and Inspection Problems 244

CLADDING AND OTHER STRUCTURAL MATERIALS

21. BEHAVIOR OF REFRACTORY MATERIALS UNDER IRRADIATION 245

Irradiation Damage to Nonfissionable Refractory Materials 245

Refractory Metal Carbides 245

Effects of Irradiation on LMFBR Fuels 254

Effects of Helium Gas Produced by Fast Neutrons in Depleted UN 254

Fast-Neutron Effects on Materials for Neutron Absorption in Fast Reactors 255

22. JOINING RESEARCH ON NUCLEAR MATERIALS 256

The Effect of Minor Variations in Chemical Composition on Weldability 256

Weldability of 18% Cr–8% Ni Class of Stainless Steel . . 256

Effect of Minor Elements on the Hot Ductility of Inconel 600 257

The Effect of Defects on the Mechanical Properties of Weldments 265

Electron-Beam Welds in Inconel 600 265

23. NONDESTRUCTIVE TESTING 266

Electromagnetic Inspection Methods (Eddy Currents) 266

Solutions for Electromagnetic Induction Problems 266
Ultrasonic Inspection Methods 267
Optical Visualization of Ultrasound 267
Frequency Analysis 268
Fabrication of Reference Notches 269
Penetrating-Radiation Inspection Methods 270
X-Ray Attenuation 270
Radiation Scattering 271
24. IMPROVEMENT OF HASTELLOY N AND RELATED COMPOSITIONS 274
Mechanical Properties of Hastelloy N and Related Compositions 274
Aging of Ti-Modified Hastelloy N 274
Statistical Treatment of Aging Data for Hastelloy N . . . 275
Development of a Modified Hastelloy N 279
Electron Microscopy of Hastelloy N 291
25. ADVANCED MATERIALS FOR STEAM GENERATORS 297
Program History 297
General Corrosion at 595 and 650°C and Weldability 301
Corrosion Studies 301
Preferential Corrosion 301
Stress-Corrosion Cracking 301

SUMMARY

PART I. FAST REACTOR TECHNOLOGY

FUELS

1. DEVELOPMENT OF FAST-REACTOR OXIDE FUELS

Pellets were fabricated for two irradiation test capsules. Capsule GCFR P-9 for the Gas-Cooled Fast Reactor (GCFR) required 91% dense dished-end annular pellets of $(U_{0.88},Pu_{0.12})O_2$. Capsule ORR SG-3 for the Oak Ridge Research Reactor (ORR) required 83% dense annular pellets made from $(U_{0.80},Pu_{0.20})O_2$. Two capsules were fabricated for transient tests in the Transient Reactor Test Facility (TREAT).

Although the maximum desirable gas release from fuel at 1600°C is 0.05 cm^3/g (STP), we have measured releases as high as 0.3 to 0.50 cm^3/g for some of our pellet fuels. This high gas content is probably due to pickup of water during storage of the pellets, and the amount of gas absorbed is proportional to the amount of open porosity in the pellets. Means have been devised to protect the fuel from moisture during storage.

An initial experiment was performed to determine the oxidation state of rare earths dissolved in $(U,Pu)O_2$ fuels. A study with Eu_2O_3 in UO_2 indicated that Eu is oxidized from the +3 state to a higher state, thus indicating the O potential of a fuel element will not rise as rapidly during burnup as previously feared.

Additional comparative tests of ammonium-diuranate (ADU) and sol-gel UO_2 specimens indicate that the deformation of UO_2 at high temperature under constant strain rates is more sensitive to grain size than to the density of the specimen. The compressive creep of UO_2 sol-gel specimens was measured under constant stress of 4910 psi between 1200 and 1400°C.

A sol-gel Sphere-Pac capsule containing $(U,Pu)O_2$ attained a burnup of 7.5% fissions per initial metal atom (FIMA) in the Engineering Test Reactor (ETR), and, after interim neutron radiographs of the capsule showed no significant changes in the fuel rods or capsules, approval was obtained from the ETR Safety Review Committee to continue the irradiation to 10% FIMA burnup.

The second instrumented capsule irradiated in the ORR, which contained two identical Sphere-Pac $(U,Pu)O_2$ fuel rods with 81% smear density, was removed from the reactor after operating normally at temperatures up to 1500°C at the fuel center. This capsule, SG-2, is now undergoing postirradiation examination. An instrumented capsule was designed for irradiation in the ETR. The hazards analysis, test specifications, and operating manual for the TREAT capsules were completed, submitted to the TREAT staff, and accepted by them with minor revisions.

Encapsulated tests of Sphere-Pac $(U,Pu)O_2$ fuel rods in subassembly X050 in the Experimental Breeder Reactor-II (EBR-II) reached a peak burnup of 3.1% FIMA, or about 63% of the currently scheduled burnup. A proposal for approval in principle for the series II unencapsulated tests, part of a test series which is to be shared with Babcock and Wilcox Company, was submitted to the AEC in August.

A series of calculations was made using computer codes developed over the past 2 years to describe various features of fuel irradiations. The results of these calculations were incorporated into a paper that compared the neutronic and thermal environments for $(U,Pu)O_2$ fuel rods clad with stainless steel operating in a fast reactor typical of those proposed for commercial application under test conditions now available in both thermal- and fast-flux test reactors.

2. DEVELOPMENT OF HIGH-PERFORMANCE LMFBR FUELS

A satisfactory process was developed for hot pressing physically mixed (U,Pu)N pellets to 98% of theoretical density. Production of pellets for irradiation tests in Na-bonded capsules is under way.

Kinetic studies showed that vacuum conversion of UV_2-C gels to UCN is much more rapid than reaction in a fluidized bed in inert gas. An apparatus has been readied for vacuum conversion of $(U,Pu)O_2$-C gels to mixed carbonitrides.

Studies of the ternary compound UVC_2 showed that it is unstable above 1900 ± 100°C. At 1800°K the free energy of formation of UVC_2 is −47.8 ± 0.3 kcal/mole.

3. EFFECT OF POWER CYCLING ON LMFBR FUEL-CLADDING BEHAVIOR

We began this quarter to design a series of reactor experiments for studying the effects of power cycling and power transients on the behavior of oxide fuel and the interactions of fuel and cladding. Calculations are now being made to establish the geometry of the capsules so that a preliminary design and cost estimate may be made for the first experiment.

4. LMFBR FUEL ELEMENT DESIGN AND MODEL DEVELOPMENT

The initial work on this program has focused on the development of the FMØDEL computer code. This code provides a flexible, numerically accurate heat transfer and mechanical analysis of a metal-clad ceramic fuel rod operating at steady-state conditions with radially symmetric boundary conditions. The fuel rod is described as a series of axial "regions," each containing radial "increments." The computer simulation uses existing models to describe release of fission gas, fuel restructuring, and swelling of the fuel. The calculational procedure for each regions follows this sequence: temperature distribution, fuel restructuring, cladding swelling, release of fission gas, fuel swelling, elastic-plastic stress-strain distribution, and creep stress-strain distribution. The temperature distribution is recalculated at various stages of the sequence to account for restructuring and changes in geometry. Although certain parts of the mechanical analysis are still being improved, we have begun use of the code for the design and interpretation of irradiation experiments with $(U,Pu)O_2$ fuel rods clad with stainless steel.

CLADDING AND OTHER STRUCTURAL MATERIALS

5. MECHANICAL PROPERTIES OF ALLOYS IN REACTOR ENVIRONMENTS AND DEVELOPMENT OF LMFBR CLADDING AND STRUCTURAL MATERIALS

Type 316 stainless steel was irradiated in the annealed, 5, 10, and 20% prestrained conditions for about 4500 hr [1.8×10^{21} neutrons/cm^2 (thermal) and 1.4×10^{21} neutrons/cm^2 (> 1 Mev)] at 650°C. Postirradiation creep-rupture tests at 650°C indicate that, for these conditions,

straining before irradiation has essentially no effect on the rupture life but significantly reduces the ductility.

Initial results of creep-rupture tests at 600°C on specimens removed from the Experimental Breeder Reactor-II (EBR-II) safety-rod thimble indicate a decrease of both the ductility and rupture life.

The dependence of the swelling induced by irradiation on fluence varies between $\frac{\Delta\rho}{\rho} \propto (\varphi t)^{0.64}$ and $\frac{\Delta\rho}{\rho} \propto (\varphi t)^{1.72}$ depending upon which data are accepted or rejected. The results of electron microscopy indicate that the void distributions are quite heterogeneous at low fluences. Measurements indicate that the void concentrations decrease with increasing irradiation temperature at a constant fluence and increase with increasing fluence at a constant irradiation temperature. Measurements have shown that a void grows to what appears to be a maximum or limiting size in a few times 10^{21} neutrons/cm^2; thereafter the growth rate decreases markedly.

We are continuing to evaluate the role that carbide morphology and distribution play in the embrittlement of Incoloy 800 alloys. A discontinuous, agglomerated carbide formed along the grain boundary by means of a special heat treatment is stable at 500°C and results in improved creep ductility after long-term exposure. Irradiation of solution-annealed Incoloy 800 at lower temperature (350°C) enhances the aging response as evidenced during creep at 650°C.

6. FABRICATION DEVELOPMENT FOR LMFBR STAINLESS STEEL TUBING

Nine extrusion billets of type 316 stainless steel were extruded into 2.1-in.-OD × 1.36-in.-ID × 50-in.-long tube shells. Two of the nine tube shells were tube reduced to 1-in.-OD × 0.8-in.-ID × 240-in.-long tube hollows. Defects on the tube hollows were traced to a misaligned tail stock. The misalignment appears to have been a consequence of the methods used to instrument the tube reducer. This problem is being corrected.

Tubing was fabricated from type 316 stainless steel (Allegheny-Ludlum Steel Corporation heat 65808) with variable reduction of area per pass and interpass annealing temperatures. Specimens from this lot of tubing are being prepared for tests of mechanical properties at 450, 550, and 650°C.

Studies of planetary swaging are under way on type 316 stainless steel. The swaging conditions caused a problem of surface flaking that became worse as the reduction per pass was increased. Concurrent work on type 304 stainless steel indicates some of the reasons for the surface cracking. A tube that was ironed and sunk by planetary swaging developed surface cracks during the second pass, at 26% total reduction, while a tube that was sunk by mandrel drawing and ironed by planetary swaging had no defects after six passes (47% total reduction).

Biaxial stress-rupture tests on planetary-swaged and mandrel-drawn tubing are in progress.

7. WELDING DEVELOPMENT FOR LMFBR VESSELS AND COMPONENTS

We have compiled existing stress-rupture data on strength and ductility of stainless steel welds and have oriented our program to determine reasons for the large scatter in data — particularly in ductility. Base plate and filler wire were procured, and preliminary welds were made that bracket the range of practical welding conditions for the submerged-arc process. Specimens for preliminary tests of mechanical properties were prepared.

Characterization of welds produced for the Fast Flux Test Facility weldment irradiation program is continuing. The electron microprobe is being used to determine the approximate composition of ferrite in the weld metal.

8. SHIELDED METAL-ARC WELDING FOR LMFBR COMPONENTS

We procured a series of electrodes with type 308 stainless steel coatings that have carefully controlled minor differences in composition. We made welds in this material under carefully controlled conditions and machined samples from them for irradiation and mechanical testing.

9. NONDESTRUCTIVE TESTING TECHNIQUES FOR LMFBR

We are developing new methods and equipment for nondestructively evaluating materials or components related to the LMFBR program. We are

using electromagnetic-induction, ultrasonic, and penetrating-radiation test methods.

We began the design of a new kind of eddy-current instrument for determining the depth of flaws beneath the inspection surface. Preliminary studies were made on the use of optical schlieren techniques on welds to aid the development of ultrasonic inspection techniques.

We prepared two sets of samples of stainless steel containing varying degrees of cold work. Preliminary measurements of magnetic permeability by an electromagnetic-induction technique on sheet specimens show good correlation.

10. SODIUM CORROSION STUDIES

We constructed a series of capsules to compare the effect of O in Na on V and V alloys at 600°C. The alloys to be tested are V–5% Cr, V–10% Cr, V–15% Cr, V–20% Ti, V–15% Cr–5% Ti, Vanstar 7, Vanstar 8, and Vanstar 9. The alloys are being exposed to Na containing 2000 ppm O in capsules of type 304 stainless steel for 100, 200, 300, and 600 hr.

A thermal convection loop with a surface area ratio of 1:4 of V to type 304L stainless steel was terminated after operating 3000 hr. Commercial and high-purity V specimens from dissimilar-alloy static capsules of type 304L stainless steel showed increases in C and N at 700 and 800°C (transfer was considerably greater at 800°C). Only the high-purity V increased in O. At 700°C, interstitial transport from type 321 stainless steel was negligible compared to that from type 304L stainless steel. The interstitial mass transport from the type 304L stainless steel led to reduced ductilities at room temperature for both grades of V, but there was no change in the tests with type 321 stainless steels.

The rates of O contamination for unalloyed V were determined from 400 to 900°C for vacuum (4×10^{-8} torr) and O_2 pressures of 2×10^{-6} and 2×10^{-7} torr. The contamination rate goes through a maximum at about 550°C. Diffusion kinetics appear to control the rate below the maximum, and there is a decrease in the number of O atoms adsorbed above the maximum.

The long-term studies (5000 hr) of the compatibility of thermal insulation with stainless steel were completed. Weight gain at 760°C showed that the scaling of type 316 stainless steel increased more between 1000 and 5000 hr in moist air than in dry air, and nearly the same scaling resulted at 760 and 730°C when the surfaces were prepared by machining or pickling. An apparatus designed to study the effect of Na on the oxidation of stainless steel was built, and the first tests are in progress.

11. DEVELOPMENT OF FAST-REACTOR NEUTRON-ABSORBER MATERIALS

Our studies are directed toward obtaining a better understanding of irradiation behavior of absorbers to be used in fast reactors. Current interest is directed toward well-characterized B_4C.

We have found that commercial grades of B_4C powder consist of mixtures of particles that vary in B:C ratio, internal porosity, and surface graphite. The electron scanning microscope was used to show surface morphology of the powders. Specialized techniques of x-ray diffraction and metallography were developed to characterize these powders. Very fine polyhedral voids are found in the material depending upon the composition. Some metastable phases were observed but as yet are unidentified.

Irradiation tests were planned, and materials for these tests are being prepared.

PART II. SPACE POWER TECHNOLOGY

FUELS

12. DEVELOPMENT OF URANIUM MONONITRIDE FUELS

The third capsule for irradiation testing of UN has operated successfully for 4500 hr with cladding temperatures up to 1400°C. The cladding is T-111 (Ta–8% W–2% Hf).

CLADDING AND OTHER STRUCTURAL MATERIALS

13. CLADDING MATERIALS FOR SPACE ISOTOPIC HEAT SOURCES

Studies of the interaction of stress and vacuum on the creep properties of Haynes alloy No. 25 were concluded. We found degradation of creep strength due to the evaporation of volatile alloying elements to be most severe in thinner materials. We attribute this behavior to the greater volume fraction of the specimen that is affected, which reduces the amount of the strengthening Laves phase that can be precipitated.

An ordered developmental alloy (Ni–38.8% Co–22.5% V) was shown to have a marked advantage in creep strength over conventional alloys, including Haynes alloy No. 25. We are investigating Pt-based alloys in an attempt to combine the advantages of higher melting point, negligible evaporative losses, superior oxidation resistance, and the strengthening provided by ordered structure. Initially, we are studying Pt-Cr and Pt-Mo alloys.

14. PHYSICAL AND MECHANICAL METALLURGY OF REFRACTORY ALLOYS

The strong age-hardening effect observed in Ta–50 wt % Hf at 850°C is attributed to the β to α eutectoid transformation of a Hf-rich phase and the precipitation of a large volume of fine particles. A similar but smaller effect was observed in a Nb–58 wt % Zr alloy. X-ray studies have not confirmed the existence of a miscibility gap in the Nb-Hf system as reported in the literature. Oxygen and nitrogen impurities may affect the phase relationship. The creep strength of TZM was shown to be a function of the reciprocal subgrain size produced by the fabrication variables. Several methods for joining Pt tubes to Ta–10% W tubes are being investigated. Various degrees of success for producing leak-tight joints were attained. The physical properties of Ta between 80 and 400°K are reported.

15. TUNGSTEN METALLURGY

We have determined the effect of starting structures and extrusion temperature on the structure of duplex extruded powder-metallurgy W tubing. At extrusion temperatures of 1450°C and higher, recrystallization and grain growth occur during preheat; but at 1150°C, a wrought extruded structure is produced if the material is recrystallized before extrusion. We are continuing to investigate methods for minimizing formation of nodules during the chemical vapor deposition of W–5% Re. Experiments with pulsing, reversing, and filtering the gas flow or increasing the H_2:(WF_6+ReF_6) gas ratio were unsuccessful in eliminating the formation of nodules. In a feasibility study on chemical vapor deposition of V, dense metal deposits were obtained by the H_2 reduction of VCl_4 and VF_5 at temperatures above 900°C.

A comparison of the creep-rupture properties of arc-melted and powder-metallurgy W–25% Re sheet at 1650 and 2200°C showed that the powder-metallurgy material has a shorter rupture life and lower rupture ductility than arc-melted material. On the basis of secondary creep rate, powder-metallurgy material is weaker than arc-melted material at 1650°C but stronger at 2200°C. This behavior is explained by difference in grain-boundary mobility and void growth.

We continued our evaluation of the long-time creep and stress-rupture properties of arc-melted W-Re alloys. Creep data at 1650°C and stress-rupture data between 1400 and 2200°C are presented for W–25% Re. We are also performing interrupted creep tests on powder-metallurgy W at 1600°C and examining void distributions and dislocation configurations at strains between 2 and 10%. Studies on the effect of low pressure O_2 on the creep properties of W show the creep rate in 7×10^{-5} torr O_2 is twice that at a base pressure of 1.3×10^{-7} torr. This behavior is attributed to the higher rate of W sublimation in low pressure O_2 and to either O dissolving in the W or O_2 increasing the rate at which creep cavities grow.

In our joining studies on W alloys, we are developing filler metals that have melting points lower than that of W to minimize thermal stresses, recrystallization, and grain growth in the heat-affected zone. Powder

metallurgy W sheet was successfully welded with Mo-Re and W-Mo-Re alloy filler metals.

16. FAST-NEUTRON IRRADIATION EFFECTS ON ELECTRICAL INSULATORS

Silicon oxynitride (Si_2ON_2) changed very little in volume during irradiation over the fast-fluence range 1.6 to 5.5×10^{21} neutrons/cm^2 (> 1 Mev) at temperatures below 100°C. There is an initial shrinkage followed by expansion at high fluences.

Translucent Lucalox Al_2O_3 was irradiated at very low temperatures (70 to 90°C) to fast fluences ranging from 1.8 to 5.5×10^{21} neutrons/cm^2 (> 1 Mev). The volume expansion at high fluences (above 3.6×10^{21} neutrons/cm^2) was very much less than was previously observed in irradiations at higher temperatures.

An assembly containing combinations of insulators and metallic conductors was irradiated in the Engineering Test Reactor. Postirradiation examinations are in progress.

17. CORROSION STUDIES OF ADVANCED REFRACTORY METALS

We have planned a series of thermal convection loop tests to evaluate the corrosion behavior of W and W-Re alloys in flowing Li at 1350°C. Loops of unalloyed W and W—25% Re are now under construction.

We have developed improved techniques for installing the W-Re thermocouples used in our Li loops. This was necessitated by failures of both sheathed and bare-wire couples during a trial run of our T-111 pumped Li loop (FCLLL-1). Three types of couples are now being installed on the loop: W-Re wires contained in a Ta sheath; bare W-Re wires spot welded directly to the loop; and bare W-Re wires mechanically tied to the loop.

Measurements of the coefficient for distribution of O between K and Zr, which heretofore had been impossible, were made by means of an improved method for determining the O content of the K. Fast-neutron activation analyses for O verified our prediction that the coefficient exceeded 1000.

When a series of Nb specimens to which 300 to 1650 ppm O had been added were exposed to Li at 600°C, the threshold O concentrations for Li penetration were found to be 400 and 800 ppm O for intergranular and transgranular penetration, respectively.

PART III. GENERAL REACTOR TECHNOLOGY

FUELS

18. FISSION-GAS RELEASE AND PHYSICAL PROPERTIES OF FUEL MATERIALS DURING IRRADIATION

Thermal diffusivity data obtained during irradiation have indicated that stored energy is present in two forms: one part results from long-term buildup with irradiation and one depends on the immediate irradiation history. The data-measuring and -processing techniques work with high precision. The mathematical processes for obtaining values of thermal diffusivity still need further development because of the erratic release of stored energy. Fission-gas release from the specimen shows that it remains in good condition.

19. DEVELOPMENT OF FUEL ELEMENT FABRICATION

A proposed technique for reducing losses caused by blistering is to provide more porosity in the filler sections by adding powdered ZrO_2 to the Al. Such plates were successfully fabricated, and the number of blisters was reduced. We found that plates fabricated from loose-fitting powder cores do not blister, while others fabricated similarly from dummy wrought cores do blister. With the powder cores, misfits in size as large as 5.3% were fabricated without blistering, while 1% misfit produced blistering in wrought cores. In studies of the effects of plate cleaning on bonding, as measured by interfacial grain growth, we found that for ranges investigated neither the concentration nor the temperature are sensitive variables in the Oakite 160-HNO_3 process. The amount of grain growth was, however, reduced by 10% by excessive use of the solution. Nickel present on the surface of the Al seriously interferes with this cleaning technique.

Studies of the mechanism by which fuel plates deform during fabrication continued. We showed that the first two rolling passes do not densify the powder cores very much, but the next three do. Cores with tapered or shaped ends increase in density more quickly than the rectangular ones since they do not elongate as much. We again found that a gap formed at the end of the core in these plates during the initial passes.

We are attempting to reduce dogboning by using low-density cores. We were able to vary the density of pressed cores by varying the compacting pressure. Cores showed comparable densities whether the fuel was U_3O_8 or UAl_x. In the degassing step, the expansion of the oxide cores was not dependent on temperature while that of the UAl_x cores was.

Miniature fuel plates with carefully determined distributions of particle sizes were fabricated to check on the effects of fuel particle size and surface area on homogeneity as measured by the scanner. Values of surface area and toluene density were measured for the various size fractions of both high-fired and burned U_3O_8 and were found to be independent of the particle size. No differences in void concentration were found in plates with cores of varying thicknesses or from the various particle-size distributions, but differences were found between the two types of oxide.

We have shown that the primary source of error in the use of radiography and densitometry in determining fuel homogeneity is the ±0.02 inaccuracy due to limitations of the densitometer for measuring film density. This can cause an error of ±5% in homogeneity data. If a step wedge is used on each radiograph, only reasonable control is required over such variables as x-ray energy, exposure time, and film processing. We found, however, that exposing used film to an amber safelight could cause erroneous readings.

The G-12 loop facility in the Engineering Test Reactor (ETR) was shut down, and all samples are being returned to Oak Ridge. We are studying the possibility of continuing the irradiation program on dispersion fuels in the High Flux Isotope Reactor (HFIR). Preliminary studies indicate that significantly fewer calendar days will be required to achieve the desired burnup in the HFIR than in the ETR. A curve

plotted from existing irradiation data indicates that swelling is primarily a function of initial void content and burnup. If these are known, the expected swelling may be predicted within ±1%.

We have now incorporated into this project a new task on refractory-metal dispersion fuel elements. We are examining in the High Radiation Level Examination Laboratory samples of W-Re-Mo clad W-UO_2 and W-UO_2-ThO_2 specimens prepared and irradiated by the General Electric Company. As the result of a fission break, the samples were removed from the Oak Ridge Research Reactor after achieving a burnup of 1.5×10^{20} of a scheduled 2×10^{20} fissions/cm^3. On examination, it was determined that the fission gas was released from a pinhole leak in a single sample. Dimensional measurements show that all samples swelled.

20. TECHNICAL ASSISTANCE IN PROCUREMENT OF FUEL ELEMENTS

Representatives of the National Lead Company visited ORNL to review recent developments in the manufacture of fuel elements. We discussed causes and control of nonuniform deformation (dogboning), manufacturing of UAl_x, procedures for use of unclad type 6061 Al in fuel plates, and the production of the High Flux Isotope Reactor fuel elements.

CLADDING AND OTHER STRUCTURAL MATERIALS

21. BEHAVIOR OF REFRACTORY MATERIALS UNDER IRRADIATION

Refractory-metal carbides were irradiated at temperature between 65 and 130°C to fast fluences from 0.1 to 0.7×10^{21} neutrons/cm^2 (> 1 Mev). Initial slopes of the curves for $\Delta V/V$ versus fast fluence were obtained from the data plots: TiC, 0.24; ZrC, 0.22; TaC, 0.15; NbC, 0.14; WC, 0.24. Specimens that had previously been irradiated at higher temperatures (175 to 400°C) were annealed out-of-reactor at temperatures up to 1100°C. In each case, there was a rapid reduction in fractional volume increase followed by a leveling off at 900 to 950°C. The annealing data aided in the development of a mechanism for neutron damage, based on irradiation annealing, that explains the initial saturation of volume expansion of carbides.

A low-temperature (about 150°C) assembly containing depleted nitride fuel specimens is now being irradiated in the Engineering Test Reactor. A high-temperature (1000°C) assembly is being prepared for a similar irradiation. These experiments are designed to evaluate the effects of He generation in nitride fuels through the $^{14}N(n,\alpha)^{11}B$ fast reaction by comparing property changes of specimens made with ^{14}N with those of specimens made with ^{15}N, which does not undergo the (n,α) reaction.

Assemblies are being designed and specimens are being prepared for irradiation of fast-neutron absorbers in the Experimental Breeder Reactor-II blanket. Specimens of B_4C of two different B:C ratios, Ta metal, TaC, and other absorbers will be irradiated at 400 and 750°C.

22. JOINING RESEARCH ON NUCLEAR MATERIALS

We metallographically examined the Inconel 600 hot-ductility specimens discussed previously and determined the effects of S, P, and Mn on their microstructures. The addition of nominal amounts of C, Mn, Si, and Cu to the ternary Ni–15.5% Cr–8% Fe alloy resulted in a grain refinement in both the unaffected base metal and the fracture area of the hot-ductility specimens. At the zero-ductility temperature (ZDT), small amounts of S resulted in liquation in the grain boundaries and, as the level of S increased, in liquation in laminations in the base metal. Phosphorus had essentially no effect on the microstructure of the annealed base metal and no apparent effect on the microstructure of the area heated to the ZDT. Additions of Mn to an alloy nominally containing 0.010% S resulted in a coarsening of the grains.

A mathematical model developed by Rensselaer Polytechnic Institute provides an acceptable statistical fit with the experimental data previously obtained on the effect of minor elements on the weldability of Inconel 600.

Shielded metal-arc stainless steel welding electrodes for depositing 0, 2, 5, 7, 10, and 15% ferrite were obtained, and welds were made with an automatic head. Bead-on-plate welds were produced at heat inputs from 10,000 to 60,000 J/in. These welds are being evaluated metallographically.

Specimens containing documented discontinuities for short-time stress-rupture and tensile tests were produced. Scanning electron microscopy is being used to characterize weld fractures in Inconel 600. These will be compared to fractures in other Ni-base weld metals.

23. NONDESTRUCTIVE TESTING

We are developing new techniques and equipment for the nondestructive testing of materials and components. The major emphasis has been on methods involving eddy currents, ultrasound, and penetrating radiation.

In our analytical work on electromagnetic phenomena we developed solutions to integral equations for additional configurations of coil and conductor, including the cases of a coil between a number of conducting plates and a coil encircling two concentric, spherical shells. We are trying to improve the accuracy of equations for the case of a defect in a conductor.

Improvements were made to our schlieren system that increase the sensitivity for pulsed operation. We can now record sequences on video tape or motion picture film. We are using a system of ultrasonic frequency analysis to study reflections from flat, circular reflectors as a function of several variables, including specimen material and the size and orientation of the reflector. We increased our capability for making and measuring precision reference notches through use of Ta tools and improved tool holders.

A preliminary study was made to determine the capability of our scanning system for x-ray attenuation to measure variations in graphite density. Data is being accumulated on the use of ^{241}Am and ^{147}Pm for measuring the thickness of cladding by methods based on radiation scattering.

24. IMPROVEMENT OF HASTELLOY N AND RELATED COMPOSITIONS

Several chemical modifications of Hastelloy N are being studied in an effort to develop an alloy with improved resistance to embrittlement by neutron irradiation. Additions of 1% Ti result in an alloy containing

the MC type of carbide with good properties both before and after irradiation. Lesser amounts of Ti lead to the formation of mixed MC and M_2C types of carbides with less attractive properties. Alloys that contain Nb, Hf, and Yt also look promising with fracture strains of 4 to 23% (compared with 0.5 to 3% for standard Hastelloy N). There still appears to be a strong correlation between good postirradiation properties and formation of the MC type of carbide.

25. ADVANCED MATERIALS FOR STEAM GENERATORS

We are determining the resistance of weldments between dissimilar metals to corrosion by steam at 595 and 650°C. Measurements of the weight gained and the thickness of the scale formed by specimens showed good resistance for most weldments at both temperatures for times to 6000 hr. However, some spallation was noted in welds of the IN 102 alloy at 650°C. Stress-corrosion studies at the lower temperature for times to 4000 hr revealed no cracks or evidence of crack propagation that could be attributed to stress corrosion.

PART I

FAST REACTOR TECHNOLOGY

FUELS

1. DEVELOPMENT OF FAST-REACTOR OXIDE FUELS

P. Patriarca A. L. Lotts

The objective of this program is to obtain an economically optimized $(U,Pu)O_2$ fuel cycle for a liquid-metal fast breeder reactor (LMFBR) by extending the performance capability and advancing the fabrication technology of oxide fuels. These fuels have the most advanced technology and greatest potential for reliable operation in first-generation LMFBR's. They have been tested in fast-flux environments but as yet have not been exposed under actual prototypic conditions. Currently, the burnup and heat rate are limited to about 50,000 Mwd/metric ton and 16 kw/ft, respectively, based on irradiation experiments with fuels that are not necessarily optimized for thermal, chemical, and mechanical performance.

The capability of oxide fuels can possibly be improved by adjusting structures or void distribution in the fuels. We emphasize irradiating fuels derived from the sol-gel process with thoroughly characterized structures and void distributions different from those of the oxide fuels irradiated heretofore. These include fuels fabricated by Sphere-Pac, vibratory compaction, extrusion, and pelletization. We compare the performance of these with the performance of reference fuels such as pellets derived from mechanically blended powders and coprecipitated material. The development of computer programs to assist in the analysis of test results and the development of a mathematical model to predict the performance of a fuel rod are integrated with the test program.

Preparation of $(U,Pu)O_2$ Fuel Materials

W. T. McDuffee[1]

Preparation of PuO_2 Sol

We prepared 315 g of Pu as PuO_2 sol by our standard precipitate-bake-peptize procedure, which results in a 1 to 3 M sol, for use in fabricating pellets for various irradiation capsules.

Preparation of Microspheres

We prepared about 600 g of $(U_{0.80},Pu_{0.20})O_2$ microspheres for use in irradiation capsules. We prepared the UO_2 sol by the CUSP process[2] in our laboratory-scale equipment. We equilibrated this CUSP sol with n-hexanol to extract the formic acid normally present in UO_2 sols, since this acid, if not at least partially removed, causes instabilities when the UO_2 and PuO_2 sols are mixed. We then blended the UO_2 and PuO_2 sols into the $(U,Pu)O_2$ sol and prepared the two sizes of microspheres required for dense packing by the Sphere-Pac process. One-third of these microspheres were < 25 μm in diameter; the rest were 400 to 600 μm in diameter.

Although we were careful to minimize aging effects and other known causes of problems, both in blending the sols and forming the spheres, the yield of good product was low (only about 50% of that usually obtained). We probably need more operating experience with mixed PuO_2 sol and UO_2 (CUSP) sol before we can pinpoint the cause of our trouble.

Development of Fabrication Processes

J. D. Sease

Fast reactors that operate at high specific powers will require fuel pins of small diameter with fuel ranging from 80 to 90% of theoretical density and a high fissile loading. Our work is to develop procedures for Sphere-Pac and pelletization and for fabricating irradiation capsules.

Sphere-Pac (W. L. Moore)

Our objective is to investigate the variables of Sphere-Pac,[3] a technique for loading fuel rods to a high density with graded sizes of fuel microspheres, and to optimize the process for use in production facilities.

Since work to date has indicated that the infiltration of the fine microspheres into the coarse bed controls the rate of the process, this quarter we studied the effects of moisture and the size of the openings in the screen used to retain the coarse bed on the time required to

infiltrate the fine microspheres and compared the amounts of fine microspheres that flow through the core and perimeter of the bed. Two sizes of ThO_2 microspheres were used for these experiments: the fine microspheres were < 37 μm in diameter and the coarse were between 530 and 590 μm in diameter. The loading tube was clamped vertically to a model F010 Syntron 60 Hz vibratory feeder[4] inclined at 45°.

To study the effects of moisture on infiltration time, we loaded microspheres that had been dried at 160°C, microspheres that had been exposed to laboratory air of 50% relative humidity at 26°C, and microspheres that had been exposed to air saturated with water for varying lengths of time into fuel rods 0.186 or 0.245 in. in inside diameter and 8 or 24 in. long. There was no significant difference in the times required for loading the dried microspheres and those that had been exposed to laboratory air. But loading time was increased when the coarse, the fine, or all the microspheres were exposed for 1 hr to air saturated with water; and, after 24 hr of exposure, the loading time was double that required for dry microspheres. Thus, under extreme atmospheric conditions, microspheres can sorb enough moisture to inhibit infiltration.

To investigate the effect of the size of the openings in the screen used to restrain the top of the coarse bed during infiltration, we loaded a series of 0.245-in.-ID × 16-in.-long fuel rods through screens with either 149- or 297-μm openings. The average time required to load a fuel rod through the 149-μm screen was 230 sec, while that for the 297-μm screen was only 145 sec. Obviously, to increase the rate of infiltration, we must use a screen with the largest opening that will still prevent microspheres from being vibrated out of the top of the bed.

To discover whether there were any differences between the rates of infiltration at the core and at the perimeter of the bed, we infiltrated fine microspheres through 1- and 2-in.-long × 0.375-in.-diam beds of coarse microspheres. These beds were supported at the bottom by screens, rather than closed with a solid plug, so that the coarse microspheres were retained while the fine microspheres were free to fall through to a collection tray. Comparison of the amounts of fine microspheres that

infiltrated through the core and through the perimeter of the coarse bed in a given time showed that there was essentially no difference between the rates of infiltration.

We also investigated four methods of feeding the fine microspheres into the bed of coarse microspheres:

1. fine microspheres poured through the normal screen funnel, which restrains the coarse microspheres at the top of the bed;
2. fine microspheres poured through a screen tube, which has a thinner wall than the normal screen funnel and, therefore, provides a greater area for the fine microspheres to enter the coarse bed;
3. fine microspheres poured directly on top of the coarse bed with no retaining screen;
4. fine microspheres poured directly on top of the coarse bed with no retaining screen and with a follower weight on top of the fine microspheres.

The rates of infiltration produced by all four methods were essentially equal.

Pelletization of Sol-Gel $(U,Pu)O_2$ (R. A. Bradley)

We fabricated pellets for two irradiation test capsules, capsule P-9 for the Gas-Cooled Fast Reactor (GCFR) and capsule SG-3 for the Oak Ridge Research Reactor (ORR). The GCFR capsule required 91% dense dished-end annular pellets made from $(U_{0.88},Pu_{0.12})O_2$ (U enriched with 9% ^{235}U). The ORR capsule required 83% dense annular pellets of $(U_{0.80},Pu_{0.20})O_2$. The fuel for both capsules was required to be substoichiometric (O:metal = 1.98 ± 0.01). We prepared the urania-plutonia powder for both of these capsules by blending UO_2 and PuO_2 sols, drying the blended sols to a gel, and grinding the gel to a powder as described previously.[5,6]

In our first attempt to calcine the powder for the 91% dense GCFR pellets, we used the same conditions we used in making the 91% dense pellets for the Transient Reactor Test Facility (TREAT):[7]

1. heat in air at 300°C/hr to 520°C;
2. change to Ar–4% H_2 and hold 4 hr at 520°C;
3. change to CO_2 and hold 1 hr at 520°C;
4. cool in CO_2.

The highest density we were able to obtain this way was 87% of theoretical. Experience has shown that failure to achieve sufficiently high density in sol-gel $(U,Pu)O_2$ is due to the introduction of gross porosity when agglomerates of crystallites sinter and shrink away from adjoining agglomerates. It appeared, therefore, that the calcination given the first batch of GCFR powder had not been effective in breaking up the agglomerates of crystallites. We reasoned that the higher U content of the powder for these GCFR pellets caused it to oxidize more readily and to sinter at a lower temperature than the TREAT powder. Therefore, we decided to reduce the temperature during the oxidation step of the calcination:

1. heat in air to 400°C and hold 1/2 hr;
2. change to Ar–4% H_2, heat to 500°C, and hold 4 hr;
3. change to CO_2 and cool to room temperature in 6–8 hr.

The pellets produced from this powder by pressing at 40,000 to 50,000 psi and sintering at 1550°C were 91% dense. We conclude that two competing processes occur when sol-gel $(U,Pu)O_2$ is calcined in air. The oxidation of the UO_2 to U_3O_8 and the associated change in volume tend to break up the agglomerates of crystallites. Simultaneously, the crystallites are sintered together by the reduction in surface energy. To produce a powder suitable for high-density pellets, one must select the calcining conditions so that the agglomerates are broken up before the crystallites sinter together.

We calcined the powder for the 83% dense pellets for the ORR capsule according to the following schedule:

1. heat in Ar at 300°C/hr to 520°C and hold 4 hr;
2. change to CO_2 and cool.

The forming pressures and densities of pellets produced in a test sinter of the powder in Ar–4% H_2 at 1450°C for 10 hr are given in Table 1.1. On the basis of this test sinter, we chose 30,000 psi as the forming pressure for fabricating the pellets for the ORR capsule. The average density of the ORR pellets was 83.5% of theoretical.

The O:metal ratio of the GCFR pellets was 1.98 ± 0.01 after they were sintered; however, the ORR pellets required heat treatment at 1300°C with a Ta foil getter after sintering to adjust the O:metal ratio to 1.98.

Table 1.1. Forming Pressure and Densities of Pellets from Test Sinter of ORR Powder

Forming Pressure (psi)	Density, % theoretical	
	Green	Sintered
$\times 10^3$		
25	44.2	82.7
30	45.2	83.6
35	45.4	84.4
40	45.7	84.3

Capsule Fabrication (R. B. Pratt, M. K. Preston,[8] R. A. Bradley)

Fabrication of the two instrumented TREAT capsules (TREAT I and II) and the fueled portions of ORR capsule SG-3 was completed. We began planning for the fabrication of the unencapsulated Experimental Breeder Reactor-II (EBR-II) fuel pins for the shared 37-pin subassembly.

TREAT Capsules. – Over the next several years we plan to fabricate a number of TREAT capsules. The first series will consist of four capsules, TREAT I through IV. This quarter we completed the assembly and thermal calibration of TREAT I and II. The major hardware components and finished assembly of TREAT I are shown in Fig. 1.1.

After final assembly and leak testing, we heated each capsule to 435°C to test the heaters and the 12 thermocouples. Heating and cooling curves were obtained for each capsule to calculate the heat capacity, and a preirradiation heating cycle to be used at the TREAT Reactor was established. All data sheets, certification papers for materials, inspection reports, and x rays were compiled. All drawings were revised to incorporate any changes made during fabrication. A final report on the fabrication of TREAT I and II is now being written.

Arrangements for shipping the TREAT capsules to the TREAT were completed. We received approval from the Department of Transportation for shipping these capsules, and we plan to ship them early in October.

ORR Capsules. – The fuel elements for ORR instrumented capsule SG-3 were fabricated and sent to the Y-12 Plant for insertion into the irradiation capsule. These fuel elements are two 3-in.-long fueled annuli

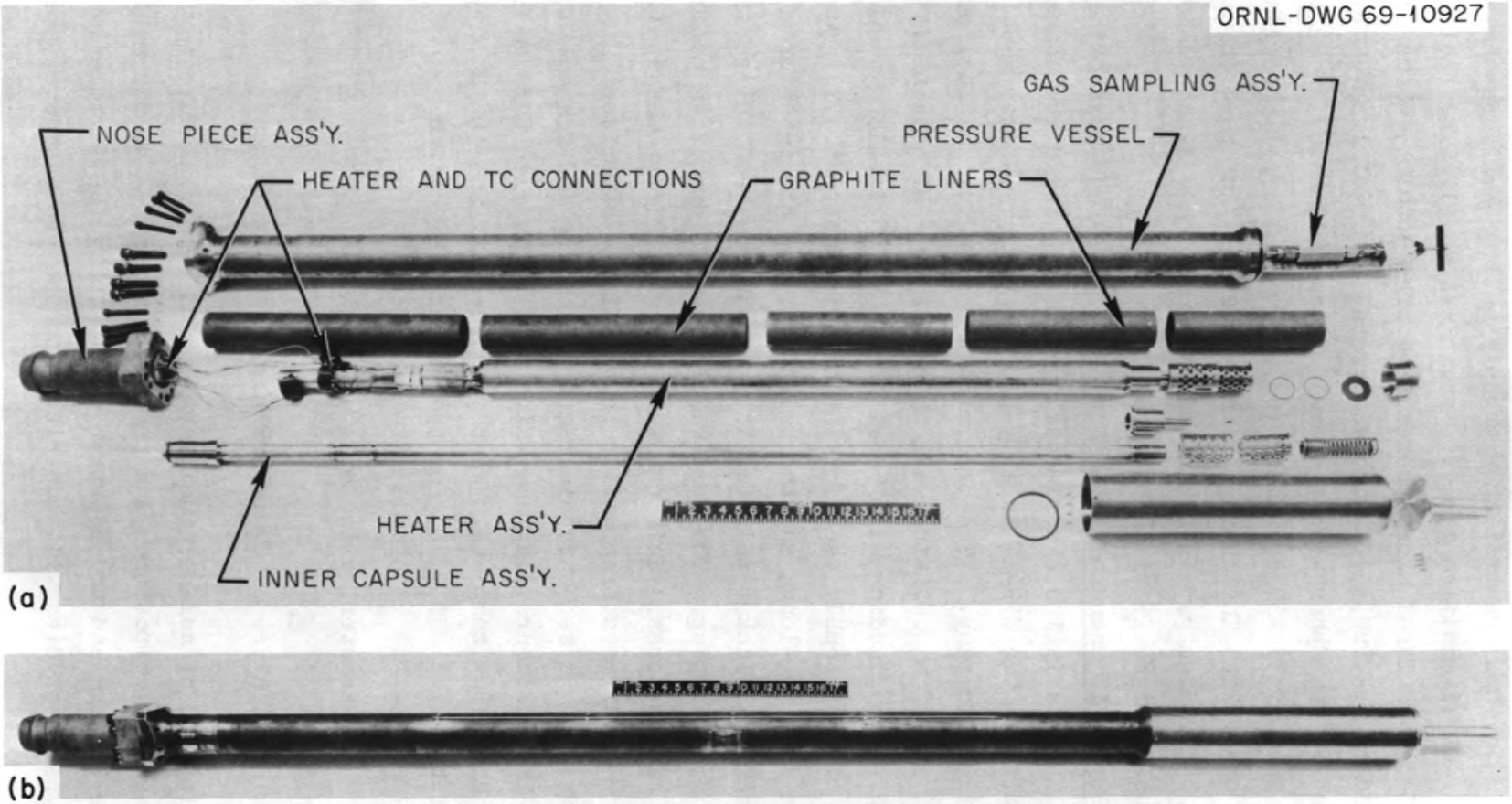

Fig. 1.1. Irradiation Capsule for TREAT I Experiment. (a) Major hardware components. (b) Completed assembly.

that have a 1/8-in.-diam central thermocouple well of W–25% Re and are clad in 3/8-in.-OD Ti-modified type 304 stainless steel. The fuel used in fuel pin SG-3A was TREAT microspheres from fuel lot 103, which nominally contained $(U_{0.80},Pu_{0.20})O_2$ with an O:metal ratio of 1.987. The fuel was loaded by the Sphere-Pac process to a smear density of 82.1% of theoretical. Fuel pin SG-3B contained $(U_{0.80},Pu_{0.20})O_2$ pellets with an O:metal ratio of 1.992. The average density was 83.5% of theoretical; when the 0.0025-in.-diam gap is taken into account, this is equivalent to a smear density of 82.2% of theoretical.

EBR-II, Series II Unencapsulated Fuel Rods. – As our next oxide-fueled fast-flux irradiation experiments, we plan to irradiate unencapsulated fuel pins in the EBR-II in a 37-pin subassembly shared with the Babcock and Wilcox Company.[9] The preliminary design for the fuel pins requires 0.250-in.-OD × 0.015-in.-wall thickness type 316 stainless steel cladding. The cladding will be either 40 or 60 in. long, depending upon the type of subassembly used for the irradiation test. The fuel column will be 13.5 in. long, and the balance of the pin interior will contain depleted UO_2 blanket pellets, ThO_2 insulators, and an extensometer shielded by a Ni plug. The fuel will be loaded either as pellets or Sphere-Pac microspheres. This quarter, our main effort was applied to studying the requirements set forth in the EBR-II experimenter's manual and developing a sequence diagram for planning and scheduling the fabrication. This sequence diagram, which will be handled through a computer, is now about 80% complete. We began preparing the $(U_{0.80},Pu_{0.20})O_2$ powder (U enriched with 93% ^{235}U) for the pellet fabrication.

Characterization of $(U,Pu)O_2$ Fuels

J. M. Leitnaker D. L. McElroy C. S. Morgan

The development of sol-gel fuel fabrication requires characterization of both the chemical composition and physical properties of the material to control the process and to interpret meaningfully the irradiation behavior. Thermodynamic studies will contribute to the process development

for the fuel and will aid in predicting fuel performance for both irradiation testing and model studies.

Analytical Chemistry (W. H. Pechin)

We are trying to find how best to use analytical chemistry for the control of the fabrication process and for the qualification of the $(U,Pu)O_2$ fuel for irradiation testing. The factors of major interest are the relevance, precision, and accuracy of the various analyses.

Gas release from the fuel at elevated temperature concerns us because of its contribution to the total pressure within a fuel rod and because of its possible effect on the chemistry of the fuel during irradiation. A desirable maximum value for gas release is 0.05 cm^3/g (STP) at 1600°C, but we have observed values as high as 0.30 to 0.50 cm^3/g for some of our pellet fuels. We devised a series of analyses of existing materials to determine the source of this gas and to find means of controlling it. The factors that we hypothesized might affect gas release were the C, N, and water contents of the fuel, because of their possible evolution in gas form (Table 1.2), and the O:metal ratio and surface area, because of their possible effects on the adsorption of water. The equipment for measuring evolved water is not yet available for alpha-emitting materials, so this analysis was omitted. The surface measurements by the Brunauer-Emmet-Teller (BET) method are not sensitive enough to detect the variation between pellet runs, so porosity measurement was substituted for that test. The gas release was measured at 1600°C in equipment described previously.[10] The material used in this study was originally prepared as fuel for transient testing; we analyzed the pellets that remained after TREAT capsules I and II were loaded. The O:metal ratios for the various sintering runs are listed in Table 1.3. Not enough pellets remained from sintering runs 82 and 83 for complete analyses.

Results of the measurements of C, N, density, and porosity are listed in Table 1.4. The data for runs 78 through 81 were treated by a technique of analysis of variance to determine which runs had analyses significantly different from the others. The C content did not vary

Table 1.2. Gas Volume Formed by Complete Reaction of 100 ppm of Several Impurities

Impurity	Gas Volume (cm^3/g)
H_2O	0.12
C	0.186
N	0.08

Table 1.3. Ratio of Oxygen to Metal in Pellets Loaded into TREAT Capsules I and II

Sintering Run	O:Metal Ratio	95% Confidence Interval
78[a]	1.992	b
	1.990	±0.056
79[a]	1.973	±0.009
	1.990	b
80	1.991	±0.017
81	1.987	±0.004
82	1.984	±0.037
83	1.983	±0.021
84	1.982	±0.016

[a]We intended to adjust the O:metal ratio during the sintering process, but where this ratio was not satisfactory after sintering, the pellets were further heat treated. Pellets from sintering runs 78 and 79 were each treated in two separate batches.

[b]Only one determination made.

Table 1.4. Analytical Results[a] for TREAT Pellets

Sintering Run	Content, ppm		Bulk Density (g/cm^3)	Porosity[b] (%)
	C	N		
78	85	40	9.14	18.17
79	71	19	9.23	17.91
80	74	54	9.04	19.46
81	77	47	8.60	23.10
82	66			
83	43			

[a]95% confidence limits: C content, 28 ppm; N content, 21 ppm; bulk density, 0.38 g/cm^3; porosity, 2.37%.

[b]Determined by Hg porosimeter.

significantly. The lower N content of run 79 is significant compared to the precision of the analysis, as is the higher porosity of run 81. The analysis of variance also gave information on the precision of each of these analyses:

Analysis	Standard Deviation
C content	20 ppm
N content	15 ppm
Bulk density	0.29 g/cm^3
Porosity	1.78%

Gas release varied greatly with the age of the pellets. The measurements from this study are shown in Fig. 1.2 with several previous measurements on pellets from these sintering runs. These data appear to fall into three general groups. The pellets with highest density from sintering run 83 increased least in gas release with age; most of the pellets with low density increased at an intermediate rate; and some of the pellets from run 79 increased more rapidly with age. We attribute the higher gas release of these pellets from run 79 to the lower O:metal

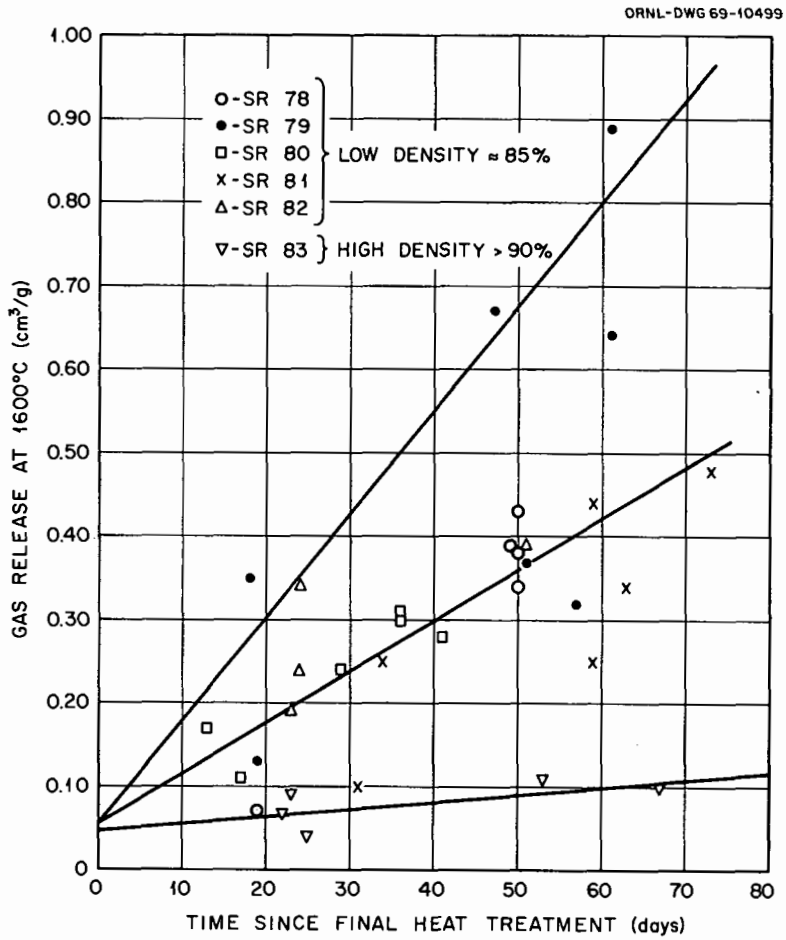

Fig. 1.2. Effect of Age on Gas Released from Mixed Oxides.

ratio that was attained by the first heat treatment. Unfortunately, the time requirements allowed us to sample only a small portion of the gas-release runs for mass spectrographic analysis. The available gas analyses are shown in Table 1.5. The percent recovery of (C + N) shown in Table 1.5 was calculated from the measured volumes of (N_2 + CO) and (N_2 + CO_2) compared to the volumes that would have been measured if all the (C + N) had been evolved as gas. The water content shown in Table 1.5 was calculated by attributing all of the evolved H_2 to the reaction of adsorbed water with the $(U,Pu)O_2$.

The evolution of gaseous products from (C + N) is not inconsistent with that found by Cordinier and Dean[11] when the differences in outgassing temperature and the form of the material are considered. The water contents calculated from the values of gas release, while undesirably

Table 1.5. Composition of Gas from Mixed Oxide Pellets

	Sample		
	Sintering Run 81	Sintering Run 78	Sintering Run 79
Gas volume, cm^3/g	0.25	0.38	0.32
Volume, %			
H_2	84.9	84.0	74.9
H_2O	0.55	1.9	< 0.6
$(N_2 + CO)$	13.8	12.3	23.3
O_2	< 0.3	1.2	0.29
Ar	0.55	0.17	0.58
CO_2	0.28	0.51	0.87
Recovery of (C + N), %	20	26	53
Water content, ppm	177	266	200

high, do not seem too high to be accepted as the explanation for the high evolution of gas. The variation of gas release with age suggests that the pellets are adsorbing water from the atmosphere. The extrapolation of the data for gas release in Fig. 1.2 to zero age indicates that all the pellets were acceptable when first removed from the furnace.

The rate at which moisture is picked up by the pellets is not so rapid that it will cause a severe limitation in handling, since exposure times on the order of minutes probably will not cause a drastic pickup of moisture. The problem does require consideration for storage, however, and means have been devised to protect the fuel from moisture during storage.

The effect of moisture on the gas release from the material described in this study was too great and the variation in C and N content was too small for us to judge the effect of these latter elements. We expect, however, that C and N will be important if the evolution of gas is to be held much below 0.05 cm^3/g.

Analytical Characterization (K. E. Spear)

The experiments reported here were performed to (1) establish standard oxide samples for determination of O content, and (2) establish the

relationship of composition, lattice parameters, and O potential in oxide fuels.[11] Previously, we were also examining the effects of different quenching rates on O distribution and the effect of temperature gradients on stoichiometry, but these experiments were discontinued for the present.

Standard Samples. — A number of standard samples were prepared by heating UO_2 samples at 1200°C for 16 hr in an atmosphere of CO and CO_2 mixed in a ratio of 10:1. Previous work[12] established that these samples are uniform in composition within our experimental error (±0.003 in the ratio of O:metal). This treatment is used to produce the defining samples of $UO_{2.000}$.

Lattice Parameter. — A thermostat was constructed and is ready to be installed in one of the x-ray cameras in the Interim Plutonium Facility. This equipment should yield more precise measurements of lattice parameters.

Behavior of Fission Products (K. E. Spear)

Fission products in mixed oxides may cause several important effects. One of these is that they may interact directly with the cladding material. A second effect is that these fission products will affect the O potential of the fuel and, as a secondary result of this effect, that O will react with the cladding material. A third effect is that the volume of the fission products may cause the cladding to swell.

Reactions Between Stainless Steel and $(U,Pu)O_2$. — We previously discussed[11] transport of stainless steel components into the fuel by I in a manner similar to the Van Arkel-DeBoer process.[13] Unless some reaction such as

$$2\ CsI(s) + Fe(s) + UO_2(s) + O_2(g) \rightarrow Cs_2UO_4(s) + FeI_2(g)$$

takes place, our thermodynamic arguments indicated that I transport would be, for all practical considerations, nonexistent.

We attempted to study the reaction directly by mixing UO_2 and CsI in powdered form, placing them in a stainless steel tube, and passing O_2 at a controlled potential over them. The gas passing over the sample

was directed onto a water-cooled collector made of Cu. In order to define the O potential, we used a 99:1 mixture of CO and CO_2. After 4 hr at 550°C, the sample was cooled, and the collector was washed with distilled water. The orthophenanthrolein test (which is able to detect about 10^{-8} mole of Fe in 10 cm^3 of distilled water) failed to indicate any trace of Fe in the water. Kinetic factors may have prevented enough transport of Fe or the stability of Cs_2UO_4 (or another Cs-U-O compound) may not have been great enough to form the Cs compound. Firm conclusions cannot be drawn, and both possibilities should be investigated.

Na-U-O System (K. E. Spear, Annabella Schaupp[14]). — Because of interest in reactions between fuel and Na coolant, we performed a number of experiments with the Na-U-O system. Regions of both low and high O potential have been studied. At the low O potential, we have discovered what is, apparently, a previously unreported compound. The experiments with high O potential have revealed that the Na uranate compounds apparently are not stoichiometric. The purposes of these experiments are (1) to determine the potential of the reaction of Na coolant with $(U,Pu)O_2$ fuel and (2) to lay the groundwork for manufacturing standard samples of these compounds.

In the region of low O potential, a new phase was produced by heating UO_2 with Na_2CO_3. The new phase was produced, as determined by x-ray diffraction, when the components were heated at 900°C in a 10:1 gas mixture of CO_2 and CO for 16 hr. X-ray diffraction showed that the new phase decomposed to UO_2 and Na_2CO_3 when heated at 900°C in a 10:1 gas mixture of CO and CO_2 for 16 hr. (Literature data indicate that Na_2UO_4 can form at both the O potentials defined by the gas mixtures used in these experiments.) That the new compound decomposed to UO_2 and Na_2CO_3 when heated at reduced O potential shows that it is not stable and suggests that Na_2UO_4 also may not be stable under these conditions.

There are two important inferences to be drawn from experiments in the region of low O potential that show that Na uranates are not as stable as thought. First, their tendency to form from interactions of fuel and coolant does not have as large a driving energy as thought. Second, the stability of Cs_2UO_4 is probably also not as great as an

extrapolation of literature correlation would indicate, and the transport of Fe by I, as discussed above, becomes less likely.

X-ray diffraction patterns of the new compound show some resemblance to orthorhombic $CaUO_3$, but the patterns have not yet been indexed. A large batch is being prepared for chemical, x-ray, and metallographic analyses.

In our experiments in the region of high O potential, we have attempted to prepare pure samples of Na_2UO_4 and $Na_2U_2O_7$ to provide background information so that the analogous compounds of mixed U and Pu can be prepared for standards for the electron microscope.

We mix Na_2CO_3 and UO_2 in the proper proportions and heat the mixture in air or O_2. So far, our samples have all been diphasic as determined by x-ray diffraction. Metallographic techniques are being tried on pressed and sintered pellets but, thus far, have yielded uncertain results. We shall not attempt to obtain chemical analyses until we learn how to obtain single-phase material.

Dissolution of Rare-Earth Oxides in $(U,Pu)O_2$ Fuels. — We previously showed that the calculated O potential of a $(U,Pu)O_2$ fuel is dependent on what is assumed to be the bound state of rare-earth oxides.[15] If the rare earths are bound as dioxides and if one started with an O:(U,Pu) ratio of 1.990, that ratio would be only 2.000 at the end of 2 years in a typical fast reactor, while if the rare earths are bound as the sesquioxide, the final ratio would be 2.032. While this difference may not seem great, the resulting difference in the O pressure would be about eight orders of magnitude at 1000°K. The importance, therefore, of fixing, quantitatively, the behavior of these fission products is to model the corrosive behavior of excess O to the cladding. A second reason for performing these studies is to obtain the solid component of the fuel swelling for the ideal case of zero porosity. Any model for a given fuel material must also take into account the geometry allowed to accommodate this swelling.

There are data on the solution of rare-earth oxides in UO_2 in the literature, but not as a function of O potential. It is, of course, O potential that is critical in assessing the reasons for chemical attack of cladding material. Table 1.6 lists the rare-earth fission products

Table 1.6. Important Lanthanide Fission Products[a] in a Typical Fast Reactor

Lanthanide	Relative Abundance[b]	Known Valences[c]
Y[d]	0.037	+3
La	0.122	+3
Ce	0.253	+3, +4
Pr	0.113	+3, +4
Nd	0.331	+3
Pm	0.032	+3
Sm	0.078	+2, +3
Eu	0.015	+2, +3
Gd	0.019	+3

[a]Values for abundance of fission products are taken from K. E. Spear, J. M. Leitnaker, and N. Engel, Fuels and Materials Development Program Quart. Progr. Rept. June 30, 1969, ORNL-4440, p. 19.

[b]Relative abundance is the ratio of the abundance of one rare earth to the sum of all the rare earths considered in this study. The rare-earth elements as a whole are about one-fourth of the total fission products, a ratio of 680:2900.

[c]Taken from T. Moeller, Inorganic Chemistry, p. 896, Wiley, New York, 1952.

[d]Yttrium is often included as a rare-earth metal because the lanthanide contraction makes it similar to the heavier members.

we wish to examine. Initially, we have selected to study oxides of Ce and Eu with UO_2. Later efforts may involve the other materials.

We chose Ce to represent one end of the rare-earth spectrum — both in weight and oxidation state. It can be oxidized to the +4 state and, in fact, is used as an oxidizing agent in analytical chemistry. Europium, on the other hand, is known only in the +2 and +3 oxidation states. Thus, its behavior in UO_2 might give a general indication of the behavior of other rare earths (lanthanide oxides) in solution in $(U,Pu)O_2$.

Initial experiments were performed on Eu_2O_3. For this study, Eu_2O_3 and UO_2 were each equilibrated separately in Pt buckets in a 10:1 mixture

of CO and CO_2 at 1200°C for 16 hr. X-ray patterns revealed the monoclinic form of Eu_2O_3 and the cubic form (a_0 = 5.47075 ± 0.00016 A) of UO_2. These materials were then ground to −325 mesh and mixed by shaking 26.4651 g of UO_2 with 3.1915 g of Eu_2O_3. A 27.0211 g sample from this mixture was heated in a 10:1 mixture of CO and CO_2 for 16 hr. An increase of 0.1005 g was measured, which seems to be outside any conceivable experimental error. If it were assumed that the weight change resulted from oxidation of the Eu in the specimen from the +3 state to a higher state, the Eu would be dissolved as $EuO_{1.88}$. This result seems to indicate that the O potential in a fuel element will not rise as rapidly during burnup as we feared. Further work must establish, quantitatively, the magnitude of the rise. X-ray patterns of the solid solution reveal that true equilibrium was not attained. Further efforts will be required to achieve this.

We performed some preliminary experiments with CeO_2-UO_2 and found it difficult to attain equilibrium in the system. Mixing powders of the two materials, pressing into pellets, and sintering in H_2 at 1450°C is insufficient to achieve equilibrium within 45 min, as determined by x-ray diffraction. Heating at 1800°C for 1 hr in vacuum (10^{-5} torr) does produce a sharp x-ray pattern, indicative of a homogeneous solid solution, but weight losses are quite high because of volatilization. Hence, weight changes are suspect. Two additional approaches were begun: (1) heat samples in a somewhat more oxidizing atmosphere and (2) coprecipitate the samples from solution and then heat at fixed O potentials.

Thermal Conductivity of Lithium Fluoride (P. H. Spindler)

The application of the Rosseland approximation,[16] which is valid only for the optically thick limit of a specimen, did not lead to satisfactory explanations of the transport properties of heat in LiF at high temperatures. Estimating calculations have shown that in both the single-crystal and polycrystal specimens, the optically thick limit may not have been achieved by the size of the specimens in our experiment (radius = 2.54 cm). It remains to be proved whether both samples are acting more or less like a window in the wavelength range in which thermal radiation occurs (0.12 to 9.0 μm); that is, whether photons are

penetrating the material without interaction. We are measuring the absorption coefficient of the polycrystal LiF so that we may calculate the depth to which radiation penetrates as a function of temperature under our measuring conditions. The results will be used as a correction for the Rosseland approximation. In the case of the single-crystal LiF, a calculation, which used negligible photon interaction in the material and assumed boundary conditions of blackbody radiation, yielded a nearly linear relation of thermal resistivity and temperature to 1100°K. This agrees quite well with the extrapolation of data from 200 to 400°K.

Radial Heat-Flow Apparatus for Measurements at 10 atm and 1400°K. — The base plate and water-cooled metal bell jar for this apparatus were tested to 10 atm. The glove box for housing this device was ordered, and delivery is expected in December. Auxiliary equipment needed for assembling the apparatus in our laboratory is being obtained.

Deformation of UO_2 (C. S. Morgan)

We continued investigating the out-of-reactor deformation characteristics of UO_2 specimens prepared from sol-gel powder. We measured the compressive creep of UO_2 sol-gel specimens under a constant stress of 4910 psi from 1200 to 1400°C. The data shown in Fig. 1.3 more nearly

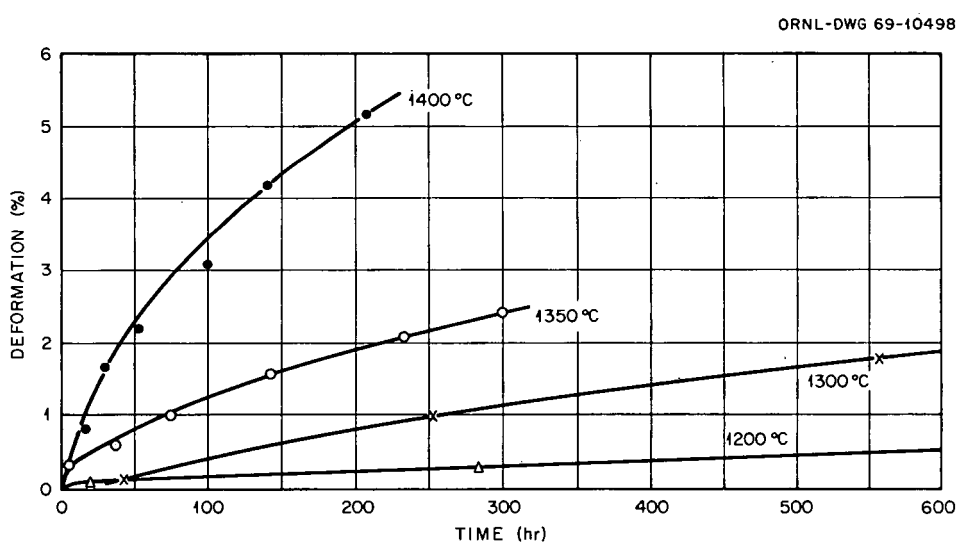

Fig. 1.3. Creep of UO_2 Sol-Gel Specimens Under a Constant Stress of 4910 psi.

represent deformation under conditions that might occur in a fuel element than would data obtained during creep at constant strain rate. (The curve shown in Fig. 1.3 for creep at 1300°C was previously reported erroneously as occurring under a stress of 2140 psi.)[17]

Data on the deformation of UO_2 under constant strain rates at high temperatures are summarized in Fig. 1.4. The primary material studied was UO_2 prepared from sol-gel powder, but specimens fabricated from

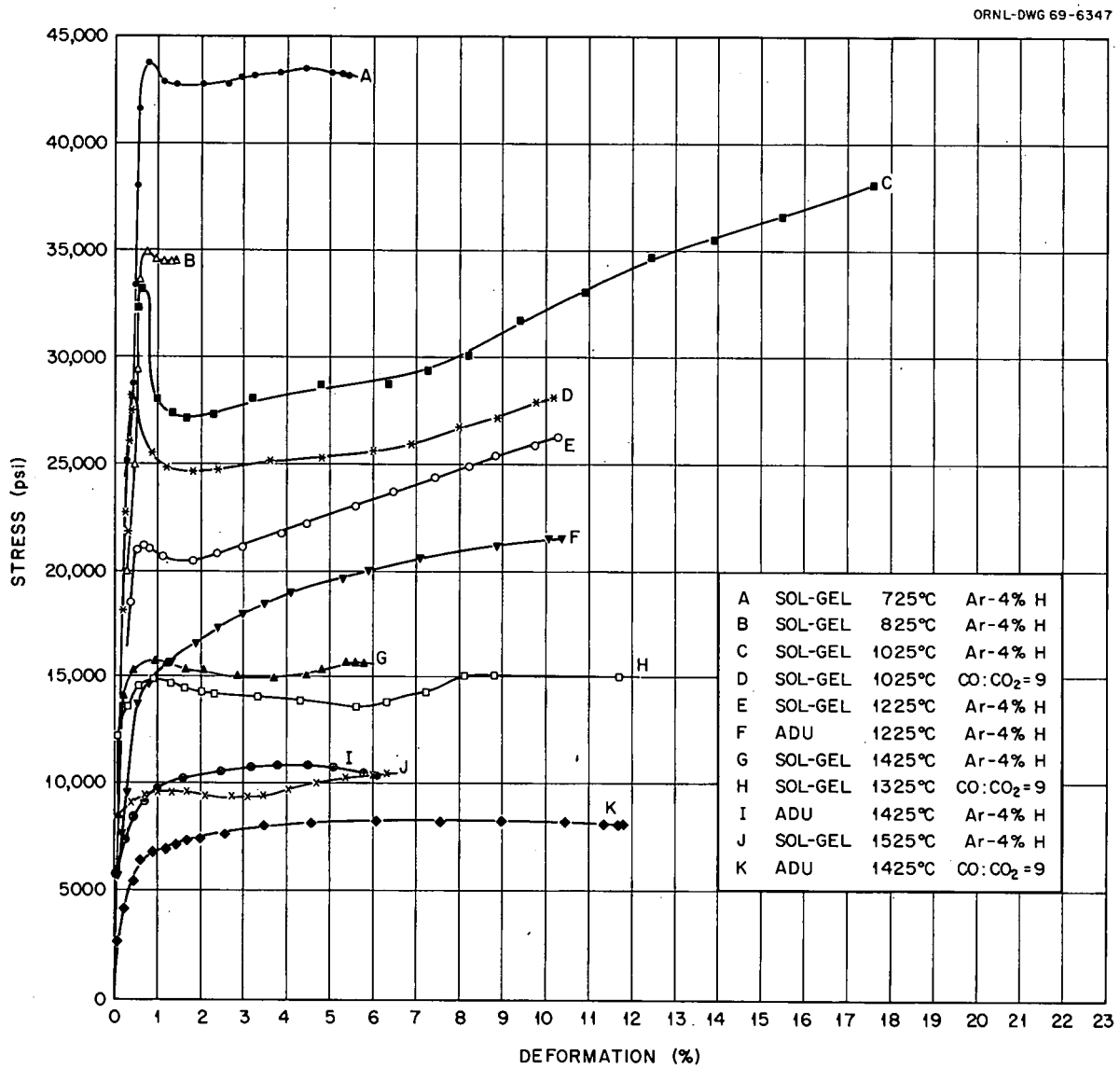

Fig. 1.4. Stress-Strain Curves for UO_2 Specimens Under Constant Compressive Strain Rate of 0.00067 min^{-1}.

powder produced by the ammonium-diuranate (ADU) process were studied for comparison. Compressive deformation behavior at different temperatures was measured at a strain rate of 0.00067 min^{-1}. Tests were made in an Ar–4% H_2 atmosphere and in an atmosphere of CO and CO_2 mixed in a ratio of 9.2:1. The ratio of O:U in these tests should have remained at 2.0 under both atmospheres. We plan further tests of the deformation of sol-gel fuel to investigate why specimens deformed at lower stresses in the atmosphere of CO and CO_2 mixed in a ratio of 9.2:1 than in an atmosphere of Ar–4% H_2.

The ADU UO_2 specimens proved more deformable than the sol-gel UO_2 specimens, even though they were of higher density (97% as compared to 92% for the sol-gel specimens). Since these data were originally reported,[18] we measured the average grain size of the ADU specimens and found 15 μm, as compared with 9 μm for the sol-gel specimens. These results tend to confirm previous observations[19] that grain size may have more effect than density does on the compressive strength of UO_2. The sol-gel specimens tended to have a definite yield point, while the ADU specimens did not. The effect of density on compressive deformation will be investigated further.

Irradiation Testing of $(U,Pu)O_2$ Fuels

C. M. Cox

The performance characteristics of mixed $(U,Pu)O_2$ fuels are being evaluated in a variety of irradiation tests for potential application in an LMFBR. We are now concentrating on comparative tests of sol-gel fuel fabricated as pellets or as microspheres using the Sphere-Pac technique. The program includes thermal-flux experiments, which permit use of instrumented capsules and the achievement of high levels of burnup in relatively short periods of time, and fast-flux experiments in which the fission rate distribution and radiation effects on the cladding are more typical of those for anticipated LMFBR operating conditions. Mathematical models of fuel behavior are being developed in conjunction with the experimental program.

Uninstrumented Thermal-Flux Irradiation Tests (A. R. Olsen, D. R. Cuneo[20])

The current status of the irradiation tests of uninstrumented capsules in the X-basket facilities of the Engineering Test Reactor (ETR) is given in Table 1.7. Each capsule contains four test rods loaded in tandem with a 3-in. fuel column in each rod.[21] This simultaneous irradiation is designed to provide comparison of the relative performance of various fuel forms. A final report on the first three capsules irradiated to low burnup in this series, capsules 43-99, 43-100, and 43-112, is in preparation, and the results will be presented this fall.[22]

Interim neutron radiographs[23] of capsule 43-113 showed no significant changes in the fuel rods or capsule. Therefore, continued irradiation to achieve the scheduled 10% fissions per initial metal atom (FIMA) burnup level has been approved by the ETR safety review committee. The capsule is to be reinserted during the shutdown after cycle 105.

During the past quarter the metallographic examination of capsules 43-103 and 43-115 was delayed because of the scheduled annual shutdown of the High Radiation Level Examination Laboratory for maintenance. This shutdown was extended beyond the normal period for installation of additional equipment, including the transfer system for the shielded microprobe. The alpha and beta-gamma autoradiographs on all selected samples from capsules 43-99, 43-100, and 43-112 and for some of the sections from capsule 43-103 were obtained during this period. In addition, samples were obtained from all four rods from capsule 43-115 for analysis of burnup.

The last four capsules, 43-116 through 43-119, are being irradiated to provide fuel that contains fission products with short half-lives for processing studies.[24] No detailed postirradiation examination of these rods is planned. The first of these capsules contained Sphere-Pac $(U_{0.85},Pu_{0.15})O_2$ fuel irradiated to slightly over 1% FIMA burnup. The studies of the dissolution of this fuel are reported elsewhere.[25] During the past quarter, the AEC requested that we concentrate in these studies on fuel for the Fast-Flux Test Reactor (FTR). Consequently, fuel made to FTR reference specifications has been ordered and will be irradiated instead of the sol-gel Sphere-Pac fuel originally planned for experiments

Table 1.7. Uninstrumented Thermal-Flux Tests of $(U,Pu)O_2$ Fuels

Experiment Number	Fuel		Number of Rods	Peak Burnup (% FIMA)[a]	Peak Linear Heat Rate (w/cm)	Peak Temperature on Inner Surface of Cladding (°C)	Status September 1969
	Form	Composition					
43-99	Sphere-Pac	$(^{235}U_{0.80},Pu_{0.20})O_{2.00}$	2	1.5[b]	1640[b]	1000	Examined
43-100	Sphere-Pac	$(^{235}U_{0.80},Pu_{0.20})O_{2.00}$	2	1.4[b]	1470[b]	900	Examined
43-103	Sphere-Pac Pellet	$UO_{2.02}$ (20% ^{235}U) $UO_{2.00}$ (20% ^{235}U)	3 1	5	690	530	Being examined
43-112	Sphere-Pac	$(^{238}U_{0.85},Pu_{0.15})O_{1.97}$ $UO_{2.02}$ (20% ^{235}U)	3 1	0.7	500	360	Being examined
43-113	Sphere-Pac	$(^{238}U_{0.85},Pu_{0.15})O_{1.97}$ $UO_{2.02}$ (20% ^{235}U)	3 1	10[c]	500[c]	380[c]	In reactor, ≅ 7.5% FIMA
43-115	Sphere-Pac	$(^{238}U_{0.85},Pu_{0.15})O_{1.97}$ $UO_{2.02}$ (20% ^{235}U)	3 1	5[c]	600[c]	460[c]	Being examined
43-116	Sphere-Pac	$(^{238}U_{0.85},Pu_{0.15})O_{1.97}$	4	1.5[c]	600[c]	460[c]	Being examined
43-117 43-118 43-119	Pellets[d]	$(^{238}U,Pu)O_{1.98}$	4	1.5[e]	600[c]	460[c]	In preparation

[a]FIMA is fissions per initial actinide metal atom.

[b]Rods failed in reactor from overpowering.

[c]These are target design values.

[d]Fabricated to Fast-Flux Test Reactor reference specifications.

[e]This is an approximate level. Test will be irradiated for two ETR cycles to produce fuel for reprocessing studies.

43-117, 43-118, and 43-119. We have on hand type 316 stainless steel tubing of 0.230 in. in outside diameter and 0.015 in. in wall thickness that has been fabricated to FTR specifications for these test rods.

ORR Instrumented Tests (R. B. Fitts, D. R. Cuneo,[20] V. A. DeCarlo,[26] K. R. Thoms[26])

The instrumented irradiations in the ORR are designed to monitor the thermal performance of test fuel rods.[27] The temperatures of the cladding and the fuel center and the rates of heat generation in the fuel rods are continuously measured and recorded. These data are being used to evaluate the thermal characteristics of various fuels in the reactor and the effects of irradiation conditions upon the temperatures and rates of structural change within the operating fuels.

The second capsule in this series, SG-2, contained two identical Sphere-Pac $(U_{0.80},Pu_{0.20})O_{1.98}$ fuel rods with 81% smear density.[28] This experiment is intended to provide more detailed confirmation of the thermal conductivity of this fuel at low temperatures and to establish the temperature at which the first metallographically observable structural change occurs during the initial heating in the reactor. The experiment operated normally at fuel-center temperatures up to 1500°C with automatic recording of time, heat generation, and temperature data. These data are being prepared for analysis by a computer code designed to facilitate manipulation of the large amounts of recorded information.

Capsule SG-2 is now undergoing postirradiation examination. The fuel rods were recovered, and their external appearance, shown in Fig. 1.5, is normal. We checked the diameter and bow of each rod by the opposed air gage profilometer and found no significant deviation from the values before irradiation. The gas contained in each fuel rod was collected by the laser puncture technique and will be analyzed for the species present; it appears, however, that one gas sample was lost due to an improper cut during capsule disassembly. Further examination will consist of metallographic studies of the fuel structure.

Capsule SG-3, the third in this series, is almost completely fabricated. It will provide a direct comparison of the Sphere-Pac and pellet fuel forms with fuel-center temperatures that approach 2000°C. The fuel

ORNL-DWG 69-10740

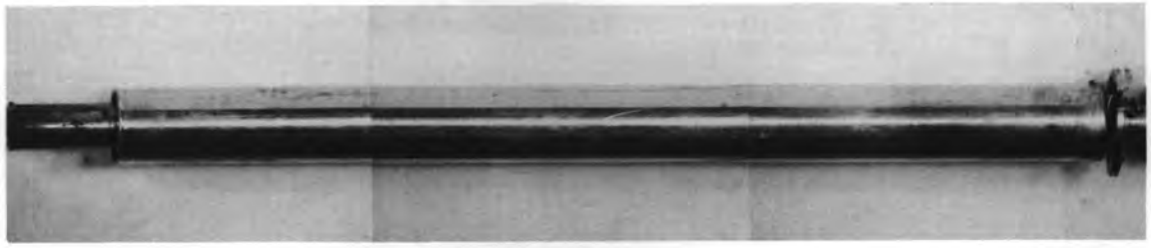

TOP BOTTOM

UPPER ROD

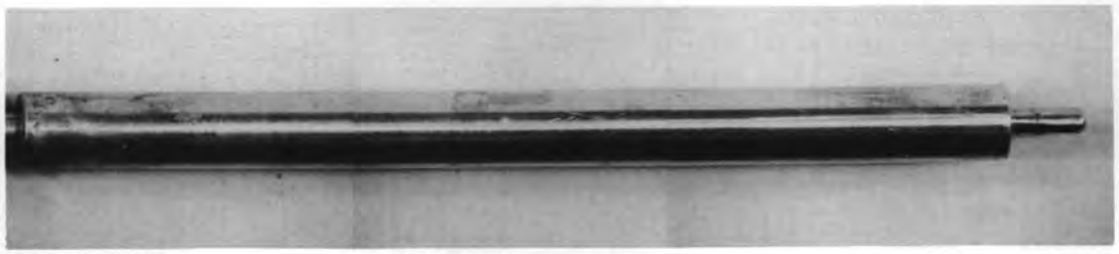

TOP BOTTOM

LOWER ROD

Fig. 1.5. Fuel Rods from Capsule SG-2.

is $(U_{0.80},Pu_{0.20})O_{1.98}$, with 82% smear density, in the form of microspheres in the upper rod and pellets in the lower rod. Both rods will contain thermocouples at the center of the fuel.

ETR Instrumented Tests (C. F. Sanders)

Four instrumented capsules will be irradiated in the ETR. Two capsules, each containing a 20-in.-long fuel column, will be irradiated to determine the performance of long fuel columns of sol-gel-derived oxide fuel fabricated by the Sphere-Pac process. The other two capsules will each contain four 3-in.-long fuel columns, two of which will contain pelletized fuels and two of which will contain Sphere-Pac fuels. These capsules will be operated at moderate peak heat rates (about 15 kw/ft) to investigate the relative swelling of Sphere-Pac and pelletized fuels under conditions of high retention of fission gas. The design specifications are given in Table 1.8.

The detail design was completed, and fabrication of the hardware was started. A request was submitted to Idaho Nuclear Corporation for

Table 1.8. Design Specifications for Instrumented Capsules to be Irradiated in Engineering Test Reactor

	Capsule Numbers	
	43-120 43-121	43-122 43-123
Fuel		
Composite composition	$(U_{0.80},Pu_{0.20})O_{1.98}$	$(U_{0.80},Pu_{0.20})O_{1.98}$
Insulator composition	UO_2	ThO_2
Sphere-Pac composition		
Coarse microspheres	$(U_{0.73},Pu_{0.27})O_{1.98}$	$(U_{0.80},Pu_{0.20})O_{1.98}$
Fine microspheres	$UO_{2.00}$	$(U_{0.80},Pu_{0.20})O_{1.98}$
Column length, in.	20	3
Maximum temperature, °C		
Surface	820	590
Center	2340	1980
Maximum burnup, % FIMA	5 (capsule 43-120) 10 (capsule 43-121)	5 (capsule 43-122) 10 (capsule 43-123)
Peak linear heat rate, kw/ft	19	15.5
Bond between fuel and cladding	He	He
Cladding		
Dimensions, in.		
Outside diameter	0.250	0.250
Wall thickness	0.016	0.016
Maximum temperature, °C		
Outer surface	600	500
Inner surface	660	550
Bond between cladding and capsule	NaK-44	NaK-44
Capsule		
Dimensions, in.		
Outside diameter	1.000	1.000
Wall thickness	0.065	0.065
Fuel rods per capsule		
Total	1	4
Sphere-Pac	1	2
Pellet	0	2
Sleeve dimensions, in.		
Outside diameter	0.625	0.625
Wall thickness	0.035	0.035

the assembly of the instrumentation and for the procurement of the necessary hardware to connect the thermocouple leads to the instruments.

Transient Testing (R. E. Adams, E. J. Manthos)

The initial transient tests will be conducted at the TREAT to compare the transient behavior of unirradiated Sphere-Pac and pelletized sol-gel $(U,Pu)O_2$ fuels. The hazards analysis, test specifications, and operating manual were submitted to the TREAT staff and accepted with minor revisions. We intend to ship capsules TREAT I and II to TREAT for transient tests in October.

Fast-Flux Irradiation Tests (A. R. Olsen)

The series I encapsulated tests described previously[29,30] are continuing their irradiation in EBR-II subassembly X050. The exposure as of August 30 (the end of EBR-II cycle 37) was 5906 Mwd of operation, and the scheduled exposure is 7500 Mwd. The calculated peak burnup for the pin with the highest heat rate in this series is 3.1% FIMA or about 63% of the currently scheduled burnup. Because of the current EBR-II experimental operation at power levels above 50 Mw, experimental fuel subassemblies were removed at the start of cycle 38. Continued exposure is proposed toward the end of cycle 38. Since the test exposure to be accumulated during this cycle is unknown, the discharge schedule for subassembly X050 is undecided. The earliest discharge will be after cycle 39 in January 1970; however, it is possible that further exposure during cycle 40 will be required.

The proposal for approval in principle for the series II unencapsulated tests was submitted to the AEC on August 21, 1969. This proposal involves a 37-pin subassembly to be shared with the Babcock and Wilcox Company; 18 positions will be used by Babcock and Wilcox, and 19 positions will be used by ORNL. The two experimental programs have been coordinated to provide complementary data on fuel performance. Each site will be responsible for the fabrication, inspection, shipping, and post-irradiation examination of its own fuel pins, but a single safety analysis will be prepared for the entire subassembly.

The objective of the ORNL irradiation tests is to establish the performance characteristics and limitations of $(U,Pu)O_2$ LMFBR fuels fabricated by different processes. Particular emphasis will be placed on the effects of fuel form and void distribution on the release of fission gas and mechanical interaction between fuel and cladding at extended burnup (> 50,000 Mwd/metric ton). These data will be used to test and modify, if necessary, the mathematical model for fuel performance being developed at ORNL.

Tables 1.9 and 1.10 show the fuels and burnup levels proposed for irradiation by each of the sites.

The ORNL test pins will contain pelletized and Sphere-Pac fuel produced by the sol-gel process. The postirradiation examination program will include a detailed study of the fuel pins for release of fission gas, fuel swelling, irradiation restructuring, distribution of fuel and fission products, and compatibility of the cladding and Na coolant.

Although we are not proceeding with specific designs for the fuel pins until we receive preliminary approval, we propose to use a fuel pin with a 0.250-in.-OD × 0.016-in.-wall thickness type 316 stainless steel cladding. The cladding material has been obtained from Battelle Memorial Institute Pacific Northwest Laboratory. The fuel column will be 13.5 in. long, and the balance of the fuel pin will contain features similar to those of the ORNL series I test pins.[29,30] The design for the fuel pins to be used by Babcock and Wilcox Company will be similar but may differ in some details. The end fittings will be designed to fit a Mark J subassembly. Since we are interested in performing these tests with maximum cladding temperatures of 550 to 650°C, we investigated the possibilities of revising the Mark J subassembly to accommodate 37 fuel pins with a 0.250-in.-OD cladding.

If we receive approval in principle by October 1, 1969, we will design and fabricate the first 37 fuel pins for delivery to the EBR-II by the end of June 1970.

Table 1.9. Proposed Program of Irradiations by Babcock and Wilcox Company in 18 Positions of a Shared 37-Pin Subassembly of the Experimental Breeder Reactor-II

Fuel Form[a]	Burnup, Mwd/metric ton				
	0	25,000	50,000	75,000	100,000
Vi-Pac	Pin 1				Pin 38
Vi-Pac	Pin 2				Pin 39
Sphere-Pac	Pin 3				Pin 40
Sphere-Pac	Pin 4				Pin 41
Sphere-Pac	Pin 5				Pin 42
Pellet	Pin 6				Pin 43
Pellet	Pin 7				Pin 44
Vi-Pac		Pin 8		Pin 45	
Sphere-Pac		Pin 9		Pin 46	
Pellet		Pin 10		Pin 47	
Vi-Pac			Pin 11		
Vi-Pac			Pin 12		
Vi-Pac			Pin 13		
Sphere-Pac			Pin 14		
Sphere-Pac			Pin 15		
Sphere-Pac			Pin 16		
Pellet			Pin 17		
Pellet			Pin 18		

[a]All types of fuel will be irradiated with a smear density of 82 ± 1% of theoretical.

Irradiation Test Calculations (A. R. Olsen, R. B. Fitts)

We made a series of calculations with the computer codes developed over the past 2 years to describe various features of fuel irradiations. The results of these calculations were incorporated into a paper presented recently.[31] This paper compares the neutronic and thermal environments for a $(U,Pu)O_2$ fuel rod clad with stainless steel and operating in a fast reactor typical of those proposed for commercial application

Table 1.10. Proposed Program of ORNL Series II Irradiation Tests in 19 Positions of a Shared 37-Pin Subassembly of the Experimental Breeder Reactor-II

Sol-Gel Fuel Form	O:Metal Ratio	Smear Density (% theoretical)	Burnup, Mwd/metric ton (0 – 25,000 – 50,000 – 75,000 – 100,000)
Sphere-Pac	1.98	80	Pin 19 / Pin 48
Sphere-Pac	1.98	80	Pin 20
Sphere-Pac	1.98	85	Pin 21 / Pin 49
Sphere-Pac	1.98	85	Pin 22
Sphere-Pac	1.98	85	Pin 23 / Pin 50
Sphere-Pac	1.98	85	Pin 24
Sphere-Pac	1.94	80	Pin 25 / Pin 51
Sphere-Pac	1.94	80	Pin 26
Sphere-Pac	1.94	85	Pin 27 / Pin 52
Sphere-Pac	1.94	85	Pin 28
Sphere-Pac	1.98	85	Pin 29 / Pin 53
Sphere-Pac	1.98	85	Pin 30 / Pin 54
Pellet	1.98	85	Pin 31 / Pin 55
Pellet	1.98	85	Pin 32
Pellet	1.98	90	Pin 33 / Pin 56
Pellet	1.98	90	Pin 34
Pellet	1.94	80	Pin 35 / Pin 57
Pellet	1.94	80	Pin 36
Pellet	1.94	85	Pin 37 / Pin 58

under test conditions now available in both thermal and fast-flux test reactors. Calculations were performed to describe the cladding fluence, radial power distribution in the fuel, temperature distributions in both fuel and cladding, fuel restructuring, and yields of fission products as functions of fuel burnup.

The calculations indicate that properly designed and interpreted thermal-flux experiments can simulate the operating conditions for the reference fuel in terms of temperature distributions and average yields of fission products. However, the fast-neutron fluences for the cladding are very low, and the radial power distributions in the fuel are atypical except at high burnup.

Simulation in the EBR-II of the conditions proposed for commercial fast reactors is, in general, quite good except for difficulties arising from the relatively low neutron flux. The maximum heat rate for mixed oxide fuel pins in typical LMFBR designs is about 16 kw/ft. This can be obtained in EBR-II with pin dimensions prototypic of LMFBR's only by fully enriching the U. The consequences of this high enrichment are an appreciable change in the yields of certain of the fission products, which may affect the activity of the O in the fuel, and a two-thirds decrease in the cladding fluence at a given fuel burnup.

References

1. Chemical Technology Division.
2. J. P. McBride, Laboratory Studies of Sol-Gel Processes at the Oak Ridge National Laboratory, ORNL-TM-1980, pp. 32–34 (September 1967).
3. F. G. Kitts, R. B. Fitts, and A. R. Olsen, "Sol-Gel Urania-Plutonia Microsphere Preparation and Fabrication into Fuel Rods," pp. 195–210 in Intern. Symp. Plutonium Fuels Technol., Scottsdale, Ariz., 1967, Nucl. Met. 13, American Institute of Mining, Metallurgical, and Petroleum Engineers, New York, 1968.
4. Syntron Company, Homer City, Pennsylvania.
5. W. L. Moore and R. A. Bradley, Fuels and Materials Development Program Quart. Progr. Rept. June 30, 1968, ORNL-4330, pp. 7–10.

6. R. A. Bradley, Fuels and Materials Development Program Quart. Progr. Rept. Sept. 30, 1968, ORNL-4350, pp. 5–7.
7. R. A. Bradley, Fuels and Materials Development Program Quart. Progr. Rept. June 30, 1969, ORNL-4440, pp. 6–12.
8. General Engineering Division.
9. A. R. Olsen, "Fast-Flux Irradiation Tests," pp. 29–32, this report.
10. W. H. Pechin, Fuels and Materials Development Program Quart. Progr. Rept. June 30, 1969, ORNL-4440, pp. 12–13.
11. J. B. Cordinier and O. C. Dean, A Study of Gas Evolution from Sol-Gel Thoria in Thoria-Urania, ORNL-TM-2268 (July 1968).
12. J. M. Leitnaker and K. E. Spear, Fuels and Materials Development Program Quart. Progr. Rept. June 30, 1969, ORNL-4440, pp. 21–22.
13. C. E. Johnson, Argonne National Laboratory, July 22, 1969, private communication.
14. Summer employee, 1969.
15. K. E. Spear, J. M. Leitnaker, and N. Engel, Fuels and Materials Development Program Quart. Progr. Rept. June 30, 1969, ORNL-4440, pp. 18–21.
16. P. H. Spindler and D. L. McElroy, Fuels and Materials Development Program Quart. Progr. Rept. June 30, 1969, ORNL-4440, p. 14.
17. C. S. Morgan, L. L. Hall, W. H. Pechin, and A. R. Olsen, Fuels and Materials Development Program Quart. Progr. Rept. Dec. 31, 1968, ORNL-4390, pp. 22–23.
18. C. S. Morgan, L. L. Hall, W. H. Pechin, and A. R. Olsen, Fuels and Materials Development Program Quart. Progr. Rept. March 31, 1969, ORNL-4420, pp. 19–20.
19. H. D. Sheets and W. H. Duckworth, Uranium Dioxide Properties and Nuclear Applications, pp. 199–206, ed. by J. Belle, U.S. Government Printing Office, Washington, D.C., 1961.
20. On loan from Reactor Chemistry Division.
21. A. R. Olsen and R. B. Fitts, Metals and Ceramics Div. Ann. Progr. Rept. June 30, 1967, ORNL-4170, pp. 125–127.

22. A. R. Olsen, C. M. Cox, and R. B. Fitts, "Low Burnup Irradiation Tests of Sphere-Pac $(U,Pu)O_2$ Fuels," paper to be presented at the American Nuclear Society Winter Meeting, San Francisco, Nov. 30–Dec. 4, 1969. Summary to be published in the proceedings.

23. A. R. Olsen, R. B. Fitts, and D. R. Cuneo, Fuels and Materials Development Program Quart. Progr. Rept. June 30, 1969, ORNL-4440, pp. 23–26.

24. A. R. Olsen, C. M. Cox, and R. B. Fitts, Fuels and Materials Development Program Quart. Progr. Rept. March 31, 1969, ORNL-4420, pp. 25–29.

25. V.C.A. Vaughen et al., LMFBR Fuel Cycle Studies Progress Report for August, No. 6, ORNL-TM-2710, p. 17 (October 1969). Results will be reported in this series on a continuing basis.

26. Reactor Division.

27. R. B. Fitts and V. A. DeCarlo, Fuels and Materials Development Program Quart. Progr. Rept. June 30, 1968, ORNL-4330, pp. 20–23.

28. R. B. Fitts, V. A. DeCarlo, and K. R. Thoms, Fuels and Materials Development Program Quart. Progr. Rept. June 30, 1969, ORNL-4440, p. 27.

29. A. R. Olsen, Experimental Description and Hazards Evaluation for the Series I ORNL Oxide Fuels Irradiation in EBR-II, ORNL-TM-2635, in press.

30. A. R. Olsen, C. M. Cox, and J. D. Jenkins, Fuels and Materials Development Program Quart. Progr. Rept. March 31, 1969, ORNL-4420, pp. 33–34.

31. A. R. Olsen, R. B. Fitts, and C. M. Cox, "Analysis of the Validity of Fast Reactor Fuel Tests in Existing Test Reactors," paper presented at the National Symposium on Developments in Irradiation Testing Technology, NASA, Lewis Research Center, Sandusky, Ohio, Sept. 9–11, 1969. To be published in the proceedings and as ORNL-TM-2716.

2. DEVELOPMENT OF HIGH-PERFORMANCE LMFBR FUELS

P. Patriarca J. L. Scott

The goals of this program are to investigate the properties and behavior of those U- and Pu-based ceramic fuels that we term conductors — such as the mononitrides, carbonitrides, and monocarbides — and to compare their potential as liquid-metal fast breeder reactor (LMFBR) fuel with that of $(U,Pu)O_2$, which by comparison is an insulator. Since the thermal conductivity of the ceramic conductors is about ten times that of $(U,Pu)O_2$, it is theoretically possible to operate a conductor at ten times the power density with the same temperature at the center of the fuel. In practice, heat-transfer limitations, thermal stresses in the cladding, and high rates of swelling at high temperatures limit the power density that can be achieved with thermal conducting fuels to about two or three times that of $(U,Pu)O_2$ — still a challenging improvement. Additionally, the margins for transient overpower in the ceramic conductors are much higher than those for $(U,Pu)O_2$.

We seek to provide the information necessary for evaluating the true potential of nitrides, carbonitrides, and carbides in comparison to each other and to mixed oxides. We need to define the structures, composition, and quality control required to achieve 150,000 Mwd/metric ton at peak linear heat ratings of 30 to 50 kw/ft. We must also demonstrate the possibility of a low-cost fuel cycle for manufacturing fuel with the needed properties. And since austenitic stainless steel is a poor conductor of heat, we seek to establish the physical and thermodynamic criteria for the new cladding material that will probably be required to exploit the conducting fuels.

Our work is now oriented toward fabricating and characterizing (U,Pu)N with controlled low or high porosity distributed in different ways. The requisite void volume in a fuel pin may be provided in several ways if dense fuel is used, such as by a large Na-filled gap between fuel and cladding or by dished or annular pellets. It may also be provided by the internal porosity of low-density fuel pellets. We use both hot pressing and cold pressing and sintering. In our characterization work,

emphasis is being placed on reliable chemical analyses of U, Pu, C, O, and N. We have glove boxes with less than 20 ppm O and 10 ppm moisture that allow us close control of O content, and we have facilities in operation for x-ray, metallographic, thermogravimetric (TGA), and differential thermal (DTA) analyses. We are also assessing the effects of temperature gradient and burnup on the activities of N, C, and O. Finally, we are developing the information needed to design the decisive experiments that will demonstrate the best type of pin for meeting LMFBR requirements.

Synthesis, Fabrication, and Characterization of Nitride Fuels

V. J. Tennery

Synthesis and Fabrication of Mixed Nitrides (E. S. Bomar)

The purpose of this portion of our program is to develop methods for preparing feed powders of high purity and to fabricate pellets of variable but controlled density for a liquid-metal fast breeder reactor (LMFBR).

Fabrication by Hot Pressing. — Our principal effort this period was experimenting further with the effects of variations in time and temperature on the hot pressing of small pellets of mixed nitrides. We have continued to use feed powders made of a mechanical mixture of UN and PuN but, recognizing that it may be difficult to obtain a homogeneous product by this route, we have arranged for prealloying of metallic U and Pu for use in future work.

Fabrication of a pellet involves the following steps: mix powders either in an oblique blender or a small mill, preform by cold pressing, load into a small graphite die, and consolidate further in the hot press. Direct contact of the nitride powder with the graphite punches and die is avoided by use of a thin refractory-metal liner. In earlier work, both W and Mo liner materials separated satisfactorily from UN pellets pressed for periods up to 3 hr at 1450°C and pressures of 1 to 3 tsi. Since 3 hr is too long to consider for routine pressing, we selected higher temperatures and shorter times for subsequent experiments. Unfortunately this change resulted in bonding between pellets and W and Mo

liner materials over temperatures ranging from 1500 to 1765°C and times from 5 to 30 min. When Ta was used, however, the circumferential liner usually separated without damaging the pellet, but the shims at either end bonded firmly.

Figure 2.1 shows a 1/4-in.-diam pellet of UN–20% PuN resting in an Mo-lined graphite die that has been split. The W end shims are still in place, but the circumferential surface of the pellet shows pullout resulting from removal of half the liner.

A second pellet, encased in its Ta liner, is shown in Fig. 2.2(a). After the Ta liner was removed from the cylindrical surface, the pellet appeared as in Fig. 2.2(b). The Ta end shims, however, are still bonded in place. The shallow depression visible on the upper portion of the pellet was caused by overlap of the 0.003-in. Ta liner.

Fig. 2.1. Pellet of UN–20% PuN Hot Pressed in Nitrogen-Argon Atmosphere at 1700°C and 3 tsi for 42 min in Graphite Die with Molybdenum Liner and Tungsten End Shims. 6×.

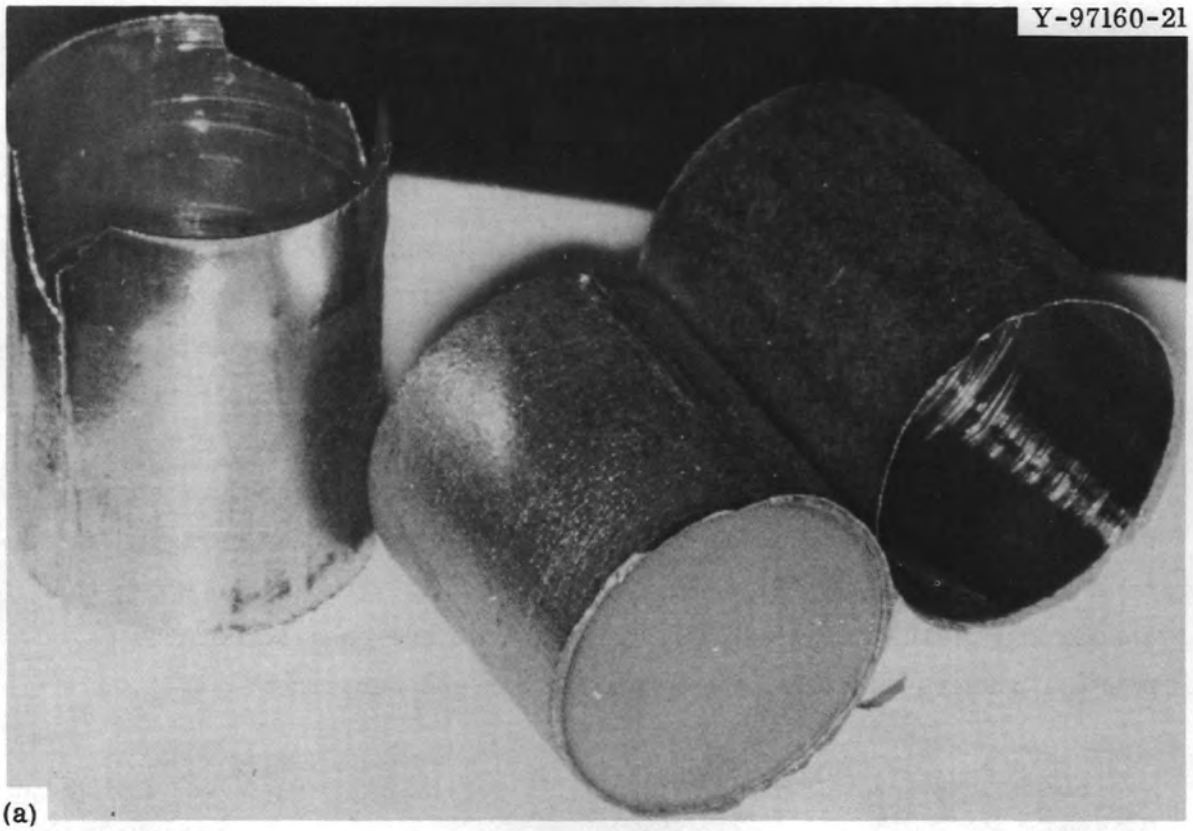

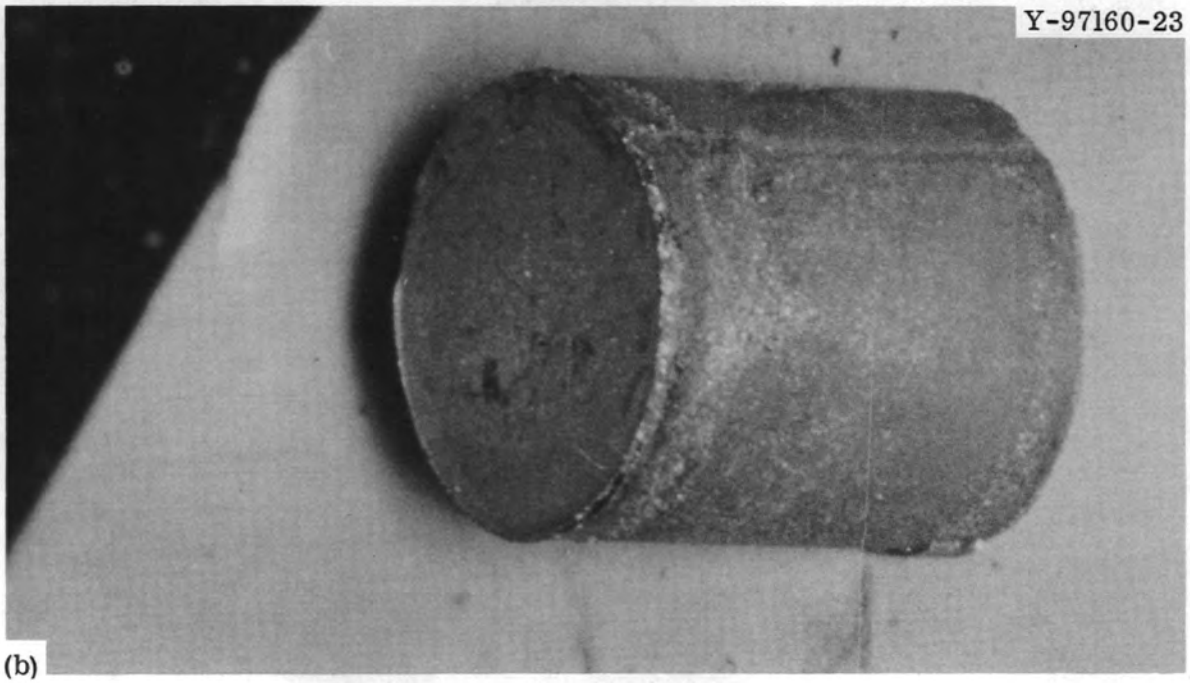

Fig. 2.2. Pellet of UN–20% PuN Hot Pressed in Nitrogen-Argon Atmosphere at 1700°C and 6 tsi for 30 min in Graphite Die with Tantalum Liner and Tantalum End Shims. (a) Pellet (center) and portions of tantalum liner (left and right). 8×. (b) Pellet stripped of tantalum liner but with tantalum end shims still in place. 10×.

The end shims are bonded primarily at the circumference of the end of the pellet; thus, if the shim is pried away with a sharp-edged tool it causes the edge of the pellet to pull off with the shim. This effect is shown in Fig. 2.3.

The density requested for the initial irradiation tests with (U,Pu)N is 95% of theoretical. A number of results are now available that relate the density of a hot-pressed pellet to the variables of time, temperature, and pressure. Table 2.1 shows that to obtain ≥ 95% of theoretical density in 30 min requires pressing at 6 tsi and 1755 to 1770°C for 1/4-in.-diam × 1/4-in.-long pellets. The maximum temperature at which we can presently operate the hot press is limited by the maximum temperature rise that can be allowed in the glove box. We plan to alter the insulation of the hot press and will examine the behavior of the mixed-nitride powders at higher temperatures for shorter times.

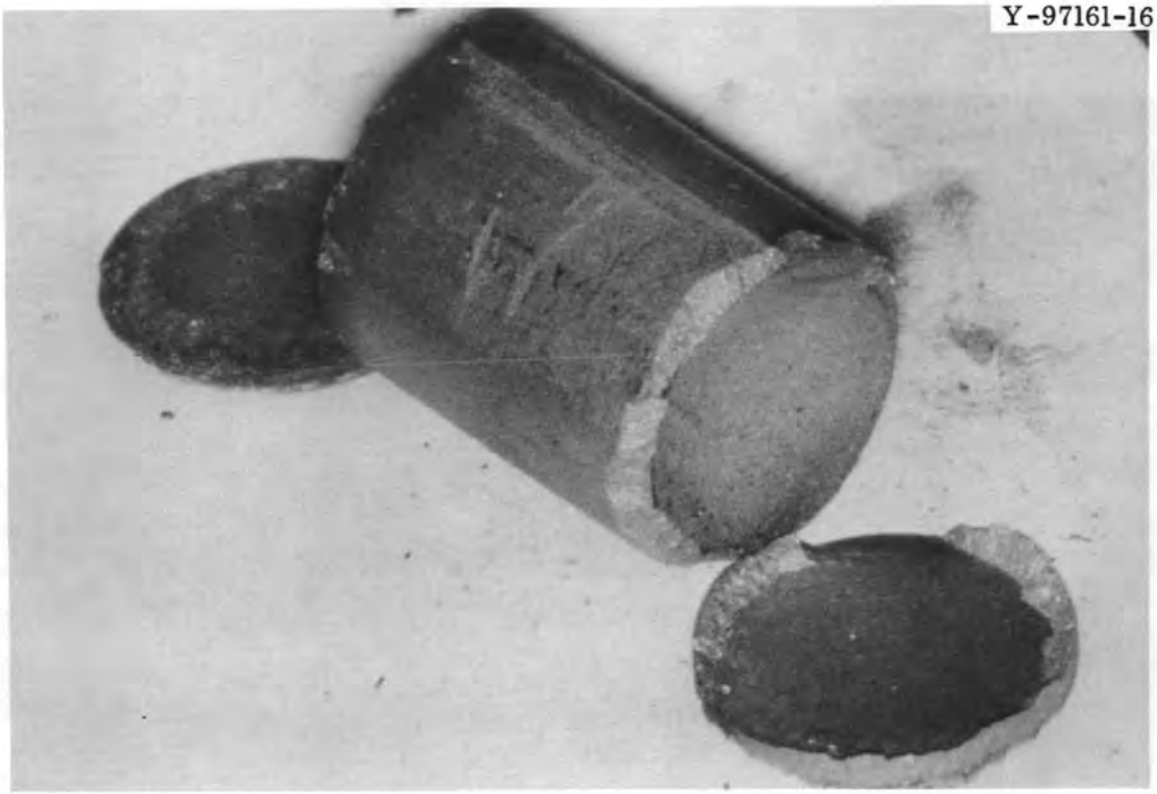

Fig. 2.3. Pellet of UN–20% PuN Hot Pressed in Nitrogen-Argon Atmosphere at 1700°C and 6 tsi for 5 min in Graphite Die Lined with Tantalum and with Tantalum End Shims. Appearance of end is typical of forced removal of end shim.

Table 2.1. Effect of Variable Conditions Used in Hot Pressing UN–20% PuN Powder Mixture[a] on Density of Pellet Product

Hot Pressing Conditions[b]			
Temperature (°C)	Pressure (tsi)	Time (min)	Density (% theoretical)
~ 1300	3	30	68
~ 1300	6.5	23	76
1700	3	42[c]	85
1700	6	5	81
		10	86
		30	90
1755–1770	6	6	80
1755–1770	6	10	85
1755–1770	6	29[c]	98
1755–1770	6	30[c]	98

[a]All samples prepressed cold in a 0.242-in.-diam steel die lubricated with stearic acid: sample weight, about 3 oz; pressure, 40 tsi; density, 63–69% theoretical.

[b]All samples hot pressed in 1/4-in.-diam graphite dies lined with 0.003-in. Ta. Furnace atmosphere was a N_2-rich mixture with Ar.

[c]Prepared from –325 mesh powders mixed in an oblique blender. All other samples were conditioned for 6 min in a "shatterbox" grinder.

Fabrication Equipment. – The glove box and its associated services for the furnace with the W resistor were installed, and the box passed the leak test. The O_2 and H_2O impurity levels of the Ar atmosphere in this box each dropped to less than 10 ppm shortly after it was put into service. We shall complete several experiments with UN that must be handled in an atmosphere with a very low level of impurities before we start work with Pu-bearing fuels.

We completed a specification for purchase of an inert-gas purifier with a capacity of 160 cfm and recommended a number of the manufacturers of this type of equipment. The purpose of the purifier is to permit recycling the glove-box atmosphere to reduce cost. Bids are being requested.

Synthesis, Fabrication, and Thermodynamic Properties of Carbonitride Fuels

J. M. Leitnaker

Manufacture of UC, UN, and U(C,N) From UO_2 (T. B. Lindemer)

The kinetics of the conversion of sol-gel UO_2 to uranium carbides, nitrides, and carbonitrides is being studied to determine the mechanisms that control the rate of the conversion processes. This information, which is fundamental to the design of reactor fuel cycles, is a prelude to the conversion of mixed $(U,Pu)O_2$ to the carbonitride.

Vacuum Conversion of UO_2-C Mixtures (T. B. Lindemer, R. L. Beatty, K. J. Notz[1])

The vacuum conversion of UO_2-C sol-gel shards to carbides is being investigated. Previous work showed that the carbothermic reduction of UO_2 microspheres is controlled by solid-state diffusion through one of the U compounds.[2] The model used indicates that the time for complete conversion of the UO_2 is inversely proportional to the square of the sphere radius. The rate constants obtained on spheres with a radius of 250 μm were used to estimate the reaction time for the approximately 200- to 1000-A particles of UO_2 in UO_2-C sol-gel material. Reaction times of a few seconds to a few minutes were indicated, depending upon the temperature used. The extrapolated reaction time also agreed within a factor of 10 with data developed by Ainsley *et al.*[3] for carbothermic vacuum conversion of UO_2 powders with a radius of 0.5 to 10 μm. These estimates, therefore, indicated that the extremely small oxide size available in sol-gel material may result in an extremely fast conversion process.

Another factor, the equilibrium pressure of CO for the reaction, is also an important consideration. For UO_2, this pressure is in the range of a few torr at the usual conversion temperatures of 1400 to 1600°C. Conversion in a stream of inert gas in a fluidized bed can be shown to be limited by the rate of the gas flow. The equilibrium CO pressure is attained in the inert gas, and further reaction is dependent on the

removal of the CO. The limit to this flow is that which would blow the particles out of the bed and is near that used normally. Therefore, conversion in a fluidized bed does not utilize the theoretical conversion rates possible in the UO_2-C sol-gel material. On the other hand, vacuum conversion of the material may proceed at the theoretical rate as long as the equilibrium pressure of CO is not attained.

Vacuum conversion was performed in the apparatus used normally for conversion in a fluidized bed. However, instead of gas flowing through the bed, a vacuum pump was attached to the apparatus to remove the CO as it was produced. In a typical experiment, the furnace was heated to 1500°C; then the UO_2-C sol-gel material was introduced. The production of CO caused active self-fluidization of the particles for about 1 min. The particles then dropped to the bottom of the reaction zone of the furnace. When this occurred, the particles were dropped out of the furnace into a collection bottle and transferred to an Ar-filled dry box. There, samples were prepared for analytical chemistry and x-ray analysis.

We have reacted −100 +120 mesh microspheres that have a C:U ratio of 7:1 and −35 +100 mesh shards that have C:U ratios of either 4.3:1 or 2.3:1. As much as 25 g of material has been reacted in about 1 min without apparently reaching the maximum charge capacity of the present equipment. A Debye-Scherrer x-ray film of the microspheres with the 7:1 ratio of C:U indicated that conversion of UO_2 was about 90% complete; the analytical results from the other runs are now being obtained. It appears that the vacuum conversion of these oxide-carbon shards uniquely approaches the rates inherently possible with these materials.

Fabrication of (U,Pu)(C,N) (W. L. Moore, T. B. Lindemer)

The mixed carbonitrides will be irradiation tested as pellets clad in stainless steel tubes. The feed material for these pellets will be obtained by the reaction of (U–20 wt % Pu)O_2 + C sol-gel shards with N_2 in a fluidized bed. We will extend the method of carbonitride synthesis from U(C,N) to (U,Pu)(C,N), determine the thermodynamics of the reaction, and study the product by x-ray diffraction. During the past quarter we set up an existing fluidized-bed furnace in an alpha glove box and made three preliminary conversion runs with depleted U.

While setting up the equipment, we replaced the heating element, graphite cone, and filter bag for the furnace. Nitrogen supply was added to the furnace, and the gas-flow meters were calibrated. Specially designed transfer containers were fabricated and installed to prevent contamination of the carbonitride by air during unloading of the furnace and transfer of the product to a facility with an inert atmosphere.

The essential steps in making the conversion runs were as follows:

1. The furnace was purged with N_2 and heated.

2. When the furnace reached temperature, the N_2 purge rate was lowered to the fluidizing rate.

3. The UO_2 + C shards were poured into the furnace.

4. After a predetermined length of time, the flow of N_2 was stopped to allow the product to fall into the transfer container.

Three charges of UO_2 + C shards were run through the furnace, and the product was chemically analyzed in the High Radiation Level Examination Laboratory. During the first of these runs at 1600°C, some unconverted charge material fell out of the furnace and was collected with the reacted product. Analytical results for O for this run were poor, since they represented only partially converted UO_2 + C shards. Before the second run, we developed a technique to eliminate from the container used for unloading the furnace any material that might fall through the furnace during loading. The second run consisted of 15 g of UO_2 + C shards exposed to N_2 for 15 min at 1600°C. Analytical results are not complete on the second batch, but we found that the O content was 2.4 to 2.7 wt %. The third batch was converted at the same temperature as the second, but the time at temperature was 1 hr rather than 15 min. The O content of the third batch of carbonitride was 1.1 wt %. We attribute this O to unconverted UO_2 and will investigate operating the furnace at a higher temperature to increase the reaction rate.

Compatibility of Mixed-Nitride and Carbonitride Fuels with LMFBR Cladding Alloys

J. M. Leitnaker

Our approach to compatibility in high-performance fuel systems is to characterize interactions that can occur between the fuel and cladding

material, since a basic understanding of these reactions may point to methods for tailoring the fuel so that the reactions cannot occur and, perhaps, to methods for hindering the kinetics of the reaction.

The work described this quarter on the U-V-N and U-V-C systems was performed to obtain a basic understanding of the chemical and thermodynamic properties of interactions of V alloys with nitride and carbide fuels. The results of these investigations will be combined to point out the critical experiments that are needed to obtain a basic understanding of the more complicated quatenary U-V-C-N system. A few selected experiments involving Pu will be needed to determine how this added element affects the basic properties of these systems.

Ternary U-V-N System (K. E. Spear)

The possible use of V alloys with nitride reactor fuels has generated interest in the phase behavior of the U-V-N system. The primary interest is in the compatibility of fuel and cladding, but it may also be possible to tailor nitride fuels with small additions of V and/or its nitrides to maintain the activity of N in the fuel at a level lower than that for the UN-U_2N_3 two-phase system.

Our preliminary results indicate that the following equilibrium tie-lines exist in the U-V-N system: UN-V, UN-UVN_2, U_2N_3-UVN_2, U_2N_3-VN, and UVN_2-VN. We still do not know the positions of the tie-lines in the UN-VN-V region of the ternary phase diagram.

As we reported earlier,[4] a new type of ternary nitride has been discovered in studies of the U-V-N system. This compound, UVN_2, has been definitely identified in 17 samples prepared by mixing UN and VN powders, pressing the mixtures into pellets, and then heating these pellets at 1400 to 2000°C in 50 to 600 torr N_2. Equilibrium is difficult to achieve in this system, but we have obtained two-phase mixtures of UN and UVN_2 with samples prepared with UN:VN molar ratios greater than 1.0. Two-phase mixtures of UVN_2 and VN were obtained with UN:VN molar ratios of 0.5 and less. Because of the small atomic weight of V in comparison with U, the x-ray lines of UN are very faint in these ternary samples unless the compound is present in large molar quantities. Thus far, the formula,

UVN_2, is derived mainly by analogy with UVC_2. The crystal structures are isomorphous as indicated by data from x-ray powder diffraction.[4]

The elimination of O contamination from the samples is difficult because the nitrides have such a high affinity for O. However, the amount of O dissolved in the nitride samples we studied appeared, from the results discussed below, to be small. A sample containing UVN_2, VN, and UO_2, according to x-ray results, was chemically analyzed and found to contain 0.78 wt % O. This quantity of O corresponds to about 7 wt % UO_2 in this particular sample. The fact that weak UO_2 lines were observed in the x-ray diffraction photograph of this sample indicates that little O was dissolved in UVN_2 and VN. The limit for detection of a phase in x-ray powder photographs is about 5 wt %. The amount of O dissolved in UVN_2 is estimated to be 0.2 wt % or less.

Ternary U-V-C System (K. E. Spear, T. B. Lindemer)

The possible use of V alloys with carbonitride fuels has generated interest in the phase behavior of the U-V-C system. Last quarter[5] we reviewed previous investigations on this ternary system, reported the results of our studies of phase equilibria, and discussed the practical implications of these results relative to nuclear reactors.

Here, we present results pertaining to (1) ternary solid solutions in the U-V-C system, (2) the composition of VC in the UC-UVC_2-VC three-phase field, (3) the decomposition temperature of UVC_2, and (4) the confirmation of the UC_2-VC equilibrium tie line. We also compare the phase behavior of the U-V-C system with that of the U-Cr-C, U-Mo-C, and U-W-C systems.

Our phase-equilibria results for the U-V-C system are shown in the diagrams in Fig. 2.4. This figure contains a schematic representation of the sample compositions, a phase diagram representing the results for cast samples (samples quenched from the melt), and the equilibrium U-V-C phase diagram for 1500 to 1600°C.

The extent of ternary solid solutions was examined by comparing lattice parameters of UC and VC in the binary and ternary samples. The results are shown on the partial ternary phase diagrams in Fig. 2.5.

ORNL-DWG 69-9194

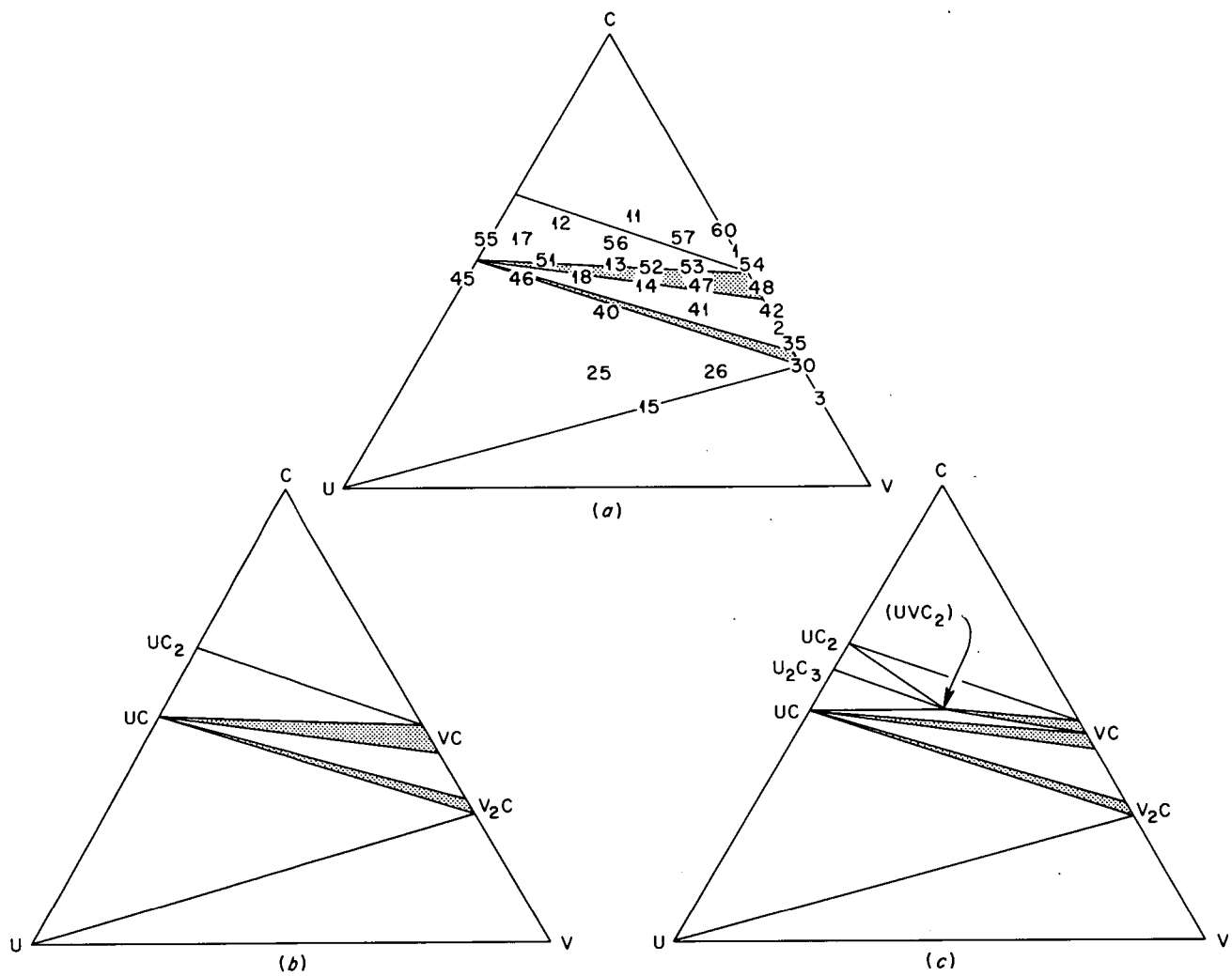

Fig. 2.4. Ternary U-V-C Phase-Diagram Results. (a) Synthetic compositions of samples in the ternary phase field are indicated by the sample numbers. (b) Phase diagram for samples as cast. (c) Phase diagram for 1500 to 1600°C.

ORNL-DWG 69-8930

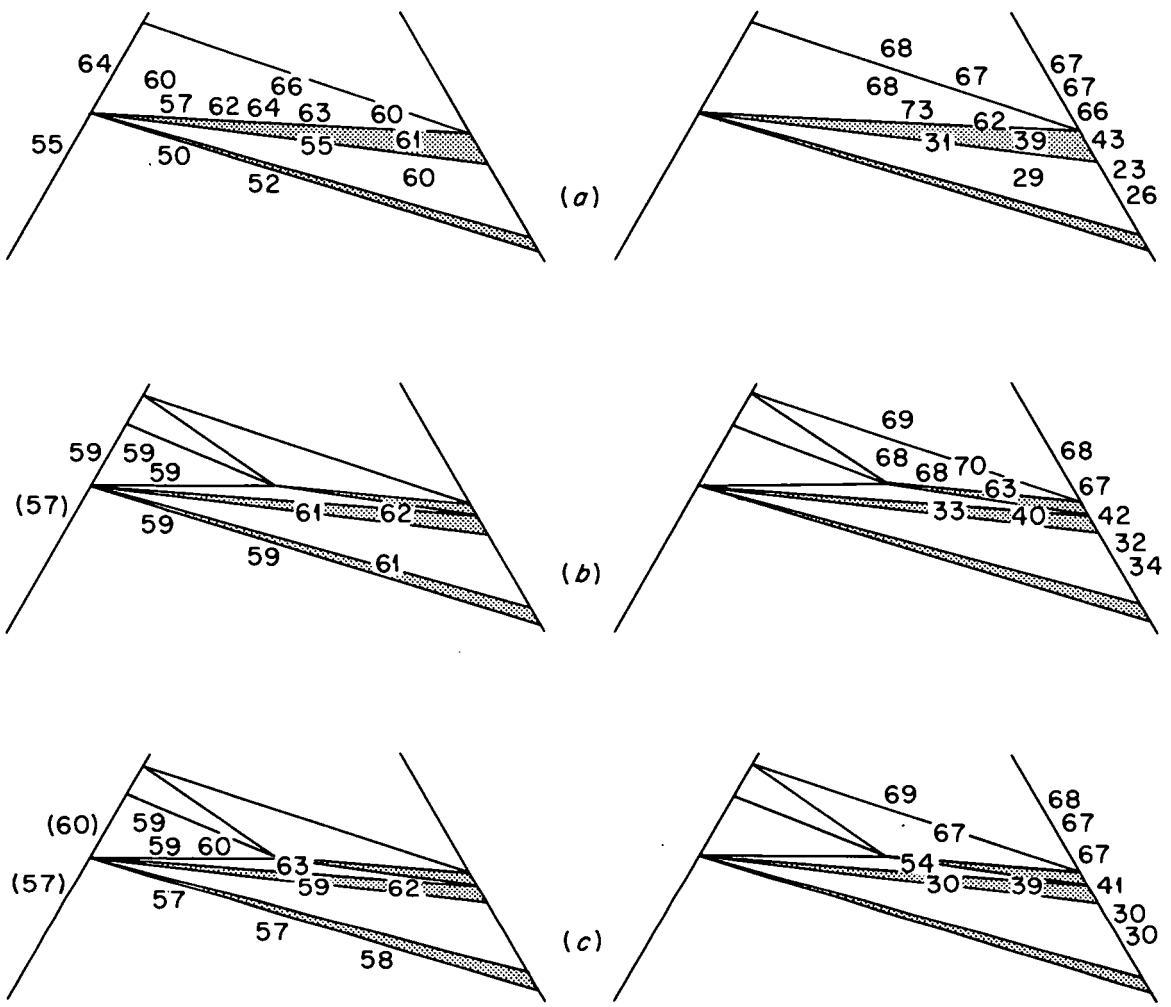

Fig. 2.5. Lattice Parameters for UC and VC. (a) Samples as cast. (b) Samples annealed at 1200°C. (c) Samples annealed at 1500 to 1600°C. The UC_2-VC tie line is the top one shown on each partial phase diagram, and the UC-V_2C tie line is the lowest one. The position of each parameter on the diagrams corresponds to the phase field for the sample as indicated from x-ray and metallographic results. The UC values in parentheses were taken from E. K. Storms, The Refractory Carbides, Academic Press, New York, 1967.

The last two digits of the parameter 4.9XX A for UC are given in the left three drawings, and the last two digits of the parameter 4.1XX A for VC are given in the right three drawings. The parameter for each sample is located on the partial phase diagram in the phase field indicated by the x-ray and metallographic results for the sample. The standard deviation was less than 0.001 A for all but four of the values, and was less than 0.002 A for these four. A comparison of the results for ternary samples with those for binary samples indicates little ternary solid solution of UC in VC and vice versa. The results for the samples as cast give some indication that the quenched compositions depend kinetically on the overall sample composition. Although ternary solutions were not determined quantitatively in the present studies, the results of the studies of the lattice parameter indicate that the approximately 20% solution of VC in UC reported by Nowotny et al.[6] is too large and should probably be about 5% or less.

We calculated the composition of VC in the ternary UC-UVC_2-VC three-phase field from the data for the lattice parameter. The lattice parameter of VC in a sample in this field annealed at 1500°C was 4.154 ± 0.001 A. This value and the data given by Storms[7] for the lattice parameter versus C:V ratio yields the estimated composition $VC_{0.81 \pm 0.02}$.

The ternary UVC_2 phase appeared when arc-melted samples with compositions in the UC-UC_2-VC region were annealed, but it was never observed in samples quenched from the melt. Therefore, the UVC_2 probably forms via the ternary peritectoid reaction of UC, UC_2, and VC. A sample as cast and containing UC_2, VC, and UC was annealed at several temperatures to determine the peritectoid temperature. At 1500°C we found mainly UC_2, VC, and UVC_2, with a minor amount of UC still unreacted. We demonstrated the existence of the UC_2-VC-UVC_2 field at 1800°C, but annealing at 2000°C resulted in UC, UC_2, and VC. Thus, UVC_2 is unstable above 1900 ± 100°C.

The U-Cr-C, U-Mo-C, and U-W-C ternary systems are similar to the U-V-C system in that they form orthorhombic ternary compounds of the UMC_2 type (where M represents a transition metal). There are, however, several differences among these four systems. The UVC_2 phase decomposes to the solid binary phases at 1900 ± 100°C, $UCrC_2$ melts congruently at

1625°C according to Briggs et al.,[8] and $UMoC_2$ melts congruently at about 2300°C according to Chubb.[9] The UVC_2 phase reacts with C to form UC_2 and VC, while $UMoC_2$ and UWC_2 are stable in the presence of C according to Chubb[9] and Rudy et al.,[10] respectively. At least at temperatures below 1500°C for V, 1315°C for Cr (ref. 8), 1800°C for Mo (ref. 9), and 1500°C for W (ref. 10), V is different from the other metals in that it will react with UC to form V_2C and U. The other three metals can exist in equilibrium with UC.

Thermodynamic Investigations of High-Performance Fuel Systems

J. M. Leitnaker

The goal of our thermodynamics program for high-performance fuels — the carbides, nitrides, and carbonitrides — is to be able to predict the limiting equilibrium behavior of fuel and cladding in fast-reactor environments. Our experiments, though limited to measurements out-of-reactor, are of value for defining and understanding the factors that affect fuel performance.

Thermodynamic Stability of UVC_2 (K. E. Spear, T. B. Lindemer)

The existence of the ternary compound UVC_2 has been confirmed in phase studies of the ternary U-V-C system,[5] and the free energy of formation, ΔG_f°, of this phase at 1800°K was calculated to have a value between −47.5 and −48.1 kcal/mole.[11]

We recently determined that the ternary UVC_2 phase is unstable above 2150°K (1900 ± 100°C) (ref. 12) and decomposes according to the reaction

$$UVC_2 \rightarrow 0.87\ UC + 0.13\ UC_{1.93} + VC_{0.88}\ .$$

This and the data for ΔG_f° at 2150°K for the binary carbides[13] result in $\Delta G^\circ_{f,2150}(UVC_2) = -47.0$ kcal/mole. The uncertainty in this value caused by the uncertainty in the decomposition temperature is about ±0.2 kcal.

The assumptions that, between 1800 and 2150°K, the heat and entropy of formation of UVC_2 are constant (that is, that the change in the heat

capacity for the formation of UVC_2 from the elements at constant pressure, $\Delta C^\circ_{p,f}$, is equal to zero) lead to the relationship

$$\Delta\ (\Delta G^\circ_f) = \Delta T\ (\Delta S^\circ_f)\ ,$$

where ΔS°_f is the entropy of formation. The value for ΔS°_f (UVC_2) calculated from this relationship is −2.3 eu, with an uncertainty of about ±1.5 eu. Combining this value with the $\Delta G^\circ_{f,2150}(UVC_2)$ value yields a heat of formation, ΔH°_f, for UVC_2 at 2150°K of −51.9 kcal/mole. The assumption that $\Delta C^\circ_{p,f}(UVC_2) = 0$ between 298 and 2150°K leads to the following values for this ternary phase at 298°K: $\Delta H^\circ_f = -48.6 \pm 3.0$ kcal/mole, $\Delta S^\circ_f = 0.5 \pm 2.0$ eu, and $S^\circ = 22.2 \pm 2.0$ eu. The uncertainties were estimated. The S°_{298} value used for U was from Storms[7] and the values for V and C were from Hultgren *et al.*[14]

Thermodynamic Stability of $UCrC_2$, $UMoC_2$, and UWC_2 (K. E. Spear, T. B. Lindemer)

Limits on the free energies of formation of $UCrC_2$, $UMoC_2$, and UWC_2 can be determined from phase data and free energies of formation for binary carbides just as they were for UVC_2 (ref. 15). The phase diagrams for U-Cr-C from Briggs *et al.*,[8] for U-Mo-C from Chubb,[9] and for U-W-C from Rudy *et al.*,[10] show the following condensed phase reactions to have negative free energies at 1800°K:

$$UC + U_2C_3 + Cr_3C_2 \rightarrow 3\ UCrC_2$$

$$2\ UCrC_2 + Cr \rightarrow 2\ UC + Cr_3C_2$$

$$UC + Mo_2C \rightarrow UMoC_2 + Mo$$

$$UMoC_2 + U \rightarrow 2\ UC + Mo$$

$$UC_{1.93} + WC \rightarrow UWC_2 + 0.93\ C$$

$$UWC_2 + U \rightarrow 2\ UC + W$$

This fact, the ΔG°_f values for the carbides of U (calculated from data in refs. 7, 14, 16, and 17), and the ΔG°_f values for the carbides of Cr, Mo, and W given by Hultgren *et al.*[14] were used to determine the following

limits for the $\Delta G^{\circ}_{f,1800}$: −36.5 and −41.7 kcal/mole for $UCrC_2$, −39.7 and −51.4 kcal/mole for $UMoC_2$, and −34.4 and −51.4 kcal/mole for UWC_2. These limits compare with the limits of −47.5 and −48.1 kcal/mole determined for $\Delta G^{\circ}_{f,1800}$ for UVC_2.

Plutonium Nitride Thermodynamics (J. DeLuca)

As a part of our study of the compatibility of mixed nitride fuels we are building a system for measuring N_2 pressures over nitrides and carbonitrides that contain Pu. We are trying to define the factors that affect fuel performance and behavior toward cladding materials.

The system under construction is similar to one described by Inouye and Leitnaker[18] except that extensive modifications were necessary to contain the Pu. The heater is made of W mesh, and the crucible is suspended inside it. This entire assembly is surrounded by a nest of shields. The furnace chamber is of stainless steel and is cooled by water. The crucible is suspended from a Cahn microbalance for two reasons. First, Pu is considerably more volatile than U, and, thus, the loss of Pu from nitrides because of vaporization may be expected to change the composition of the solid nitrides. Second, determining by means of weight change the amount of N_2 added will – at low temperatures where Pu vaporization is not a problem and at high temperatures after suitable correction – give us a check on the addition by measurement of PV relationship, and give us freedom to make additional rate studies where collection of a permanent gas may not be practical.

We have inventoried all components on hand, ordered all necessary additional components, and removed from the laboratory for machining the parts of the vacuum system that were damaged or needed modification.

Measurements of the Physical Properties of (U,Pu)N Alloys

D. L. McElroy S. C. Weaver

Because it is important to know temperature distributions to predict irradiation behavior, we are beginning a study of the thermal conductivity of (U,Pu)N alloys. Fuel swelling, release of fission gas, distribution of fission products, redistribution of Pu, and other effects of irradiation

very strongly depend on the temperature distribution and, therefore, the thermal conductivity of the fuel. We plan to study the effects of fuel density, including the effects of pore size and shape, the effects of impurities such as C and O, and the effects of varying compositions of U and Pu.

The equipment to be placed in the Interim Plutonium Facility has been designed, and fabrication has begun. Fabrication of the components for the comparative heat-flow apparatus is nearly complete; the components are being fitted onto the base plate. The bell jar for this apparatus is also finished.

All equipment to be purchased from outside vendors has been ordered. Nearly all of the instrumentation for the three pieces of equipment has been received by the Plant and Equipment Division and is being assembled into the Budd racks. The vacuum systems were ordered and are due to be received October 2, 1969. We expect the first glove box, which will house the comparative heat-flow apparatus and the absolute thermal-conductivity apparatus, to be delivered October 31, 1969; the second box is due December 15, 1969.

We began measuring the electrical resistivity and Seebeck coefficient on a square, pressed-and-sintered rod of UN for the temperature range 300 to 1700°K.

Irradiation Testing of Nitride Fuels for LMFBR Applications

T. N. Washburn

The objective of this program is to establish the irradiation performance of the U,Pu nitrides and carbonitrides. The nitrides and carbonitrides have a thermal conductivity about 10 times higher, a theoretical density 30% higher, and a metal content in the compound 7% higher than the oxides. These properties make the nitrides and carbonitrides strong contenders as advanced fuel for an LMFBR.

Thermal-Flux Irradiation Tests (T. N. Washburn)

We had initially planned to perform the thermal flux irradiation tests in the Engineering Test Reactor (ETR), but a recent evaluation

indicates that the Oak Ridge Research Reactor (ORR) may offer certain advantages over the ETR. We investigated the possible use of two test facilities (B-2 and F-2) in the ORR that are available for reassignment and requested that they be assigned to this Division for use in the high-performance fuels irradiation testing program. If only one facility can be obtained, we would recommend the F-2 facility, since it has a slightly higher neutron flux, a slightly higher flow rate in the closed water-circulation loop, the capability for independent control of four separate gas loops, and no modification or preoperation maintenance required to begin operation of the loop. The B-2 facility is currently inoperative and would require replacement of the bearings in the water pump in order to be used in our program.

Both these facilities are located inside the reactor tank, and each is adjacent to a fuel-element position. A hole with the maximum possible diameter is bored into an Al block the same size as the fuel element, and a stainless steel facility tube about 2 3/4 in. in outside diameter and 0.065 in. in wall thickness is inserted into the Al block. The facility tube is connected to a closed water-circulation loop that can be operated independently of the ORR coolant/moderator system.

These facilities are of special interest to the high-performance fuels irradiation program for the following reasons:

1. A constant cladding temperature can be maintained throughout the tests. The hydraulic positioner in each facility enables small movement of the specimen location to compensate for both changes in the flux profile of the reactor and burnup of the fissile content of the fuel specimen.

2. Instrumentation of each facility is excellent. It is capable of monitoring and recording 16 thermocouples as well as pressure and flows of both water and gas loops.

3. The ORR operates 85 to 90% of the time, compared to 55 to 60% for the ETR, which reduces by 40% the calendar time required to achieve a specified burnup at a given heat rating.

4. The peak neutron flux of 2×10^{14} neutrons cm^{-2} sec^{-1} will permit us to test the high-performance fuels to linear heat ratings of about 40 kw/ft.

5. Each facility has its own closed-cycle water loop for cooling the test specimens.

6. Each facility has a 2 1/2-in.-diam × 20-in.-long test space that will permit us to test capsules with specimens loaded either in clusters or in tandem.

7. Each facility is equipped with gas-flow loops that can be used to supply a low heat-transfer barrier around the test specimen and also serve as a monitor for release of fission gas from the test specimen.

Liquid-Metal Bonding of Fuel to Cladding (M. K. Preston[19])

In the initial tests in a thermal-neutron flux, the (U,Pu)N and (U,Pu)C,N pellets will be thermally bonded to the stainless steel cladding with NaK-19 (Na–19 wt % K). A system for loading the liquid metal into the 0.010-in. radial gap between fuel and cladding has been designed, and installation is about 75% complete. In this system, the liquid metal is forced, by either a vacuum or applied pressure, to flow into the radial gap around the fuel pin via a capillary tube connected to the reservoir of liquid metal. By containing the NaK-19 in a completely closed system during loading operations, we can keep the level of O contamination low. After the NaK-19 is loaded into the gap, the fuel pins will be centrifuged to minimize the probability of gas bubbles in the thermal bond. The Materials Compatibility Group prepared 3 kg of NaK-19 alloy for checking the loading system and refining the loading and bonding techniques. A glove box for containing the loading system was ordered, and delivery is scheduled for November.

References

1. Chemical Technology Division.
2. T. B. Lindemer, M. D. Allen, and J. M. Leitnaker, J. Am. Ceram. Soc. 52, 233 (1969).
3. R. Ainsley et al., New Nuclear Materials Inducing Non-Metallic Fuels, IAEA-349 (1963).
4. K. E. Spear and J. M. Leitnaker, Fuels and Materials Development Program Quart. Progr. Rept. March 31, 1969, ORNL-4420, pp. 58–65.

5. K. E. Spear, T. B. Lindemer, and J. M. Leitnaker, Fuels and Materials Development Program Quart. Progr. Rept. June 30, 1969, ORNL-4440, pp. 38–41.

6. H. Nowotny et al., Monatsh. Chem. 88(3), 336–343 (1957).

7. E. K. Storms, The Refractory Carbides, pp. 47–60, 171–213, Academic Press, New York, 1967.

8. G. Briggs et al., "Phase Relationships in the Systems U-Cr-C, U-Ni-C, and U-Fe-Cr-C," pp. 231–245 in Carbides in Nuclear Energy, Vol I, ed. L. E. Russell et al., Macmillan, London, 1964.

9. W. Chubb, J. Nucl. Mater. 23, 336–340 (1967).

10. E. Rudy et al., Monatsh. Chem. 93(2), 522–535 (1962).

11. K. E. Spear, T. B. Lindemer, and J. M. Leitnaker, Fuels and Materials Development Program Quart. Progr. Rept. June 30, 1969, ORNL-4440, pp. 42–43.

12. K. E. Spear, T. B. Lindemer, and J. M. Leitnaker, "Ternary U-V-C System," pp. 46–50, this report.

13. The values for UC, $UC_{1.93}$, and $VC_{0.88}$ were calculated from data for the free-energy function (fef°_{T}) and for $\Delta H^{\circ}_{f,298}$. The fef°_{T} values for U and $VC_{0.88}$ were taken from Storms,[7] those for V and C from Hultgren et al.,[14] and those for UC and $UC_{1.93}$ from Leitnaker and Godfrey.[17] The $\Delta H^{\circ}_{f,298}$ value for UC, −23.2 kcal/mole, was taken from Storms and Huber;[16] that for $UC_{1.93}$, −20.5 kcal/mole, was chosen after considering data in Storms and Huber[16] and Leitnaker and Godfrey;[17] and that for $VC_{0.88}$, −24.5 kcal/mole, was taken from Storms.[7]

14. R. Hultgren et al., Supplement to Selected Values of Thermodynamic Properties of Metals and Alloys, College of Engineering and Lawrence Radiation Laboratory, University of California, Berkeley, California. Carbon data, May 1965; vanadium data, May 1966; chromium-carbon data, October 1966; molybdenum-carbon data, July 1966; tungsten-carbon data, May 1966.

15. K. E. Spear, T. B. Lindemer, and J. M. Leitnaker, "Thermodynamic Stability of UVC_2," pp. 50–51, this report.

16. E. K. Storms and E. J. Huber, Jr., J. Nucl. Mater. 23, 19–24 (1967).

17. J. M. Leitnaker and T. G. Godfrey, J. Nucl. Mater. 21, 175–189 (1967).

18. H. Inouye and J. M. Leitnaker, J. Am. Ceram. Soc. 51, 6–9 (1968).

19. General Engineering Division.

3. EFFECT OF POWER CYCLING ON LMFBR FUEL-CLADDING BEHAVIOR

O. Sisman

This program investigates the effects of power cycling and transients on fuel behavior and the interaction of fuel and cladding for a liquid-metal fast breeder reactor (LMFBR), first for mixed oxide fuel and stainless steel cladding and later for other fuels and claddings. The objectives of this study are to compare the mechanical interactions of fuel (flat-ended pellets, dished pellets, and particulate fuel) and cladding during thermal-cycling conditions typical of those to be expected in an LMFBR. Fuel relocation is periodically monitored by neutron radiography. Relocation and cracking of the fuel, reactions between fuel and cladding, and the migration of Pu and fission products will be studied by postirradiation examination.

Power Cycling of Mixed Oxide Fuel with Stainless Steel Cladding to Moderate Burnup

J. G. Morgan

We began this quarter to design a series of reactor experiments for studying the effects of power cycling and power transients on the behavior of oxide fuel and the interactions of fuel and cladding. Calculations are now being made to establish the geometry of the capsules so that a preliminary design and cost estimate may be made for the first experiment.

4. LMFBR FUEL ELEMENT DESIGN AND MODEL DEVELOPMENT

P. Patriarca C. M. Cox

This is a new program for which progress is being reported for the first time. The objective of the program is to develop analytical methods for predicting the performance characteristics of LMFBR fuel rods and fuel elements. Such methods will be applied in several areas:

1. in the systematic evaluation of data from irradiation tests,
2. in evaluating the influences of materials properties on the performance of fuel elements,
3. in identifying specific areas where experimental research needs to be intensified, and
4. in predicting the probability and cause of failures of fuel elements under both steady-state and transient conditions.

The computer models are written in modular form so that obsolete ideas and concepts may easily be replaced when more sophisticated versions are available. Although it is intended that the scope of this work will eventually include the nuclear, mechanical, chemical, and thermal-hydraulic analysis of an entire fuel-element assembly, we are now working on the mechanical interactions of fuel and cladding and the behavior of fission gas in single fuel rods. The individual models for this analysis are assembled into an integrated performance code called FMØDEL.

Model Integration

FMØDEL Computer Code (F. J. Homan)

Figure 4.1 is the present flow diagram for the FMØDEL computer code. The code provides a flexible heat-transfer and mechanical analysis of a metal-clad ceramic fuel rod operating at steady-state conditions with radially symmetrical boundary conditions. This type of analysis is important in determining the basic interactions between fuel and cladding and can be used to investigate the sensitivity of these interactions to materials properties and design variables.

ORNL-DWG 69-7273

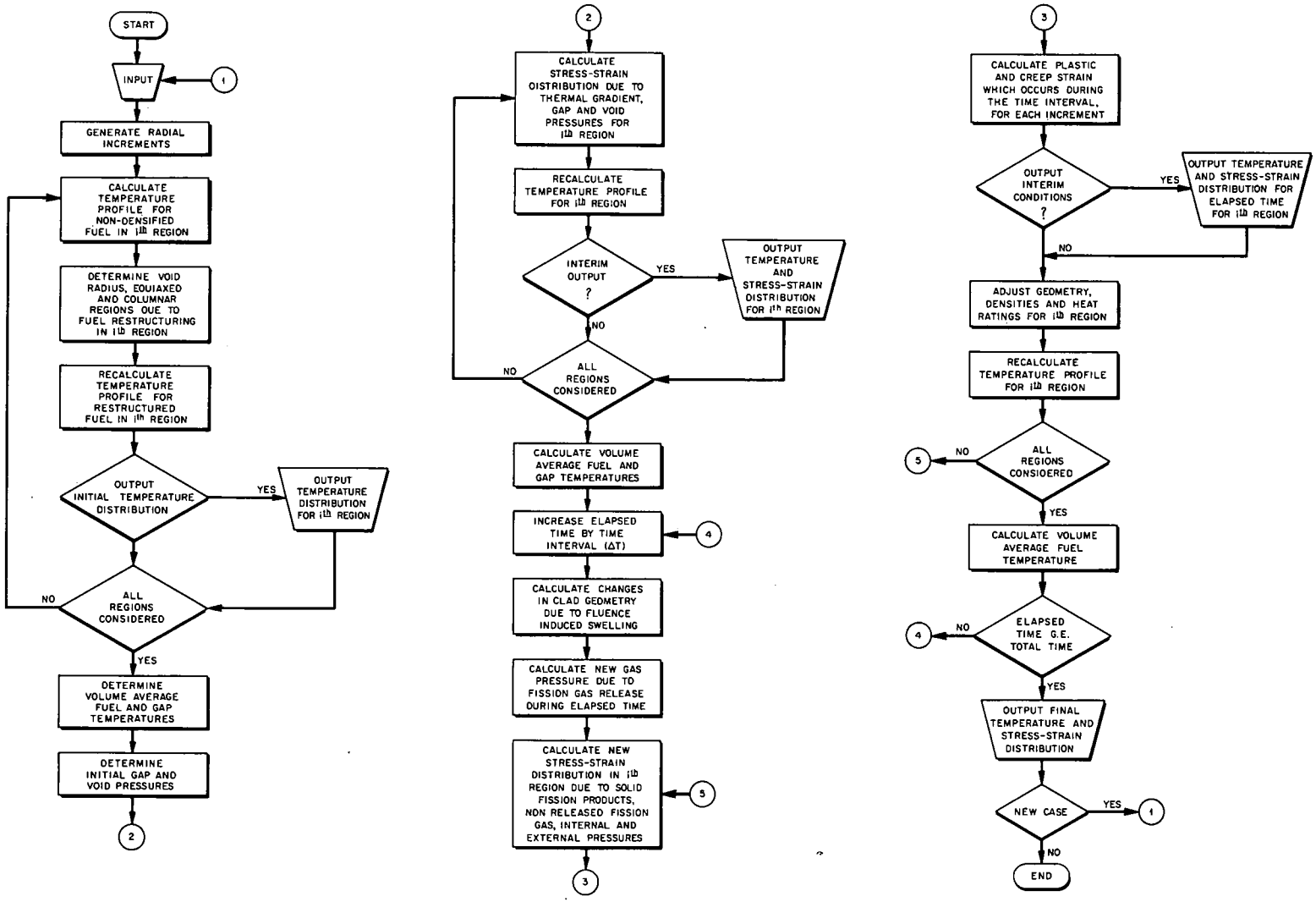

Fig. 4.1. FMØDEL Flow Diagram.

In FMØDEL, the fuel rod is described as a series of axial "regions," each containing radial "increments." The models used to describe the release of fission gas, restructuring of the fuel, and swelling of the fuel represent several degrees of sophistication, as described in the following sections. Some of these models are not completely adequate, but the modular form of the simulation makes it simple to replace these as better models are developed.

The calculational procedure for each region follows this sequence: temperature distribution, fuel restructuring, cladding swelling, release of fission gas, fuel swelling, elastic-plastic stress-strain distribution, and creep stress-strain distribution. The temperature distribution is recalculated at various stages of the sequence to account for restructuring and changes in geometry. Although certain parts of the mechanical analysis are still being improved, we have begun use of the code for the design and interpretation of irradiation experiments with $(U,Pu)O_2$ fuel rods clad with stainless steel.

Fuel Performance

We are developing models for heat transfer, distribution of fission gas, restructuring of the fuel, and swelling caused by fission products.

Heat Transfer (F. J. Homan)

Because of variations in thermophysical properties and the kinetics of chemical phenomena as functions of temperature, an accurate analysis of heat transfer is required to model fuel behavior realistically. The details of our steady-state, one-dimensional heat-transfer analysis for cylindrical ceramic fuel rods were reported previously.[1] In addition to the one-dimensional analysis, we are supporting the modification of an existing multidimensional code for analyzing heat transfer in fuel rods. The modifications involve introducing material properties that are temperature dependent and some reprogramming for operation on IBM/360 computers. Preliminary checks have indicated that the code is operating

properly with these changes. The multidimensional code will give us the capability of accounting for axial heat flow and nonuniform boundary conditions.

Distribution of Fission Gas (F. J. Homan)

The principal loads to which the cladding is subjected arise from pressure built up by release of fission gases from the fuel to the gas plenum and to swelling of the fuel after it contacts the cladding. The distribution of fission gases must be predicted to evaluate each of these phenomena.

We are now using a homogeneous nucleation, random-walk migration model proposed by Greenwood and Speight[2] to describe the formation and growth of gas bubbles. We recognize that the Greenwood-Speight treatment is inadequate for LMFBR fuel, and we plan to replace this module with one that accounts for the driving forces of the temperature gradients and other aspects of growth and motion of bubbles.

The amount of gas released is predicted on the basis of empirical data. This approach relates the amount of gas released to the temperature of the fuel. Clearly, this is an oversimplification. The amount of gas released will depend upon the fuel's fabrication form, density, depletion, and stress state and numerous other variables. We have begun a detailed analysis of available experimental data in an attempt to define the relations between gas release and these variables.

Fuel Restructuring (F. J. Homan)

Due to the high operating temperatures and large temperature gradients, the oxide fuel will generally be restructured so that it has a central void and variable densities. This affects both the heat-transfer and mechanical analyses. We are using a three-region empirical model[1] to describe the restructuring of the fuel in the reactor. This model assumes that stable fuel densities are reached rapidly by comparison with the irradiation times of interest.

Swelling Caused by Fission Products (F. J. Homan)

Our present model assumes that some fraction (depending on temperature) of the fuel porosity remaining after restructuring is available to accommodate solid fission products and unreleased gaseous fission products. The rate at which available porosity is filled is calculated by assuming a constant swelling rate due to the accumulation of solid fission products and adding directly the amount of unreleased fission gas.

Cladding Performance

We are now developing models for the analysis of mechanical interaction between fuel and cladding, swelling of the cladding due to fast-neutron fluence, and cladding failure caused by propagation of cracks.

Mechanical Interaction (F. J. Homan, B. R. Dewey,[3] W. E. Stillman[3])

We have developed a method, based on the work of Johnson[4] and Puthoff,[5] for calculating the distribution of stress and strains in the fuel and cladding. The fuel and cladding cylinders are considered to be symmetrical around the longitudinal axis and are divided into an arbitrary number of increments. The temperature distribution is determined as previously described and the temperature at each individual incremental boundary defines the mechanical properties at that point. By satisfying the compatibility and equilibrium conditions at each boundary and using the boundary conditions at the inner and outer surfaces of the cylinder, we derive a set of 2N simultaneous equations, where N is the number of incremental boundaries. The set of equations is solved by means of a standard banded-matrix solution for the radial and tangential stress at each boundary.

The stresses calculated are the result of the temperature gradient in the cylinder and the pressures on the inner and outer cylindrical surfaces. The stresses calculated by the banded-matrix solution are based on the original incremental dimensions. If the stress state is

high enough to exceed the elastic limit of the material in the cylinder, plastic deformation will occur and reduce the level of stress. The stresses will be further reduced by creep.

We expect that the most interesting and useful information that will come from the analysis of the mechanical interactions is the state of stress at the inside surface of the cladding after the gap between fuel and cladding has closed. The fuel and cladding are then assumed to be homogeneous, continuous cylinders. The state of stress at the inside surface of the cladding is needed for all analyses of damage to the cladding.

The model for analysis of mechanical interaction assumes plane strain and depends upon axial symmetry. This limitation prevents extending the model to the problem of bowing and nonsymmetric boundary conditions. To correct this shortcoming, we have begun developing a simplified discrete-element technique. We use circular shell elements that are connected at the inner and outer radii and at the ends by boundary conditions of force, displacement, and thermal conditions. The individual elements may have arbitrary temperature and material properties, with deformation occurring by elastic or plastic action and by creep. The method has the potential for extension to problems that involve crack propagation and bowing.

The boundary conditions for axisymmetric rings were studied through two cases for which closed-form solutions are available. The agreement with the exact solution for a thick cylinder of isotropic, elastic, homogeneous material loaded by pressure or thermal gradient is shown in Table 4.1. Note that while the dimensionless radial and tangential stresses are not sensitive to the number of elements, the discontinuity of the tangential stress at the element interface is sensitive to the number of elements.

We are now extending the discrete-element technique to inelastic action.

Table 4.1. Comparison of Discrete Elements with Exact Theory for Thick Cylinder[a] with Pressure and Thermal[b] Loading

Number of Elements	Difference,[c] %				Discontinuity Error for Thermal Loading (%)
	Pressure Loading		Thermal Loading		
	$\frac{\sigma_r}{E}$	$\frac{\sigma_t}{E}$ (Averaged)	$\frac{\sigma_r}{E}$	$\frac{\sigma_t}{E}$ (Averaged)	
5	0.0	0.0	−9.0	−8.4	9.5
10	0.0	0.0	−9.0	−8.7	4.7
25	0.0	0.0	−9.0	−8.8	1.9

[a]Ratio of outside radius to inside radius = 2.

[b]Thermal strain ($\alpha\Delta T$) = 0.004.

[c]σ_r = radial stress; σ_t = tangential stress; E = Young's modulus of elasticity.

Swelling of the Cladding Due to Fast-Neutron Fluences (F. J. Homan, B. R. Dewey,[3] W. E. Stillman[3])

Experimental observations[6–10] indicate that stainless steel cladding exposed to a high-energy neutron flux will swell due to the formation of internal voids. The following equation has been suggested to describe this swelling, with a saturation at 12% $\frac{\Delta v}{v_o}$ (ref. 11).

$$\% \frac{\Delta v}{v_o} = 5.0 \times 10^{-36} \ (\Phi t)^{1.66} \left[e^{\frac{-6800}{RT}} - 1.87 \times 10^4 \ e^{\frac{-27,000}{RT}} \right], \quad (4.1)$$

where

Δv = the change in volume,

v_o = the original volume,

Φt = the neutron fluence (> 0.1 Mev),

R = the gas constant, and

T = the absolute temperature.

We view this swelling as a positive effect from the standpoint that the swelling of the cladding permits additional space for accommodation of fuel swelling. There are insufficient data to predict any influences

on mechanical properties. From the design standpoint, the expanded cladding might present a problem of restricted coolant passages or bowing due to flux gradients which we have not yet studied.

Cladding Failure Due to Crack Propagation and Grain-Boundary Cavitation
(F. J. Homan, B. R. Dewey,[3] W. E. Stillman[3])

Once the stress states at the inner and outer surfaces of the cladding have been described as a function of time, cladding failure can be analyzed. Gittus[12] derived an equation for the propagation of a crack in cladding experiencing a tensile stress:

$$\frac{d\ell}{dt} = \frac{\Pi^2 \ \ell \ \sigma^2}{8 \ \overline{T}^2} \dot{\epsilon} \quad , \tag{4.2}$$

where

$\frac{d\ell}{dt}$ = the rate of crack growth,

$\overline{T}$ = the tensile fracture stress,

ℓ = the current crack length,

σ = the tensile stress, and

$\dot{\epsilon}$ = the creep rate.

From this same analysis, a critical crack length is defined as:

$$\ell_{critical} = t(1 - \frac{\sigma}{\overline{T}}) \quad , \tag{4.3}$$

where

$\ell_{critical}$ = the length of the crack at failure, and

t = cladding thickness.

When the crack reaches the critical length, it will fail immediately. The expression for the rate of crack growth [Eq. (4.2)] contains the creep rate. An expression developed[13] for the creep rate is very useful in describing this material property for the cladding for reactor fuels. Because of the way in which nuclear reactors are operated (i.e., periods of intermittent operation and shutdown), the usual form of creep equation employed in cladding models is of limited use. Normally, an equation would consider only secondary creep, or at best consider a

brief period of primary creep followed by secondary creep. If the reactor were shut down and then started up again, the equation would calculate deformation on the assumption that secondary creep resumed. However, if the creep process is viewed as being controlled by the concentration of mobile dislocations, with the creep rate decreasing as mobile dislocations interact and otherwise become entangled until the rate of dislocation generation becomes equal to the rate of entrapment (steady-state condition), a more realistic calculation is possible. After a reactor shutdown (which corresponds to a reduction in the stress state of the cladding) a new period of primary creep would be predicted due to the release of trapped mobile dislocations by thermally activated climb during the period of time at low cladding stress. The cladding equation, derived in detail in ref. 13, is summarized below:

$$\dot{\epsilon} \propto b \rho v , \tag{4.4}$$

where

$\dot{\epsilon}$ = the creep rate,

b = Burgers vector,

ρ = the density of mobile dislocations, and

v = the velocity of mobile dislocations;

$$\dot{\epsilon} = \dot{\epsilon}_1 R , \tag{4.5}$$

where

$\dot{\epsilon}_1$ = the initial creep rate (on loading), and

R = the ratio of the density of mobile dislocations to the density of mobile dislocations before loading;

and

$$\dot{R} = \dot{\epsilon}_1 (R - R_\infty) (\alpha R + \beta) + \gamma (1 - R) , \tag{4.6}$$

where

R_∞ = the asymptote toward which the ratio of the density of mobile dislocations to the initial density of mobile dislocations moves as time approaches infinity,

α = rate of hardening by the second-order reaction of immobilization of dislocations (intersection of mobile dislocations on orthogonal glide systems),

β = rate of hardening by the first-order interaction of glide polygonization of dislocations, and

γ = rate constant for the recovery process.

In order to solve Eq. (4.5) for the strain rate, Eq. (4.6) must be integrated numerically.

Mitra and McLean[14,15] used this equation for creep successfully to predict data for Ni exposed to changing stresses during the creep experiment. Work is in progress to test the equation on creep data for type 316 stainless steel.

Grain-boundary cavitation is another mode by which the cladding might fail. An equation was developed from the work reported in ref. 16 to describe a cumulative damage parameter, p, due to the formation of cavities at the grain boundaries:

$$\frac{dp}{dt} = A\ \sigma\ \gamma\ \epsilon\ , \tag{4.7}$$

where A is the time constant for rupture under constant stress.[17] If the lifetime of the fuel rod is considered as a discrete number of time increments, each at constant stress, a value for p can be calculated for that time increment. When the cumulative value of p reaches 1, failure is assumed to have occurred by intergranular rupture.

References

1. C. M. Cox and F. J. Homan, PRØFIL — A One-Dimensional FØRTRAN IV Program for Computing Steady-State Temperature Distributions in Cylindrical Ceramic Fuels, ORNL-TM-2443 (March 1969), and Addendum (August 1969).
2. G. W. Greenwood and M. V. Speight, J. Nucl. Mater. 10(2), 140–144 (1963).
3. Consultant from the University of Tennessee.
4. D. F. Johnson, Analysis of Elastic-Plastic Stress Distribution in Thin-Wall Cylinders and Spheres Subjected to Internal Pressure and Nuclear Radiation Heating, NASA TND-271 (April 1960).

5. R. L. Puthoff, A Digital Computer Program for Determining the Elastic-Plastic Deformation and Creep Strains in Cylindrical Rods, Tubes, and Vessels, NASA TMX-1723 (January 1969).

6. C. Cawthorne and E. J. Fulton, Nature 216, 575 (Nov. 11, 1967).

7. J. O. Stiegler, E. E. Bloom, and J. R. Weir, Trans. Am. Nucl. Soc. 11(1), 146 (1968).

8. J. J. Holmes and H. R. Brager, Trans. Am. Nucl. Soc. 11(2), 479 (1968).

9. T. Lauritzen et al., Trans. Am. Nucl. Soc. 11(2), 479–480 (1968).

10. S. D. Harkness et al., Trans. Am. Nucl. Soc. 11(2), 480 (1968).

11. W. K. Appleby et al., Oxide Fuel Element Development Quart. Progr. Rept. June 30, 1969, WARD-3791-39, p. 4.

12. J. H. Gittus, "A Theory of Crack-Propagation During Tension-Tension Fatigue in a Material Exhibiting Time-Dependent Plasticity." To be published.

13. J. H. Gittus, "A Model of Creep Embodying Work Hardening and Recovery." To be published.

14. S. K. Mitra and D. McLean, Proc. Roy. Soc. (London) Ser. A, 295(1442), 288–299 (Dec. 6, 1966).

15. S. K. Mitra and D. McLean, Metal Sci. J. 1, 192–198 (1967).

16. J. H. Gittus, "Theory of Fatigue Failure by Cavity Formation," Thermal and High Strain Fatigue, Conference organized by Institute of Metal and Iron, and Steel Institute, held at Church House, London, June 6–7, 1967. Published by Metals and Metallurgy Trust of Institute of Metals and Institution of Metallurgists (1967).

17. J. P. Smith and J. T. Berling, AEC Fuels and Materials Development Program Progress Report No. 74, GEMP-1006 (June 29, 1969).

CLADDING AND OTHER STRUCTURAL MATERIALS

5. MECHANICAL PROPERTIES OF ALLOYS IN REACTOR ENVIRONMENTS AND DEVELOPMENT OF LMFBR CLADDING AND STRUCTURAL MATERIALS

J. R. Weir, Jr. H. E. McCoy, Jr.

This program is concerned with the effects of irradiation on the mechanical properties of various metals of potential use in nuclear reactors. The materials of primary concern are types 304 and 316 stainless steel, both materials of interest for liquid-metal fast breeder reactors (LMFBR). These alloys are being exposed to high neutron fluences, and the resulting changes in density, microstructure, and mechanical properties are being measured. Other materials under study include Incoloy 800 and V. Some attention is also being given to the use of particle accelerators to simulate neutron damage.

Austenitic Stainless Steels

Effects of Irradiation on Mechanical Properties of Type 316 Stainless Steel (E. E. Bloom)

We are evaluating the mechanical properties of standard type 316 stainless steel and type 316 stainless steel containing 0.23 wt % Ti in both the unirradiated and irradiated conditions. Experimental variables being investigated include annealing temperature, amount of cold work, thermal aging, and irradiation conditions.

Previous results[1] showed that for type 316 stainless steel at a test temperature of 650°C, 5% prestrain has no significant effect on either the rupture life or minimum creep rate and that 20% prestrain doubles the rupture life and decreases the minimum creep rate by an order of magnitude.

Specimens of this heat of type 316 stainless steel (composition Fe–0.044% C–17.5% Cr–12.6% Ni–2.8% Mo–0.05% Ti–2.1% Mn–0.8% Si–0.012% P–0.014% S–0.0005% B–0.03% Co–0.1% Cu–0.1% V) were irradiated at 650°C to 1.8×10^{21} neutrons/cm^2 (thermal) and 1.4×10^{21} neutrons/cm^2 (> 1 Mev). The irradiation time was about 4500 hr. One set of samples was given only a preirradiation heat treatment of 1 hr at 1050°C; the other set was given the same heat treatment and then prestrained 5, 10, or 20%.

Figure 5.1 shows the effect of irradiation on the stress-rupture properties of annealed type 316 stainless steel. Irradiation under these conditions reduced the rupture life to 1/8 to 1/6 of its original value. The ductility was also reduced by irradiation, but compared to previous results[2] on another heat of type 316 stainless steel the values are relatively high. This difference may be due to the presence of about 0.05% Ti in this heat as compared to less than 0.01% Ti in the previous heat. These earlier results showed that very small additions of Ti significantly improve the postirradiation ductility. Irradiation at 650°C also increased the minimum creep rate (Fig. 5.2), due to thermal aging of the alloy, and reduced the ductility as a result of the neutron irradiation.

Results on specimens irradiated at 650°C in the 5, 10, and 20% prestrained condition are shown in Fig. 5.3. These preliminary results indicate that prestraining has no significant effect on the rupture life after irradiation. The total elongation was reduced by straining before irradiation. Preliminary examination of curves showing strain versus time indicates that prestrained specimens have lower creep rates than specimens irradiated in the annealed condition.

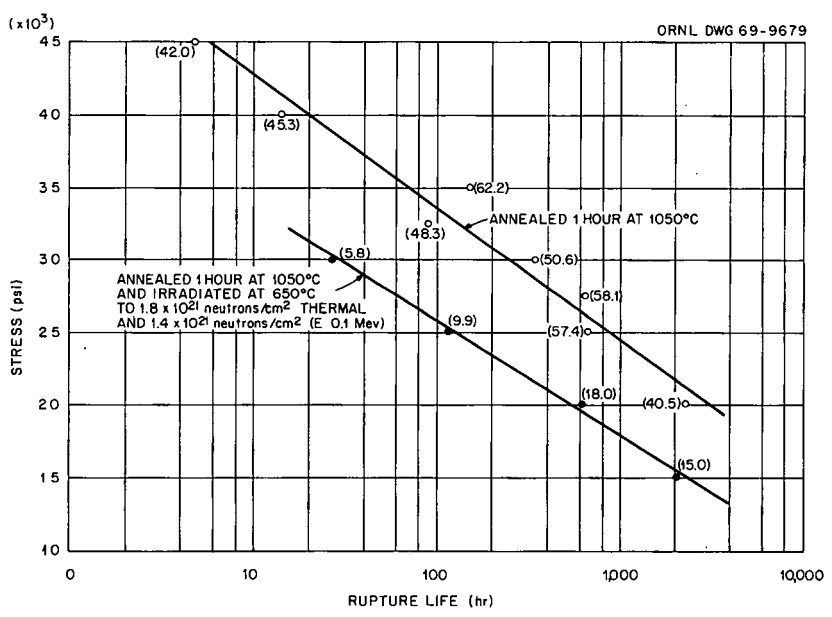

Fig. 5.1. Effect of Irradiation on the Rupture Life of Type 316 Stainless Steel at 650°C. The fracture strains are shown in parentheses.

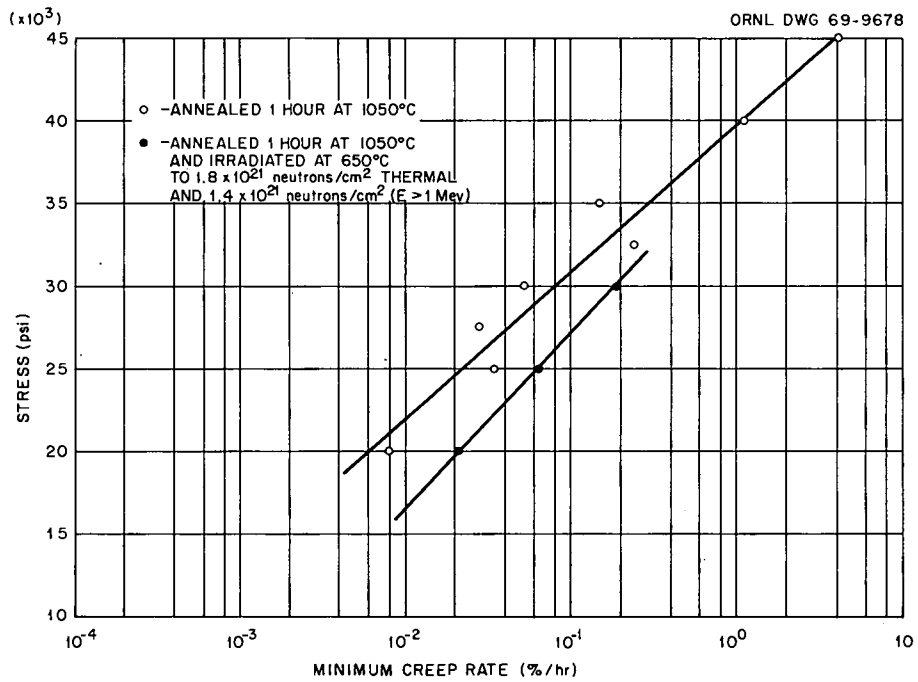

Fig. 5.2. Effect of Irradiation on the Minimum Creep Rate of Annealed Type 316 Stainless Steel at 650°C.

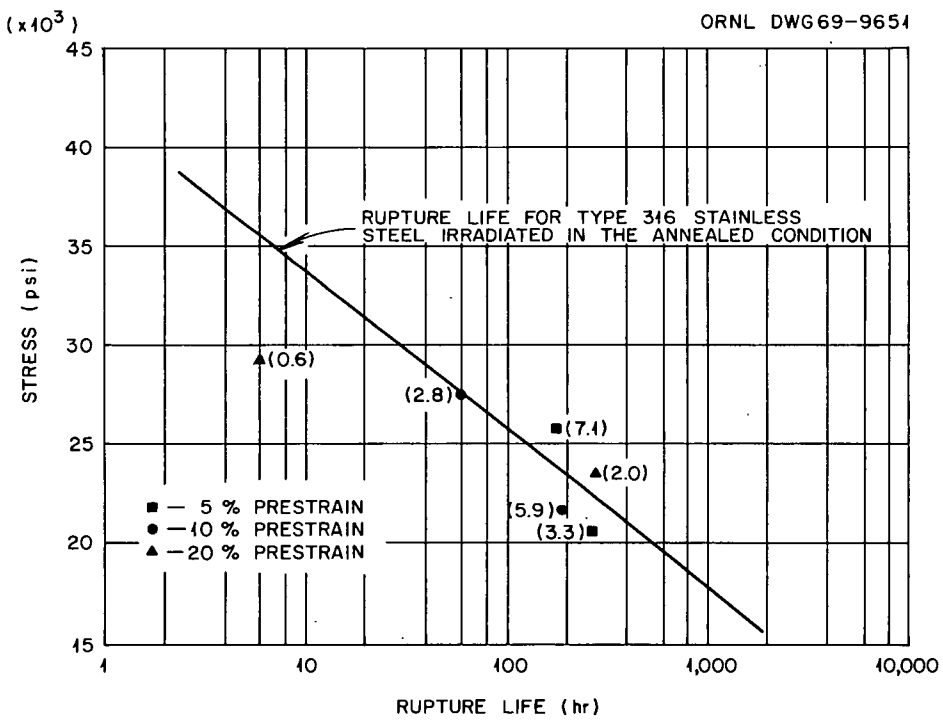

Fig. 5.3. Effect of Prestrain on Postirradiation Rupture Life and Ductility of Type 316 Stainless Steel Irradiated and Tested at 650°C. Fracture strains of the irradiated samples are shown in parentheses.

Mechanical Properties of EBR-II Safety-Rod Thimble (E. E. Bloom)

Specimens of the design shown in Fig. 5.4 were machined from flat C of the (3-D-1) safety-rod thimble for the Experimental Breeder Reactor-II (EBR-II). Specimens of the same design have been machined from portions of an unirradiated thimble that was supplied by Argonne National Laboratory from the same heat as the irradiated thimble.

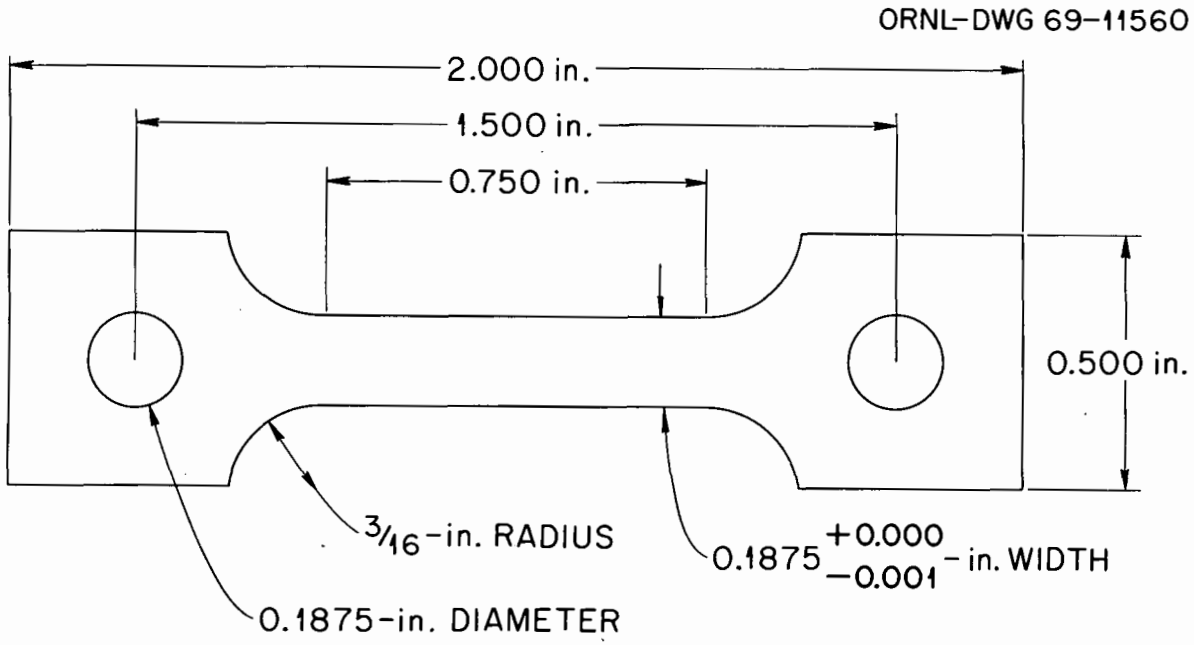

Fig. 5.4. Test Sample Made From the EBR-II Safety-Rod Thimble for Tests of Mechanical Properties.

Figure 5.5 shows the creep-rupture properties of the unirradiated thimble at a test temperature of 600°C. Over this range of rupture lives the elongation at fracture ranged from 15 to 40%.

The effect of fast-neutron fluence (measured at the center of the gage section) on the rupture life at 600°C and a stress of 27,500 psi is shown in Fig. 5.6. The rupture life was reduced from about 185 hr in the unirradiated condition to about 50 to 80 hr at a fluence of only 3×10^{21} neutrons/cm^2 (> 0.1 Mev). At constant fluence, specimens irradiated at 370°C had shorter rupture lives than specimens irradiated at 460°C. At each temperature, the rupture life decreased with increasing

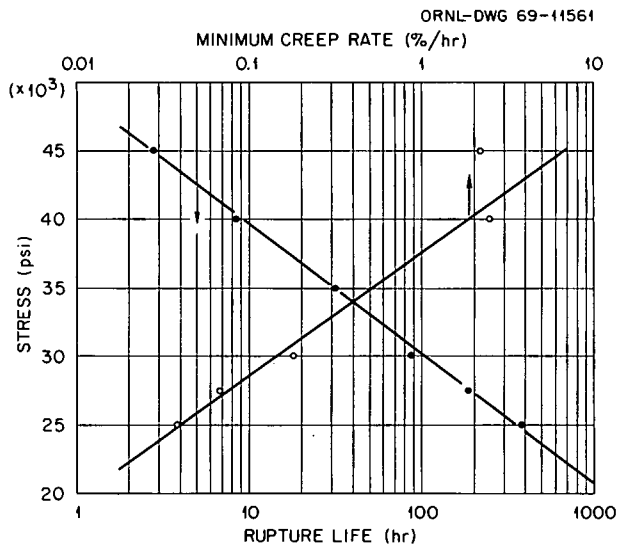

Fig. 5.5. Creep-Rupture Properties of Unirradiated EBR-II Safety-Rod Thimble at 600°C.

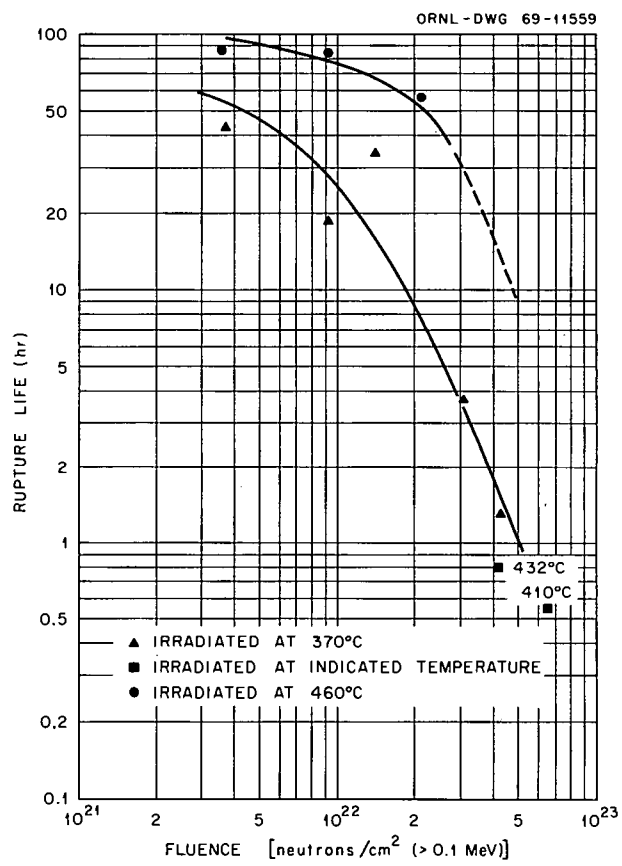

Fig. 5.6. Postirradiation Rupture Life of Type 304 Stainless Steel at 600°C and 27,500 psi. The rupture life of an unirradiated specimen tested at this temperature and stress was 185 hr.

fluence. A specimen removed from the region of the thimble extending from 1 to 3 in. above the midplane had a rupture life of 0.55 hr. The fluence received by this specimen was 6.5×10^{22} neutrons/cm^2 (> 0.1 Mev).

Figure 5.7 is a plot of total elongation as a function of fluence. Irradiation to approximately 3×10^{21} neutrons/cm^2 (> 0.1 Mev) reduced the elongation to about 2–3%. The elongation was further reduced with increasing fluence and reached a value of 0.13% after irradiation to 6.5×10^{22} neutrons/cm^2 (> 0.1 Mev). The elongation appears to be independent of the irradiation temperature over the range studied.

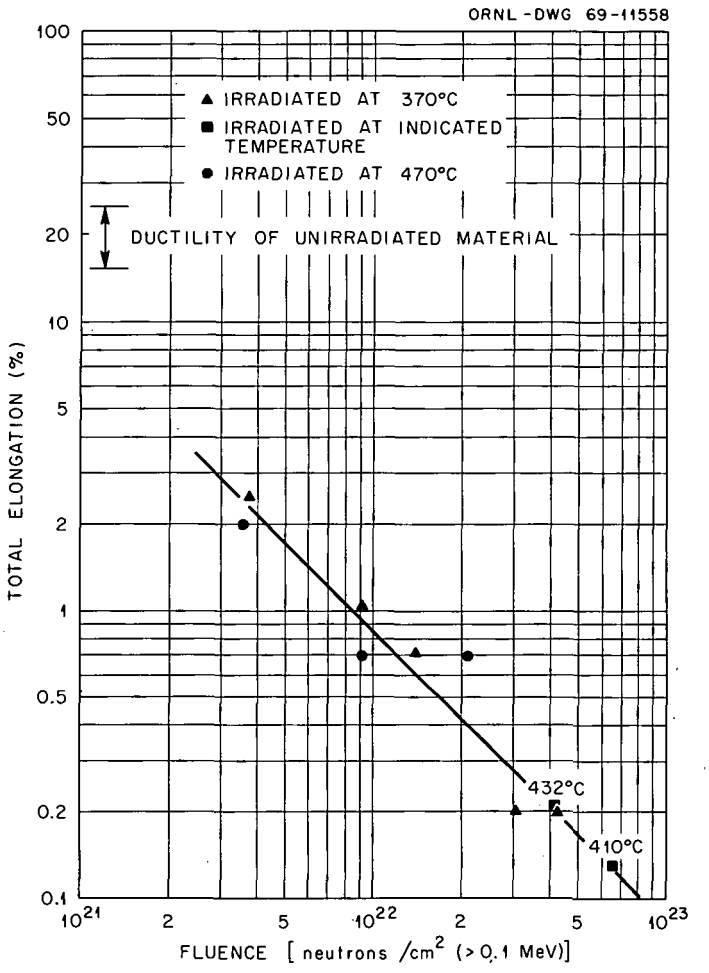

Fig. 5.7. Postirradiation Ductility of Type 304 Stainless Steel Tested at 600°C and 27,500 psi.

Curves showing strain versus time for these tests are being evaluated. Initial trends indicate that the irradiated specimens exhibit little primary or teritary creep and that the minimum creep rate for irradiated specimens is lower than that for unirradiated specimens.

A specimen of this material was removed from that portion of the thimble located at the reactor midplane and analyzed for He. Results indicated a concentration of about 16 ppm (atomic) He. Results reported by King[3] indicate that at 600°C and a stress of 30,000 psi a uniform concentration of 20 ppm (atomic) He reduces the rupture life of type 304 stainless steel from 900 to 40 hr, while the elongation remains almost unchanged at about 13%. The present results on material irradiated in the EBR-II indicate that the damage is more severe than that produced simply by the presence of He.

Effects of Irradiation Variables on Swelling and Formation of Voids
(E. E. Bloom, J. O. Stiegler)

We are following the development of radiation damage in austenitic stainless steels by measurements of immersion density and examination by transmission electron microscopy. Specimens from three components of the EBR-II (cladding for the driver fuel, shroud tube from subassembly XG05, and 3-D-1 safety-rod thimble) and specimens that were irradiated in capsule AS-26 of subassembly X010 are being examined.

The results of measurements of immersion density of specimens removed from flat C of the EBR-II safety-rod thimble are shown in Fig. 5.8. The maximum decrease in density, 3.35%, occurred about 2 in. above the midplane. Figure 5.9 is a plot of the available data[4] on decrease in density as a function of fast-neutron fluence for type 304 stainless steel irradiated in the EBR-II at temperatures between 370 and 480°C. Attempts were made[5] to fit these data to an empirical expression of the form

$$\frac{\Delta\rho}{\rho} = A\ (\varphi t)^B \exp(-C/RT)\ , \qquad (5.1)$$

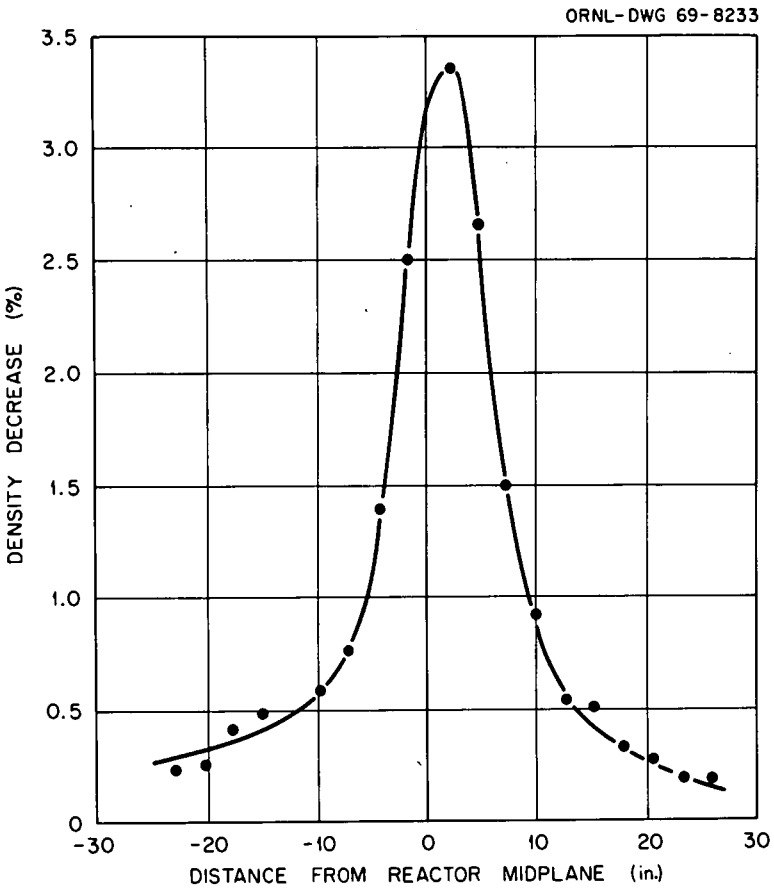

Fig. 5.8. Immersion Density of Specimens From Flat C of EBR-II Safety-Rod Thimble.

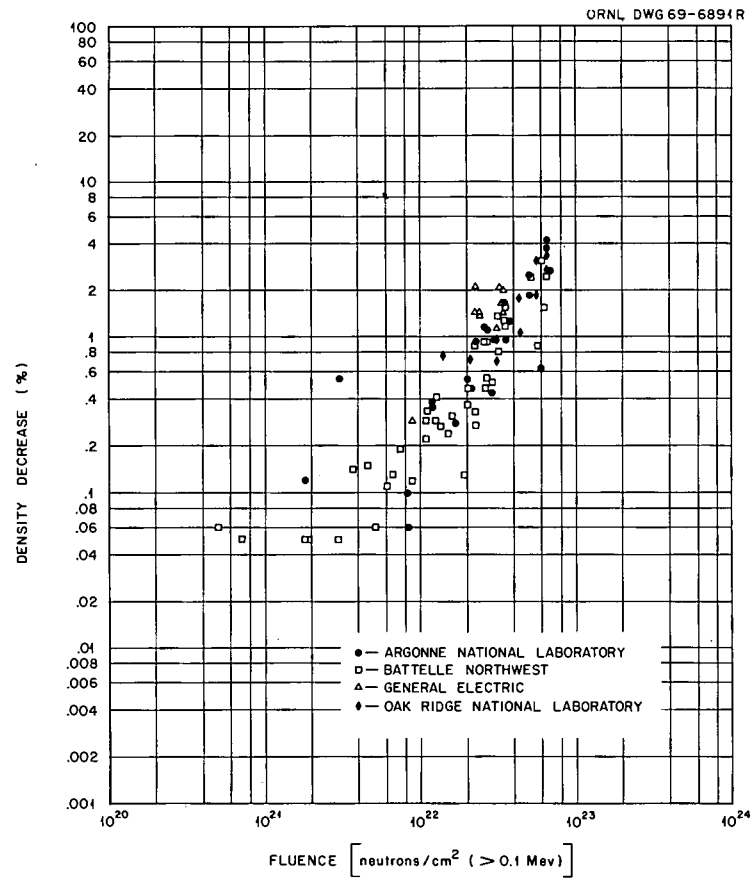

Fig. 5.9. Summary of Available Data on the Decrease in Density Induced by Irradiation of Types 304 and 304L Stainless Steel. (Data summarized from T. T. Claudson et al., "Fast-Reactor Radiation-Induced Changes in Cladding and Structural Materials," paper presented at International Atomic Energy Agency Symposium on Radiation Damage in Reactor Materials, Vienna, June 2–6, 1969. To be published in the proceedings.)

where

ρ = density,

φ = neutron flux,

t = time,

R = gas constant,

T = absolute temperature, and

A, B, and C = adjustable constants.

Of particular interest is the value of B or the slope of a plot of $\log \frac{\Delta\rho}{\rho}$ versus $\log \varphi t$. When the original ground rules[5] are applied (use only those data from specimens irradiated within ±10 in. of the core midplane and adjust each datum point by subtracting 0.05%), the value of B determined from a least-squares fit of the data with temperature and fluence as the independent variables is 1.7. We have examined the data using somewhat different ground rules. When all data are considered and not adjusted, the least-squares fit gives a value of 0.78 for B. When only the data for specimens ±10 in. from the core midplane are used and adjusted by subtracting 0.06% instead of 0.05% from each datum point, the value for B is 1.72. An examination of Table 5.1 shows that the value of B is very sensitive to the data considered. We believe that the best data available come from those specimens irradiated near the bottom or the top of the core, where the temperature is known to be 370 to 380°C or 460 to 470°C, respectively, and from those specimens within ±10 in. from the reactor midplane, where the flux and neutron spectrum are best known. When determined this way, the value of B is 0.64 or 0.71, depending upon whether or not the data are adjusted by 0.06%. These values agree rather well with the values obtained when all data are considered.

We have extended the analysis one step further by extracting and analyzing separately the data for those specimens irradiated at 370 to 380°C and 460 to 470°C. The data are plotted in Fig. 5.10. At 370 to 380°C, a least-squares fit gives $\frac{\Delta\rho}{\rho} \propto (\varphi t)^{0.84}$ and $(\frac{\Delta\rho}{\rho} - 0.06) \propto (\varphi t)^{1.05}$. At 460 to 470°C, a least-squares fit gives $\frac{\Delta\rho}{\rho} \propto (\varphi t)^{1.04}$ and $(\frac{\Delta\rho}{\rho} - 0.06) \propto (\varphi t)^{1.24}$. Equation (5.1) assumes that the slopes of the $\ln \frac{\Delta\rho}{\rho}$ vs $\ln (\varphi t)$ curves are constant and independent of temperature and

Table 5.1. Analysis of Swelling Data

Data Used	Number of Data Points	Equation Used in Fit[a]	Value of Constants		
			A	B	C
All data	93	(5.1)	1.1×10^{-17}	0.78	1180
	85	(5.2)	2.1×10^{-23}	1.06	2120
Only data from ±10 in. of core midplane	55	(5.1)	2.2×10^{-32}	1.54	4680
	55	(5.2)	2.5×10^{-36}	1.72	5040
Only data from ±10 in. of core and only irradiation temperature of 370 to 380°C and 460 to 470°C	17	(5.1)	6.9×10^{-12}	0.64	5080
	17	(5.2)	2.5×10^{-13}	0.71	5470

[a]Equation (5.1): $\frac{\Delta\rho}{\rho} = A\ (\varphi t)^B \exp(-C/RT)$.

Equation (5.2): $\frac{\Delta\rho}{\rho} - 0.06 = A\ (\varphi t)^B \exp(-C/RT)$.

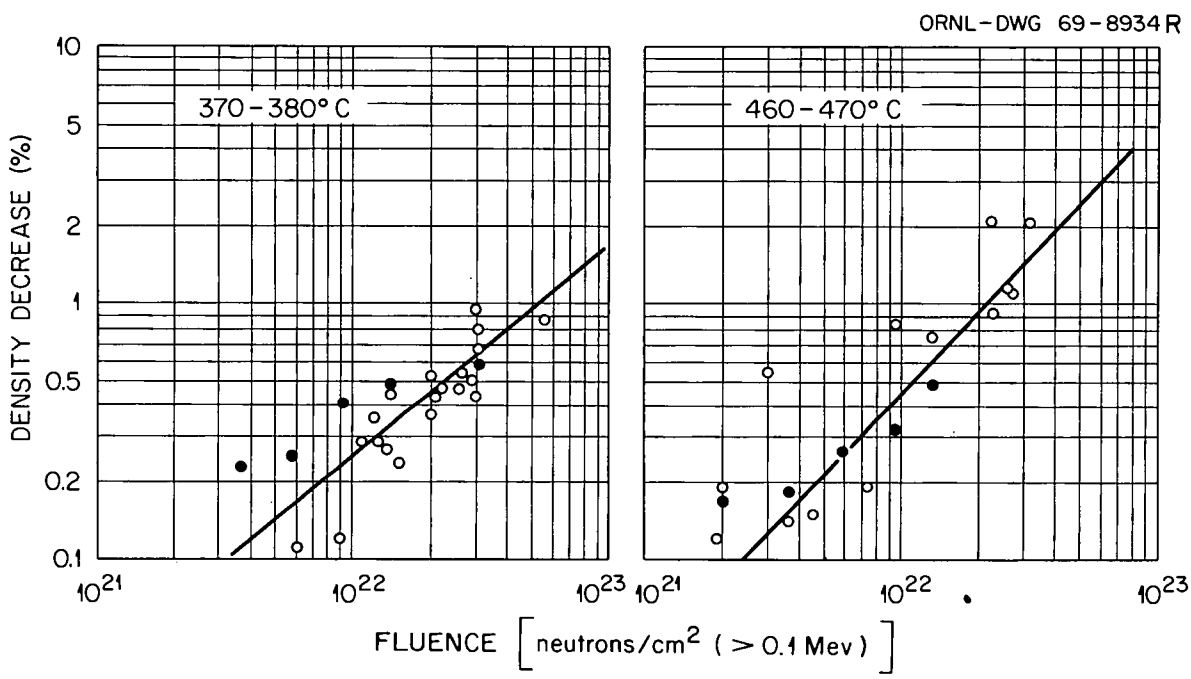

Fig. 5.10. Decrease in Density of Type 304L Stainless Steel Irradiated to Temperatures of 370 to 380°C and 460 to 470°C.

that curves for specimens irradiated at different temperatures are merely displaced from one another by an amount given by the temperature-dependent term.

Our analysis strongly suggests that the fluence dependency of the swelling is not constant but is at least a function of irradiation temperature. This conclusion is substantiated by electron microscopy observations of void concentrations and sizes as functions of irradiation temperature and fluence. We shall discuss in detail only observations made at 370 to 380°C and at 460 to 470°C, although all other observations are consistent with these findings.

Previously reported observations[6,7] of the cladding of the EBR-II driver fuel showed that between irradiation temperatures of 370 and 470°C void concentrations decreased and void sizes increased as the irradiation temperature increased. Similar behavior was also found for the XG05 shroud tube and the 3-D-1 safety-rod thimble. Void concentrations at 370 to 380°C and 460 to 470°C are plotted as functions of fast-neutron fluence in Fig. 5.11. Concentrations at 370 to 380°C are always higher than those at 460 to 470°C, but at a fluence of about 10^{22} neutrons/cm^2 the concentrations at 460 to 470°C increase at a faster rate than they do at 370 to 380°C. Slopes of the solid lines drawn in Fig. 5.11 are 0.6 at 370 to 380°C and 1.4 at 460 to 470°C. Clearly, these slopes could not have persisted since the beginning of the irradiation or the void concentrations at 370 to 380°C could not be higher than those at 460 to 470°C.

These measurements, coupled with our earlier observations[8] of stainless steel specimens irradiated in EBR-II to a fluence of 1.4×10^{20} neutrons/cm^2 (> 0.1 Mev), suggest that the fluence at which damage is first observed is temperature dependent and that the slope of the curve for concentration versus fluence may not be constant at a given temperature but may also be a function of fluence. The micrographs from the experiment at low fluence show only black spots, most of which have been identified as dislocation loops but a few of which have spherical strain fields. The concentration of spots decreases with increasing temperature, as can be seen in Fig. 5.12, and at this fluence no observable damage exists above an irradiation temperature of 524°C.

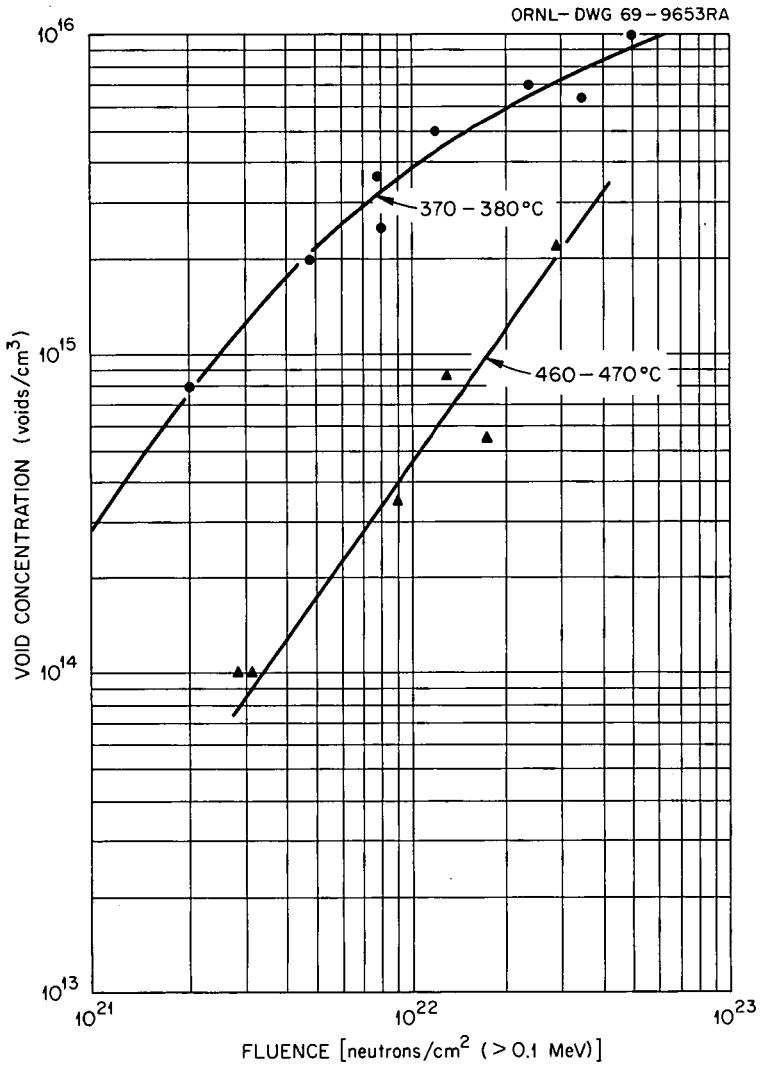

Fig. 5.11. Void Concentration as a Function of Fluence for Type 304L Stainless Steel Irradiated at Temperatures of 370 to 380°C and 460 to 470°C.

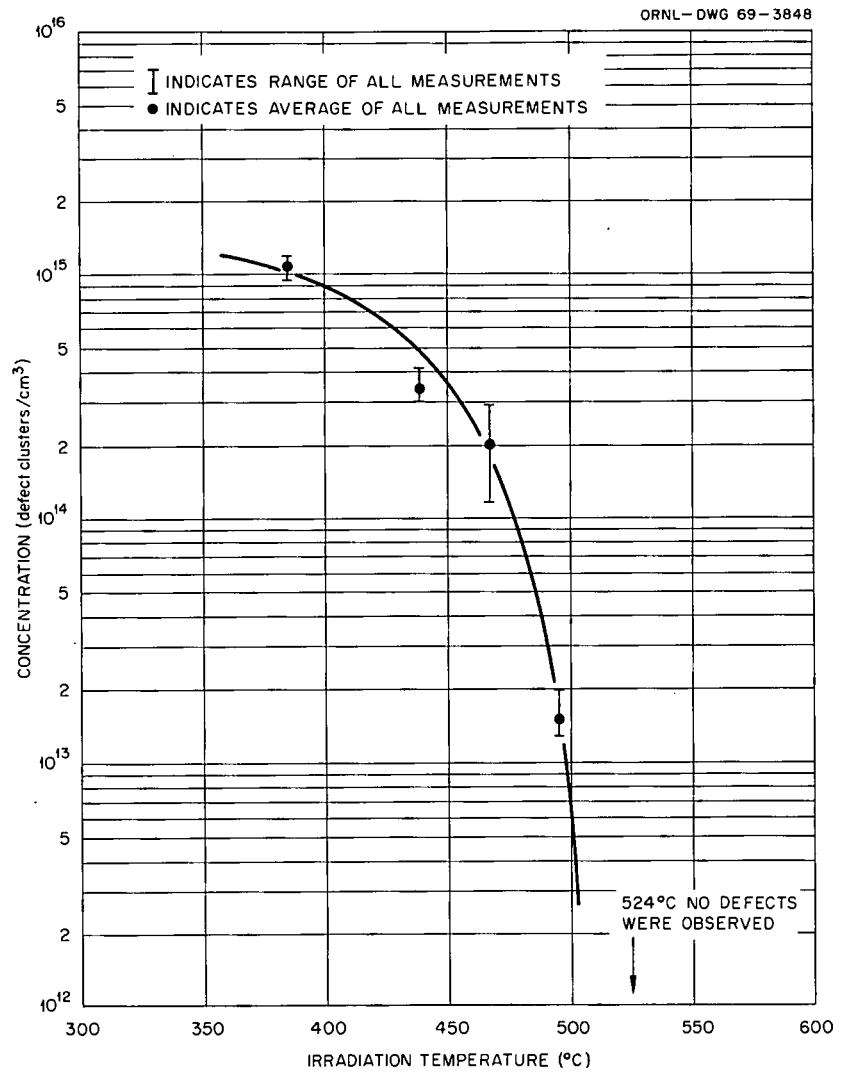

Fig. 5.12. Total Concentration of Defect Clusters as a Function of Temperature for Type 304L Stainless Steel Irradiated to 1.4×10^{20} neutrons/cm^2 (> 0.1 Mev).

However, numerous observations[9–11] at higher fluences have shown that voids and dislocation loops may be formed at appreciably higher temperatures. This indicates that the fluence at which damage first occurs increases with increasing irradiation temperature. At a temperature of 370°C, the concentration of spherical defects, which could be small voids, is significantly less than the concentration of voids to be expected from extrapolation of the curve shown in Fig. 5.11 to a fluence of 1.4×10^{20} neutrons/cm^2. It is possible, however, that we are not able to resolve all the voids present, and any statement regarding the dependence of the slope on fluence must await examination of specimens irradiated to about 10^{21} neutrons/cm^2.

Our values for void concentration agree well with those that Claudson et al.[4] obtained on similar materials.

As was mentioned earlier, both the average and maximum void sizes increase with increasing temperature. The average void size also increases with increasing fluence, but the maximum void size increases little, if any, at fluences above 10^{22} neutrons/cm^2. This is illustrated in Fig. 5.13, where photomicrographs of specimens irradiated to 460°C to fluences of 3×10^{21}, 9×10^{21}, and 2×10^{22} neutrons/cm^2 are compared. The maximum void diameter is equal in all the photomicrographs. Plots of maximum void diameter as a function of fluence at 370 and 470°C, given in Fig. 5.14, confirm this observation. No comparable decrease in the rate of void growth has been detected in high-purity Al irradiated up to 10^{22} neutrons/cm^2 (ref. 12).

It appears, therefore, that voids in stainless steel grow very quickly, in a fluence increment of a few times 10^{21}, to a limiting size above which their rate of growth is very slow, possibly zero. In this case the rate of swelling approximately reflects the nucleation rate. Comparison of Figs. 5.10 and 5.11, in which data for swelling and void concentration are presented as a function of fluence, shows that the swelling and the void concentration increased at comparable rates with increasing neutron fluence.

No account has been taken of differences in flux in these graphs. We have, however, examined a few specimens irradiated to similar fluences

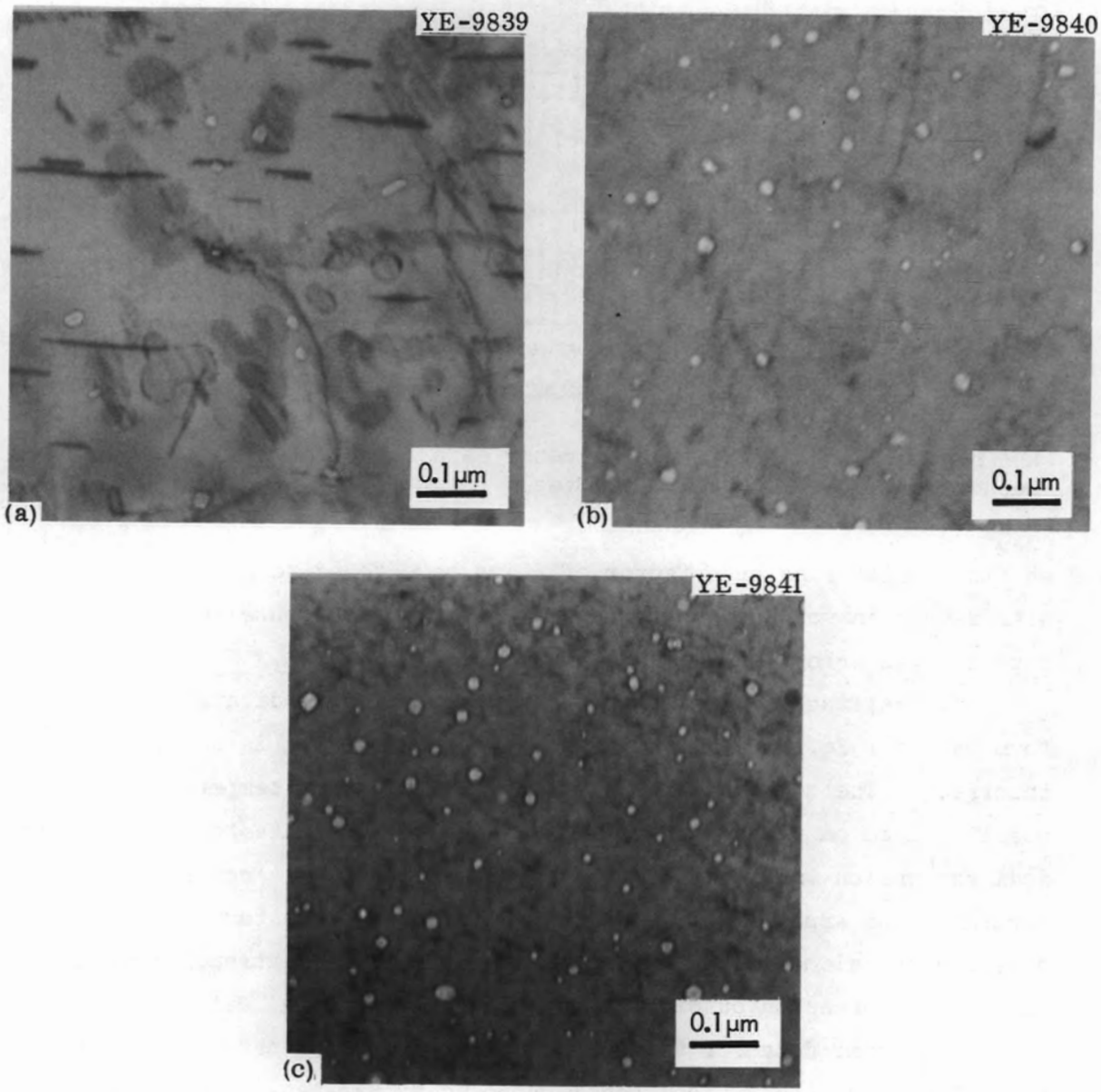

Fig. 5.13. Voids in Type 304L Stainless Steel Irradiated at 460°C to Fluences of (a) 3×10^{21}, (b) 9×10^{21}, and (c) 2×10^{22} neutrons/cm^2 (> 0.1 Mev).

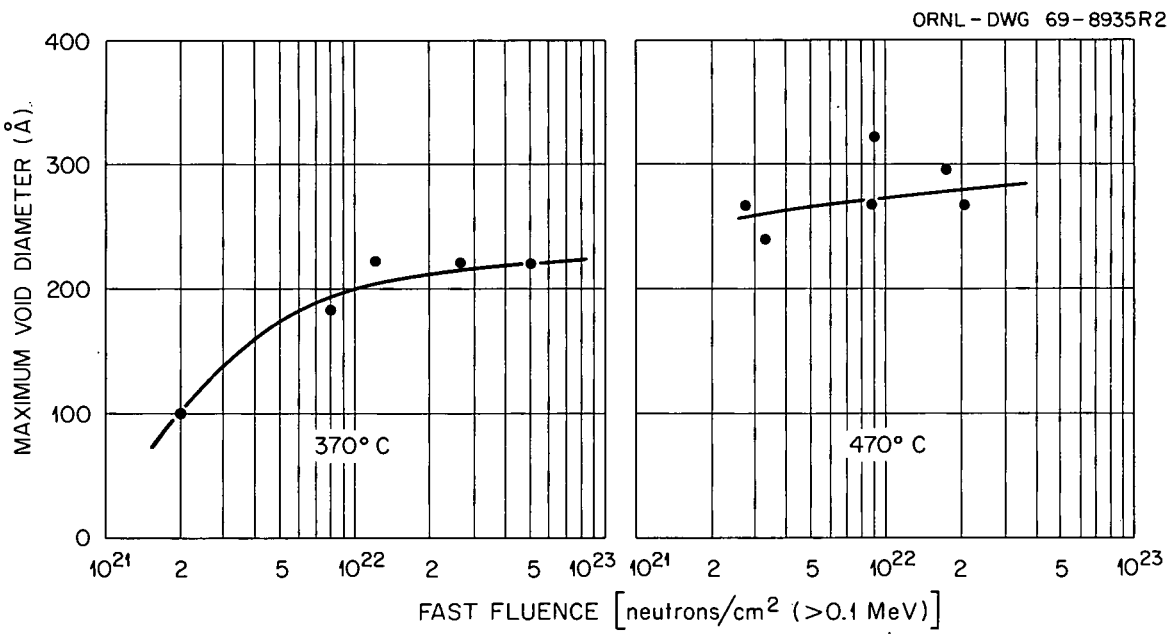

Fig. 5.14. Maximum Void Diameter as a Function of the Fast-Neutron Fluence for Type 304L Stainless Steel.

at fluxes differing by a factor of 6 and have found no appreciable differences in void concentration or size distribution within our experimental error.

The swelling and microstructural observations indicate that the form used for Eq. (5.1) to describe the swelling data is basically incorrect. The constant B is certainly dependent on temperature and possibly also on fluence. Attempting to force the data to fit an empirical expression in which the temperature dependence is contained in a separate term appears to inflate the value of the constant B. These observations also make questionable the validity of extrapolating the empirical expression outside the range of experimental data.

These same data for void concentration and size can also be used to evaluate the theoretical model proposed by Harkness and Che-Yu Li[13] to explain the temperature dependence of the swelling, since the model also predicts these quantities. The model gives a maximum nucleation rate and hence void concentration at about 430°C, with the rate at 470°C being 2 or 3 times greater than at 370°C. Experimentally, we observe that void concentration is significantly greater at 370°C than at 470°C,

decreases with increasing temperature, and does not go through a maximum in this temperature range. Although a maximum in the swelling is observed around 500 to 550°C, the model predicts a much stronger temperature dependence than is found experimentally. For example, the model indicates that the swelling at 470°C is over an order of magnitude greater than at 370°C, although a difference of no more than a factor of 2 has been measured.

The model also concludes that the swelling should vary as the fluence raised to the 2.5 power. Experimental values are significantly smaller, and the exponent appears to be temperature dependent.

The peculiar growth pattern in which the voids grow rapidly to some limiting size is not contained in the model, which predicts that the void radius should vary as the square root of the void lifetime.

We conclude that nucleation and growth of voids is considerably more complex than the processes envisioned in the theoretical interpretations advanced to date.

Comparison of Swelling and Formation of Voids Induced by Irradiation in Two Austenitic Stainless Steels (E. E. Bloom, J. O. Stiegler)

The formation of voids and a resultant decrease in density have been observed in several austenitic stainless steels subjected to neutron irradiation at temperatures between about 350 and 650°C (refs. 7, 11, 14, 15). The voids observed by electron microscopy generally range from about 50 A in diameter (the smallest observable) up to a maximum of a few hundred angstroms in diameter and are present in concentrations as high as 10^{16} voids/cm^3. The mean void diameter increases and the void concentration decreases as the irradiation temperature increases when the fluence is held constant. To date most of the investigations have been conducted on either type 304 or type 316 stainless steel, and these two alloys appear to exhibit similar changes in density and microstructure for a given irradiation condition. Recently, Lauritzen *et al.*[15] reported significant differences in the swelling of type 304 and type 347 stainless steels and Incoloy 800 after irradiation in the EBR-II to 3.4×10^{22} neutrons/cm^2 (total) at about 660°C. The type 304 and 347 stainless steels became 1.21 and 0.54% less dense, respectively.

Transmission electron microscopy revealed that the voids in type 347 stainless steel were much smaller than those in type 304 stainless steel, although the concentration was slightly higher.

To further investigate the effects of composition on the decrease in density and changes in microstructure, we irradiated a standard type 304 stainless steel and a type 304L stainless steel modified by the addition of approximately 0.2% Ti in a row 7 position of the EBR-II. The alloys, which had compositions listed in Table 5.2, were cold worked 50% and then annealed 1 hr at 1040°C before irradiation. The specimens were irradiated in axially adjacent positions of the same experimental assembly. Since the specimens were in contact with one another and in axially adjacent positions, they were irradiated nearly identically. The calculated irradiation temperature was 450 ± 50°C, and the neutron fluences were 1.75×10^{22} neutrons/cm^2 and 1.53×10^{22} neutrons/cm^2 (> 0.1 Mev) for the standard and Ti-modified alloys, respectively.

The density of unirradiated and irradiated specimens of these two alloys was measured by an immersion technique. The average result of five independent density measurements on each specimen is listed in Table 5.3. The decrease in the density of the standard type 304 stainless steel was larger by about a factor of 4 than that for the Ti-modified type 304L stainless steel.

The void distribution observed in the electron microscope is shown in Fig. 5.15. The voids appeared to be homogeneously distributed throughout the matrix and were not observed at grain boundaries. Measurement of the distribution of void sizes gave a maximum void diameter of about 240 A and a mean void diameter of 140 A in each alloy. The void concentrations were determined by measuring the foil thickness by stereo microscopy; the results were 4.9×10^{15} and 1.1×10^{15} voids/cm^3 in the standard and modified alloys, respectively. The changes in density calculated from the distribution of void sizes and the void concentrations were 0.67 and 0.16% for the standard and modified compositions, respectively, which agree closely with the results of measurements of immersion density.

Table 5.2. Composition of Standard Type 304 and Titanium-Modified Type 304L Stainless Steels

Alloy	Composition, wt %									
	C	Cr	Ni	Ti	Mn	Si	P	S	B	Fe
Standard type 304 stainless steel	0.057	18.0	9.0	< 0.01	0.76	0.48	0.020	0.016	0.0003	Bal
Ti-modified type 304L stainless steel	0.014	18.3	10.0	0.18	1.54	0.72	0.005	0.005	0.0014	Bal

Table 5.3. Results of Measurements[a] of Immersion Density

Alloy	Density		
	Unirradiated (g/cm^3)	Irradiated (g/cm^3)	Decrease (%)
Standard type 304 stainless steel	7.8964	7.8514	0.57
Ti-modified type 304L stainless steel	7.9058	7.8950	0.14

[a]Density was measured at 23 ± 1°C.

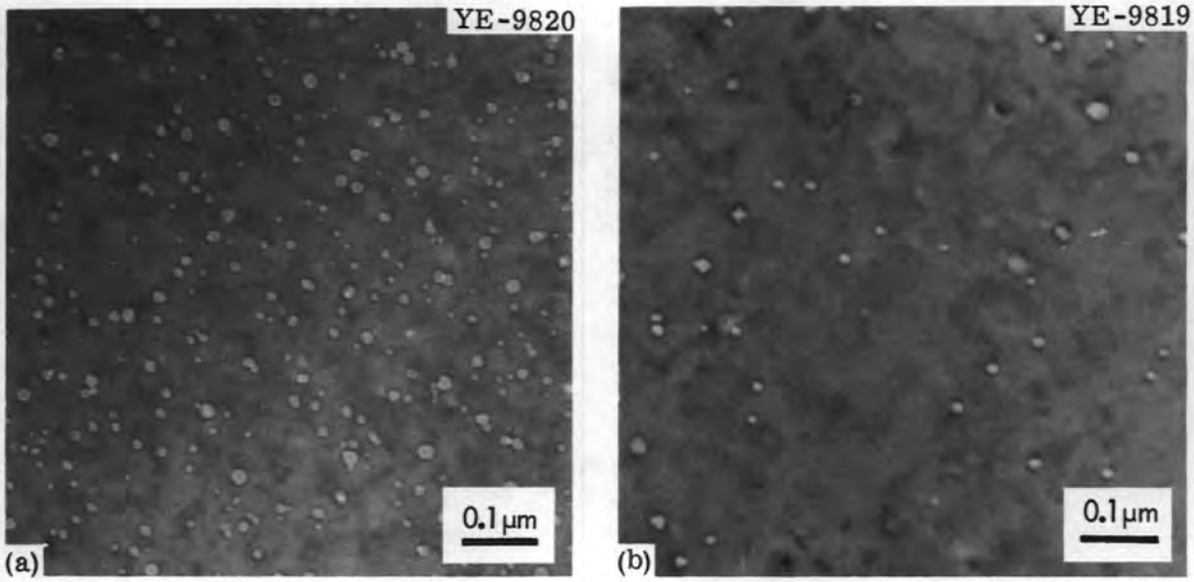

Fig. 5.15. Voids in Stainless Steel Irradiated in the EBR-II at 450 ± 50°C. (a) Standard type 304 stainless steel irradiated to 1.75×10^{22} neutrons/cm^2 (> 0.1 Mev). (b) Titanium-modified type 304L stainless steel irradiated to 1.5×10^{22} neutrons/cm^2 (> 0.1 Mev).

These observations support the previous findings of Lauritzen *et al.*,[15] that relatively minor changes in the composition of austenitic stainless steels can have significant effects on the extent of swelling produced by neutron irradiation. In that study, void growth appeared to be reduced in type 347 stainless steel from that found in type 304 stainless steel. In our work, we compared standard type 304 stainless steel and a Ti-modified type 304L stainless steel and found that the latter

alloy swelled less, primarily as a result of a reduced rate of void nucleation.

Stainless steel is much too complex an alloy to allow speculation of possible mechanisms that might explain these results. These observations do, however, provide strong motivation for more basic studies of the effects of composition on the characteristics of void nucleation and growth.

Irregular Void Distributions (E. E. Bloom, J. O. Stiegler)

It is generally stated[4–10] that the voids formed in stainless steels are homogeneously distributed except for small denuded zones adjacent to grain boundaries. Recently, Stiegler *et al.*[16] have reported observations of nonhomogeneous void distribution in high-purity Al, and Farrell[17] has found even more striking examples of irregular void configurations in deformed-and-recovered high-purity Fe. Close examination of stainless steels, particularly after irradiation to low fluences, has also shown nonhomogeneous void distribution.

This is illustrated in Fig. 5.16, which shows voids located on dislocation lines in type 304 stainless steel exposed to 4×10^{21} neutrons/cm^2 at 460°C. Stereo microscopy has confirmed that these voids lie on the lines, which we believe are grown-in dislocations, possibly poisoned by impurities.

Although these observations do not allow us to specify a mechanism of void nucleation, they demonstrate that under certain irradiation conditions homogeneous nucleation and spike nucleation processes are not dominant and that impurities and structural irregularities can be important.

Incoloy 800

Aging Studies (D. G. Harman)

We have previously reported experimental results showing that radiation enhances the aging of Incoloy 800 containing 0.1% Ti and 0.12% C. By preaging to allow excess C to precipitate from solution and form less harmful globular carbides along the grain boundaries, we retained the good creep strength of the large grain size and improved the postirradiation ductility.

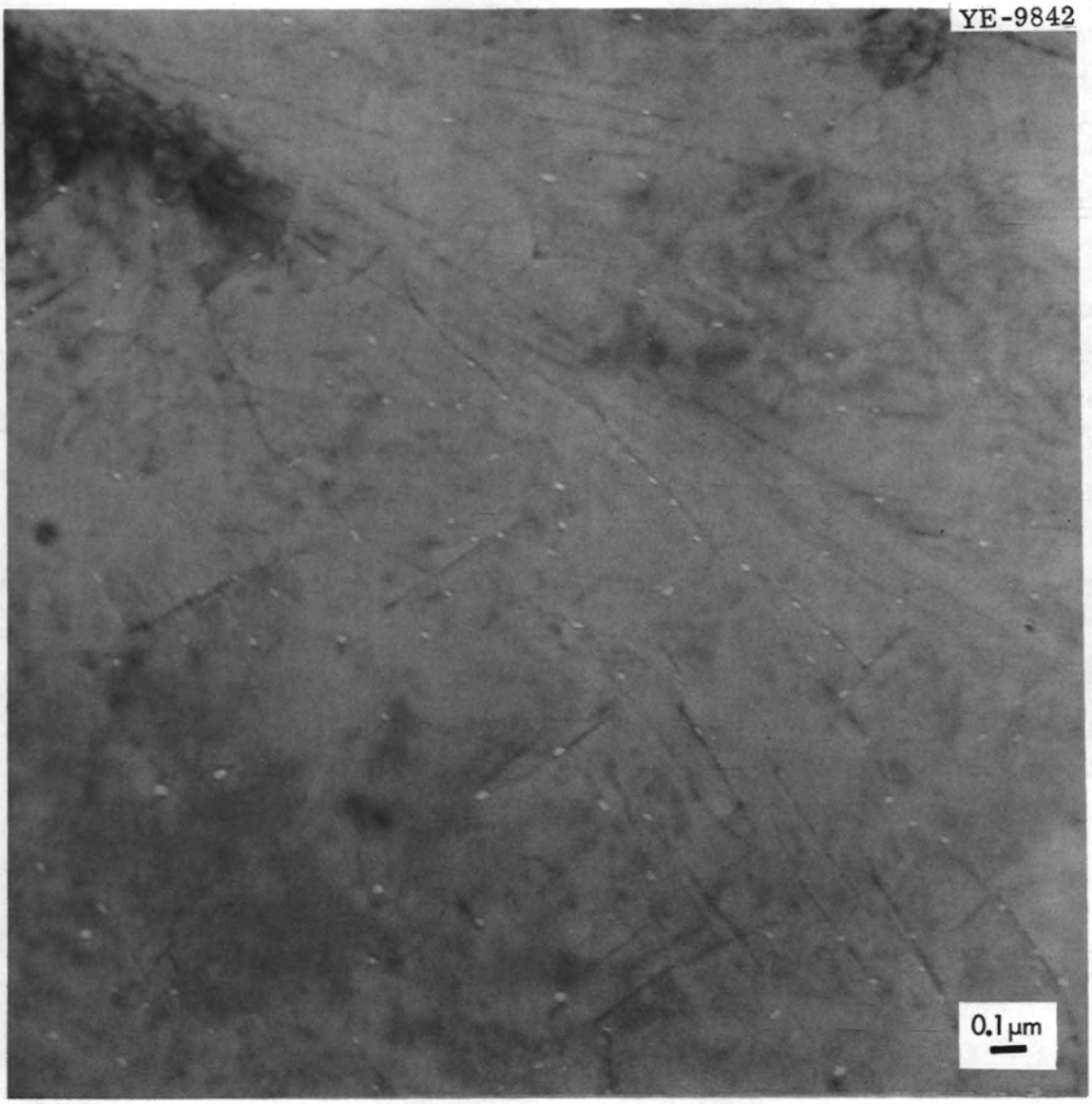

Fig. 5.16. Irregular Void Distributions in Type 304L Stainless Steel Irradiated at 460°C to Approximately 4×10^{21} neutrons/cm^2 (> 0.1 Mev). Nearly all of the voids lie along dislocation lines, some of which are visible in residual contrast.

We have recently used the scanning electron microscope to better illustrate the carbide morphology. Figure 5.17 shows the structure of this alloy after being solution annealed at 1150°C and aged 2200 hr at 500°C. A continuous grain-boundary precipitate is present that has been identified as $M_{23}C_6$. Figure 5.17 was obtained from the buttonhead of a creep specimen that showed only 25% total creep elongation at 650°C. Utilizing the carbide agglomerating treatment (solution anneal followed by 100 hr at 800°C) before the long-term exposure at 500°C resulted in the structure shown in Fig. 5.18 for the same heat of Incoloy 800. The $M_{23}C_6$ carbides are now much larger and are discontinuous along the grain boundaries. Figure 5.18 was obtained from the buttonhead of a creep specimen that showed 59% total creep elongation at 650°C after being exposed 2200 hr at 500°C, as was that shown previously in Fig. 5.17.

Fig. 5.17. Structure of Incoloy 800 Containing 0.12% C and 0.1% Ti Annealed at 1150°C and then Aged 2200 hr at 500°C. This scanning electron photomicrograph was prepared by T. A. Nolan, Physics Division, Oak Ridge Gaseous Diffusion Plant.

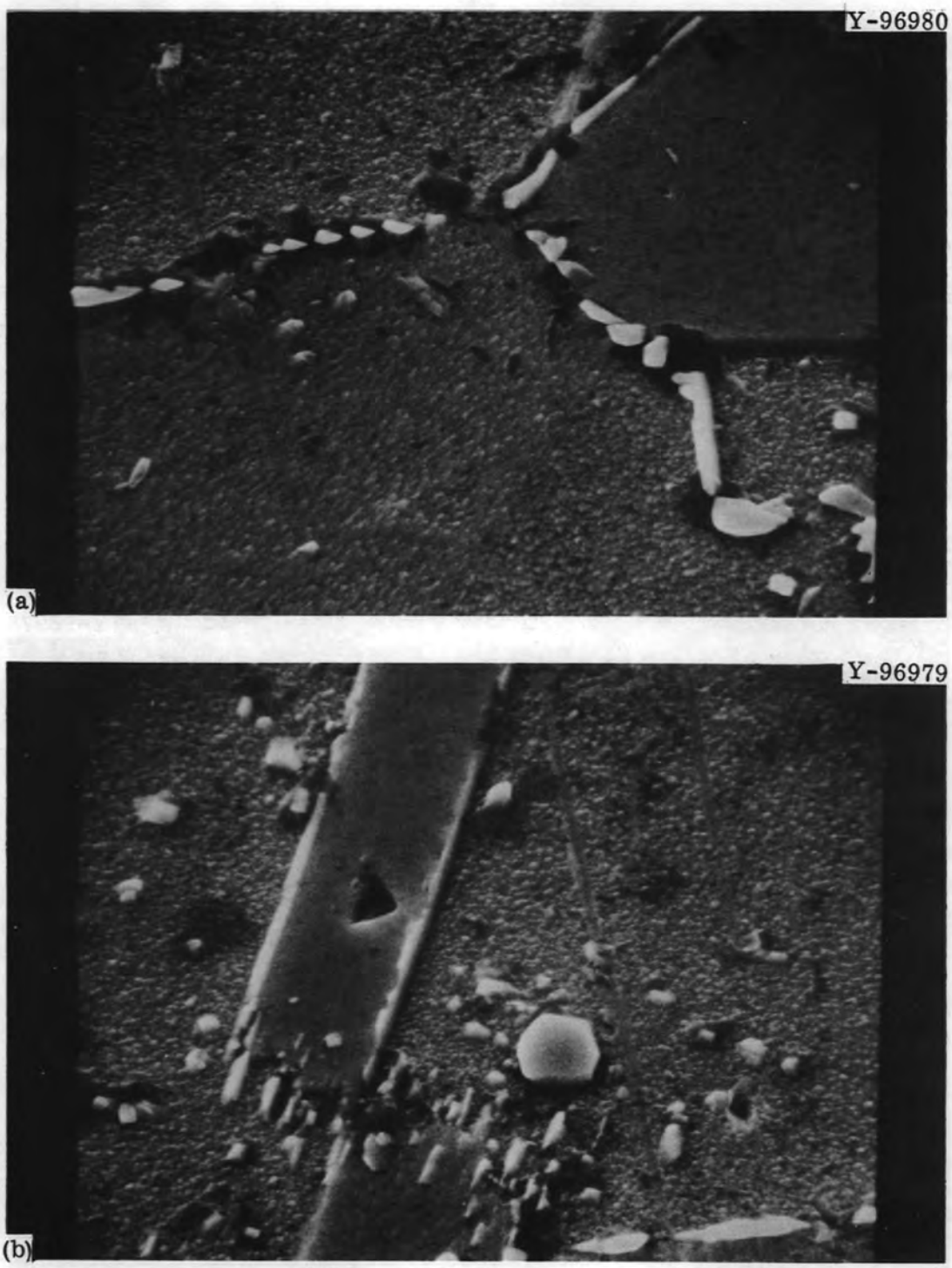

Fig. 5.18. Structure of Incoloy 800 Containing 0.12% C and 0.1% Ti Annealed at 1150°C and Aged 100 hr at 800°C and then Aged 2200 hr at 500°C. (a) Area around junction of three grains, and (b) coherent and incoherent twin boundaries. 5000×. These electron scanning photomicrographs were prepared by T. A. Nolan, Physics Division, Oak Ridge Gaseous Diffusion Plant.

The presence of the globular carbides shown in Fig. 5.18 results in a lower shear stress along the boundary (stress is proportional to the free length of boundary) and is also a formidable obstacle to the propagation of a crack at the grain boundary. Another contributing effect might be that the globular carbides could act as "sponges" that soak up the unwanted tramp elements that can form thin, nearly continuous films at grain boundaries.

Another interesting observation is that the out-of-reactor aging seems to reach a limit after about 2000 hr, while the in-reactor aging does not. We also noted that even after essentially all (about 95%) of the B had been transmuted, the postirradiation ductility continued to decrease significantly with increased irradiation. It is possible that fast-neutron damage continues to strengthen the matrix, thus forcing the "unhardened" boundaries to sustain a disproportionate amount of deformation and resulting in intergranular fracturing after small amounts of overall elongation of the specimens.

Figure 5.19 shows creep curves for a specimen irradiated at 350°C to 1.6×10^{21} neutrons/cm^2 (thermal and fast) and for a control specimen. Both specimens were aged about 4400 hr at 350°C and tested at 650°C at a stress of 30,000 psi. The creep curve for the control specimen shows that the aged structure is not stable at the test conditions; that is, a discontinuity occurs after about 20 hr and results in a more rapid rate of creep than that established in the early part of the test. The creep curve for the irradiated specimen, on the other hand, shows no discontinuity, indicating a stable structure, and retains the very low creep rate throughout the test. This results in an extended rupture life.

Aging studies now under way should lead to a better understanding of the aging observed for this heat of material and may possibly explain the significantly lesser effects for the alloys that contain 0.03 and 0.006% C. These alloys show better postirradiation ductility after irradiation at 500°C than at higher temperatures, and the alloys with 0.03% C are relatively unaffected by the aging treatment before irradiation.

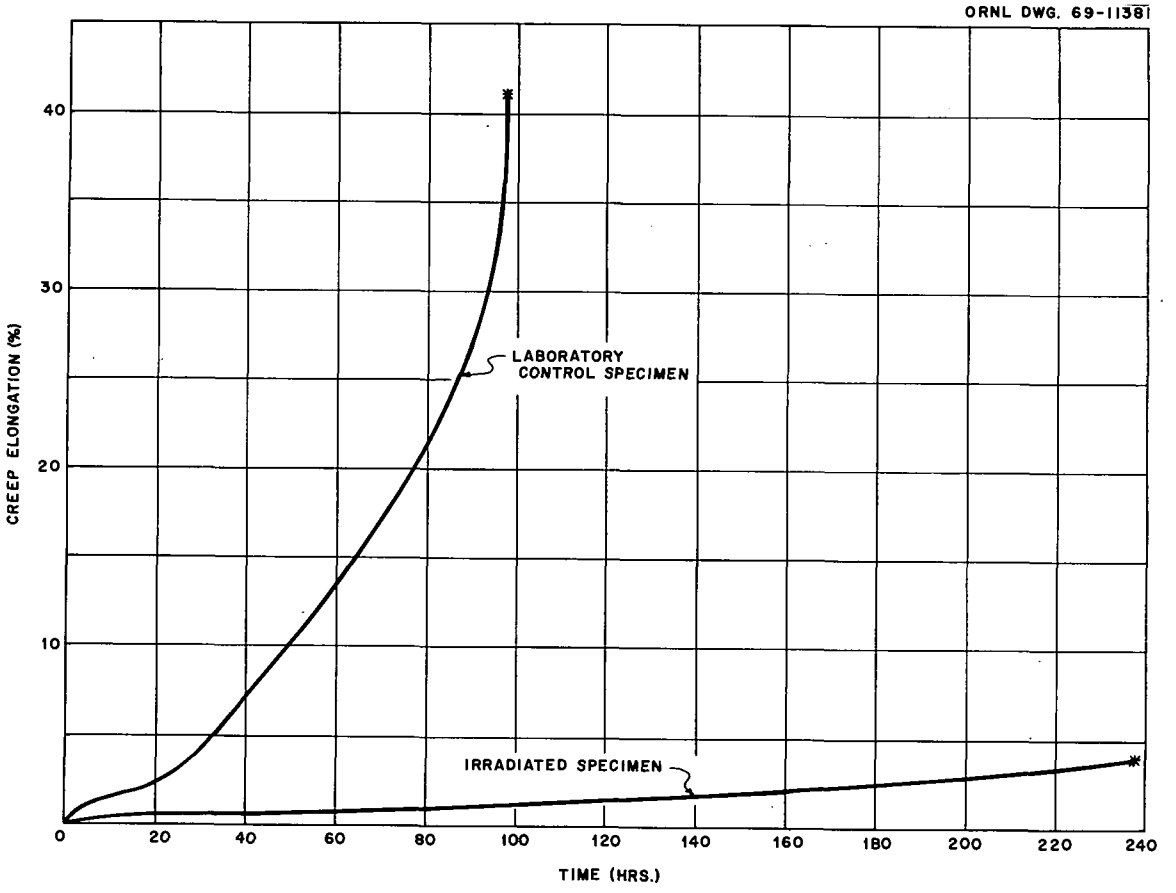

Fig. 5.19. Creep Curves for Irradiated and Control Specimens of Incoloy 800. Test was conducted in air at 30,000 psi and 650°C. Irradiation was conducted in the Oak Ridge Research Reactor at 350°C to a fluence of 1.6×10^{21} neutrons/cm^2 (thermal and fast). The control specimen was held in a laboratory furnace in air for an equivalent time (about 4400 hr).

References

1. E. E. Bloom, Fuels and Materials Development Program Quart. Progr. Rept. June 30, 1969, ORNL-4440, pp. 117–123.
2. E. E. Bloom, Trans. Am. Nucl. Soc. 12(1), 129–130 (June 1969).
3. R. T. King, Fuels and Materials Development Program Quart. Progr. Rept. June 30, 1968, ORNL-4330, pp. 176–183.
4. T. T. Claudson et al., "Fast-Reactor Radiation-Induced Changes in Cladding and Structural Materials," paper presented at International Atomic Energy Agency Symposium on Radiation Damage in Reactor Materials, Vienna, June 2–6, 1969. To be published in the proceedings.

5. J. L. Straalsund and H. R. Brager, Quarterly Progress Report April, May, June, 1969, Reactor Fuels and Materials Development Programs for Fuels and Materials Branch of USAEC Division of Reactor Development and Technology, BNWL-1144, pp. 12.15–12.22.
6. J. O. Stiegler, E. E. Bloom, and J. R. Weir, Fuels and Materials Development Program Quart. Progr. Rept. June 30, 1968, ORNL-4330, p. 183.
7. J. O. Stiegler and E. E. Bloom, "The Effects of Large Fast-Neutron Fluences on the Structure of Stainless Steel," to be published in Journal of Nuclear Materials.
8. E. E. Bloom and J. O. Stiegler, Fuels and Materials Development Program Quart. Progr. Rept. March 31, 1969, ORNL-4420, p. 146.
9. C. Cawthorne and E. J. Fulton, The Nature of Small Defect Clusters, AERE-R-5269, p. 446 (1966).
10. C. Cawthorne and E. J. Fulton, Nature 216, 575 (1967).
11. J. J. Holmes et al., Acta Met. 16, 955 (1968).
12. N. H. Packan, Oak Ridge National Laboratory, private communication.
13. S. D. Harkness and Che-Yu Li, "A Model for Void Formation in Metals Irradiated in a Fast Neutron Environment," paper presented at International Atomic Energy Agency Symposium on Radiation Damage in Reactor Materials, Vienna, June 2–6, 1969. To be published in the proceedings.
14. C. Cawthorne and E. J. Fulton, Nature 216, 515 (1967).
15. T. Lauritzen et al., Nucl. Eng. Des. 9, 265–268 (1969).
16. J. O. Stiegler, K. Farrell, C.K.H. DuBose, and R. T. King, "High Fluence Neutron Irradiation Damage in Aluminum," paper presented at International Atomic Energy Agency Symposium on Radiation Damage in Reactor Materials, Vienna, June 2–6, 1969. To be published in the proceedings.
17. K. Farrell, Oak Ridge National Laboratory, private communication.

6. FABRICATION DEVELOPMENT FOR LMFBR STAINLESS STEEL TUBING

W. O. Harms W. R. Martin

This program involves development techniques for fabricating high-quality type 316 and modified type 304 stainless steel tubing in sizes of interest to the liquid-metal fast breeder reactor (LMFBR) program.

The general scope includes using fabrication techniques that may be transferred to commercial vendors and sufficient nondestructive and destructive testing of the intermediate and final products to assure and demonstrate the quality.

Fabrication Studies on Type 316 Stainless Steel

A. C. Schaffhauser

We are concentrating our fabrication efforts on type 316 stainless steel tubing. We have received a special 10-ton melt of type 316 stainless steel purchased by Battelle Memorial Institute Pacific Northwest Laboratories (BNWL) from Crucible Steel Company for use in our LMFBR and Fast Flux Test Facility (FFTF) programs. This material was received as 4 1/2-in.-diam bar rolled from a 16-in.-diam ingot arc-melted twice in vacuum and as 7 1/2-in.-diam bar rolled from a 18-in.-diam ingot arc-melted three times in vacuum. As part of the FFTF program for BNWL, we shall add C and N during remelting of the 7 1/2-in.-diam bar and shall extrude, tube reduce, and draw this material to evaluate the effect of changes in chemistry. For the LMFBR program, we are extruding, tube reducing, and drawing or planetary swaging the 4 1/2-in.-diam material arc-melted twice in vacuum to study fabrication variables and the effect of defects. Preliminary studies of drawing and planetary swaging used tube hollows from Allegheny-Ludlum Steel Corporation heat 65808 and commercial pipe of type 316 stainless steel.

Melting, Extrusion, and Tube Reducing (R. E. McDonald)

A single 7 1/2-in.-diam bar from the Crucible Steel Company heat 073306 was quartered to make four consumable electrodes for our studies

of the effects of C and N additions. The first electrode was consumably vacuum arc-melted at 5×10^{-5} torr into a 6-in.-diam water-cooled Cu mold. The power required was 3200 amp at 35 v.

The 240-lb ingot was stripped from the mold, and the top and bottom were cropped and sampled for chemical analysis. Based on the results of this chemical analysis, the compositions of the three remaining heats will be adjusted to produce three additional ingots that contain, respectively, low N and high C, high N and low C, and high N and high C. The four ingots will be forged to octagonal bars, machined into extrusion billets and extruded into tube shells.

Nine 3.950-in.-OD × 1.500-in.-ID × 10-in.-long extrusion billets were machined from 4 1/2-in.-diam bars from the Crucible Steel Company heat 065219. The billets were heated to 1150 to 1200°C in a neutral salt and held 1 hr at temperature. The reduction ratio and extrusion speeds were held nearly constant for all eight extrusions, as shown in Table 6.1. The extruded tube shells were nominally 2.1 in. in outside diameter by 1.36 in. in inside diameter by 50 in. long and were machined to 2.0 in. in outside diameter by 0.25 in. in wall thickness.

The newly installed Aetna-Standard tube reducer[1,2] was instrumented to give parting force, mandrel pull, speed, power input, etc. We are presently interested in the parting force and the mandrel pull, since these data indicate how much work the machine performs and the effectiveness of the lubricant. With our present rolls and mandrels, we can reduce a 2.0-in.-OD × 0.25-in.-wall thickness × 50-in.-long tube shell to a 1.0-in.-OD × 0.1-in.-wall thickness × 240-in.-long tube hollow in a single operation.

We have tube reduced Crucible Steel-Fast Flux Test Facility (CSFFTF) tube shells 1 and 2. Unfortunately, CSFFTF-1 had surface defects, and CSFFTF-2 was badly scored on the outside surface because of a misaligned tail stock traced to the private contractor's failure to pin the tail stock after the strain gage was installed. This problem is now being corrected. The lubrication broke down on the inside surface of the tube shell during tube reduction of both CSFFTF-1 and -2. The tube shells were not galled but were somewhat marked. We shall provide continuous lubrication for the inside surface of the next tube shell.

Table 6.1. Data for Type 316 Stainless Steel Tube Shells[a] Extruded from Crucible Steel Company Heat 065219 for Studies in Support of the Fast Flux Test Facility Program

Tube Shell Identification Number	Extrusion Number	Extrusion Ratio	Pressure, tons		Temperature (°C)	Speed (in./sec)	Extrusion Factor (K) (psi)
			Maximum	Minimum			
CSFFTF-1	0785	5.90	700	480	1150	0.80	70,000
CSFFTF-2	0786	5.90	710	520	1150	0.71	71,000
CSFFTF-3	0787	5.90	610	415	1150	0.50	61,000
CSFFTF-4	0788	5.90	770	620	1150	0.60	77,000
CSFFTF-5	0794	5.67	810	540	1200	0.66	82,000
CSFFTF-6	0795	5.67	765	570	1200	0.71	77,000
CSFFTF-7	0796	5.67	770	530	1200	0.56	78,000
CSFFTF-8	0797	5.67	600	440	1200	0.71	61,000
CSFFTF-9	0798	5.67	620	490	1200	0.62	63,000

[a]Billet dimensions: 3.950-in. outside diameter, 1.500-in. inside diameter, 10-in. length; 90° conical nose with 1.562-in.-diam flat.

Drawing of Type 316 Stainless Steel Tubing (G. A. Reimann)

Continuing efforts on Allegheny-Ludlum Steel Corporation heat 65808 (refs. 3, 4) will concentrate on evaluation of the material rather than on fabrication of more tubing. All tubing is being tested nondestructively. We submitted several tubes that had passed nondestructive testing for burst tests at elevated temperature to compare the properties of cold-worked, stress-relieved, and fully recrystallized tubing at 450, 550, and 650°C.

For the remainder of the tubing fabrication studies, we shall use the tube hollows of type 316 stainless steel from Crucible Steel Company heat 065219 (ref. 5).

We machined 0.013 in. from the outside surface of tube hollow CSFFTF-1 to provide defect-free material for planetary swaging and studies of the microstructure of this heat. Drawing studies on this material are under way.

We have planetary swaged samples of types 304 and 316 stainless steel to investigate several variables. The ORNL planetary swager (Fig. 6.1) is patterned after the British design but is more rigidly constructed and is capable of a greater range of sizes (2-in. to 1/4-in. outside diameters) because it can accommodate ball-and-cone assemblies of several sizes. Since the original V-belt drive was unsatisfactory, gear pulleys and belts were installed to prevent slippage. Also, since the 1 1/2 hp variable-speed motor is not sufficient for heavy reductions on the larger sizes of tubing, a 7 1/2 hp motor will be substituted. A geared reducer was installed as an interim measure to increase the available torque; but this reduced the head speed to 450 rpm, and the corresponding reduction in bench speed makes this process very slow.

The initial studies of planetary swaging were performed on type 316 stainless steel from Allegheny-Ludlum Steel Corporation heat 65808. The 1 1/2-in.-OD × 0.0134-in.-wall thickness tubes were mandrel drawn to 1.145 in. in outside diameter by 0.098 in. in wall thickness in one pass and annealed 15 min at 925°C. The same mandrel (0.950 in.) was used throughout this experiment so that planetary swaging concentrated on wall ironing. We obtained a total of 50% cold work in one tube sample

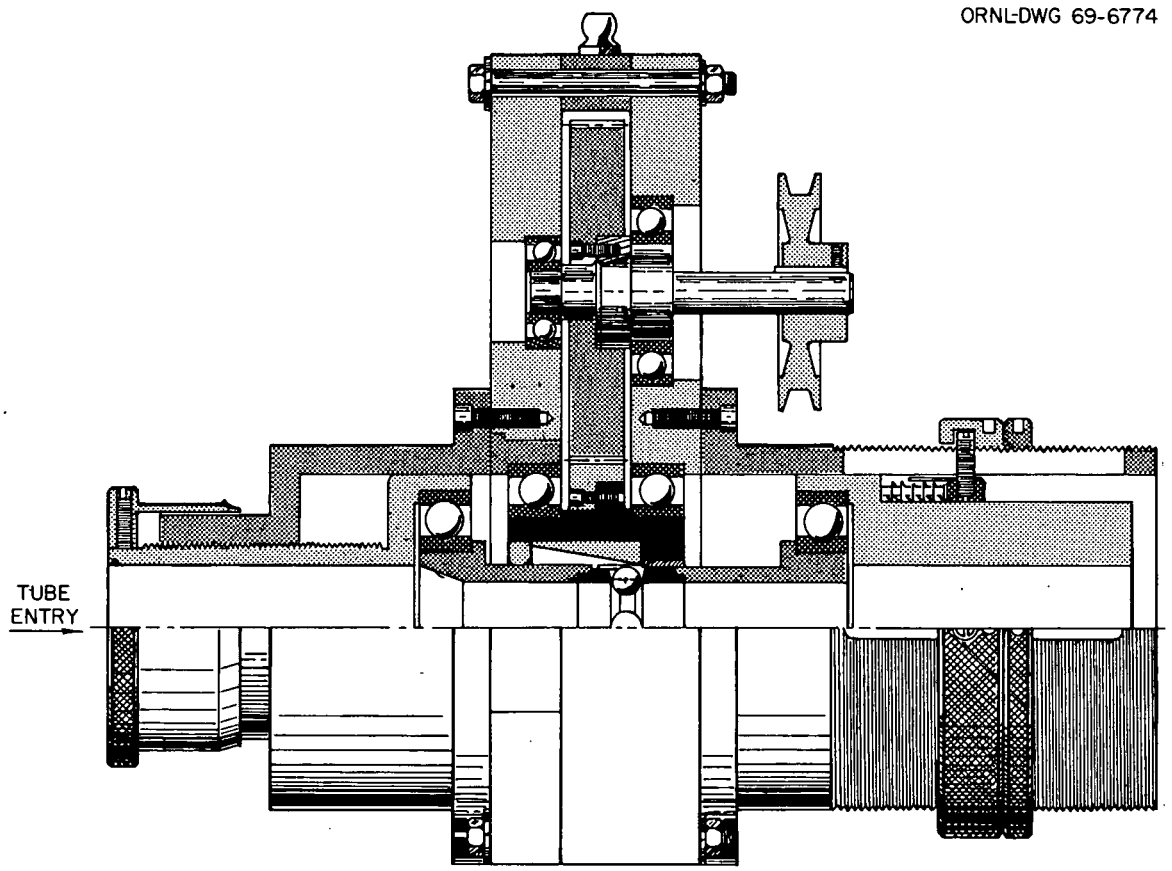

Fig. 6.1. Sectional View of ORNL Planetary Swager.

by reducing 10% per pass and loosening the tube from the mandrel, when necessary, by reeling. In this case, the swager head was rotating 380 to 400 rpm and the bench speed was 7 1/2 in./min. Surface flaking developed during the second pass of this schedule and became more pronounced after each additional pass.

The drive motor for the swager could not maintain head speed when we tried a 15% reduction on the 1.145-in.-diam tube at 7 1/2-in./min bench speed, so we reduced the bench speed to 4 in./min. The first pass of the 15% reduction schedule produced severe surface flaking – even more severe than what occurred previously after six passes of 10% reduction. No additional reductions were made on this tubing; the swager requires disassembly for cleaning after each pass when flaking occurs.

We procured some commercial type 304L stainless steel for additional tests. The 1.0-in.-OD × 0.072-in.-wall thickness tube was planetary

swaged six passes of 10% each, with no intermediate anneals, at a head speed of 400 to 410 rpm and a bench speed of 3 3/4 in./min. An 0.850-in. mandrel was used for all six passes; light reeling between passes loosened the tube from the mandrel. No flaking or other flaws developed in this tube, and a total of 47% reduction in area was obtained by wall thinning.

Figure 6.2 shows transverse photomicrographs of the planetary-swaged type 304L stainless steel tubing after 47% reduction in area in six passes. No surface defects were noted in the tube reduced by ironing only, but there were defects on both outside and inside surfaces when the inside diameter was decreased with each reduction. Also, the outside surface of the tube is very heavily cold worked.

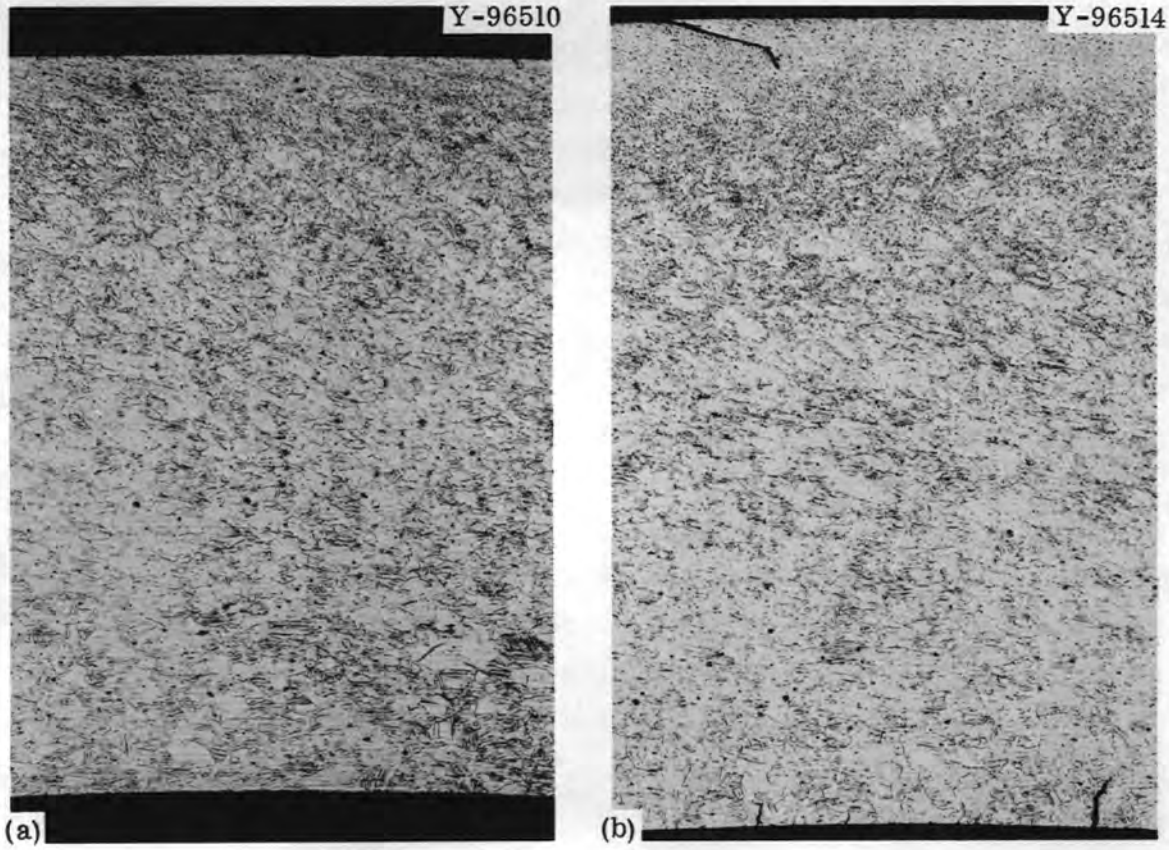

Fig. 6.2. Transverse Sections of Planetary-Swaged Type 304L Stainless Steel Tubing Reduced 10% Per Pass. 100×. (a) Ironing, (b) sinking.

We planetary swaged a section of the type 304L stainless steel tubing at the same 10% reduction per pass and the same speed conditions, but, instead of using the 0.850-in. mandrel for the entire schedule, we decreased mandrel diameter by 0.050 to 0.025 in. for each pass. This reduced the inside diameter of the tube as well as thinned the wall. Surface cracking was visible after the third pass (26% total reduction) and became worse after each subsequent pass until complete failure occurred.

Since reduction of the inside diameter during fabrication by commercial techniques of mandrel drawing does not produce such unfavorable results, we compared sinking by planetary swaging alone for one schedule and a combination of sinking by mandrel drawing and ironing by planetary swaging for the other. Both tubes were drawn at 15% reduction per pass and the same mandrel sizes used for the 10% reduction per pass described above. The tubes were annealed 15 min at 925°C after the third pass (38% total reduction).

The tube that was planetary swaged only developed surface cracks during the second pass (26% total reduction), while the tube that was mandrel drawn and ironed by planetary swaging had no defects after six passes (47% total reduction). A longitudinal section of this successful tube is shown in Fig. 6.3. Also shown in Fig. 6.3 is a longitudinal section of the planetary-swaged tube after the third pass, which shows the beginning of surface flaking.

The firmest conclusions we have drawn thus far is that reductions in inside diameter should be avoided during planetary swaging. We have not definitely ascertained the cause for surface flaking (as opposed to cracking), but we believe it is related to wall thickness and surface conditions. Planetary swaging will be studied further next quarter with tubing from Crucible Steel Company heat 065219 so that the influence of planetary swaging on the properties of the final product may be determined more clearly.

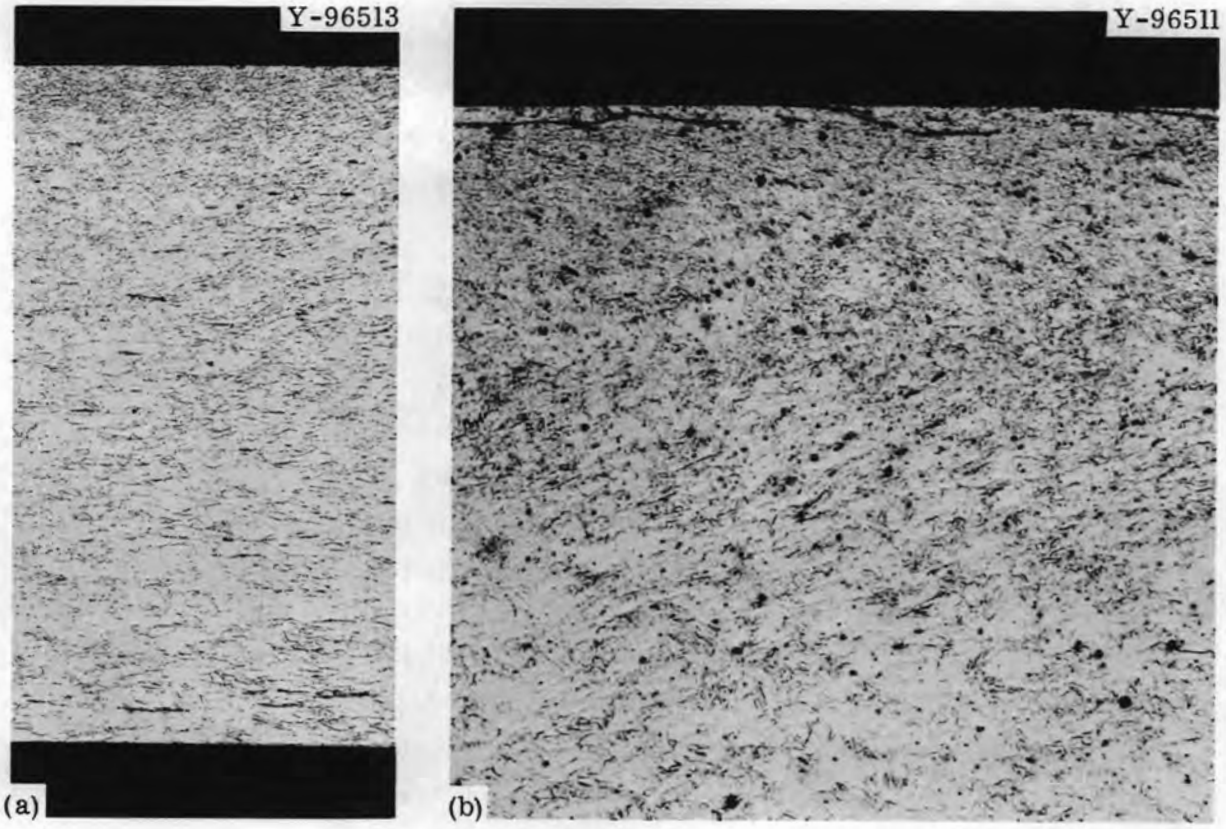

Fig. 6.3. Longitudinal Sections of Planetary-Swaged Type 304L Stainless Steel Tubing. (a) Tubing fabricated by mandrel drawing for the sinking steps and planetary swaging for the ironing steps. 100×. (b) Tubing fabricated by planetary swaging only and showing onset of surface flaking. 250×.

Biaxial Stress-Rupture Testing of Stainless Steel Tubing

H. E. McCoy, Jr.

Comparison of Tubing Produced by Mandrel Drawing and Planetary Swaging (R. T. King)

We fabricated tubes from type 304L stainless steel modified with 0.2% Ti (Allvac heat 3756) to compare the properties produced by mandrel drawing and planetary swaging. Tubes from both fabrication routes were inspected for wall thickness by ultrasonic testing for both longitudinal and transverse discontinuities. Specimens of tubes that had no discontinuity signals were sorted from those that did have discontinuity signals so that we might compare the behavior of sound tubing with that of what we have previously referred to as "defective" tubing.

We tested the biaxial stress-rupture strength at 550 and 650°C, using high-purity Ar as the pressurizing medium. The circumferential ductility of these tubes has not yet been measured; however, the data for rupture life at 550°C are summarized below:

Hoop Stress (psi)	Rupture Life (hr)
35,000	3.0
32,500	6.5
30,000	13.1
25,000	72.1
22,500	Test in progress
20,000	Test in progress

Specimens of nondefective tubing produced by planetary swaging were annealed at 925°C for 1 hr in H_2 and are scheduled for testing next quarter. We are annealing other specimens of this tubing for 1 hr at 1038°C in H_2 to determine the effect of heat treatment on biaxial stress-rupture properties. Specimens of defective tubes are being prepared and will also be tested after similar annealing treatments.

We are processing the data from nondestructive tests of mandrel-drawn tubes of type 316 stainless steel tubing (Allegheny-Ludlum Steel Corporation heat 65808) in preparation for making tube-burst specimens.

References

1. R. E. McDonald, Fuels and Materials Development Program Quart. Progr. Rept. Sept. 30, 1968, ORNL-4350, p. 230.
2. R. E. McDonald, Fuels and Materials Development Program Quart. Progr. Rept. March 31, 1969, ORNL-4420, p. 177.
3. G. A. Reimann, Fuels and Materials Development Program Quart. Progr. Rept. March 31, 1969, ORNL-4420, p. 211.
4. G. A. Reimann, Fuels and Materials Development Program Quart. Progr. Rept. June 30, 1969, ORNL-4440, p. 176.
5. R. E. McDonald, "Melting, Extrusion, and Tube Reducing," pp. 96–98, this report.

7. WELDING DEVELOPMENT FOR LMFBR VESSELS AND COMPONENTS

J. R. Weir, Jr. G. M. Slaughter

We are evaluating the behavior of weldments in austenitic stainless steel at 370 to 650°C as a function of both the welding process and the variables within a process for application to liquid-metal fast breeder reactor (LMFBR) vessels and components. The solidification substructure (the finest structural detail that can be resolved by an optical microscope) markedly influences the mechanical properties of a weldment at elevated temperatures. Since the size and type of substructure in a weldment are significantly influenced by factors that the welder can control, our approach is to determine the effects of different welding processes and of the variables within each process (current, voltage, travel speed, etc.) upon mechanical properties.

Literature Search

Mechanical Properties of Austenitic Stainless Steel Weldments at Elevated Temperatures (G. M. Goodwin)

We collected the available data[1] concerning the mechanical properties of austenitic stainless steel weldments at elevated temperatures. The little information that is available is inconsistent. For example, Fig. 7.1 is a graph of the readily available data on the stress-rupture strength at 650°C of type 347 stainless steel welds produced by the shielded metal-arc process. Each type of symbol on the figure represents a different source of data. Since the scatter increases markedly with increasing rupture life, this information is of limited value for the desired extrapolation to rupture lives in excess of 100,000 hr. The ductility values for these tests are shown in Fig. 7.2. These data, which theoretically should conform to a straight-line relationship, show no pattern. This is disconcerting, for minimum ductility is being considered as a criterion for such important structures as the Fast-Flux Test Reactor (FTR) vessel.

Figures 7.3 and 7.4 show similar scatter in the data for welds made on type 304 stainless steel plate with type 308 stainless steel filler

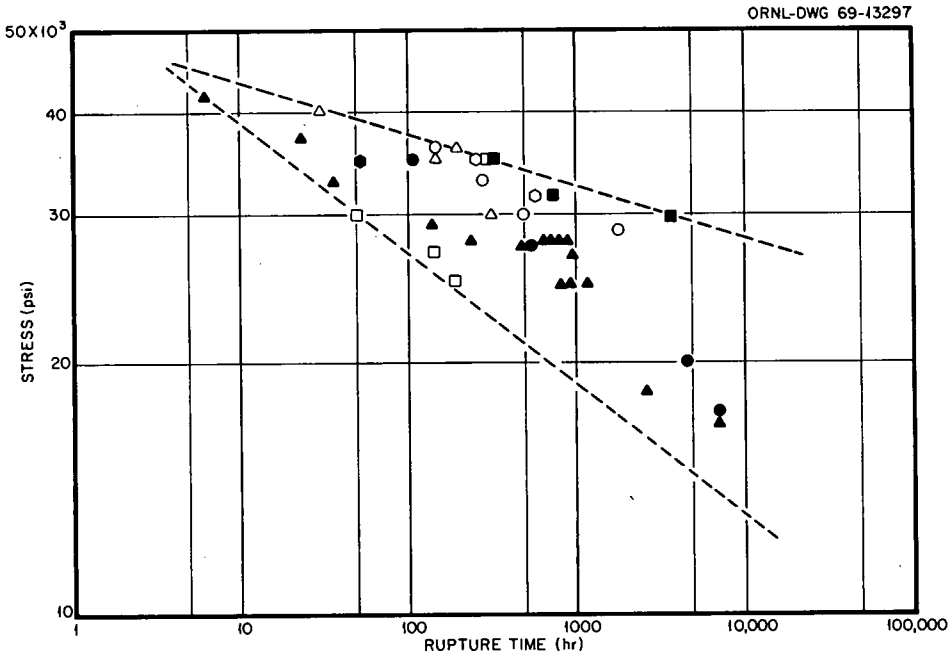

Fig. 7.1. Available Data for Stress-Rupture Strength at 650°C of Type 347 Stainless Steel Weld Metal Deposited on Type 347 Stainless Steel Plate. Each type of symbol represents a different source of data.

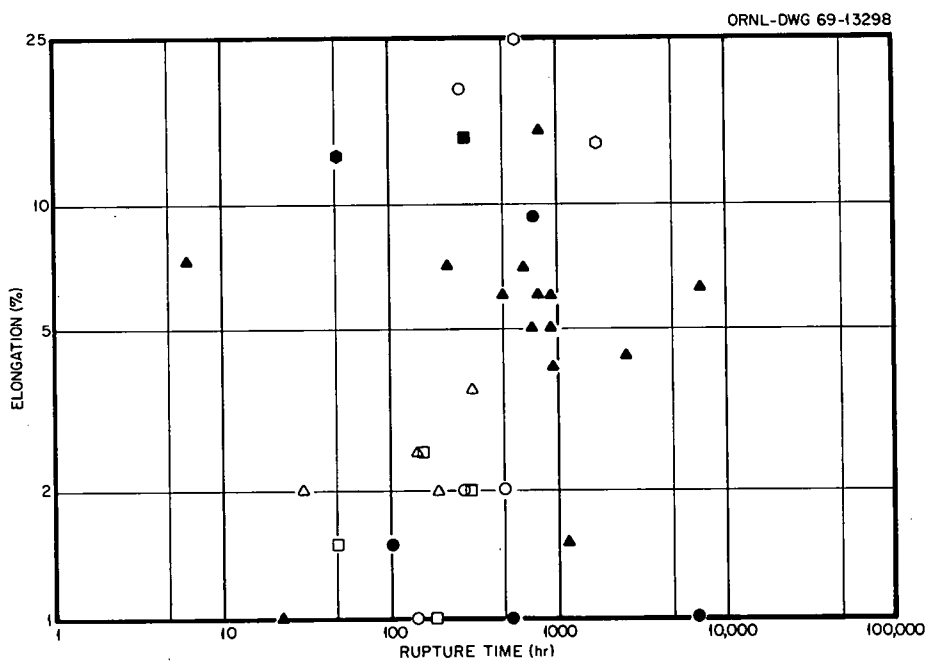

Fig. 7.2. Available Data for Rupture Ductility at 650°C of Type 347 Stainless Steel Weld Metal Deposited on Type 347 Stainless Steel Plate. Each type of symbol represents a different source of data.

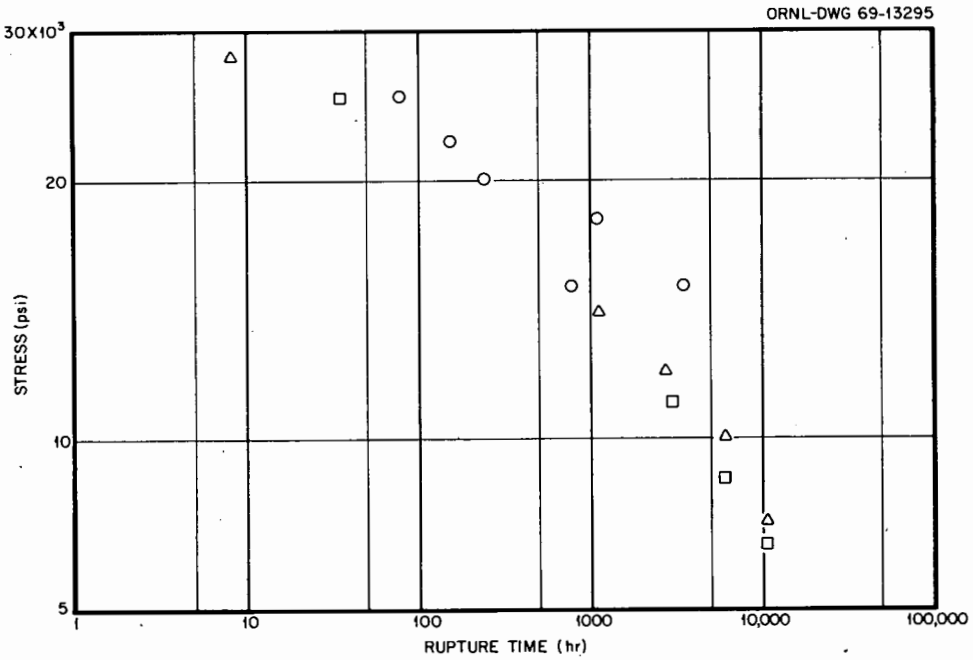

Fig. 7.3. Available Data for Stress-Rupture Strength at 650°C of Type 308 Stainless Steel Weld Metal Deposited on Type 304 Stainless Steel Plate. Each type of symbol represents a different source of data.

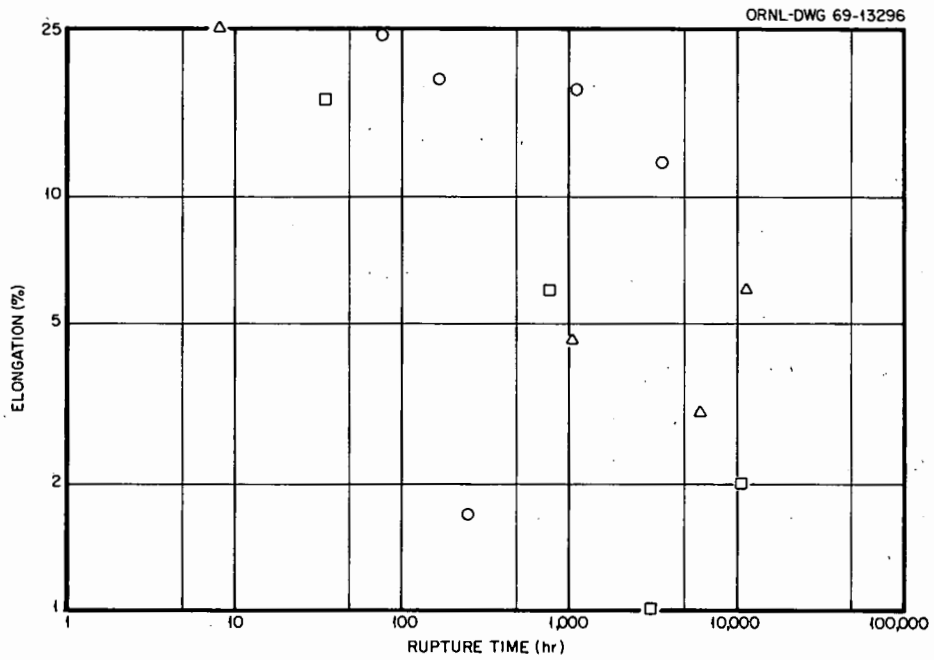

Fig. 7.4. Available Data for Rupture Ductility at 650°C of Type 308 Stainless Steel Weld Metal Deposited on Type 304 Stainless Steel Plate. Each type of symbol represents a different source of data.

metal. The scatter in the values for stress-rupture strength is less (probably because there are fewer data points from fewer sources), but the values for ductility are random.

Both this program and the program Shielded Metal-Arc Welding for LMFBR Components[2] are attempts to determine whether variables such as changes in welding conditions and minor changes in composition are, as we believe, responsible for the scatter in the available data. Our experiments will indicate the effects, if any, of several factors that were not considered in the experiments that produced the data summarized in Figs. 7.1 and 7.2. We hope to provide reference data in a field where virtually no reliable data exist.

Study of Submerged-Arc Process

Materials Procurement and Preliminary Welding Studies (G. M. Goodwin, D. G. Harman, Nancy C. Cole)

We began trying to procure stainless steel base plate and welding wire that conform with applicable RDT standards for this program but have found this a difficult task, primarily, we believe, due to the vendor's lack of familiarity with the newly developing RDT standards and the relatively small quantity of material required for this program. We were able to purchase two 48 × 96 × 1-in. plates of type 304 stainless steel, however, and expect delivery in the near future. We have upgraded wire purchased to ASTM specifications so that it now conforms with specification RDT-M-271, "Corrosion Resisting Chromium and Chromium Nickel Steel Welding Rods and Bare Electrodes."

We utilized existing materials for 32 bead-on-plate submerged-arc welds in 1-in. type 304 stainless steel plate. These welds bracket the range of practical conditions for this process; welding current ranged from 600 to 1200 amp, voltage from 34 to 60 v, and travel speed from 3 to 120 in./min. Weld energy input ranged from 10.2 to 240 kJ/in. The specimens will be sectioned and examined metallographically. They

should cover the range of solidification substructures practically attainable with this process.

Multipass welds were also made with materials on hand, and specimens of weld metal were machined from these for preliminary studies of mechanical properties. Initial tests are under way to determine the need for a protective atmosphere during creep-rupture testing.

Study of Gas Metal-Arc Process

Characterization of Welds (G. M. Goodwin, Nancy C. Cole)

We are continuing a detailed characterization of the welds produced for the FFTF weldment irradiation program.[3] Initial microprobe analyses for specimens produced by the gas metal-arc process are shown in Table 7.1, and a typical microstructure on which these measurements were made is shown in Fig. 7.5. Note that, as might be expected, the delta ferrite is rich in Cr (a ferrite stabilizer) and lean in Ni (an austenitic stabilizer). Analyses are being performed for other elements. Similar studies will be made for the other welding processes — submerged-arc, shielded metal-arc, and gas tungsten-arc.

Table 7.1. Results of Microprobe Analysis of Stainless Steel Gas Metal-Arc Welds

Element	Content, %	
	In Matrix[a]	In Ferrite
Fe	64.2	63.4
Cr	9.0	5.8
Ni	21.4	25.7

[a]Each value is the average of at least three readings, uncorrected for the effects of absorption, secondary fluorescence, or atomic number.

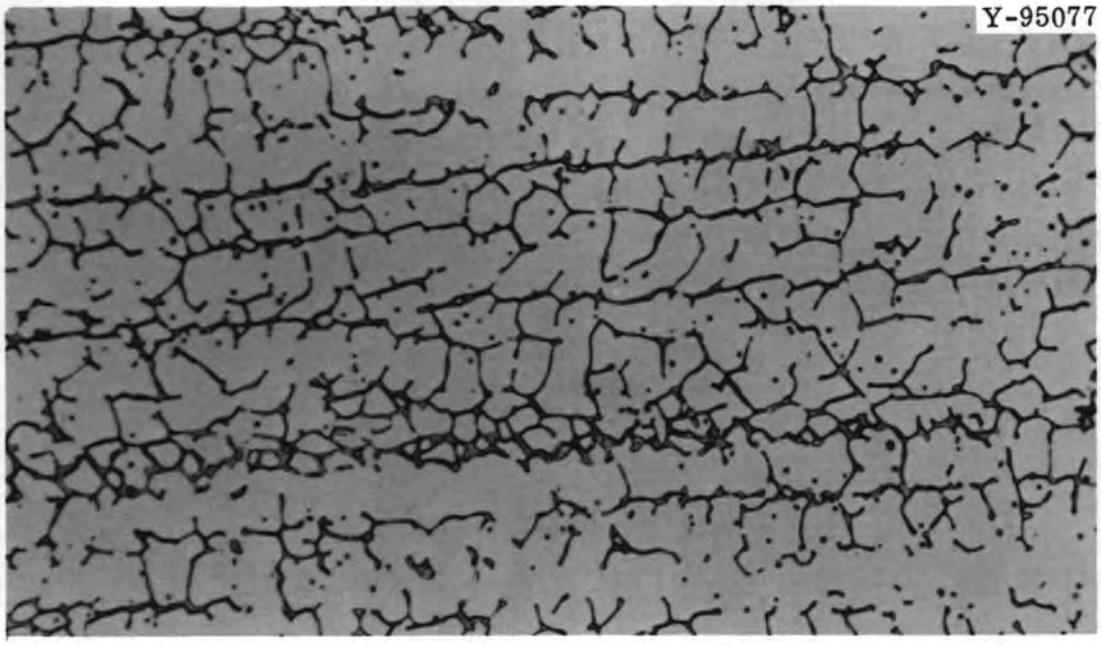

Fig. 7.5. Typical Distribution of Delta Ferrite (Dark Regions) in an Austenitic Matrix in Type 308L Stainless Steel Welds Produced by the Gas Metal-Arc Process (See Table 7.1). Etchant: aqua regia. 500×.

References

1. H. R. Voorhees and J. W. Freeman, The Elevated-Temperature Properties of Weld-Deposited Metal and Weldments, Amer. Soc. Test. Mater. Spec. Tech. Publ. 226, American Society for Testing and Materials, Philadelphia, 1958.
2. W. O. Harms and G. M. Slaughter, "Shielded Metal-Arc Welding for LMFBR Components," pp. 111–113, this report.
3. G. M. Goodwin and Nancy C. Cole, Fuels and Materials Development Program Quart. Progr. Rept. June 30, 1969, ORNL-4440, pp. 167–174.

8. SHIELDED METAL-ARC WELDING FOR LMFBR COMPONENTS

W. O. Harms G. M. Slaughter

The objective of this new program is to evaluate the shielded metal-arc (stick electrode) welding process for fabricating and repairing certain stainless steel components for liquid-metal fast breeder reactors (LMFBR). There is extreme variability in the mechanical properties of welds, particularly in their creep ductility.[1] Through very slight modifications to the flux coatings of electrodes, we should be able to determine the influence of minor elements on the mechanical properties of the weld metal. These coatings have traditionally been evaluated and selected by the relative ease with which weld metal can be deposited; bead contour, arc stability, and deposition efficiency are usually prime considerations. The effect of the coating on the properties at high temperatures has not been seriously considered.

Effect of Variations in Flux Coatings

Welding Studies (N. C. Binkley, G. M. Goodwin, D. G. Harman)

Materials for electrode coatings have usually been formulated empirically. Moreover, the actual compositions are usually held as highly proprietary information by the various manufacturers, which makes unbiased research on electrode coatings even more difficult. We have been fortunate that a major manufacturer of electrodes agreed to supply us with a series of 5/32-in.-diam electrodes with type 308 stainless steel core wire and flux coatings that have carefully controlled minor differences in composition. The deposit chemistry of each batch in this series appears in Table 8.1.

We produced welds from each of the 14 batches of electrodes. We used 1-in.-thick base plate of type 304L stainless steel upgraded to conform to RDT standards to produce the 32-in.-long welds. All welding was done in the downhand position with the plate unrestrained. The "J-groove" was prepared with an 80° included angle, 1/8-in. land, 1/16-in.

Table 8.1. Chemical Analyses of Welds Made with Type 308 Stainless Steel Electrodes

Reference Number	Composition, wt %												Remarks
	Si	S	P	Mn	C	Cr	Ni	Mo	Cu	N	Co	B	
1	0.46	0.015	0.011	1.72	0.044	19.94	9.97	0.03	0.06	0.040	0.01	0.001	Lime
2	0.47	0.016	0.012	1.76	0.044	19.80	9.92	0.03	0.06	0.040	0.01	0.001	Lime-TiO_2
3	0.46	0.017	0.012	1.73	0.044	19.98	9.97	0.03	0.07	0.042	0.02	0.001	TiO_2
4	0.29	0.015	0.011	1.86	0.043	20.31	10.03	0.04	0.07	0.041	0.02	0.001	Low Si
5	0.73	0.013	0.010	1.90	0.044	19.62	10.02	0.04	0.07	0.041	0.03	0.001	High Si
6	0.43	0.014	0.009	1.80	0.044	20.02	9.96	0.05	0.05	0.043	0.03	0.001	Low P
7	0.47	0.012	0.034	1.82	0.043	19.90	10.08	0.04	0.07	0.042	0.02	0.001	High P
8	0.42	0.006	0.011	1.73	0.042	19.89	9.95	0.03	0.06	0.041	0.01	0.001	Low S
9	0.45	0.027	0.011	1.77	0.042	19.88	10.01	0.04	0.07	0.042	0.02	0.002	High S
10	0.46	0.014	0.013	1.78	0.035	19.84	10.11	0.04	0.08	0.040	0.02	0.001	Low C
11	0.52	0.015	0.013	1.84	0.074	20.7	9.91	0.04	0.06	0.039	0.02	0.001	High C
12	0.46	0.015	0.016	1.77	0.042	20.08	10.01	0.03	0.05	0.041	0.02	0.004	Low B
13	0.47	0.015	0.017	1.80	0.042	20.03	10.01	0.03	0.05	0.040	0.02	0.006	High B
14	0.44	0.016	0.023	1.73	0.045	19.97	10.02	0.03	0.06	0.042	0.02	0.001	Medium P

nose, and 1/8-in. root gap. A 3/16-in.-thick backup strip was tack welded to the assembly before welding. The plates were welded at about 140 amp, 20 v, and 9-in./min travel speed. Special care was taken to remove all slag and grind craters. Each pass was begun at the same end of the plate as was the previous pass, and interpass temperatures were maintained below 120°C.

All 14 weldments were completed and radiographed. We began machining specimens from several weldments, and removed samples for chemical analysis and metallography.

We modified and calibrated several lever-arm creep-testing facilities. Several weld specimens were machined, and testing will begin soon.

References

1. J. R. Weir, Jr. and G. M. Slaughter, "Welding Development for LMFBR Vessels and Components," pp. 105–110, this report.

9. NONDESTRUCTIVE TESTING TECHNIQUES FOR LMFBR

W. O. Harms R. W. McClung

We are developing new methods, techniques, and equipment for nondestructively evaluating materials or components related to the liquid-metal fast breeder reactor (LMFBR). Among the methods studied are electromagnetic induction, ultrasonics, and penetrating radiation. Special emphasis is being given to developing techniques for measuring the degree of cold work in stainless steel tubing with a small diameter.

Development of Advanced Nondestructive Testing

Development of Eddy-Current Instrument (C. V. Dodd)

One of the major problems with detection of defects by means of eddy currents is properly identifying those signals that are from defects. Defects near the surface and other surface irregularities produce signals that obscure internal defects that may be in a more critical region in terms of failure of a component. Our analytical studies indicate that by measuring the phase shift of the signal we can determine the depth of the defect below the surface. We should then be able to use this information to correct the amplitude of the signal so that all defects of the same size have the same amplitude. In addition, defect signals from a noncritical region could be ignored.

We have begun design of a prototype instrument to investigate these potential benefits. Since the proposed instrument will measure phase shift, we can use many of the modules in the phase-sensitive eddy-current instrument. We are having a modular phase-sensitive eddy-current instrument constructed for this purpose.

Ultrasonic Schlieren Techniques for Evaluation of Welds (H. L. Whaley, K. V. Cook)

We are using an optical-bench schlieren technique to investigate techniques of ultrasonic inspection of welds. Several butt-welded samples were designed and fabricated for the study. The samples are

consumable-electrode welds in 1-in.-thick (2.54 cm) Al plate with a 90° included angle. Three of these contained a gross defect of the following types: cold lap, incomplete penetration, or porosity. The fourth weld sample was made as free of defects as possible. The weld crowns were ground flat before inspection.

The welds were examined at three different angular orientations of the transducer axis: (1) normal to the surface of the welded plate, (2) at a small incident angle at which both longitudinal and shear waves were propagated into the plate, and (3) at a larger incident angle greater than the critical angle for the longitudinal mode and such that the shear would be normally incident on the weld interface. A unique advantage of the optical technique is that all the primary transmitted and reflected beams can be observed simultaneously, so that the probability of observing some indication of a randomly oriented flaw is increased over that for a conventional technique.

All intentional defects in the samples were located easily with a 1.9-cm-diam (0.75 in.) 2.25-MHz transducer, although no reflections from defects could be seen propagating back to the transducer. Normal incidence was best for locating root defects, while angled incidence was best for detecting flaws in the interface. The areas of high porosity in one sample caused pulses traveling through them to become much fainter than if they had traveled through good weld material. Significant variations were also seen in the quality of the "good" weld. Further tests are planned for these samples, including correlation with conventional techniques of ultrasonic testing for welds.

Measurement of Cold Work in Stainless Steel Tubing

Measurement of Changes in Magnetic Permeability (C. V. Dodd, W. A. Simpson)

We are investigating methods for nondestructively measuring the degree of cold work in stainless steel tubing that has a small diameter. We emphasize the use of electromagnetic induction for detecting the changes in magnetic permeability produced by cold work.

We prepared two sets of samples of type 316 stainless steel that contained different known amounts of cold work, ranging from none to 50%. One set is a series of tubes 0.250 in. in diameter by 0.015 in. in wall thickness; the other is a series of sheets 0.015 in. thick. Our first efforts, with the flat sheet, are to establish quantitative instrument response relative to cold work without the problems that might possibly be caused because of the small radius of curvature on the tubes.

Correlation has been observed between cold work in some austenitic stainless steels and the magnetic permeability.[1] An increase in relative permeability from 1.003 to 1.01 in the normal ranges of cold work and values as high as 10 for severe cold work are reported. Using the relationship we previously developed,[2] we calculated the response that we can get from a low-frequency inductance bridge circuit and determined that we could measure permeability changes between 1.003 and 1.01 by this technique. We have constructed on a breadboard a system for making these measurements and are operating it in a "bridge unbalanced" mode, similar to many eddy-current tests, to separate the conductivity variations from the permeability variations. Figure 9.1 relates the instrument

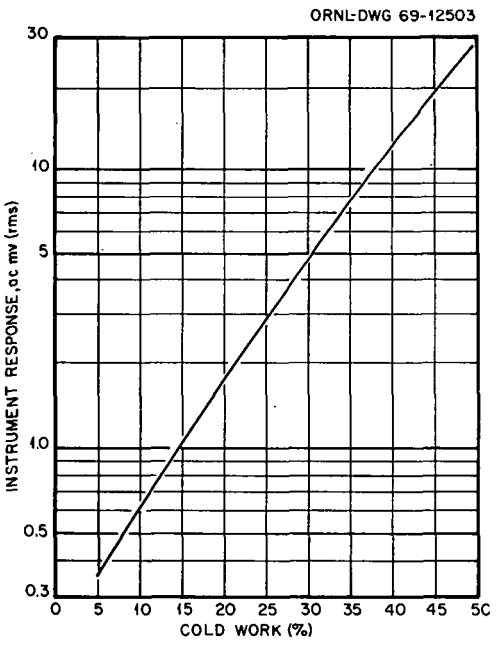

Fig. 9.1. Variation in Instrument Response as a Function of the Degree of Cold Work in Type 316 Stainless Steel.

reading to cold work on the sheet specimens. Each point represents the average of six readings. While these preliminary measurements are very encouraging, a considerable amount of refinement is needed in both the circuitry and the technique to optimize this method.

References

1. Taylor Lyman (ed.), Metals Handbook, pp. 423, 793, vol I, 8th ed., American Society for Metals, Metals Park, Novelty, Ohio, 1961.
2. J. W. Luquire, W. E. Deeds, C. V. Dodd, and W. G. Spoeri, Computer Programs for Some Eddy Current Problems, ORNL-TM-2501 (August 1969).

10. SODIUM CORROSION STUDIES

W. O. Harms J. H. DeVan A. P. Litman

The purpose of this program is to investigate the chemical and metallurgical effects produced in structural materials during exposure to molten Na. The program is designed to guide the selection of container materials for Na-cooled fast breeder reactor (LMFBR) systems and provide guidelines for specifying insulating materials for use with stainless steel components in the Fast-Flux Test Reactor (FTR).

Comparative Corrosion Tests on Refractory Alloys

J. H. DeVan

Although V alloys are highly resistant to dissolution by Na, they are quite reactive with nonmetallic impurities in Na, particularly with C, N, and O. Accordingly, we are investigating the mechanisms by which V alloys are attacked in Na at impurity levels typical of service conditions in a reactor. Our program is concerned with four basic aspects of the oxidation process for V alloys in Na: (1) the partitioning of O between V alloys and Na; (2) the effects of alloying additions of Cr and Zr on the diffusion coefficient of O in V; (3) the effects of Cr and Zr in V on the oxide formed and on the dissolution of the alloys in Na; and (4) the solubility of V in Na as affected by the presence of O in either metal. We are also examining the kinetics of the transfer of C, N, and O between V alloys and types 304 and 321 stainless steel in a Na circuit.

Effect of Oxygen on the Compatibility of Vanadium and Vanadium Alloys With Sodium (R. L. Klueh)

We are continuing our investigation of the effect of O in Na on the compatibility of V and V alloys with Na. Vanadium and its binary alloys containing 5, 10, and 15 wt % Cr were melted, cast, and rolled to 0.04-in.-thick sheet. The following alloys (also in 0.04-in.-thick sheet stock) were obtained from Westinghouse Astronuclear Laboratory: V–20% Ti, V–15% Cr–5% Ti, and the Westinghouse alloys Vanstar 7 (V–9% Cr–3% Fe–1.3% Zr–0.05% C), Vanstar 8 (V–8% Cr–10% Ta–1.3% Zr–0.05% C),

and Vanstar 9 (V–6% Fe–5% Nb–1.3% Zr–0.05% C). Specimens 1 × 1/2 in. were cut from the sheet material, chemically polished, and vacuum annealed for 1 hr at 900°C. Table 10.1 gives the interstitial contents of the test materials after this preparation.

Table 10.1. Concentration of Interstitial Elements in Vanadium and Vanadium Alloys

Material	Concentration of Interstitials, ppm		
	O[a]	N[b]	C
V	80	8	70
V–5% Cr	120	60	80
V–10% Cr	90	55	140
V–15% Cr	150	10	60
V–15% Cr–5% Ti	1550	87	160
V–20% Ti	1250		
Vanstar 7	1400	77	620
Vanstar 8	1250	75	620
Vanstar 9	1600	84	600

[a]Determined by fast-neutron activation.

[b]Determined by vacuum-fusion analysis.

Static capsules are being tested to compare the effect of O on a given alloy with the effect on pure V. Two specimens — the alloy being tested along with a specimen of pure V — were put into a capsule of type 304 stainless steel and exposed to Na with 2000 ppm O (added as Na_2O) for 100, 200, 300, and 600 hr. The specimens are being examined for changes in weight, chemistry, and metallographic appearance.

Mass Transport of Interstitial Impurities Between Vanadium Alloys and Type 300 Series Stainless Steels (D. H. Jansen)

We are continuing studies of interstitial mass transport between stainless steel and V in bimetallic thermal convection loops. Of principal interest are the effects of C, N, and O on the mechanical properties

of V and V alloys. The first loop in this series, fabricated of type 304L stainless steel with a V hot leg, was terminated after operating 3000 hr and is now awaiting disassembly and evaluation. A similar test of type 321 stainless steel and V was started. Operating conditions are given below:

Temperature at heater outlet, °C	712
Temperature at heater inlet, °C	562
Rate of Na flow,	
fpm	11.6
gpm	557
Chamber pressure, torr	1×10^{-8}
Surface area of V tubing, in.^{2}	27
Surface area of stainless steel tubing, in.^{2}	140
Surface area of specimens, in.^{2}	
V	9
Stainless steel	9
Scheduled operation, hr	3000

In these tests, the ratio of the surface area of V to that of stainless steel was 1:4. Another loop is being fabricated in which the ratio between the surface areas of V and type 304L stainless steel will be 1:1. Also included in this program is a series of static tests[1] in which tensile specimens of 0.040-in.-thick V sheet are being exposed to Na in stainless steel containers.

Table 10.2 lists the operating conditions for four experiments completed in this series of tests. Three of the experiments were conducted with type 304L stainless steel and the fourth with type 321 stainless steel. Two grades of V were tested, one with a relatively high and one with a relatively low initial concentration of interstitials. As shown in Table 10.3, the higher purity V increased in O as well as C and N, whereas the lower purity material gained only C and N. Thus, the latter material, on the average, gained less weight (Table 10.3). The transport of C and N from type 304L stainless steel to the V was considerably greater at 800°C than at 700°C. Interstitial transport from the type 321 stainless steel, stabilized with Ti, was negligible at 700°C compared to that from type 304L stainless steel.

Table 10.2. Operating Conditions[a] for Static Tests of Vanadium and Stainless Steel

Type of Stainless Steel	Ratio of Wetted Surface Area of V:Stainless Steel	Surface Area of V, in.^{2}		Test Temperature (°C)
		Purified[b]	Commercial[c]	
304L	0.25	5.3	8.0	800
304L	0.25	8.0	5.3	800
304L	0.25	5.3	8.0	700
321	0.25	13.4	0	700

[a]All tests operated for 500 hr.

[b]Purified: 80 ppm O, 2 ppm N, 30 ppm C.

[c]Commercial: 1400 ppm O, 550 ppm N, 320 ppm C.

Table 10.3. Chemical Compositions[a] and Weight Changes of Tensile Specimens of Vanadium Sheet After Exposure[b] to Sodium in Stainless Steel Containers

Test Variables			Weight Change (mg)	Interstitial Content, ppm			
Type of V	Type Stainless Steel Container Material	Temperature (°C)		O	N	H	C
Commercial	(as received)			1400	550	1	320
Commercial	304L	700	1	1500	800	3	470
Commercial	304L	800	2	1600	1100	1	940
Purified[c]	(as received)			79	2	6	30
Purified[c]	321	700	2	190	14	10	120
Purified[c]	304L	700	7				
Purified[c]	304L	800	11	500	420	9	430

[a]Total 0.040-in. cross sections were analyzed.

[b]All exposures were for 500 hr.

[c]Vacuum-induction melted from electrolytic flake V supplied by Bureau of Mines.

The effects of interstitial mass transport on the mechanical properties of the V specimens are shown in Table 10.4. Values are compared against properties of control specimens exposed to Ar for 500 hr at 700°C. Tensile ductilities, measured at room temperature, were reduced for both grades of V after testing in Na with type 304L stainless steel. In contrast, testing with type 321 stainless steel produced no measurable change in either strength or ductility compared to the control test in Ar.

Table 10.4. Room-Temperature Tensile Properties of Vanadium Specimens Tested in Sodium

Test Variables[a]			Weight Gain (mg)	Elongation (%)	Strength, psi	
Type of V[b]	Type Stainless Steel Container Material	Temperature (°C)			Yield[c]	Tensile
					$\times 10^3$	$\times 10^3$
Purified	321	700	2	37.5	13.5	23.0
Purified	304L	700	7	21.0	22.3	31.3
Purified	304L	800	11	19.6	30.7	36.2
Purified	(control in Ar)	700	0	34.0	17.5	22.3
Commercial	304L	700	1	15.2	48.6	58.0
Commercial	304L	800	2	6.5	51.5	54.4
Commercial	(control in Ar)	700	0	20.0	48.3	57.6

[a]All tests operated for 500 hr.

[b]Purified: 110 ppm total impurities; commercial: 2300 ppm total impurities.

[c]At 0.2% offset.

Interstitial Contamination of Vanadium and Its Alloys (R. L. Wagner)

We are studying the interaction of V with gaseous interstitial impurities to characterize the effects of alloying additions on the rate and nature of interstitial contamination and to determine the influence of interstitial contamination on the creep strength of V and its alloys.

We evaluated the contamination of unalloyed V in vacuum and in O_2 from 400 to 900°C. The nominal content of interstitials in the V before the test was 400 ppm C, 500 ppm N, and 300 ppm O. Data are shown in Fig. 10.1 for 0.020-in.-thick specimens vacuum annealed at $< 1 \times 10^{-6}$ torr and 900°C for 1 hr and exposed at 2×10^{-6} to 4×10^{-8} torr O_2 pressures.

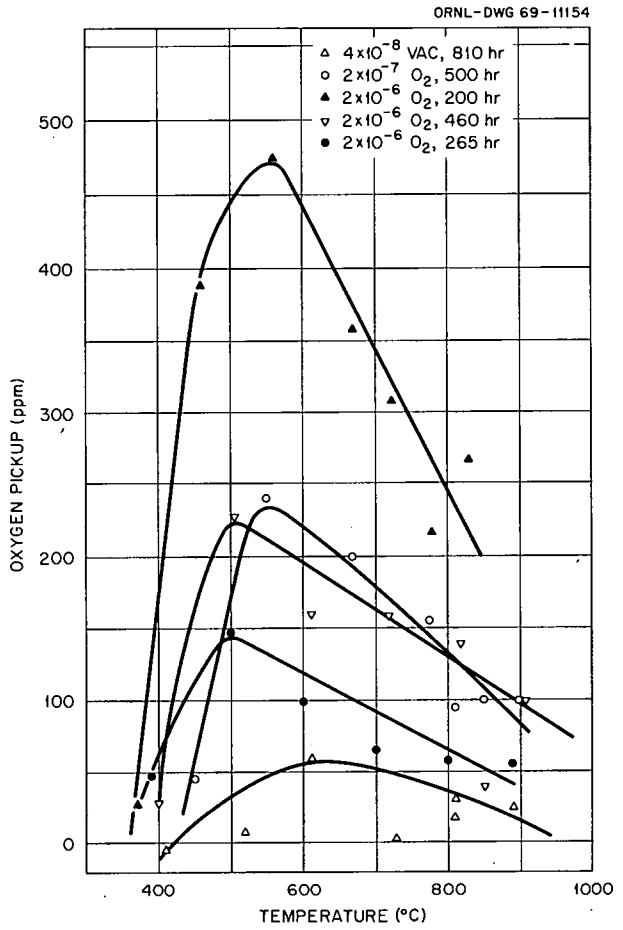

Fig. 10.1. Oxygen Contamination of Unalloyed Vanadium as Functions of Temperature and Oxygen Pressure.

The results for 200 hr at 2×10^{-6} torr O_2 appear to be inconsistent with the rest of the data. Because of a thermocouple failure, these particular samples were unintentionally cooled in O_2 rather than under vacuum. This set of data suggests that an oxide film may be formed below about 400°C. With the exception of this set of data, contamination rates as functions of temperature and pressure are given in Fig. 10.2.

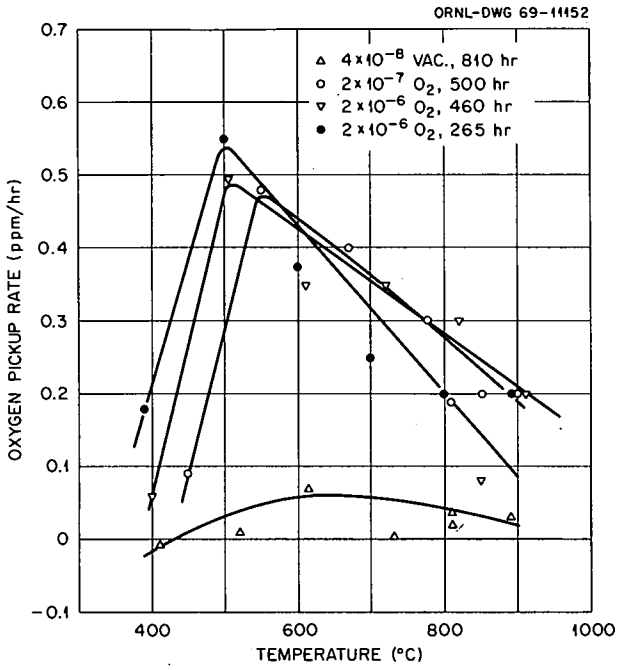

Fig. 10.2. Rate of Contamination of Unalloyed Vanadium as Functions of Temperature and Oxygen Pressure.

(These data assume that the contamination rate is constant with time.) On the low-temperature side of the maxima, the rate may be slightly dependent on pressure; on the high-temperature side of the maxima, however, at a pressure of $> 10^{-7}$ torr O_2, the rate appears to be independent of pressure. The decrease in contamination rate below 600°C suggests that diffusion kinetics control the process. The decrease above 600°C indicates a decrease in the number of O atoms adsorbed.

Additional experiments will be conducted on V alloys with temperature and O_2 pressure held constant. The V alloys of interest are binary systems that contain various concentrations of Cr, Zr, Mo, and Ti.

Interactions of Sodium with Nonmetallic Materials

A. P. Litman

Compatibility of Stainless Steel and Insulation for LMFBR Systems (C. D. Bopp[2])

The temperature proposed for Na-cooled fast breeder reactors is considerably above that for present power reactors. Among the problems that may arise from this higher operating temperature are a possible

interaction of thermal insulation with reactor construction materials and oxidation of the construction materials in the event of a Na leak. Accordingly, we are studying the reaction of commercial insulating materials with austenitic stainless steels between 370 and 760°C. A related study deals with the effect of Na on the oxidation of stainless steels, both insulated and uninsulated.

Oxidation of Insulated Stainless Steel. — The oxidation of couples of stainless steel and insulation[3,4] has now been studied to 5000 hr. The test conditions are listed in Table 10.5. Visual examination after 5000 hr showed that the scale on insulated sections of stainless steel was darker than that on the uninsulated sections. The couples are being examined metallographically to determine whether the thickness of the scale was affected by the presence of insulation.

Table 10.5 compares the weight changes for the 5000-hr tests with data for shorter tests. Comparison of runs 8 and 9 with run 13 shows that after 5000 hr, nearly the same scaling resulted on type 316 stainless steel at 760°C when the surface was prepared by machining as at 730°C when the surface was prepared by pickling. As discussed previously,[3,4] this effect apparently results from the enhanced diffusion of Cr that is produced by work hardening.

For type 316 stainless steel with a machined surface, the scaling at 760°C between 1000 and 5000 hr increased more in moist air (run 9) than in dry air (run 8). There was also more exfoliation in moist air. We suggest that lowering of the fatigue resistance of high-strength steel by moisture[5] may be a related effect. We note that recent work by Edwards and Nicholson[6] confirms our previous conclusion[3,4] that the oxidation resistance in moist air at 760°C is poorer for type 316 stainless steel than for the 18% Cr–8% Ni stainless steels, which do not contain Mo.

We are studying the oxidation of insulated types 304 and 316 stainless steel at 760°C in an atmosphere of 98% N_2, 2% O_2, and 100 ppm H_2O, since this is the atmosphere proposed for use in the cells enclosing the closed loops in the Fast-Flux Test Facility.

Effect of Sodium on the Oxidation of Stainless Steel. — We began a series of experiments to determine the effect of Na on the oxidation

Table 10.5. Oxidation of Couples of Stainless Steel and Insulation[a]

Run Number	Type Stainless Steel	Surface Treatment of Stainless Steel Before Test	Test Temperature (°C)	Atmosphere	Frequency of Thermal Cycling (hr)	Metal Oxidized (mg/cm^2)			
						100 hr	500 hr	1000 hr	5000 hr
9	316	Machined	760	Moist air[b]	6	0.62	0.75	0.75	2.0
8	316	Machined	760	Dry air	6	1.3	1.4	1.5	2.0
13	316	Pickled	730	Moist air[b]	40	1.4	1.5	1.6	2.5
14	304L	None	760	Moist air[b]	40	2.1	2.3	2.4	2.7
10	304L	None	760	Moist air[b]	40	3.2	3.8	4.0	4.7
11	304L	Pickled	760	Moist air[b]	40	1.2	1.3	1.3	

[a]Stainless steel was 3/4-in.-OD solution-annealed tubing; thermal insulation was fibrous Al_2O_3-SiO_2 Kaowool, a product of the Babcock and Wilcox Company.

[b]Saturated at 20°C.

behavior of austenitic stainless steels. The experiments will provide data for oxidation in two environments: (1) an atmosphere of 98% N_2, 2% O_2, and 100 ppm H_2O; and (2) moist air.

The apparatus designed for these studies is pictured in Fig. 10.3. A tube containing pure Na (tube A) is connected to a tube with a defect (tube B) in an Ar chamber. A plastic sleeve is slipped over the tube with a defect, and both tubes are transferred to a glove box with a controlled atmosphere (Fig. 10.1). After the tubes are connected to an Ar manifold, the plastic sleeve is removed, the tubes are heated by direct resistance, and Na is forced into the tube with the defect. The Ar pressure on the tube is then varied to produce the desired amount of Na leakage. Oxygen consumption is measured chromatographically or, when fast results are required, by a paramagnetic O_2 analyzer. Oxidation will be studied both with and without the presence of insulation. The extent of corrosion will be evaluated metallographically.

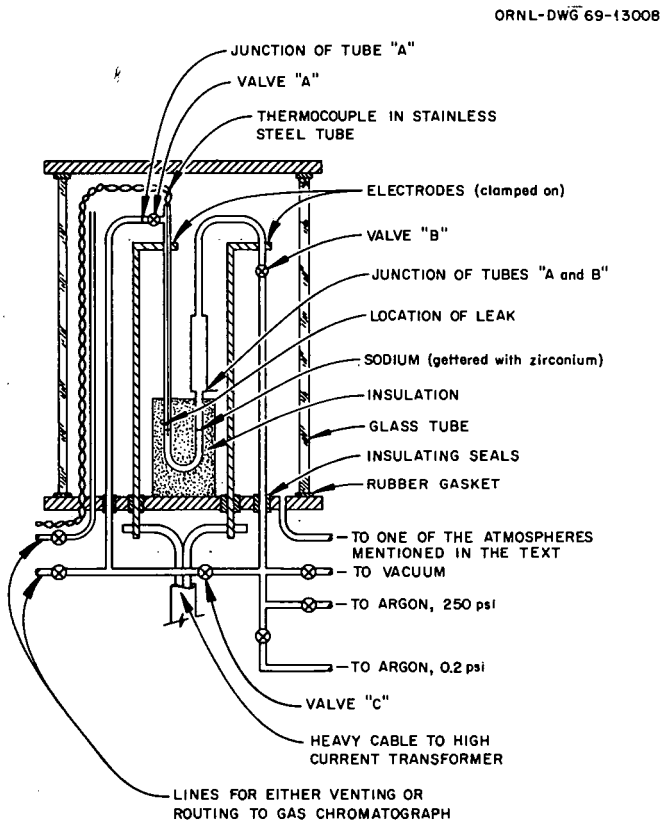

Fig. 10.3. Apparatus for Study of Corrosion of Stainless Steel by Leaking Sodium.

It was recently shown[7] that very small leaks (those with He leak rates of 10^{-4} atm cm^{-3} sec^{-1} or less) may be plugged by sodium oxide so that leakage of Na to an air atmosphere may be delayed for several weeks at 650°C and for several months at 400°C. The hydrostatic pressure of the Na in these studies was 10 psig. In the course of our experiments, we plan to measure unplugging times for somewhat larger leaks (0.001 to 0.05 cm in diameter). Unplugging will be determined from the rate at which O_2 is consumed from the external atmosphere.

Since there are indications[8,9] that the cover gas over the Na may become contaminated with N_2 when Na leaks develop, we may be able to detect such small leaks simply by monitoring the cover gas for N_2. Accordingly, we will analyze the Ar cover gas chromatographically for N_2 at intervals during some of our experiments.

References

1. J. H. DeVan and D. H. Jansen, Fuels and Materials Development Program Quart. Progr. Rept. June 30, 1969, ORNL-4440, p. 78, 80.
2. On loan from Reactor Chemistry Division.
3. C. D. Bopp and A. P. Litman, Fuels and Materials Development Program Quart. Progr. Rept. March 31, 1969, ORNL-4420, pp. 92–100.
4. C. D. Bopp and A. P. Litman, Fuels and Materials Development Program Quart. Progr. Rept. June 30, 1969, ORNL-4440, pp. 84–89.
5. T. R. Shives and J. A. Bennett, J. Mater. 3, 695 (1968).
6. A. M. Edwards and A. Nicholson, J. Iron Steel Inst. (London) 207, 1067 (1969).
7. J. P. Brainard and D. C. Kirkpatrick, Sodium Leak Studies, LA-4129 (March 1969) and personal communication.
8. R. L. Young and E. L. Zebroski, Sodium Components Development Program. Mass Transfer Investigations in Liquid Metal Systems. Quarterly Progress Report No. 5, March–May 1968, GEAP-5648, p. 63 note.
9. R. L. Young and E. L. Zebroski, Sodium Components Development Program. Mass Transfer Investigations in Liquid Metal Systems. Quarterly Progress Report No. 4, December 1967–February 1968, GEAP-5602.

11. DEVELOPMENT OF FAST-REACTOR NEUTRON-ABSORBER MATERIALS

G. M. Adamson, Jr. W. R. Martin G. W. Keilholtz[1]

The prime candidate material for the safety and shim rods in the Fast-Flux Test Reactor (FTR) and liquid-metal cooled fast breeder reactor (LMFBR) is B_4C pellets in a stainless steel cladding. In spite of the widespread uses of B_4C as a neutron absorber in thermal reactors, basic data for the carbide have never been obtained. The material has never been fully characterized for structure, homogeneity ranges, effect of fabrication variables, and the effects of varying composition. The objective of our work is to characterize the material sufficiently for our irradiation studies. The irradiation studies will emphasize basic damage experiments. The characterization is necessary to provide measurable control parameters to properly evaluate fabrication techniques, compatibility experiments, and the effects of irradiation. The investigation might also reveal characteristics that could be used to advantage for improvements in fabrication, irradiation, or compatibility.

Characterization of Boron Carbide

Powder Characterization (R. S. Mateer,[2] G. L. Copeland)

X-Ray Diffraction Studies. — The most recent phase diagram for the B-C system[3] gives a single compound, designated B_4C but covering B:C ratios of 4 through 7 (78 to 87 wt % B). The lattice can be represented as rhombohedral. At the ideal stoichiometric ratio, 12 B atoms cluster as icosahedra at the corners of the unit cell, and three C atoms lie along the c-axis.[4] Studies[5] of single-crystal material show that radiation damage is associated with displacement of the central C atom into interstitial sites. The c-axis contracts accordingly. Annealing at 700°C restores the c-axis to its original dimension. The lattice locations of Li and He generated in the (n,α) reaction of ^{10}B are not known.

The dimensions of the unit cell change with the B:C ratio of the compound. It appears that B atoms substitute for some of the C atoms. Elliott[6] correlated the position of a high-angle x-ray diffraction peak with B:C ratio but did not assign Miller indices to the line. We have observed such line shifts, which we associate with differences in B:C ratios and have developed specialized techniques with a focusing camera to measure them precisely. This is probably adequate for quality control, but we are unable to index these high-angle lines[7] and consequently do not know the exact geometry of the distortion. The rhombohedral structure proposed by Clark and Hoard[4] explains only the low-angle lines of the Cu radiation powder pattern. Krantz[8] believes that the structure is of lower symmetry — not higher than monoclinic and probably triclinic. Glaser, Moskowitz, and Post[9] suggest that the compound is actually a terminal solid solution of C in the rhombohedral lattice of B. Monochromatic Debye-Scherrer patterns of Norbide 325-F powder and Weissenberg patterns from selected coarse crystals have not yet clarified the uncertainty about the crystal structure.

Our x-ray studies of commercial powders show that the coarse grades have split peaks, which we interpret as mixtures of crystals that have different lattice parameters. The finer grades give more clearly defined peaks and a weak, broad graphite peak. Heat treatment shifts the peaks in the finer grades, and the broad graphite peak simultaneously disappears.

Microstructure of Powders. — Particles of all grades were angular fragments. The fracture surfaces were generally planar but gave no indication of being crystallographic. Occasional growth faces were seen. In metallographic section, some of the larger particles showed radial markings, which we attribute to a divorced eutectic of graphite separating the dendrites of primary B_4C. This is shown in Fig. 11.1. A few of the larger particles had internal pores. Under polarized light, the particles were shown to be made up of twinned crystals. This is shown for an unusually large particle in Fig. 11.2. Etching with Murakami's reagent revealed grain boundaries in some of the coarse particles; others were unattacked. This supports the theory that the split x-ray peak indicates that particles of different composition are present in the coarser grades.

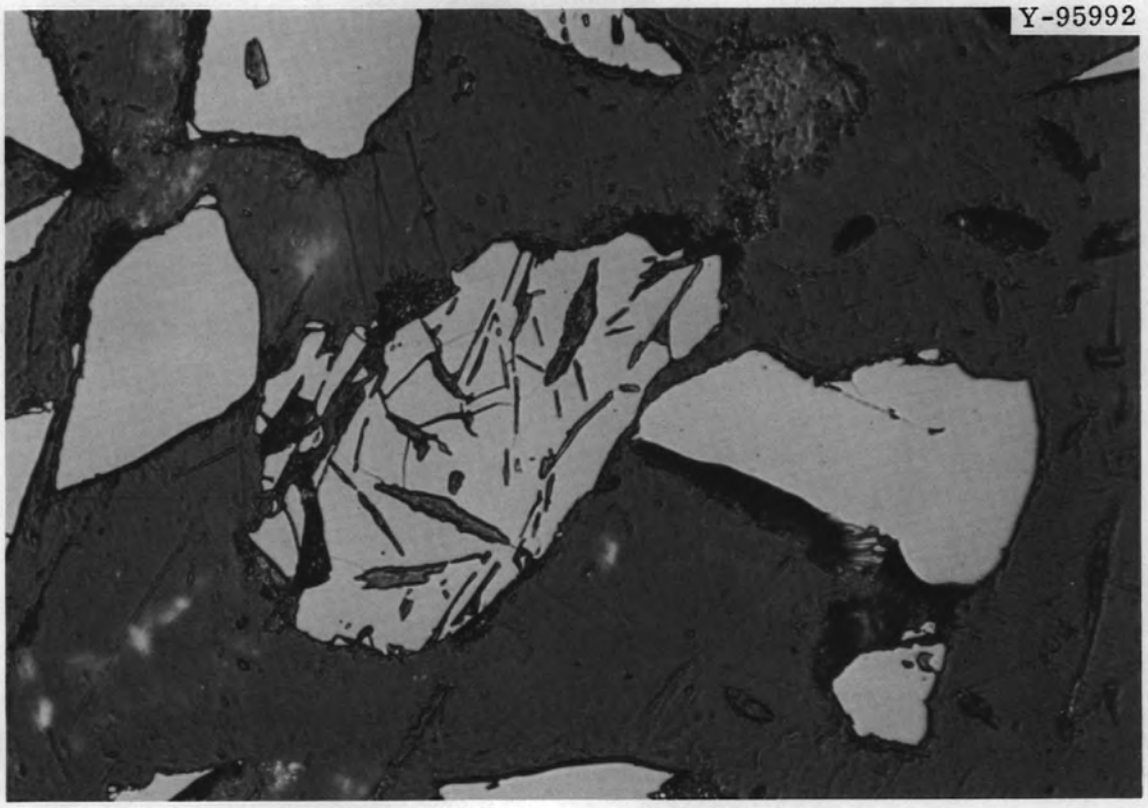

Fig. 11.1. Particles of Boron Carbide Powder in Metallographic Section. One particle shows radial markings believed to be eutectic graphite. Fracture during crushing occurs along these seams and leaves graphite at the surface of the particles. 500×.

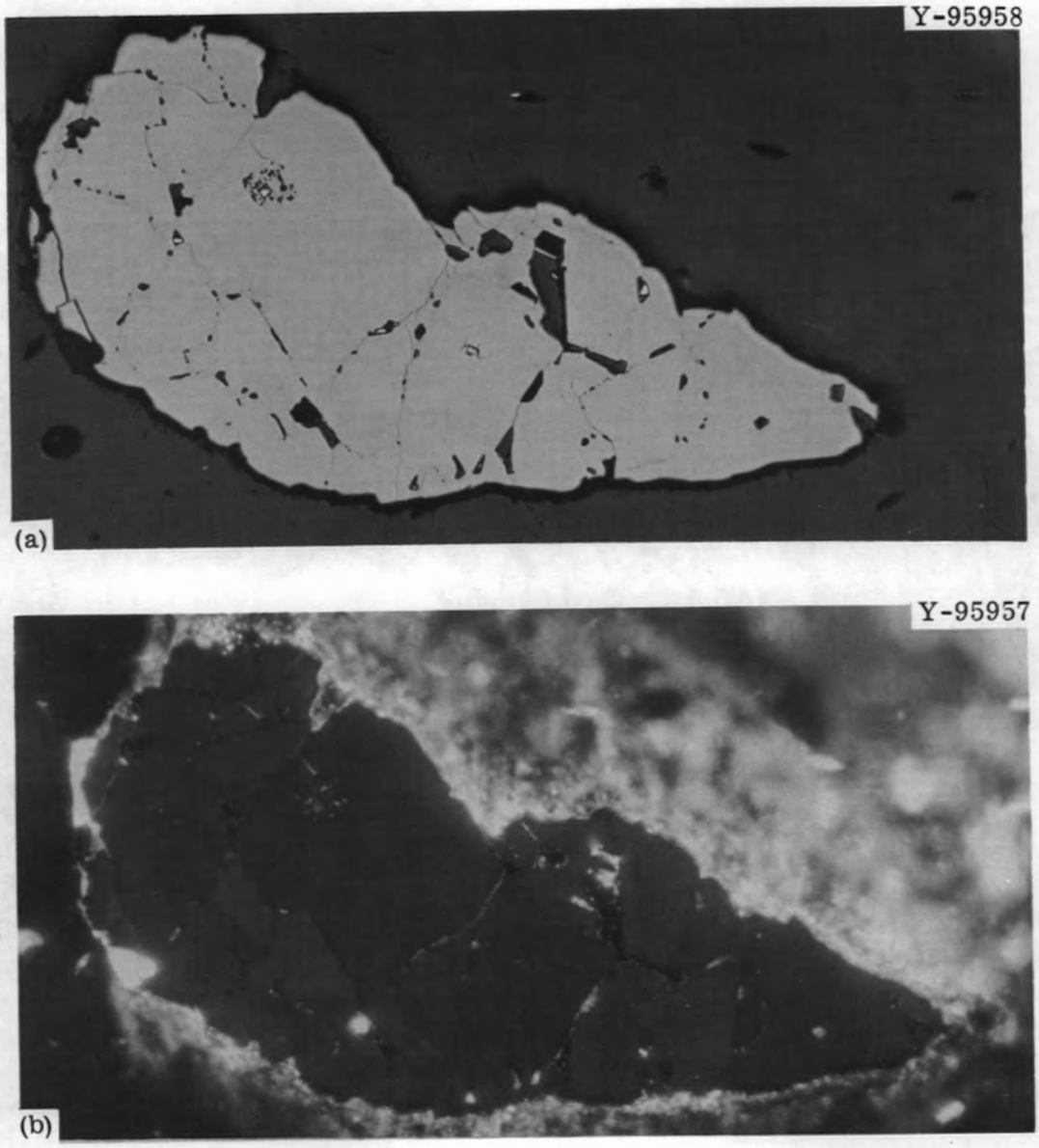

Fig. 11.2. Coarse Particle of Boron Carbide Shown in Metallographic Section Under Bright-Field Illumination. (a) Particle shows pores, stringers of segregate, and cracks. (b) Particle under polarized light. Optical activity reveals that the particle is polycrystalline. Stringers of segregate separate the grains, which are characteristically twinned, translucent, and blue. 50×.

Optical and electron microscopy of unmounted particles suggested fine speckle markings for the fine grades of Norbide 325-F and Carborundum-325. The scanning electron microscope revealed these in detail (Fig. 11.3). We believe that the arc-melted products fracture along the seams during crushing (Fig. 11.1), leaving graphite particles embedded in the surfaces and a sound internal structure of B_4C. This may explain why the finer grades tend to be high in C, since the particles with the graphite segregate should break down more readily in crushing. Similarly, the range of lattice parameters as evidenced by split x-ray peaks for the coarser grades can be rationalized as representing the full range of B:C ratios of proeutectic B_4C. The B_4C of the finer sizes, being adjacent to the graphite, would have formed at the eutectic temperature, corresponding to the B:C ratio for C saturation.

Chemical Composition and Density of Commercial Grades of Powder
(R. S. Mateer,[2] G. L. Copeland)

Major impurities in B_4C are unreacted B_2O_3, Al, Si, and Fe at levels up to 0.4 wt % each. Table 11.1 gives compositions and densities of eight lots of powder examined at ORNL.

X-ray diffractometer tracings showed graphite peaks that were particularly strong (corresponding to perhaps 5 wt %) in the fine grades of Norbide 325-F and Carborundum-325. This graphite was not separable by water elutriation.

The density of the commercial powders ranged from 2.49 to 2.52 g/cm^3. This latter figure is generally accepted[10] as the true density, although values as high as 2.6 have been reported.[9] In view of the porosity observed in some of the larger particles and the graphite associated with the finer ones, we conclude that density is not a good parameter for characterization.

Behavior of Boron Carbide Particles in Pressing and Sintering
(R. S. Mateer,[2] G. L. Copeland)

Structural Changes on Annealing of Powders. — Boron carbide powders have high surface energy (as suggested by hygroscopic behavior) that provides the driving force for densification in sintering and hot pressing.

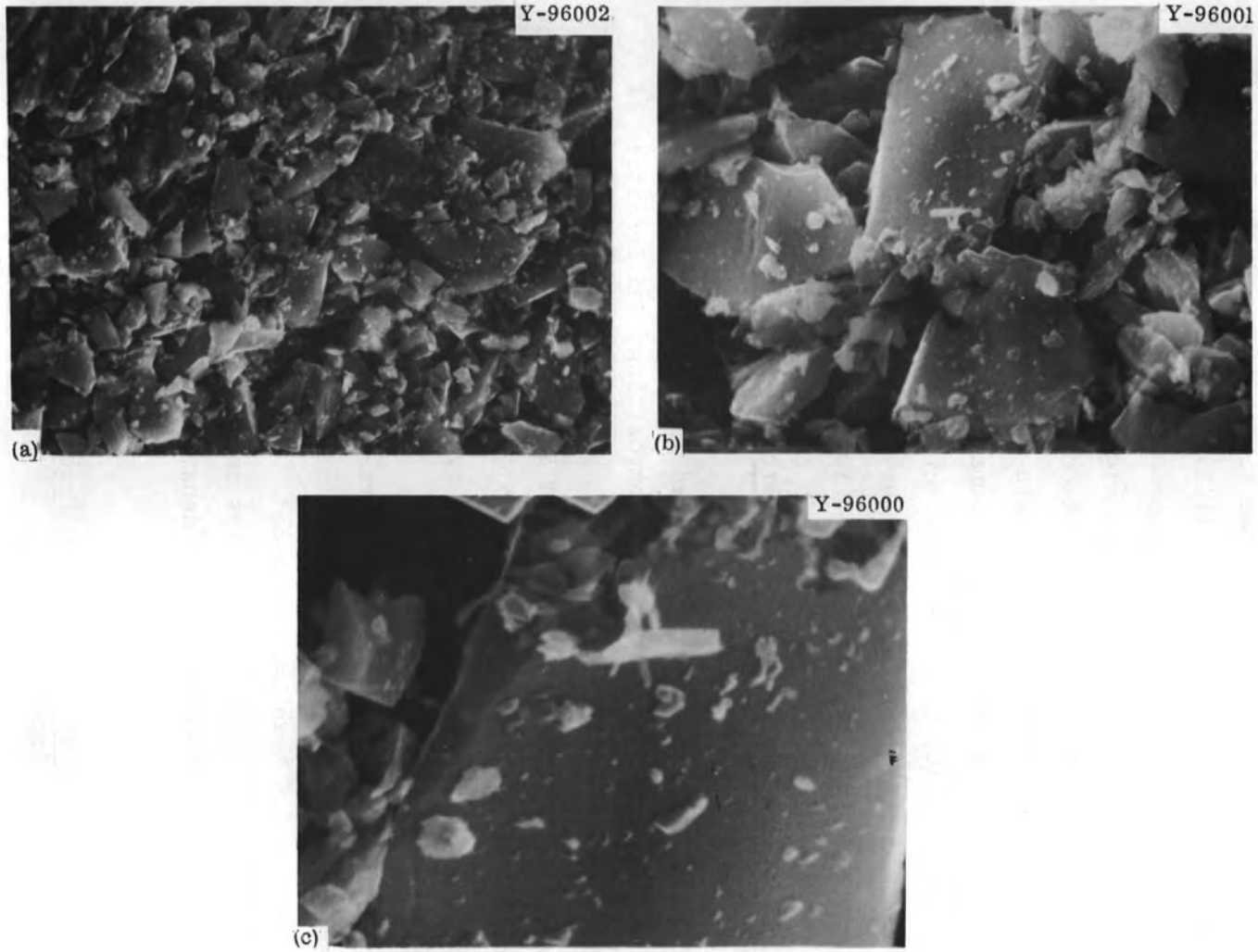

Fig. 11.3. Norbide 325-F Grade Boron Carbide Powder Viewed by Scanning Electron Microscope at Three Different Magnifications. Surfaces of the angular particles show white specks believed to be graphite. (a) 1000×, (b) 3000×, (c) 10,000×.

Table 11.1. Composition and Density of Commercial Grades of Boron Carbide Powder

Commercial Product	Particle Size (mesh)	Composition, wt %					Density (g/cm^3)
		B	C	Fe	Si	Al	
Norbide 325-F		75	23	0.03	0.4	0.1	2.525
Norton TG-101	−100	73	26	a	a	a	2.504
Norton HB-6822	−100	77	22	a	a	a	2.503
Norton M-103-B	−100	80	19	a	a	a	2.498
Carborundum	−14 +20	79	19	0.7	0.1	0.04	2.474
Carborundum	−60 +140	77	22	0.09	0.04	0.04	2.510
Carborundum	−180	75	24	0.1	0.04	0.025	2.478
Carborundum	−325	72	26	0.1	0.7	0.025	2.498

[a]Not determined.

Fine powders are preferable for achieving high densities because the voids between particles are small and the interfacial area is high. These factors have focused our interest on the Norbide 325-F for these evaluations.

Chemical and structural changes occur when Norbide 325-F powder is heated to 1850°C in high vacuum. A volatile substance, probably B_2O_3, condenses on the furnace window, and there is a weight loss of about 2%; the toluene density increases from 2.52 to 2.57 g/cm^3; the graphite peak becomes very weak in the x-ray pattern, and the high-angle peaks of the B_4C shift; the angular surface speckles (Fig. 11.3) coalesce to oval shapes (Fig. 11.4); the sharp edges of the B_4C particles become rounded; and polyhedral voids grow within some of the particles. The size of the pores depends on the annealing temperature. Figure 11.5(a) shows the dense structure of the starting powder in metallographic section. In Fig. 11.5(b) and 11.5(c) are shown the structures after annealing at 1500 and 2000°C, respectively. The pore size ranges from about 1 to 3 μm in diameter. We believe this is a Kirkendall diffusion phenomenon in which B atoms migrate from the interior of the particles to react with graphite particles on the surface. This efflux

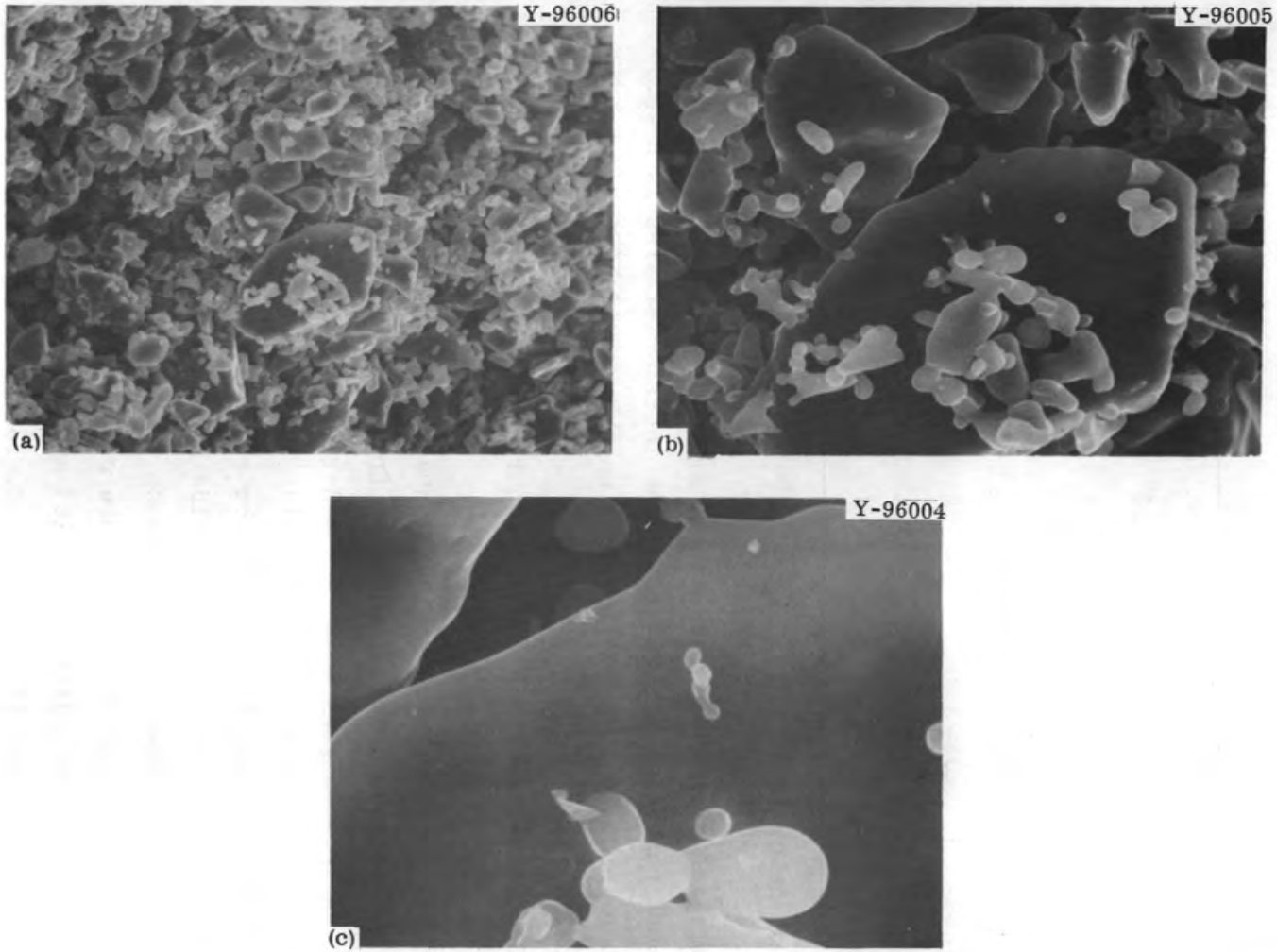

Fig. 11.4. Norbide 325-F Grade Boron Carbide Powder, Vacuum Annealed 1 hr at 1850°C, Viewed by Scanning Electron Microscope at Three Different Magnifications. Comparison with Fig. 11.3 shows that sharp fracture edges have become round. The angular specks have coalesced into ovals, believed to be boron carbide. (a) 300×, (b) 1000×, (c) 3000×.

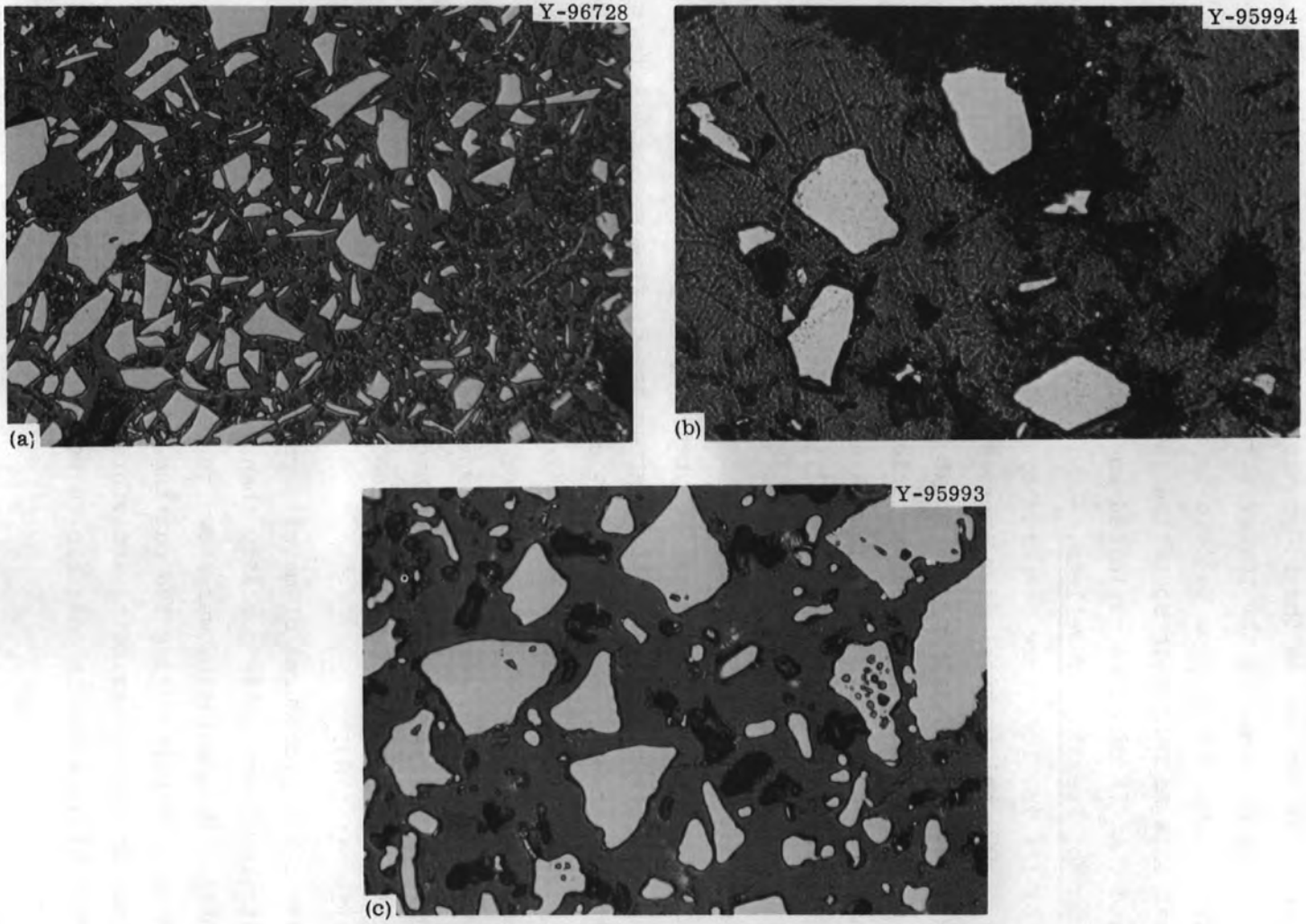

Fig. 11.5. Metallographic Section Through Norbide 325-F Grade Boron Carbide Powder. (a) Powder, as received, has a dense internal structure. Graphite specks believed to be on the surfaces cannot be detected optically. (b) Powder after vacuum annealing 1 hr at 1500°C. Numerous closed pores, less than 1 μm in diameter, have formed in several of the particles. (c) Powder after vacuum annealing 1 hr at 2000°C. Pores about 3 μm in diameter have formed in some of the particles. 500×.

is not balanced by the inward diffusion of C. The difference appears as vacancies, which condense to form the isolated, polyhedral voids. The lattice parameter changes as the B:C ratio decreases. The process is dependent on time. Passing the powder through an Ar plasma torch causes no change in x-ray diffraction pattern or surface appearance. It is likely that this mechanism is operative in other powder-metallurgy systems and that it might be exploited to improve properties.

Vacuum Hot Pressing of Pellets. — Cylindrical pellets 1/2 in. in diameter by 1/2 in. long were prepared by cold compacting Norbide 325-F powder at 50,000 psi in steel dies lubricated with stearic acid followed by hot pressing at 2000 psi for 1/2 hr in graphite dies heated by induction. A mechanical pump provided sufficiently good vacuum to prevent oxidation of the graphite. Initial work at 1650°C yielded pellets 60% of the accepted theoretical density of 2.52 g/cm^3. Increasing the temperature to about 1850°C yielded pellets 92% of theoretical density.

The microstructure shown in Fig. 11.6(a) was observed throughout Norbide 325-F hot-pressed pellets. Polyhedral pores similar to those in the annealed powders are visible as groupings of fine specks. A few light particles that appeared bright yellow to direct observation were shown by microprobe analysis to be rich in Fe. Concentrations at the edges of the pellets suggest that some of them originated as scrapings from the wall of the die during cold compacting. Most of the irregularly shaped particles in this photomicrograph have the fine-grained structure typical of graphite. This same area is shown under polarized light in Fig. 11.6(b).

Conventional procedures of metallographic preparation indicated much higher levels of gross porosity than indicated by water density measurements. This porosity was shown to be due to pullouts and fragmentation of particles during the cutting of the samples on a diamond wheel. Only by diamond grinding and vibratory polishing with alumina for a period of days was it possible to reveal the dense structure shown in Fig. 11.6.

Grain size is revealed by chromic acid electrolytic etch (Fig. 11.7). The larger grains are characteristically twinned and appear to be slightly larger than the original particles. The surrounding particles are much

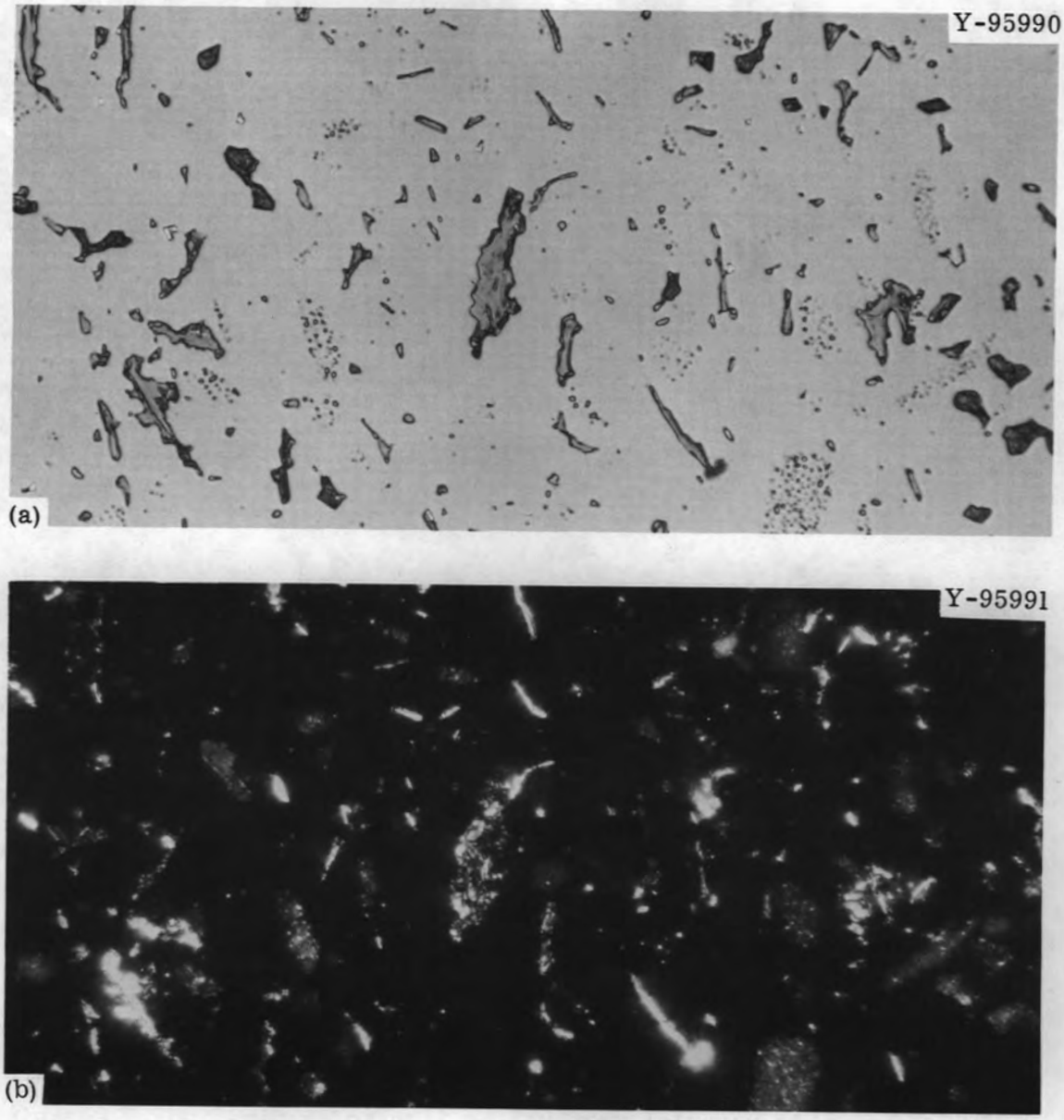

Fig. 11.6. Polished Microstructure Typical of Norbide 325-F Boron Carbide Vacuum Hot Pressed at 1850°C. (a) Closed porosity, similar to that in annealed powder shown in Fig. 11.5(b), appears in clusters. Irregular particles of second phase appear to be graphite. Specimen is 92% of theoretical density. (b) Same area as shown in (a), here shown in polarized light. Bright, elongated particles have extinction characteristics like those of graphite. Clusters of light specks are internal reflections from polyhedral voids. 500×.

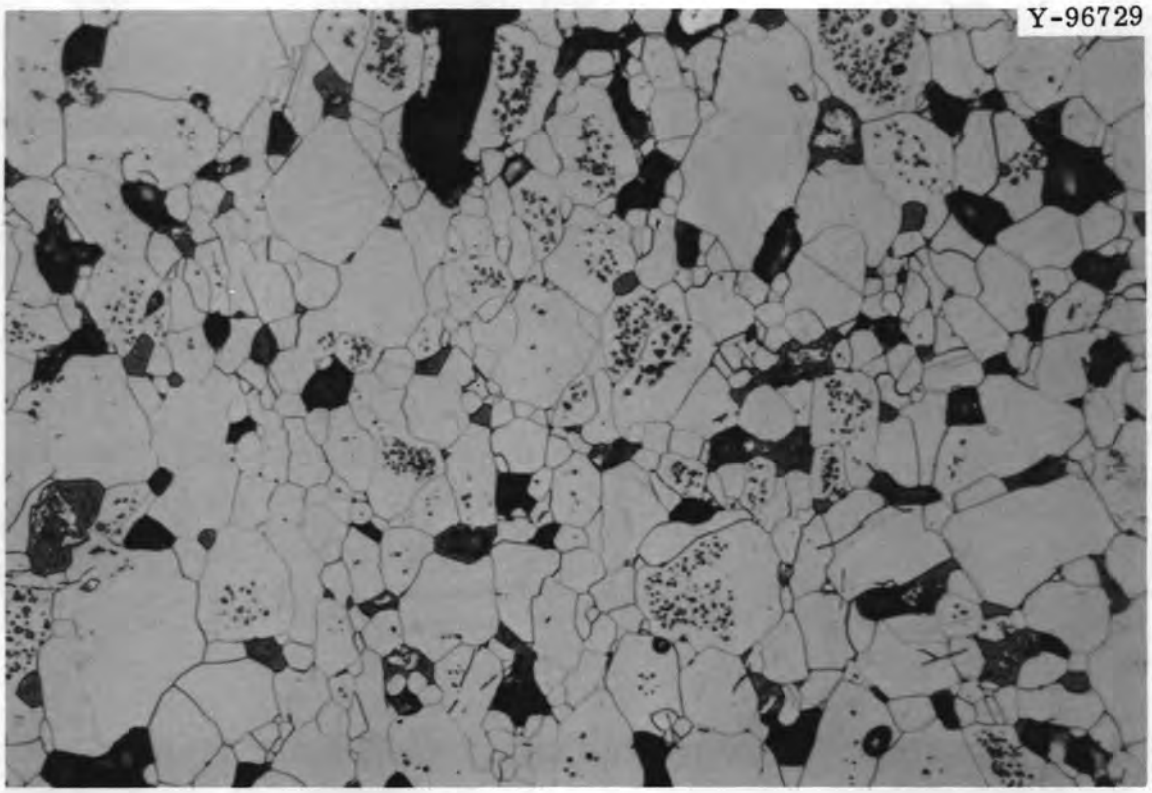

Fig. 11.7. Grain Structure of Norbide 325-F Boron Carbide Pellet Hot Pressed at 1850°C. Dark islands are regions of polyhedral porosity that have been attacked selectively. Intergranular porosity is exaggerated by this etchant. Large, twinned grains probably correspond to the original particles. Finer grains would then result from surface conversion of graphite to boron carbide. 500×.

finer. Presumably these twins formed from the reaction of surface graphite with B that diffused from the interior of the particles.

We examined some commercial B_4C plates that were available in the laboratory and found them to be slightly more dense than our vacuum hot-pressed Norbide 325-F pellets but very similar in structure. Fracture surfaces from this material were well-suited to examination by scanning electron microscopy. Details of the polyhedral pore structure found in the commercial product are shown in Fig. 11.8.

Control of Polyhedral Voids (R. S. Mateer,[2] G. L. Copeland)

Closed pores are generally not believed to be important to irradiation damage to B_4C; for basic studies of irradiation damage, however, the size and distribution of these pores must be controlled. Figure 11.5 shows that their size can be controlled, in bulk powder, by simple heat

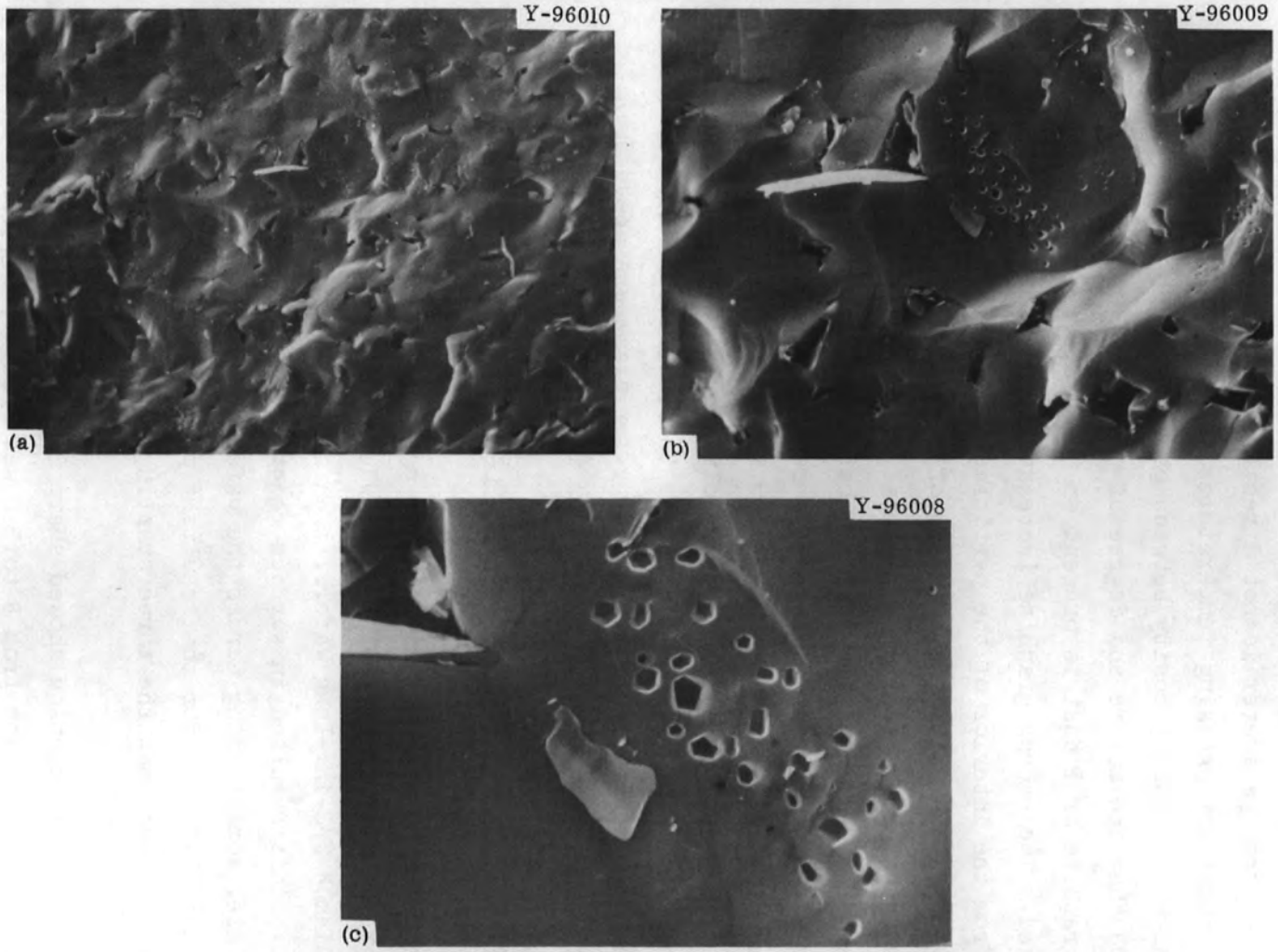

Fig. 11.8. Fracture Surface of Commercial Boron Carbide Plate As Viewed by Scanning Electron Microscope. In metallographic section, this plate was identical to the pellet of Fig. 11.6(a). Intergranular porosity appears as irregular, black holes. White streak is possibly a graphite flake. Polyhedral porosity is visible in central portions of the grains. (a) 300×, (b) 1000×, (c) 3000×.

treatment. The structure shown in Fig. 11.5 would presumably be stable when such particles were incorporated into metallic matrices by conventional powder-metallurgy procedures at low temperatures.

This control parameter is not directly available for high-density pellets because hot-pressing temperatures of about 1850°C are required to eliminate the gross porosity between particles. We have shown (see Fig. 11.9) that the nature and degree of polyhedral porosity can vary if free graphite or B dust is present on the B_4C particles before they are pressed. The excess graphite increases the amount of B that must diffuse from the interior of the particles, and porosity increases accordingly. Conversely, the addition of B reduces porosity. To date, the porosity has been observed by optical microscopy. When the pellets are sintered to eliminate the porosity between particles and when the B:C ratio is near 4, optical microscopy reveals no fine voids up to magnifications of 1000×. We do not know if the porosity has been eliminated or only reduced to a size not resolvable at 1000×. We are investigating the use of small-angle scattering to resolve porosity for sizes less than 50 A and of electron microscopy for diameters above 50 A. Both of these techniques will be used on irradiated B_4C wafers.

Some Observations on Boron Carbide Phase Equilibria (R. S. Mateer,[2] G. L. Copeland)

To explore phase boundaries in the system, diffusion couples in the form of graphite-Norbide 325-F B_4C-B powders were cold compacted as 1/2-in.-diam × 3/8-in.-long wafers, then stacked for vacuum hot pressing at 1850°C. This resulted in surface reaction of the B wafer with the graphite die, some bonding across the wafer interfaces, and sufficient internal consolidation for the resultant pellets to be handled. X-ray diffraction showed that the three starting powders had not intermixed nor reacted in bulk.

Metallographic section showed sharp interfaces for B or B_4C against graphite. The transition from B to B_4C was gradual, however. In the regions of high B content, a faint, spotty structure was visible in the dense, translucent matrix. This is shown in Fig. 11.10(a) and is clearly visible in a photomicrograph of this region made with polarized light

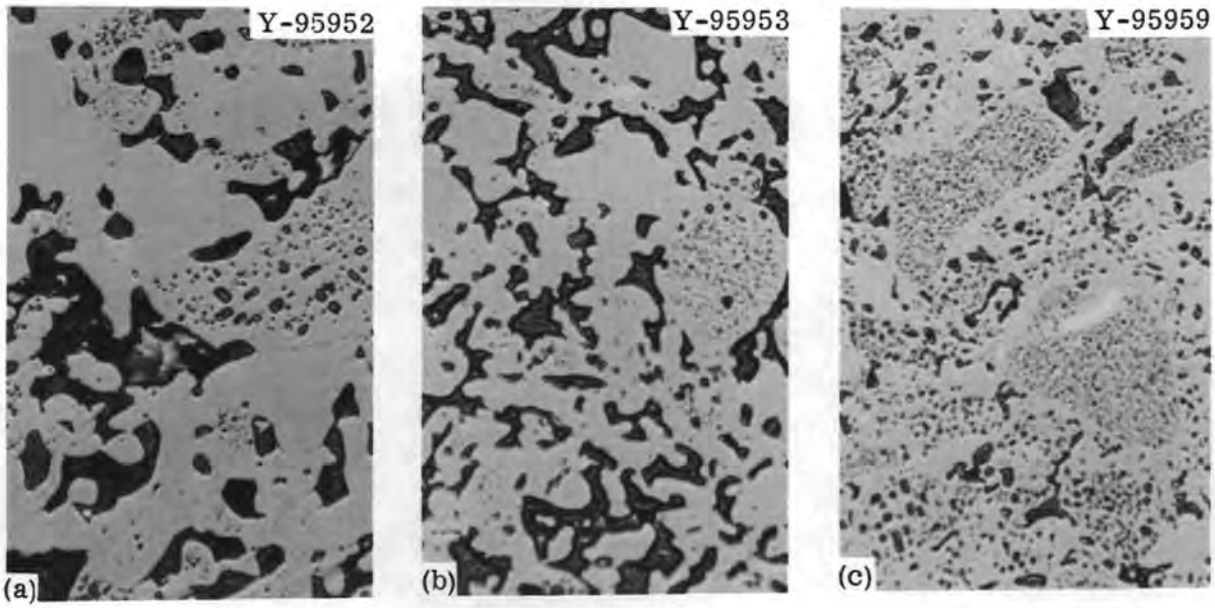

Fig. 11.9. Structure of Pellets Hot Pressed at 1850°C. (a) Norbide 325-F Grade Boron Carbide Powder. Microprobe analysis identifies the small, bright regions as high in iron, presumably iron boride. Dark, irregular regions are pullouts that remain after conventional metallographic preparation. (b) Powder blend of 95 wt % Norbide 325-F boron carbide and 5% B. Polyhedral porosity is reduced in comparison to (a). (c) Powder blend of 95 wt % Norbide 325-F boron carbide and 5% graphite. Polyhedral porosity is increased in comparison to (a). 500×.

[Fig. 11.10(b)]. An x-ray diffractometer scan of a fracture surface in this vicinity showed only rhombohedral B with some weak lines, possibly from tetragonal B. Our tentative interpretation is that the twinned matrix is rhombohedral B consolidated during hot pressing and that the spots are tetragonal regions formed during cooling under pressure. These spotty regions disappear in the B_4C region of the diffusion couple. At the same time, the grain size of the twinned matrix decreases and the color, as seen reflected from surface imperfections in polarized light, changes from red to blue.

The absence of distinct interfaces between B and B_4C in this rough experiment gives support to the position of Glaser et al.[9] that B_4C is not a distinct compound but, rather, a terminal solid solution of C at preferred sites in the rhombohedral B lattice.

To explore laboratory production of experimental grades of B_4C, we tungsten arc melted Norbide 325-F B_4C with B and graphite additions in a Cu-hearth button furnace under an Ar atmosphere. X-ray diffraction

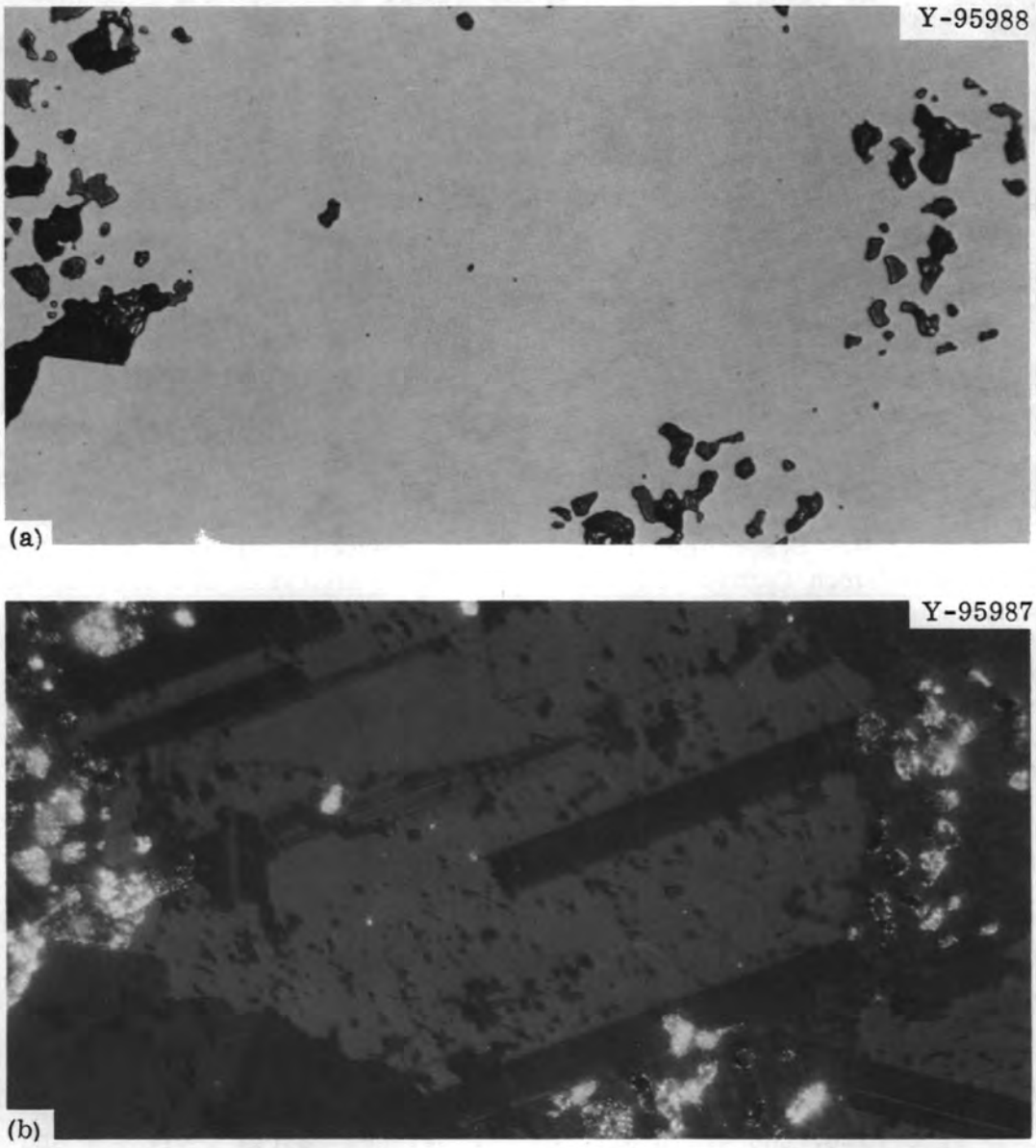

Fig. 11.10. Metallographic Section Through Boron-Rich Portion of Boron-Boron Carbide-Graphite Diffusion Pellet Vacuum Hot Pressed at 1850°C. (a) Bright-field illumination. Black regions are porous zones. X-ray diffraction pattern shows rhombohedral boron plus extra lines, possibly corresponding to tetragonal boron, that probably arise from the faint gray phase. (b) Polarized light. The white areas are pores. Matrix is composed of coarse, twinned grains. The phase that appeared faint gray in bright-field illumination appears as dark specks. The matrix is translucent and red. 500×.

showed the presence of B_4C in each ingot, but strong, unidentified lines also appeared. The ingot was composed of several phases, and the microstructural appearance was complex. A structure similar to that of eutectic graphite flakes in cast Fe was observed in a melt that contained excess C, and this identification was confirmed by x-ray diffraction.

These exploratory experiments suggest that the B-graphite system is prone to generation of metastable phases. These depend on production history and have undoubtedly contributed to the discrepancy in the literature as to the crystal structure of "boron carbide" and the existence of other compounds in the system. Commercial grades appear to be blends in which no single particle may be considered as "typical."

Irradiation Behavior of Boron Carbide

Irradiation Tests (G. L. Copeland, R. S. Mateer[2])

Our program for the irradiation testing of B_4C has two parts. First, we shall irradiate powders and wafers of B_4C with a given B:C ratio and internal porosity in capsules in the High Flux Isotope Reaction (HFIR) and the Oak Ridge Research Reactor (ORR) to examine the basic behavior of Li and He generated from the $^{10}B(n,\alpha)$ reaction. Nine variations of composition and density will be studied, but all the powders will have approximately equivalent grain size. These initial tests will be in uninstrumented capsules, but we are examining means of evaluating in-reactor gas release and swelling behavior with instrumented assemblies.

The second part of our program calls for irradiating pellets (0.375 in. in diameter by 0.375 in. long and 92 to 95% of theoretical density) at 400 and 700°C in the Experimental Breeder Reactor-II (EBR-II). Two types of powder are being prepared, one with a B:C ratio of 4.0 and one with a ratio of about 5.0. These powders are two of the nine types to be examined in the capsule tests. These pellets are now being made, and the assembly will be shipped to the EBR-II sometime in December. Results from these tests of pellets will be compared to those from the more detailed irradiation tests of powders and wafers to be conducted in the HFIR and ORR.

References

1. Reactor Chemistry Division.
2. Consultant from the University of Kentucky.
3. R. P. Elliott, First Supplement, Constitution of Binary Alloys, pp. 110–113, McGraw-Hill, 1965.
4. H. K. Clark and J. L. Hoard, J. Am. Chem. Soc. 65, 2115–2119 (1943).
5. C. W. Tucker and Peter Senio, Acta Cryst. 8, 371–378 (1955).
6. R. P. Elliott, The Boron Carbide System, ARF-2200-12 (May 1960–61).
7. ASTM Data Cards 6-0555 (Boron Carbide), 12-212 (Graphite), and 11-618 (Boron), Inorganic Index to the Powder Diffraction File, 1969, ASTM Publ. PD1S-19i, American Society for Testing and Materials, Philadelphia.
8. R. Kranz, Hambrug Beitr. Angew. Mineral. Kristallphys. Petrogen. 2, 99–115 (1959).
9. F. W. Glaser, D. Moskowitz, and B. Post, J. Appl. Phys. 24(6), 731–733 (1953).
10. A Handbook on Boron Carbide Elemental Boron, and Other Stable, Boron-Rich Materials, Norton Company, Worcester, Mass., 1955.

PART II

SPACE POWER TECHNOLOGY

FUELS

12. DEVELOPMENT OF URANIUM MONONITRIDE FUELS

J. L. Scott

Uranium mononitride (UN) is potentially attractive as fuel for space-nuclear reactors because of its excellent stability at high temperatures, high thermal conductivity, and good irradiation stability up to 1000°C. The purpose of this program is to determine the basic mechanisms of fuel swelling and gas release at temperatures above 1000°C. Results will be used to develop a model for predicting the performance of UN as a function of temperature, burnup, and cladding restraint.

Irradiation Testing

T. N. Washburn

The basic objective of the ORNL program[1] for irradiation testing of UN is to investigate the performance capability of this material at temperatures of 1000 to 1550°C at the fuel center and 900 to 1400°C on the outside surface of the cladding and linear heat ratings from 5 to 10 kw/ft. Fuel properties of most interest are swelling rate, release of fission gas, and compatibility with the cladding materials. The irradiation tests are conducted in the poolside facilities of the Oak Ridge Research Reactor (ORR). These facilities allow adjustment of the position of the test capsule relative to the reactor face, thereby providing a constant temperature at a selected reference point on the test specimen as the flux profile in the reactor changes and/or as the fissile content of the test fuel is diminished.

The major design items and operating conditions for the test specimens are tabulated in Table 12.1.

Capsules UN-1 and UN-2 (S. C. Weaver)

The design, operating history, and postirradiation examination results for these two capsules were reported previously.[2]

Table 12.1. Summary of Design and Operating Conditions for Capsules UN-1 Through UN-6

	UN-1			UN-2			UN-3			UN-4			UN-5			UN-6		
	Top	Middle	Bottom	Top	Middle	Bottom	Top	Middle	Bottom	Top	Middle	Bottom	Top	Middle	Bottom	Top	Middle	Bottom
Fuel pellets																		
Density, % theoretical	94	95[a]; 100[b]	95	94	94[a]; 83[b]	95	94	95.5	95.5	85	85	95	85	95	85	85	95	95
Enrichment, % ^{235}U	20	20	13.9	20	20	12.9	20	12.9	12.9	20	11	11	20	11	11	20	11	11
Outside diameter, in.	0.300	0.250	0.300	0.300	0.250	0.300	0.300	0.300	0.300	0.308	0.308	0.308	0.308	0.308	0.308	0.308	0.308	0.308
Inside diameter, in.	0.105	c	c	0.105	c	c	0.105	c	c	c	c	0.100	c	0.100	c	c	0.100	0.100
Cladding																		
Material	W–26% Re	W–26% Re	W–26% Re	W–25% Re	W–25% Re	W–25% Re	W–25% Re	T-111	T-111	T-111	T-111	T-111	T-111	T-111	T-111	W–25% Re–30% Mo	W–25% Re–30% Mo	W–25% Re–30% Mo
Outside diameter, in.	0.365	0.365	0.365	0.365	0.365	0.365	0.365	0.365	0.365	0.375	0.375	0.375	0.375	0.375	0.375	0.375	0.375	0.375
Wall thickness, in.	0.030	0.030	0.030	0.030	0.030	0.030	0.030	0.030	0.027	0.0285	0.0285	0.0285	0.0285	0.0285	0.0285	0.0325	0.0325	0.0325
Length, in.										4.5	4.5	4.5	4.5	4.5	4.5	4.5	4.5	4.5
Cladding liner																		
Material									W deposit	W tube	W tube	W tube	W tube	W tube	W tube			
Outside diameter, in.										0.316	0.316	0.316	0.316	0.316	0.316			
Inside diameter, in.										0.310	0.310	0.310	0.310	0.310	0.310			
Wall thickness, in.										0.003	0.003	0.003	0.003	0.003	0.003			
Fuel pin																		
Gap between fuel and cladding, in.	0.005	0.055	0.005	0.005	0.055	0.005	0.005	0.005	0.005	0.002	0.002	0.002	0.002	0.002	0.002	0.002	0.002	0.002
Thermal bond between fuel and cladding	He	Li	He	He	Li	He	He	He	He	He	He	He	He	He	He	He	He	He
Fuel smear density, % theoretical	91.5	64[a]; 67[b]	92	91.5	64[a]; 56[b]	92	91.5	92	92	84	84	84	84	84	84	84	84	84
Fuel-column length, in.	3	3	3	3	3	3	3	3	3	3.615	3.615	3.615	3.615	3.615	3.615	3.615	3.615	3.615
Operating conditions (time averaged)																		
Linear heat rate, kw/ft			8.5			8.5			8.9	8.6	8.6	9.2	8.6	8.6	9.2	8.6	8.6	9.2
Cladding temperature, °C	1040	1100	1200	d	1175	1350	1220	1225	1370	1000	1000	1040	1000	1000	1040	1000	1000	1040
Fuel-center temperature, °C	1200	1250	1400	~ 2100	1325	1550			1550									
Fuel burnup, at. %	1.78	2.26[a]; 2.45[b]	1.83	0.05	0.05	0.05	2.5	3.0	3.0									
Irradiation test time, hr (as of Aug. 19, 1969)	8155	8155	8155	220	330	330	4074	4074	4074									
Current status	Postirradiation examination complete			Postirradiation examination complete			Under irradiation testing			Being designed			Being designed			Being designed		

[a]Cold pressed and sintered pellets.

[b]Arc-cast bi- and tri-crystals.

[c]Solid pellets.

[d]Surged to 1545°C due to loss of NaK.

Capsule UN-3 (S. C. Weaver)

Irradiation testing of this capsule began in January 1969, and is continuing satisfactorily. The accumulated exposure is about 4500 hr of the scheduled 10,000 hr. Two thermocouples (TE-501 and -502), located on the surface of the cladding of the bottom fuel pin, have failed. All other thermocouples are operating satisfactorily. The control variable for this experiment is the rate of heat generation in the bottom fuel pin, which is being held constant at 8.8 kw/ft.

Capsules UN-4, UN-5, and UN-6 (S. C. Weaver)

Detailed engineering design and thermal analysis of the capsule design are in progress. The specifications for the W-Re thermocouples were completed, and a purchase order was placed. Some of the capsule components are currently being fabricated.

References

1. The current program includes work sponsored by the Atomic Energy Commission (AEC), and work sponsored by the National Aeronautics and Space Administration (NASA) under Interagency Agreement 40-184-69, NASA Order C-54536-B. Specifically, capsules UN-1, UN-2, UN-3, and UN-6 are funded by AEC, and capsules UN-4 and UN-5 are funded by NASA.
2. S. C. Weaver, Fuels and Materials Development Program Quart. Progr. Rept. June 30, 1969, ORNL-4440, pp. 16–30.

CLADDING AND OTHER STRUCTURAL MATERIALS

13. CLADDING MATERIALS FOR SPACE ISOTOPIC HEAT SOURCES

P. Patriarca R. G. Donnelly

The immediate tasks of this program are (1) to evaluate the more promising superalloys that are available commercially and (2) to develop improved alloys and eventually qualify those that show greatest promise for containment of radioisotopes in space power systems. The superalloy tasks include studies of mechanical properties, evaluation of embrittling aging reactions, determination of evaporation characteristics, and studies of the interaction of stress and vacuum on properties at elevated temperatures. In the alloy development portion of the program, the creep strength and resistance to evaporation and to oxidation in air are of primary concern.

Creep Studies of Cobalt Superalloys

H. Inouye

Interaction of Stress and Vacuum on the Creep Properties of Haynes Alloy No. 25 at Elevated Temperatures (D. T. Bourgette)

We completed an investigation of the creep behavior of Haynes alloy No. 25 (Co–20% Cr–15% W–10% Ni) that showed that the creep strength of this alloy in vacuum at 785 and 900°C depends on the thickness of the specimen (Fig. 13.1). We attribute this behavior to evaporative loss of the elements that have higher vapor pressures – Cr, Mn, Fe, and Ni – which affects a greater volume fraction of the thinner specimens. At a given temperature the evaporative losses per unit area are the same for all specimen thicknesses. In the case of the thicker specimens, however, the resulting compositional change is limited to the surfaces, so that the effect on creep strength is minimized. Further, an aging reaction (precipitation of a Laves phase – Co_2W) greatly improves the strength of the alloy at 750 to 900°C. In the thicker specimens, therefore, the loss of creep strength due to evaporation is overshadowed by the gain in strength due to aging. For the thinner specimens, however, initial

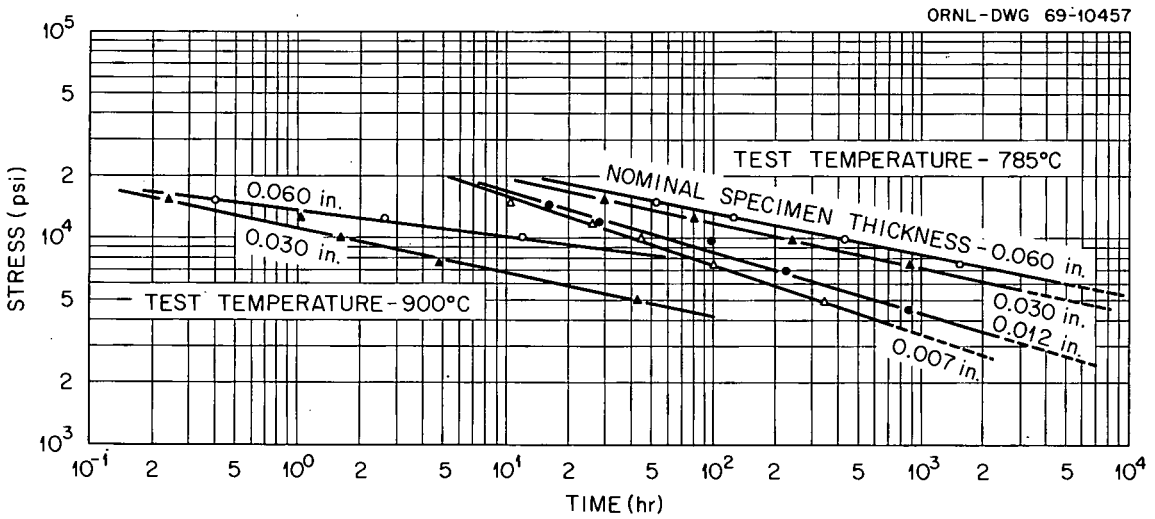

Fig. 13.1. Effect of Thickness and Stress on the Time Necessary to Produce 1.0% Plastic Strain in Haynes Alloy No. 25 in a Vacuum of 10^{-7} to 10^{-9} torr at Test Temperatures of 785 and 900°C.

evaporative losses occur before appreciable aging and result in a greater deterioration of creep strength. Therefore, curves of the type shown in Fig. 13.1 will diverge with time. When the evaporative losses are excessive, as in the case of long-term tests at low stresses, the curves will deviate from linearity and bend toward the time axis.

Specimens tested in Ar and air did not lose weight by evaporation; and, for equal stresses, test temperatures, and section thicknesses, they were stronger than specimens tested in vacuum. In addition, the degree of divergence of the 1% creep-strain curves for Ar, as compared to that for tests in vacuum, decreases with an increase in specimen thickness. This behavior, illustrated in Fig. 13.2, further substantiates the effect of vacuum and thickness on the creep properties of Haynes alloy No. 25.

Development of Improved Alloys

H. Inouye

Creep Tests of Experimental Alloys (C. T. Liu)

The effect of long-range order on the creep behavior of V-Ni-Co alloys at high temperatures is being determined as a function of temperature (T) and stress (σ) up to 40×10^3 psi. The steady-state creep

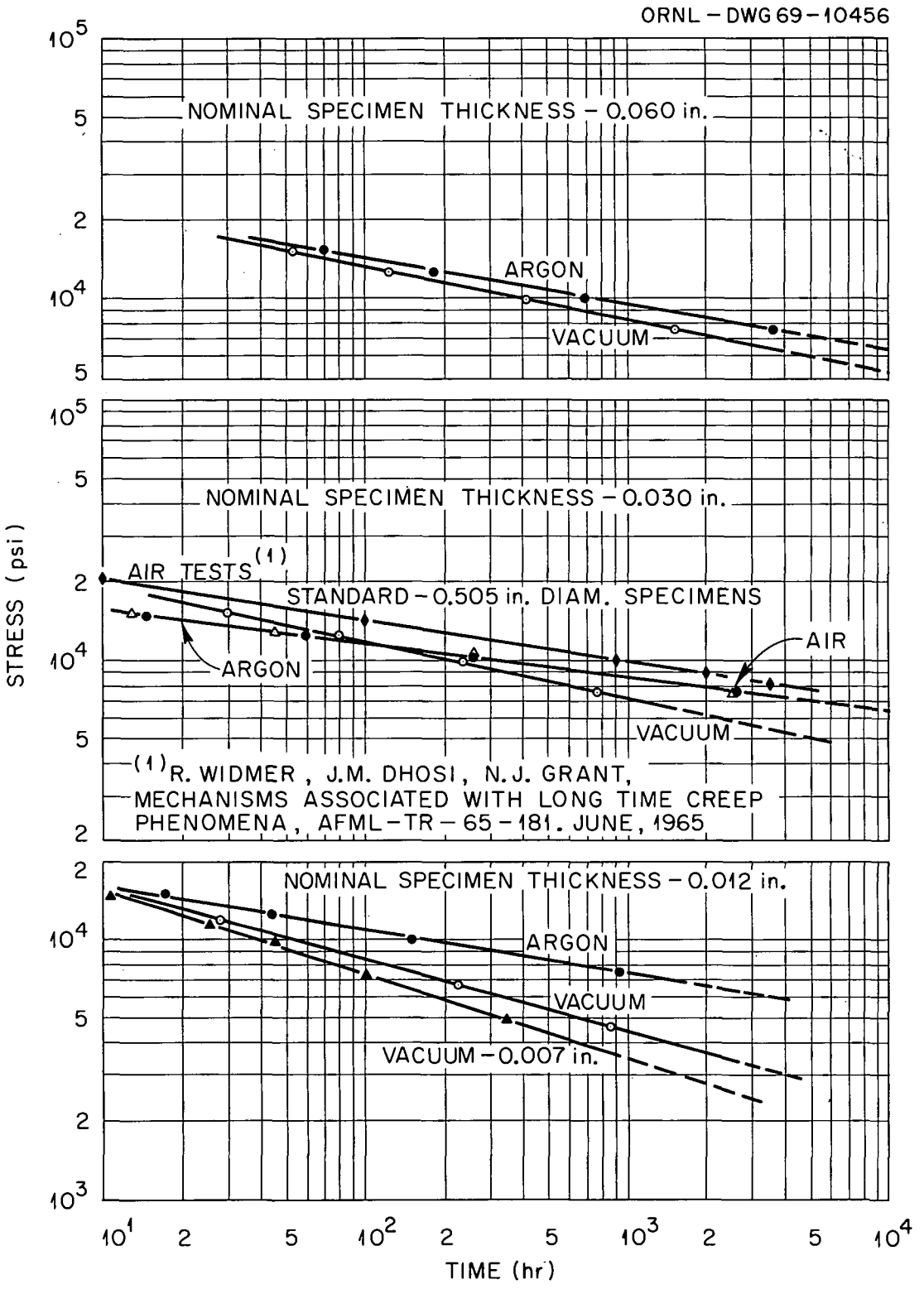

Fig. 13.2. Effect of Thickness and Stress on the Time to Produce 1.0% Plastic Strain in Haynes Alloy No. 25 at 785°C in Vacuum, Argon, and Air.

rate ($\dot{\epsilon}$) of ordered alloy S-4 (Ni–38.8% Co–22.5% V) and disordered alloy S-3 (Ni–46.4% Co–7% V) can be described by

$$\dot{\epsilon} = K \sigma^n e^{-Q/RT} ,$$

where K and n are materials constants, R is the gas constant, and Q is the activation energy for creep. A plot of the log of the creep rate versus the reciprocal of time shows a large increase in Q caused by long-range order. Calculated values of Q for ordered and disordered alloys are 83 and 58 kcal/mole, respectively.

It is significant that the creep rate of alloy S-4 is much less sensitive to the applied stress (n = 2) than is the creep rate of alloy S-3 (n = 5). At 700°C and 1×10^4 psi, the creep rate of alloy S-3 is higher than that of alloy S-4 by a factor of 10; but for a stress of 2×10^4 psi, the creep rate of alloy S-3 is higher than that of alloy S-4 by a factor of 100. Thus, the ordered alloy shows particular promise in applications that require high stresses.

In terms of the time to produce 1% strain, alloy S-4 is comparable with Haynes alloy No. 25 between 700 and 800°C. At higher temperatures, the creep data show that alloy S-4 is significantly stronger than Haynes alloy No. 25. Restricted by their melting points, the V-Ni-Co alloys cannot be used at temperatures above 1300°C. The present study does reveal the superior properties of ordered alloys below this temperature, however.

Our efforts are now concentrated on the alloy systems that have melting points above 1300°C. The Pt-base alloys are particularly interesting to us for these reasons:

1. high melting point (about 1770°C);
2. resistance to evaporation under high vacuum;
3. resistance to oxidation if the alloying content is less than about 10 wt %.

We believe that strength can be achieved at high temperatures in these alloys either by ordering or by precipitation of stable, ordered second phases.

Russian work[1] indicates that the ordered alloy, Pt_3Cr, possesses superior creep resistance under a bend test. Accordingly, we arc melted and drop cast two ingots with the same composition, Pt–8% Cr (Pt_3Cr), but with two different grades of Cr. The alloy containing higher levels of interstitial impurities had poorer ductility. Neither ingot could be fabricated successfully at room temperature in either the quenched or annealed condition. The recast ingots were canned in a Mo jacket and are ready for extrusion at about 1200°C.

The Pt-rich end of the Pt-Mo system contains an ordered phase, $MoPt_2$. The work of Nishimura and Kimura[2] indicates that alloys containing less than 6 wt % Mo can possibly be fabricated at room temperature and that the oxidation rate increases rapidly as the Mo content increases above 5 wt %. As a preliminary study, a Pt-base alloy containing 5 wt % Mo was arc melted and drop cast into a 5-in.-long × 7/16-in.-diam ingot. The ingot could not be cold swaged satisfactorily because of the formation of central longitudinal cracks throughout the ingot. The work-hardening rate of this alloy is high. For example, 8% reduction of area causes the hardness to increase from 21 to 45 on the Rockwell D scale. We found, however, that the recast button could be cold forged and rolled without difficulty. Tensile and creep specimens are being prepared from the rolled stock.

References

1. I. I. Kornilov and R. S. Polyakova, "Investigation of the Heat Resistance of Alloys of Platinum with Rhodium, Iridium, Ruthenium, Chromium, and Aluminum by the Bent-Test Method," Doklady Inst. Met. im. A. A. Baykova, No. 5, 139–144 (1960); JPRS-4039.
2. H. Nishimura and H. Kimura, J. Japan Inst. Metals 23, 616 (1959).

14. PHYSICAL AND MECHANICAL METALLURGY OF REFRACTORY ALLOYS

P. Patriarca R. G. Donnelly

The purpose of this program is to provide a broad, base-technology evaluation of high-temperature alloys for use in high-performance nuclear reactors and isotopic heat sources for advanced space, terrestrial, and civilian power applications. Principal emphasis is placed on materials problems involving Ta-, Nb-, Mo-, and V-based alloys for systems that use alkali metals as thermodynamic working fluids and heat-transfer media.

Physical Metallurgy

H. Inouye

Development of Age-Hardening Refractory Alloys (C. T. Liu, P. G. Marden[1])

We are attempting to strengthen refractory alloys at high temperatures through the precipitation of stable phases. The binary systems Ta-Hf, Nb-Hf, Ta-Zr, and Nb-Zr are being studied because of their potential for precipitating a high volume of uniformly distributed fine particles. These systems have miscibility gaps at high temperature and eutectoid reactions at low temperature. We studied precipitation hardening associated with eutectoid transformations in Ta-Hf (eutectoid temperature = 1050°C) and in Nb-Zr (eutectoid temperature = 610°C).

Figure 14.1 shows the variation of hardness in Ta–50 wt % Hf during aging to 6×10^3 min at room temperature. The hardness initially drops rapidly at 1150°C and remains relatively constant up to 10^3 min (curve A). Within 5 min, aged specimens show a uniform dispersion of fine particles that gradually coarsen to platelike shapes with increasing aging time. The hardening caused by aging below the eutectoid temperature is tremendous: aging for 1 min at 850°C increases the diamond pyramid hardness from 460 to 675 DPH (curve C). The aging response at 850°C is typical; that is, within a short time (10 min) the hardness reaches its maximum value (about 790 DPH), and thereafter drops continuously.

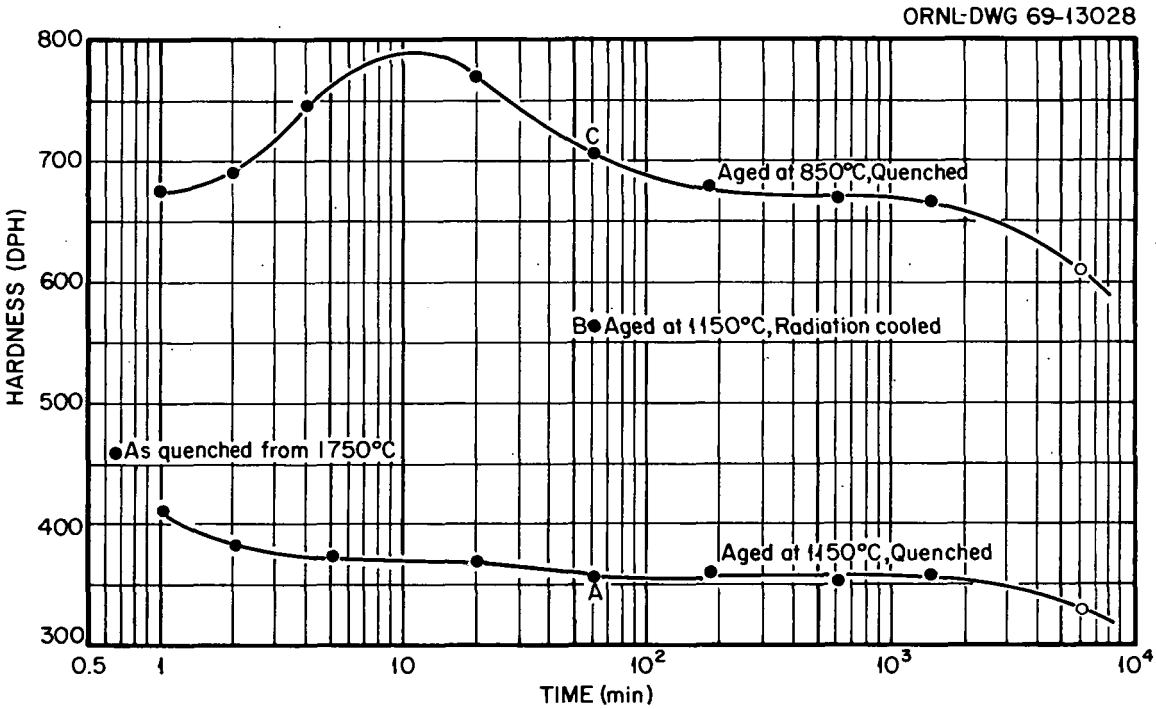

Fig. 14.1. Diamond Pyramid Hardness at Room Temperature Versus Aging Time for Ta–50 wt % Hf Alloy.

The data for curves A and C in Fig. 14.1 were obtained from specimens that were quenched after the aging treatment. In order to study the strengthening mechanism involved, we aged a specimen 1 hr at 1150°C but allowed it to cool by radiation. The hardness of this specimen was 565 DPH (datum point B in Fig. 14.1). Optical photomicrographs show no difference in precipitate morphology between this specimen and a quenched specimen similarly aged. We believe, therefore, that the first increase in hardness from 355 to 565 DPH during slow quenching is due to the the transformation of Hf-rich precipitate from the β phase to the α phase and that the second increase from 565 to 705 DPH is due to a high volume fraction of fine particles. Studies by x-ray or electron diffraction are needed to confirm this interpretation.

A similar study was also made for Nb–58 wt % Zr alloy. The hardness curves obtained from aging treatments at 500 and 750°C (Fig. 14.2) are similar to those obtained for Ta–50 wt % Hf alloy except that the hardening effect is much smaller in this case. A uniform distribution of precipitates is not observed in this alloy; instead, discontinuous precipitation occurs on the grain boundaries.

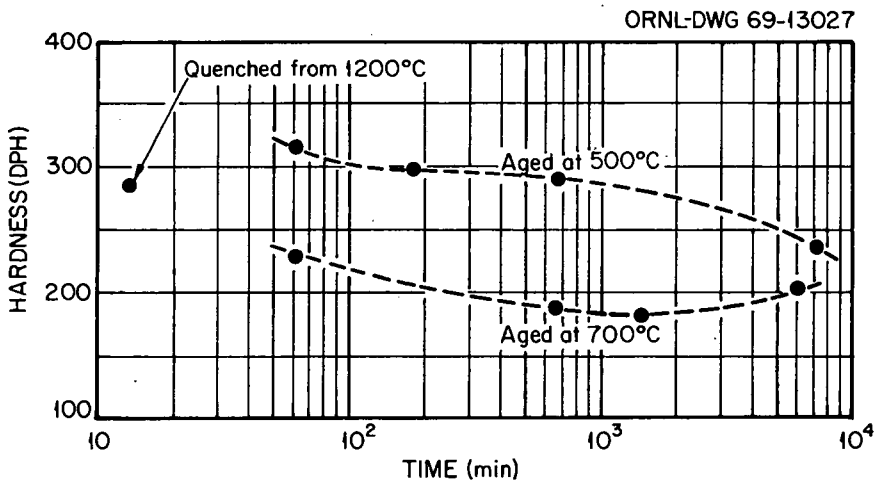

Fig. 14.2. Diamond Pyramid Hardness at Room Temperature Versus Aging Time for Nb–58 wt % Zr Alloy.

A detail examination by x-ray powder diffraction of Nb-Hf alloys after aging to 168 hr at 600 to 1450°C did not confirm the reported[2] existence of a miscibility gap associated with the body-centered cubic (bcc) β phase. All alloys showed either a simple bcc pattern or a two-phase bcc plus hexagonal close-packed (hcp) pattern. Streaking of the bcc diffraction lines, with a suggestion of a subsidiary maximum on the low-angle side was observed in alloys with high Hf contents after short aging times. However, the separation of the subsidiary maximum and the parent lines would correspond to a very small difference in Nb content. The hcp α phase has not been observed clearly in the Nb–40 wt % Hf alloy and has been found only in relatively limited amount in the Nb–53 wt % Hf alloy below about 1100°C.

These results are generally in accord with those of Taylor and Doyle,[3] who proposed a simple α, α + β, β sequence of phases at low temperature for increasing Nb content. A disturbing factor is that the a_o and c_o lattice parameters of the hcp phase, which are even larger than those for pure Hf, tend to increase with aging time and aging temperature, and the expected reduction in the volume of the unit cell as Nb substitutes for Hf has not been seen. This could imply that the alloys are slowly becoming contaminated with interstitial atoms as aging proceeds. Since all fine needles used for x-ray work could be more susceptible to contamination and would have a different quenching rate from

the more massive samples used for metallography, a number of the metallographic samples were examined on a diffractometer. In all cases, the phases observed were identical to those in the corresponding powder specimens.

In an attempt to avoid any ambiguity involved by quenching of aged alloys, we examined samples in a high-temperature Debye-Scherrer camera at temperatures up to 1000°C. In no case have two bcc patterns been detected, and the results are in good agreement with those observed in the studies at room temperature. Reaction with O_2 or diffusion of O_2 through the quartz capillary could have contaminated the samples, and, indeed, lines attributable to monoclinic hafnia were observed after prolonged aging at temperature. Chemical analysis suggested that the final content may be about 1000 ppm O. We have concluded, therefore, that if a miscibility gap does exist in Nb-Hf alloys, it must require very little O_2 or N_2 to close it.

Mechanical Properties of Commercial Refractory Alloys

H. E. McCoy, Jr.

Molybdenum-Based Alloys (R. L. Stephenson, K. Farrell)

We recently published a study of the effects of fabrication variables on the long-time creep properties of Mo alloys.[4] Fabrication variables were shown to affect the creep properties of TZM profoundly. We are now examining this alloy by transmission electron microscopy in the hope of discovering the mechanism responsible for the observed changes.

Representative electron photomicrographs of TZM before and after test at 980°C in each of four conditions are shown in Fig. 14.3. The most obvious difference in these microstructures is that they have widely varying grain sizes. The yield and creep strengths of various materials have been shown to correlate with grain diameter (ℓ) in various ways. In some materials, the creep strength at intermediate temperatures has been shown to correlate with ℓ^{-1}.

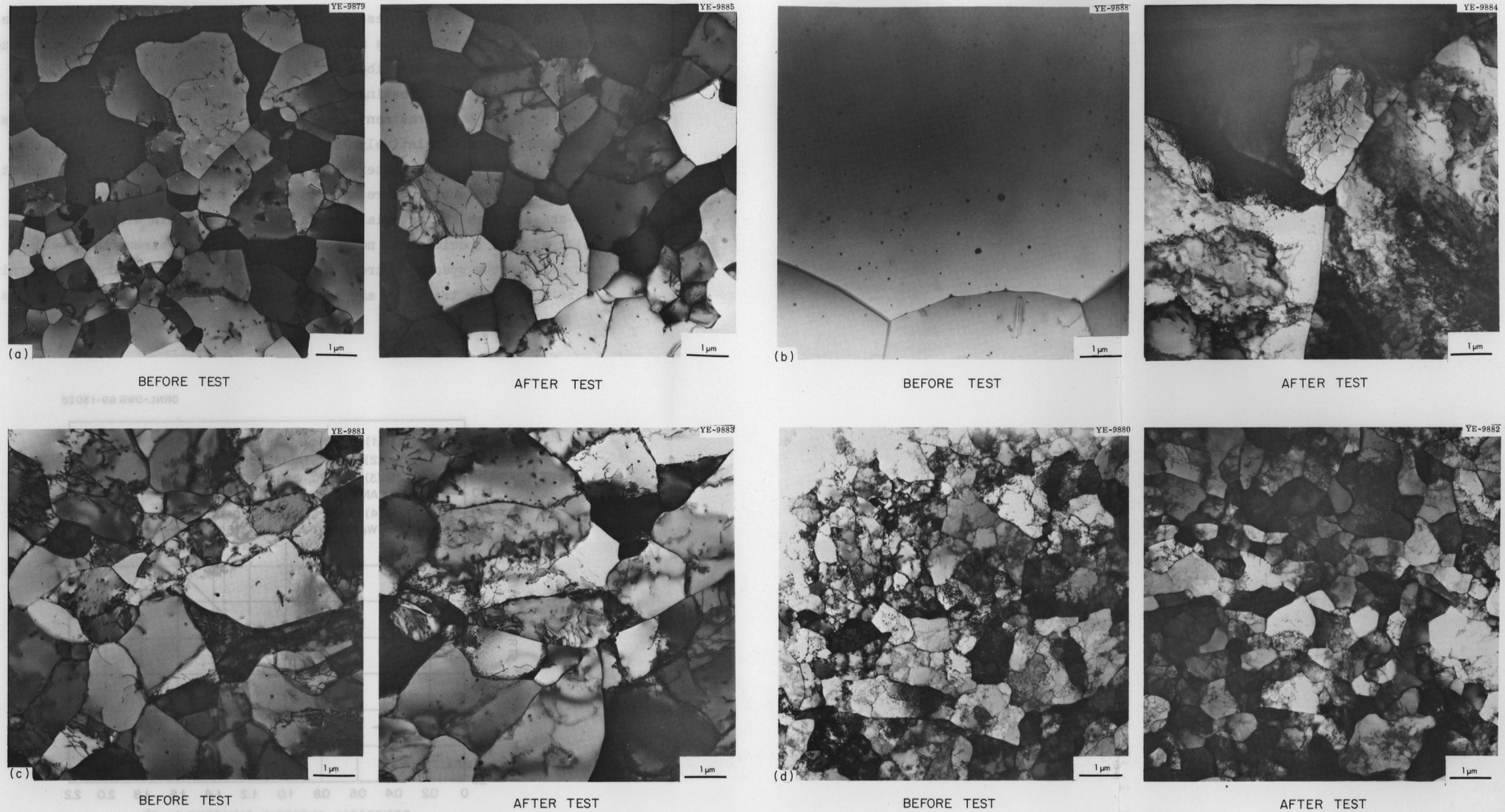

Fig. 14.3. Comparative Transmission Electron Photomicrographs of Alloy TZM in Four Conditions, Before and After Testing at 980°C. (a) Stress relieved at 1230°C, (b) recrystallized at 1540°C, (c) recrystallized at 1540°C, warm worked at 1040°C, and stress relieved at 1230°C, and (d) recrystallized at 2095°C and reextruded and warm worked at 1315°C.

In Fig. 14.4 the stress required to produce a secondary creep rate of 10^{-3} hr^{-1} is plotted as a function of the reciprocal of subgrain size. The heat treatments described for Fig. 14.4(a), (c), and (d) produced substructures before testing that were almost identical to those after testing. The heat treatment described for Fig. 14.4(b) produced recrystallization and a relatively large grain size before testing. In the course of testing this material, some low-angle boundaries were evident, but a distinct substructure was not formed; hence, it was not possible to characterize the material accurately by a subgrain size. The grain size of this specimen did not correlate with creep strength as well as it did for the specimens treated as above but moved toward a finer grain size during the test. We are continuing to examine the microstructures

ORNL-DWG 69-13025

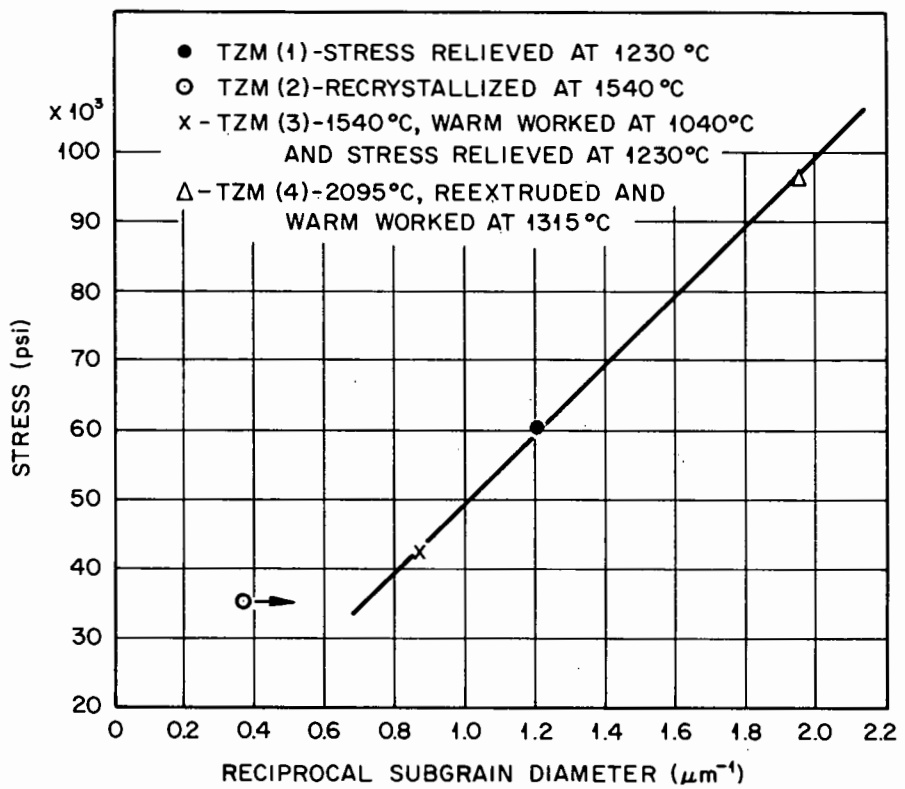

Fig. 14.4. Stress to Produce a Secondary Creep Rate of 10^{-3} hr^{-1} at 980°C Versus Reciprocal Subgrain Diameter.

of these alloys in search of additional evidence that substructure is important in controlling creep strength.

Welding and Brazing

G. M. Slaughter

Evaluation of the Weldability of Tantalum and Molybdenum Alloys
(D. A. Canonico, Nancy C. Cole, G. M. Goodwin, R. E. McDonald)

The efforts this quarter were directed toward the problem of joining Pt tubes to refractory-metal tubes for a specific application. The joint must be leakproof after long times in vacuum at elevated temperatures. Our task is to conceive methods for making highly reliable joints and to test them cursorily to determine the probability of their meeting the requirements outlined. We have conceived three primary methods for joining Pt tubing to Ta–10% W tubing.

Coextrusion (Duplex Tube). – Three different techniques of coextrusion will be investigated for making a transition joint: (1) Pt butted against Ta–10% W and coextruded within an Mo body, (2) Pt tubing placed within Ta–10% W tubing and coextruded to provide a duplex tube, and (3) a process similar to the first except that it may be necessary to provide a buffer material between the Pt and Ta–10% W.

Brazing. – Two techniques are being investigated: (1) conventional brazing with a filler metal (selection is based on melting point, flowability, and the vapor pressure of the individual elements) and (2) a braze-welding technique that employs an electron-beam welder. We refer to this process as braze welding because of the extreme difference in the melting points of the materials.

Swagelok. – This is a joint that obtains and maintains intimate contact mechanically.

Combinations or slight variations of these three techniques will also be investigated.

We obtained high-quality scrap Pt which we remelted and cast to provide the material from which the desired Pt components could be fabricated.

Our initial attempts to coextrude tubing were unsuccessful. We have found that a severe reaction occurs between the Mo body and Pt at the processing temperatures. We redesigned the capsule so that there is no intimate contact between the Mo and Pt and will rerun these experiments.

Brazing studies showed that a number of filler metals we thought applicable tend to erode the Pt or Ta–10% W. We formulated a number of new brazing alloys, and one (Pd–10% Ag) exhibited excellent wetting and flowing characteristics. Joints brazed with this alloy, although visually acceptable, did not pass the initial leak test. These brazes are being investigated metallographically.

The braze-weld studies (electron-beam process) have progressed satisfactorily. We designed a tongue-and-groove joint (Ta–10% W groove) and made joints in 1/8-in.-OD × 1/32-in.-ID tubes. Six specimens were produced; three passed the initial leak test, and two are being aged. This 50% acceptance rate seems low, but increasing the specimen size and automating the welding process should increase the yield.

Swagelok joints were fabricated. The externals in all instances are Ta–10% W. The internals (ferrules) have been of both Ta–10% W and Pt. The initial studies were conducted with the Ta–10% W ferrules. Six specimens were prepared; three marginally passed the initial leak test, but their leak rates were unacceptable after aging. Specimens with Pt ferrules all had leak rates below the allowable minimum value. These specimens are now being aged.

We have purchased a number of pressure-bonded joints of Pt and Ta–10% W. These have also satisfactorily passed the initial leak test and are now being aged.

Physical Properties

D. L. McElroy

Measurements of the Physical Properties of Tantalum (R. K. Williams, J. P. Moore)

Electrical resistivity data to 2600°K were reported previously for a Ta specimen.[5] Further measurements of this sample at 80 to 400°K are

Table 14.1. Smoothed Values for the Thermal Conductivity, Electrical Resistivity, and Absolute Seebeck Coefficient of an Electron-Beam Melted Tantalum Specimen

Temperature (°K)	Electrical Resistivity (μΩcm)	Thermal Conductivity (w cm^{-1} deg^{-1})	Wiedemann-Franz Ratio (volume^2/deg^2)	Absolute Seebeck Coefficient (μv/deg)
80	2.562	0.5875	1.881	+0.59
100	3.625	0.5841	2.117	+0.22
120	4.664	0.5818	2.261	−0.15
140	5.693	0.5801	2.359	−0.50
160	6.703	0.5788	2.425	−0.84
180	7.667	0.5779	2.461	−1.19
200	8.644	0.5775	2.496	−1.51
220	9.625	0.5774	2.526	−1.83
240	10.580	0.5774	2.545	−2.17
260	11.521	0.5776	2.559	−2.50
280	12.455	0.5780	2.571	−2.82
300	13.390	0.5786	2.582	−3.11
320	14.316	0.5792	2.591	−3.38
340	15.246	0.5797	2.599	−3.58
360	16.170	0.5801	2.606	−3.70
380	17.070	0.5805	2.608	−3.72
400	17.979	0.5809	2.611	−3.72

included in Table 14.1 as smoothed data of thermal conductivity, electrical resistivity, absolute Seebeck coefficient, and the measured Wiedemann-Franz ratio. The thermal conductivity was found to be nearly independent of temperature, but the Wiedemann-Franz ratio appears to increase throughout the whole range of measurements. The latter change, which amounts to only 1% between 300 and 400°K gives a hint that the electronic Lorenz function of Ta may behave like that of Pt (ref. 6). Despite this possibility, we have applied a curve-fitting technique[7] to get an estimate of the relative sizes of the electronic and phonon contributions to the thermal conductivity. These calculations indicate that phonons carry about 10% of the heat near room temperature and that the electronic Lorenz function does not significantly exceed the Sommerfeld limit, L_o, at temperatures below 400°K. In contrast to these results, we believe that the electronic Lorenz function of the neighboring element, W, exceeds the Sommerfeld value at about 200°K and

remains constant at about 1.15 L_o between 300 and 1300°K. Also, although the relative contributions from phonon transport are roughly equal in the two metals, the magnitudes of the two contributions are different, since Ta has a considerably smaller phonon conductivity.

References

1. On loan from Atomic Energy Research Establishment, Harwell, England.
2. M. A. Tylkina, I. A. Tsyganna, and E. M. Savitskin, Russ. Inorg. Chem. 99, 893 (1964).
3. A. Taylor and N. J. Doyle, J. Less-Common Metals 7, 37–53 (1964).
4. R. L. Stephenson, Trans. Met. Soc. AIME 245(5), 997–1001 (1969).
5. R. K. Williams, Fuels and Materials Development Program Quart. Progr. Rept. June 30, 1969, ORNL-4440, p. 235.
6. D. R. Flynn and M. E. O'Hagan, J. Res. Nat. Bur. Std. C 71(4), 255–284 (1967).
7. R. K. Williams and W. Fulkerson, pp. 389–456 in Thermal Conductivity, Proc. 8th Conf., ed. by C. Y. Ho and R. E. Taylor, Plenum Press, New York, 1969.

15. TUNGSTEN METALLURGY

P. Patriarca A. C. Schaffhauser

The object of this program is to develop economical methods for producing high-quality W and W-alloy tubing with good creep-rupture properties at high temperatures, good microstructural stability, good ductility at low temperatures, and good weldability. We fabricate tubing both by modification of conventional techniques based on extrusion, tube reduction, and warm drawing and by direct chemical vapor deposition (CVD) through the H_2 reduction of heavy-metal halides. Our program includes complete physical and metallurgical evaluation of both fabrication processes.

Primary and Secondary Working of Tungsten Alloys

A. C. Schaffhauser

Extrusion of Tungsten Tubing (R. E. McDonald)

We completed our initial investigation of the structure and mechanical properties of extruded powder-metallurgy W tubing. The results from the first series of experiments for recrystallized primary extrusions duplex extruded at 1750, 1650, 1450, and 1250°C were described in previous quarterly reports. Tensile tests of rings cut from these extrusions showed significantly greater ductility for the lower temperature extrusions that had an elongated grain structure. A second series of duplex extrusions was made at 1760, 1450, and 1150°C with material that had a wrought starting microstructure from the primary extrusion. A recrystallized starting microstructure was also extruded at 1150°C for comparison. The microstructures of these extrusions (Figs. 15.1 and 15.2) show that the duplex extrusion at 1760°C recrystallized during preheat and that the grains grew larger during extrusion. The additional heat produced by deformation could have increased the temperature of the billet to 1900°C. The billet extruded at 1450°C also recrystallized during preheat, but no further change was noted in the extruded structure.

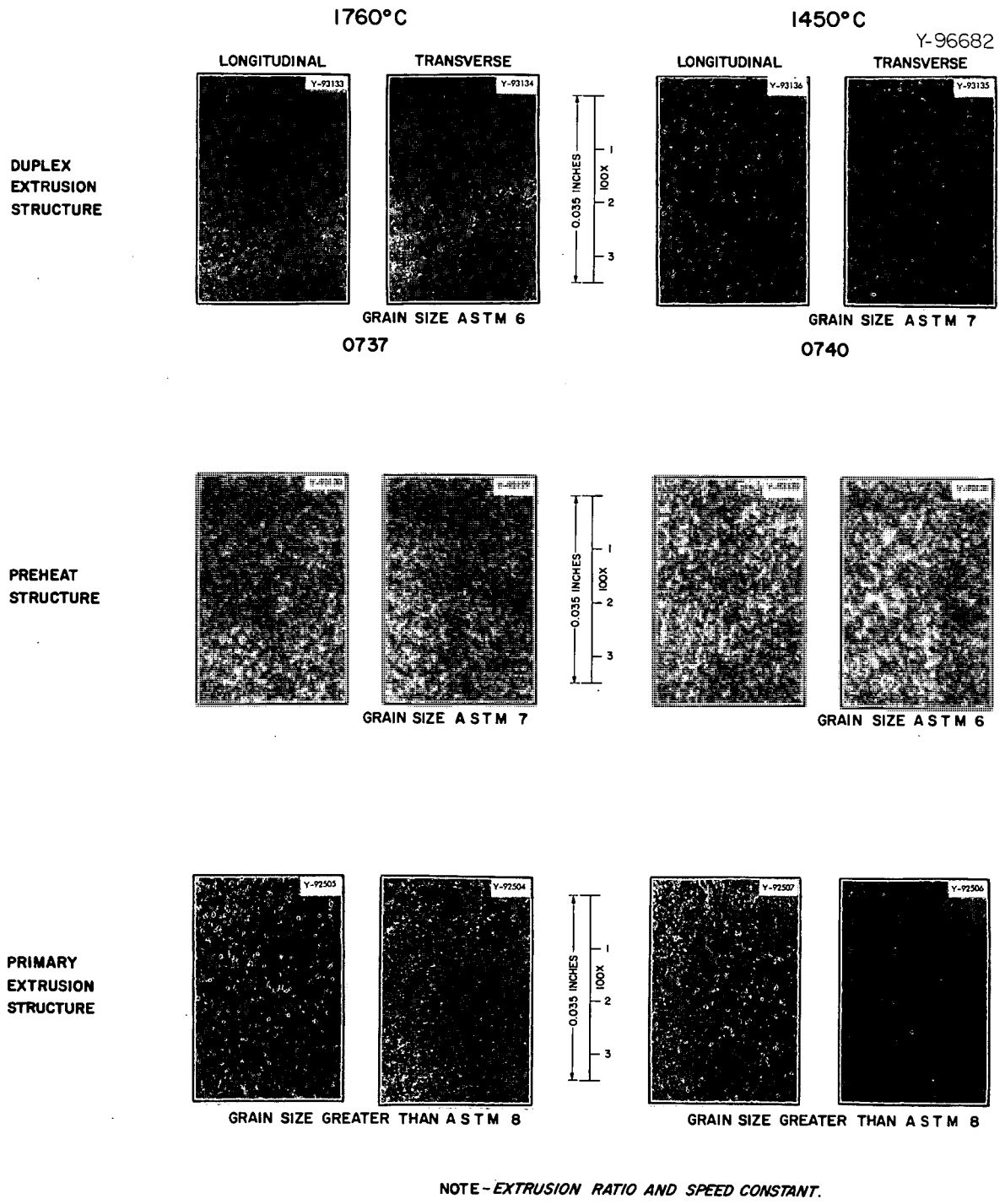

Fig. 15.1. Microstructures of Starting Primary Extrusion of Powder-Metallurgy Tungsten after Preheating to 1760 and 1450°C and after Duplex Extrusion.

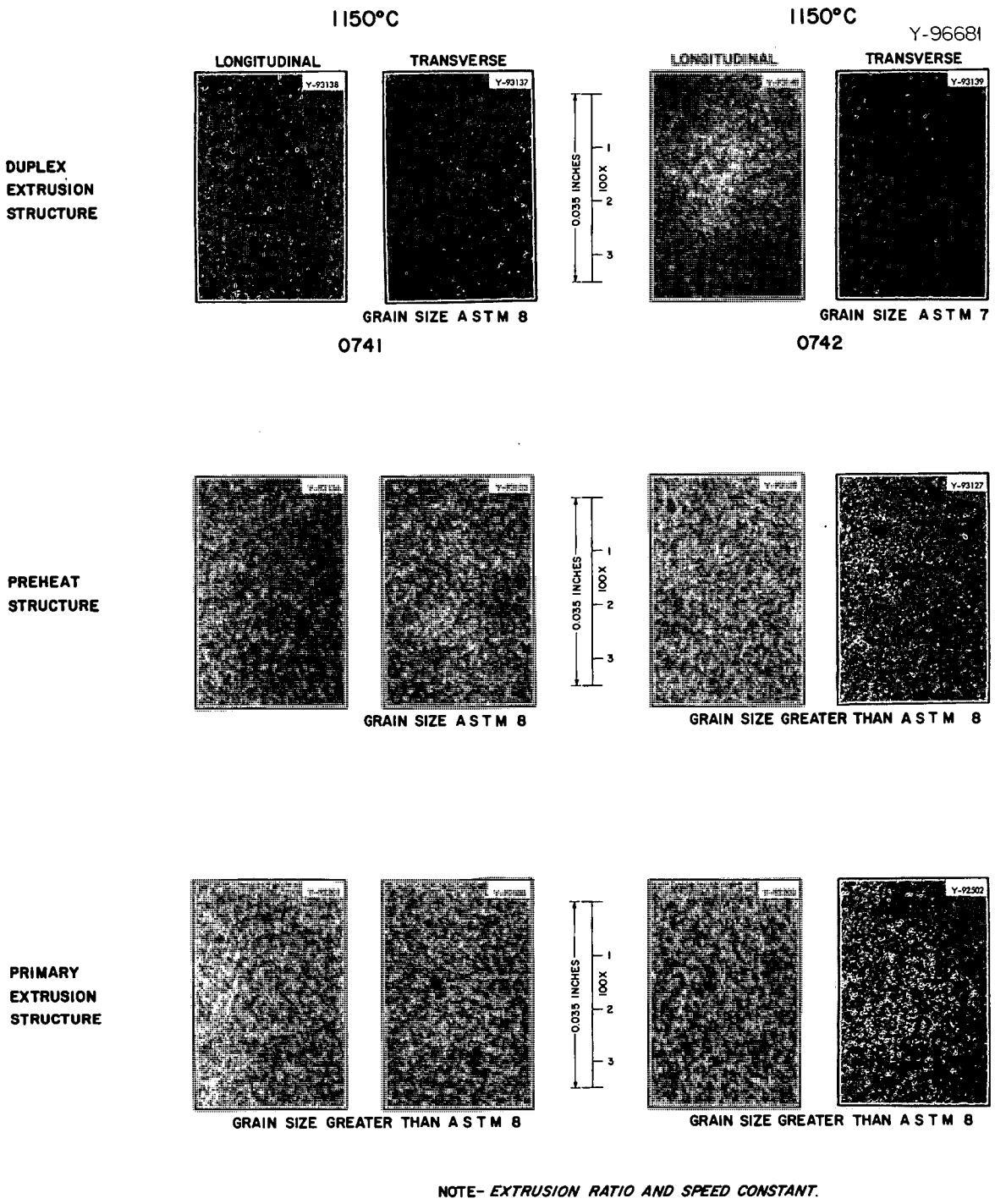

Fig. 15.2. Microstructures of Starting Primary Extrusion of Powder-Metallurgy Tungsten after Preheating to 1150°C and after Duplex Extrusion.

The wrought structure did not change during the preheat at 1150°C but did partially recrystallize during extrusion. The recrystallized structure was stable during the preheat at 1150°C, and the extruded structure shows many elongated grains.

In summary, at extrusion temperatures of 1450°C and higher, wrought structures recrystallize during preheat while recrystallized structures are stable for the short preheat times. The wrought structure and the recrystallized structure are both stable during preheat at 1150°C, but the increase of 150 to 200°C during the extrusion process is enough to recrystallize the starting wrought structure.

Similar extrusion experiments are under way for arc-melted W alloys. An 8-in.-diam ingot of unalloyed arc-melted W was procured from the Specialty Metals Division of American Metal Climax, Inc. This ingot was successfully extruded at 1775°C under our supervision at the Fansteel Metals Center to 3.25 in. in diameter. Billets for the extrusion of tube shells are being machined from the primary extrusion. Ingots of arc-melted W–5% Re from Wah Chang Corporation, Albany, Oregon, and W–4 at. % Re–0.35 at. % Hf–0.35 at. % C from National Aeronautics and Space Administration-Lewis Research Center are also being prepared for extrusion to tube shells.

Chemical Vapor Deposition of Tungsten Alloys

J. I. Federer

Chemical Vapor Deposition of W–5% Re Sheet and Tubing (J. I. Federer)

We continued deposition of W–5% Re alloy sheet stock for evaluation of mechanical properties. Alloy deposits are being prepared by H_2 reduction of WF_6 and ReF_6 on Mo–0.5% Ti substrates heated by resistance. Attempts to minimize nodules and grown-in porosity by pulsing the flow of WF_6 and ReF_6 were reported previously.[1] In one of those experiments the WF_6 and ReF_6 flows were pulsed 15 min on and 2 min off, and the direction of the gas flow was reversed every 30 min. In a recent experiment, under the same conditions except that the WF_6 and ReF_6 flows were

pulsed 2 min on and 2 min off, the deposit contained 6.2 ± 0.2% Re over about 83% of the 14 1/2-in. length and about 5.8% Re over the remainder.

The pulse technique was based upon the premise that new grains would nucleate each time the WF_6 and ReF_6 flows were pulsed. If so, the deposition process would remain continually in the early stage, which is characterized by a very fine-grained structure. Nodule formation would be minimized because nodules usually form in the columnar grains that grow from the initial fine-grained layer. However, both deposits prepared by pulsing and reversing gas flows contained numerous nodules. The microstructures of these deposits show that pulsing the WF_6 and ReF_6 flows does not cause complete nucleation of new grains.

The microstructure of a sample from the deposit prepared by pulsing the WF_6 and ReF_6 flows 15 min on and 2 min off is shown in Fig. 15.3. The layers in the microstructure correspond to the periodic reversals of gas flow, while some of the fine structure within the grains is apparently due to pulsing. Since many grains extend over several layers, there is frequently enough thickness for the nucleation of nodules.

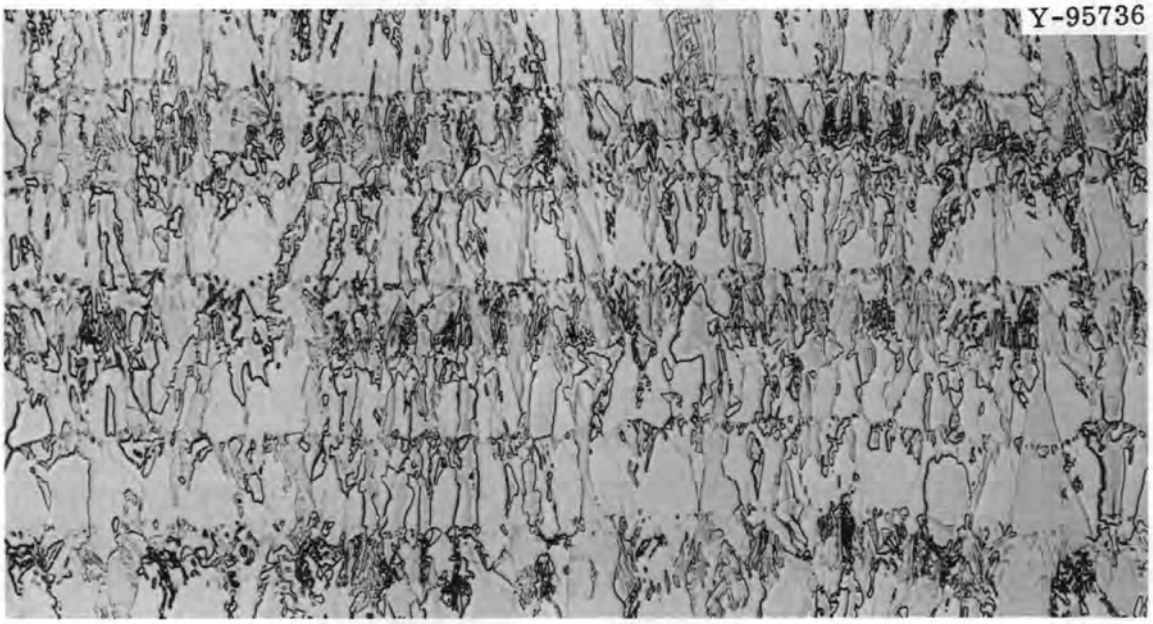

Fig. 15.3. Deposit of W-3.4% Re Prepared by Pulsing and Reversing Gas Flows. WF_6 and ReF_6 flows pulsed 15 min on and 2 min off. Etchant: 1 part NH_4OH, 1 part H_2O_2. 200×.

Figure 15.4 shows the microstructure of a sample from the deposit prepared by pulsing the WF_6 and ReF_6 flows 2 min on and 2 min off. This treatment produced much fine structure within the grains, but some grains appear to extend over a distance of several mils. The deposits also contained a small amount of grown-in porosity, mainly along grain interfaces. A typical example is shown in Fig. 15.5.

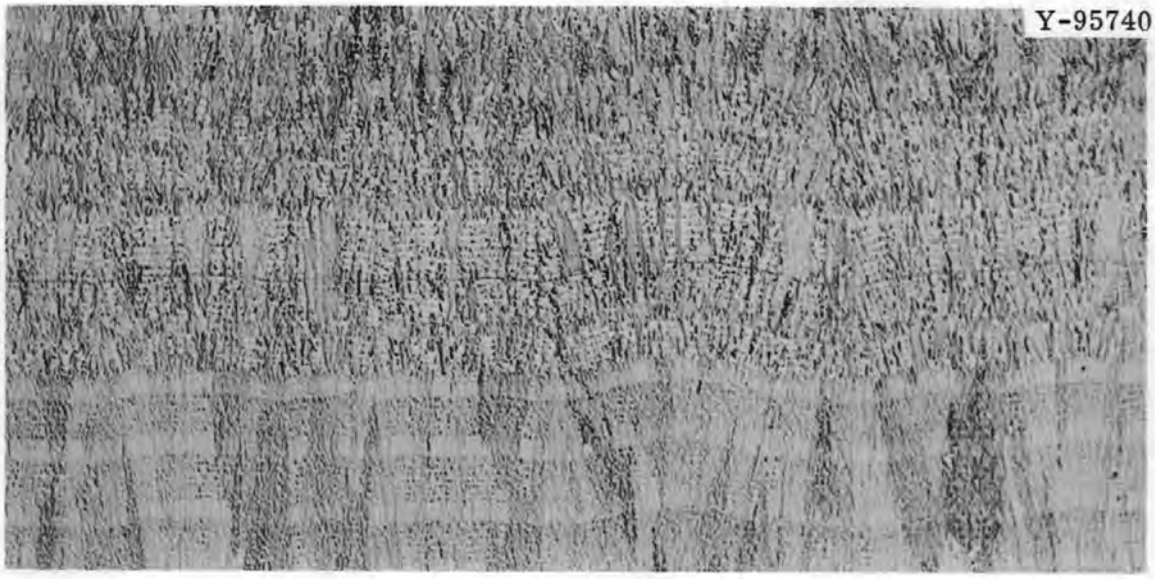

Fig. 15.4. Deposit of W–5.8% Re Prepared by Pulsing and Reversing Gas Flows. WF_6 and ReF_6 flows pulsed 2 min on and 2 min off. Etchant: 1 part NH_4OH, 1 part H_2O_2. 200×.

We are also depositing tubing in the apparatus used for preparing sheet stock. Potential applications for W tubing are as cladding for fuel elements, for containment of liquid metals, and in thermionic converters. We are depositing tubing on 18-in.-long × 3/4-in.-OD stainless steel substrates heated by electrically insulated internal resistance heaters. If the substrate were also the heater, as in the case of sheet substrates, temperature gradients would produce thickness gradients in the deposits. The use of a heater tube inside the substrate tube avoids this difficulty.

Nominal W–5% Re tubes were deposited at 750°C, 5 torr, and a H_2:(WF_6+ReF_6) gas ratio of 15 with unidirectional gas flow. These

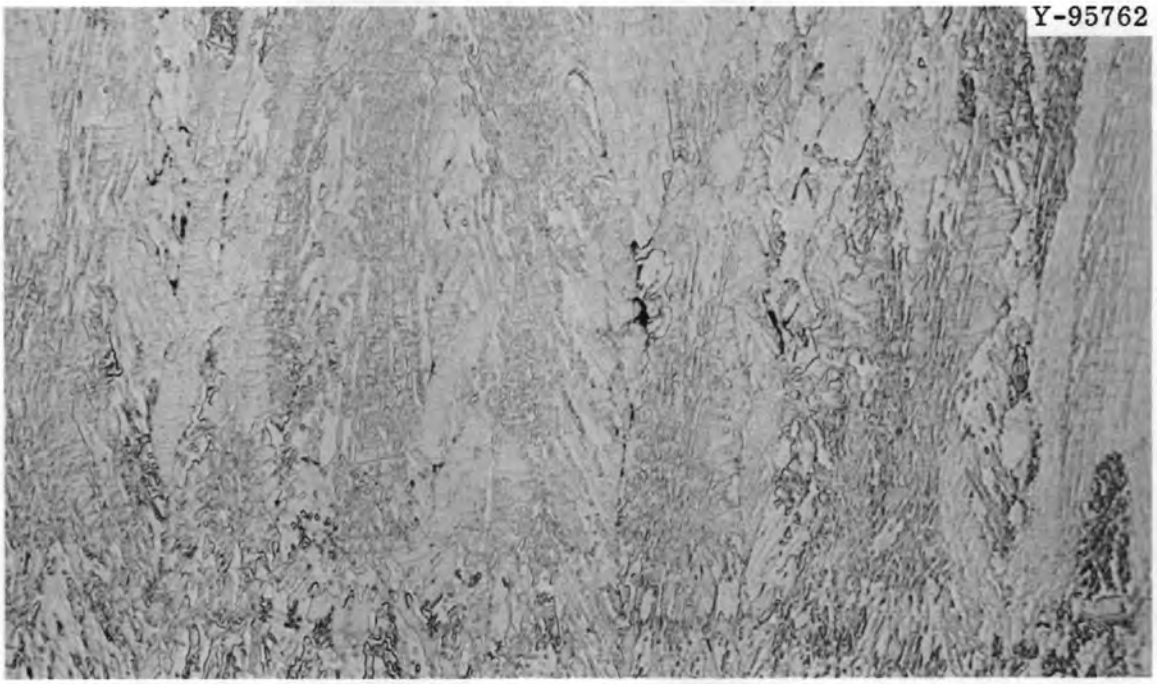

Fig. 15.5. Deposit of W–5.8% Re Showing Grown-In Porosity. Etchant: 1 part NH_4OH, 1 part H_2O_2. 200×.

deposits were thinner near the gas outlet due to depletion of the gas. The surface of the deposits was mostly nodular. We believe the "seed" around which the nodules formed was from two possible sources: (1) solid foreign particles in the feed gas and (2) solid intermediate fluoride compounds, such as WF and ReF_3. A 5-μm filter was installed in the gas feed line, but subsequent deposits still contained nodules. The possibility of an intermediate fluoride compound persisting long enough on the surface of the deposit to serve as a nucleation site for nodules would be lessened by high temperature, high H_2:(WF_6+ReF_6) ratio, and low pressure. Since temperature is fixed at about 750°C by composition[2] and since a pressure of about 5 torr is as low as can be obtained with available equipment, we prepared a deposit with a H_2:(WF_6+ReF_6) ratio of 100. The larger flow of H_2 unavoidably increased the pressure in the system to 20 torr. This deposit also contained numerous nodules. Thus, neither action taken to minimize nodules was successful.

Chemical Vapor Deposition of Vanadium (J. I. Federer)

We completed a feasibility study of chemical vapor deposition of V. Vanadium was deposited by H_2 reduction of VCl_4 and VF_5. The temperature of 900°C or higher required to reduce these compounds is a serious limitation of the process.

We prepared VCl_4 by chlorinating V metal with Cl_2 at 400°C. The VCl_4 then passed through a transfer line heated to 400°C to a reaction chamber heated by a furnace. The reaction chamber contained a 3/4-in.-OD tubular liner of steel or stainless steel that served as a deposition substrate.

The conditions and some results of deposition experiments using VCl_4 are shown in Table 15.1. In each experiment, V scrap was chlorinated at 400°C in a stream of Cl_2 metered at 100 cm^3/min. This flow rate was sufficient to chlorinate V to VCl_4 at a maximum rate of 6.8 g V/hr; the average rate was 6.1 g V/hr.

Table 15.1. Conditions[a] and Results of Vanadium Chlorination and Deposition Experiments

Experiment Number	Time (hr)	Temperature (°C)	Vanadium Chlorinated at 400°C (g)	Vanadium Deposited (g)	Efficiency of Deposition (%)
5	1	1100	8.8	b	
6	1	1200	7.9	3.6	46
7	1	1200	6.8	4.0	59
8	4.5	1200	27.1	c	
9	3	1200	21.2	c	
10	3	1200	5.9	c	
11	2.5	1200	18.7	10.3	55
16	2.5	1100	16.3	7.3	45
17	2.5	1000	13.6	c	
18	3	900	18.0	1.5	8

[a]Flow rates: H_2, 1500 cm^3/min; Cl_2, 100 cm^3/min. Pressure: 5 torr.

[b]Not determined.

[c]Chlorine corrosion caused air leak in the deposition chamber; therefore, the amount of V deposited could not be determined reliably.

We determined the efficiency of deposition from the fraction of V chlorinated that was reduced to metal. The efficiency ranged from 45 to 59% at 1100 and 1200°C, but decreased to only 8% at 900°C. In several experiments (8, 9, 10, and 17) the Cl_2 that passed unreacted through the chlorinator after most of the available V had been converted to VCl_4 reacted with the deposition chamber and caused an air leak. The amount of V deposited could not be determined reliably in these cases. In experiments 10 and 17, part of the Cl_2 bypassed the V in the chlorinator and flowed directly into the deposition chamber.

Metal deposits were accompanied in every case by deposits of chloride compounds on cool parts of the substrate. The amount of these compounds relative to the amount of metal decreased with increasing deposition temperature. In some cases, the cross section of the tubular substrate was filled by a yellow-green compound, probably consisting of VCl_2 and one or more oxychlorides. Some VCl_3, a purple-red compound, formed in each experiment. Thermodynamic data, as shown in Table 15.2, indicate that the formation of lower chlorides during H_2 reduction of VCl_4 is quite likely. At temperatures up to 1000°K, only VCl_2 and VCl_3 would form. At 900°K, VCl_3 decomposes to VCl_2 and VCl_4. The data show that the tendency to form VCl_2 is still strong at 1500°K, and that the tendency to form V increases with increasing temperature. Experimental results agree qualitatively with the thermodynamic data.

Table 15.2. Thermodynamic Data for the Reaction of VCl_4 with H_2

Reaction	Free Energy of Reaction at Indicated Temperatures (kcal/mole of Cl)		
	900°K	1000°K	1500°K
$VCl_4 + 1/2\ H_2 \rightarrow VCl_3 + HCl$	−9[a]		
$VCl_4 + H_2 \rightarrow VCl_2 + 2HCl$		−18	−16
$VCl_4 + 2H_2 \rightarrow V + 4HCl$		+11	−4

[a]Above 900°K, VCl_3 decomposes to VCl_2 and VCl_4.

We also deposited V from VF_5. The vapor pressure of VF_5, which was prepared by fluorination of V powder with F_2 at about 400°C, is high enough that it can be transferred at room temperature. Hydrogen reduction of VF_5 at 900°C produced only VF_3, a green compound. At 1000°C, about 80% of the V transferred as VF_5 was reduced to metal, while the other 20% was only partially reduced and was present as VF_3. At 1200°C, the efficiency of reduction was 100%. These experimental results are also in qualitative agreement with thermodynamic data.

Chemical analyses for several V deposits are shown in Table 15.3. These data demonstrate the high affinity of V for interstitial impurities. In two experiments, we added $TiCl_4$ to the reacting gases in an effort to deposit a V-Ti alloy; only a very small amount of Ti (< 0.5%) was deposited, however.

In summary, V can be deposited by H_2 reduction of VCl_4 and VF_5, but the process is limited to temperatures of about 1000°C and higher because stable intermediate halides form at lower temperatures. The deposits that we analyzed contained about 0.5 to 1.5% total impurities; however, no specific effort was made to reduce the impurity content. This study is complete, and a final report is being prepared.

Metallurgical Properties of Tungsten Alloys

H. Inouye

Effect of Low-Pressure Oxygen on the Creep Properties of Tungsten (H. Inouye)

The creep properties of refractory alloys in a nuclear device that operates at high temperature could be significantly different from the properties measured in the laboratory under the antiseptic conditions of a high vacuum because of their interaction with environmental impurities such as O_2, C, and N. These interstitial impurities originate from other structural components, the heat-transfer media, and the decomposition of ceramic nuclear fuels. This task is concerned with the determination of the creep behavior of W and its alloys in low-pressure O_2 that simulates the effect of interaction between cladding and oxide fuel in a thermionic device. For our initial studies, we are using 0.040-in.-diam

Table 15.3. Results of Chemical Analysis of Vanadium Deposits

Experiment Number	Source Compound	Deposition Temperature (°C)	Composition of Deposit, %						
			C	H	N	O	Cl	F	Ti
11	VCl_4	1200	0.026	0.0010	0.11	1.01	0.025		
12	VF_5	1200	0.095	0.0020	0.082	0.88		0.015	
16	VCl_4	1100	0.17	0.0013	0.14	0.25	< 0.005		
Ti-1	VCl_4, $TiCl_4$	1100	0.17	0.0092	0.13	0.28	0.020		< 0.5
Ti-2	VCl_4, $TiCl_4$	1100							< 0.5

W wire, produced from powder-metallurgy material, and an apparatus described previously.[3]

The interaction of refractory metals with O_2 at thermionic temperatures causes the metal to sublime as volatile oxides. The rate of sublimation is proportional to the O_2 pressure, P_{O_2}, and the variation of the rate with temperature at a given pressure shows a maximum that is characteristic of the metal, as shown in Fig. 15.6. The temperature and pressure at which the maximum rate of sublimation occurs vary according to an expression of the form P_{O_2} = constant $\exp(-\Delta H/RT)$, where ΔH is the heat of sublimation.

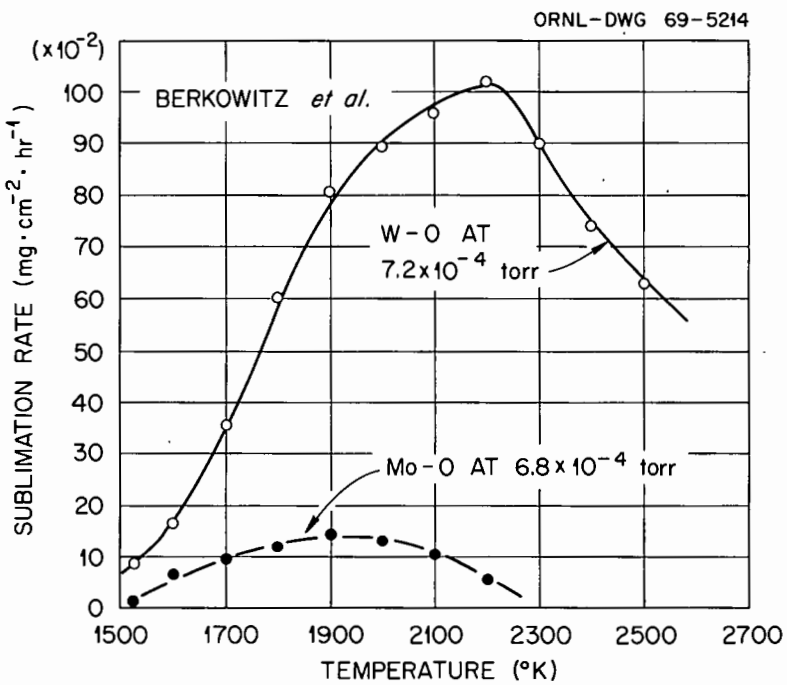

Fig. 15.6. Sublimation Rates of Tungsten and Molybdenum in 10^{-4} torr of Oxygen as a Function of Temperature. [Ref. J. B. Berkowitz-Mattuck et al., J. Chem. Phys. 39(10), 2722–2730 (1963).]

Figure 15.7 shows that at 2000°C the creep rate of W in 7×10^{-5} torr of O_2 is about twice that at a base pressure of 1.3×10^{-7} torr. Because the increase in the rate coincides with the increase in the O_2 pressure, it is clear that the O_2 environment was responsible for the rate change. The maximum rate at which W sublimes in 7×10^{-5} torr of O_2 occurs at

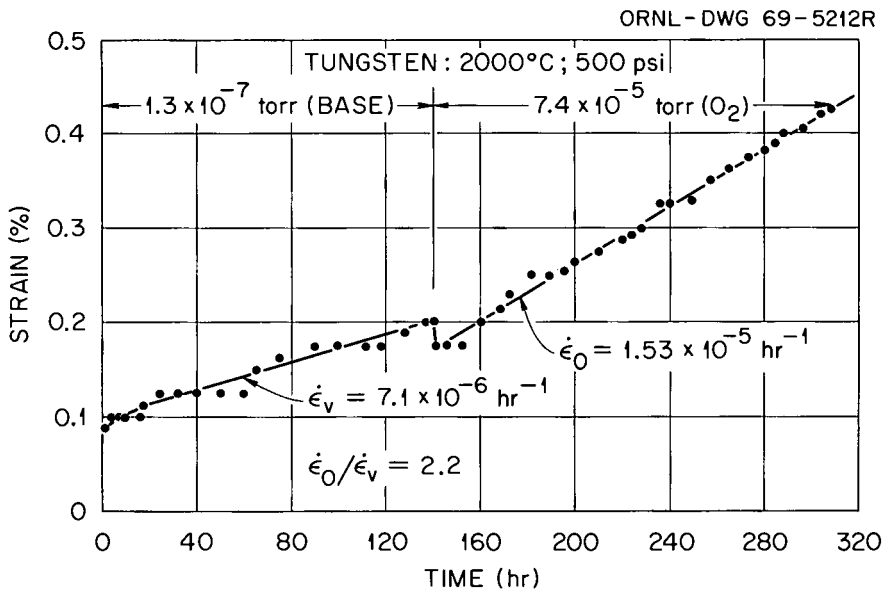

Fig. 15.7. Effect of 10^{-5} torr of Oxygen on the Creep Rate of Tungsten at 2000°C and 500 psi. Creep rate in oxygen = $\dot{\epsilon}_o$; creep rate in vacuum = $\dot{\epsilon}_v$.

about 1650°C. Therefore, if sublimation is a factor in weakening the material, the maximum degradation of the creep strength, expressed as the quotient of the creep rate in O_2 divided by the creep rate in vacuum, $\dot{\epsilon}_o/\dot{\epsilon}_v$, would also be expected to occur at this temperature. The values shown in Table 15.4 confirm the expected correlation.

Table 15.4. Effect of Temperature and 7×10^{-5} torr of Oxygen on the Creep Rate of Tungsten

Temperature (°C)	Stress (psi)	$\dot{\epsilon}_o$(a) (hr^{-1})	$\dot{\epsilon}_v$(b) (hr^{-1})	$\dot{\epsilon}_o/\dot{\epsilon}_v$ (a,b)
		$\times 10^{-5}$	$\times 10^{-5}$	
1500	4000	3.5	2.4	1.5
1650	2000	10.1	2.3	4.4
2000	500	1.5	0.7	2.2

(a) $\dot{\epsilon}_o$ = creep rate in O_2.
(b) $\dot{\epsilon}_v$ = creep rate in vacuum (base pressure).

Figure 15.8 shows the creep curve for W when the testing environment is cycled between the base pressure and about 1×10^{-5} torr of O_2. The reversibility of the creep rates from a low rate at the base pressure to a high rate in O_2 suggests that sublimation is only one of the factors that influence the creep behavior. Tentatively, we attribute this cyclic behavior either to O dissolving in the W or to O_2 increasing the rate at which creep cavities grow in W.

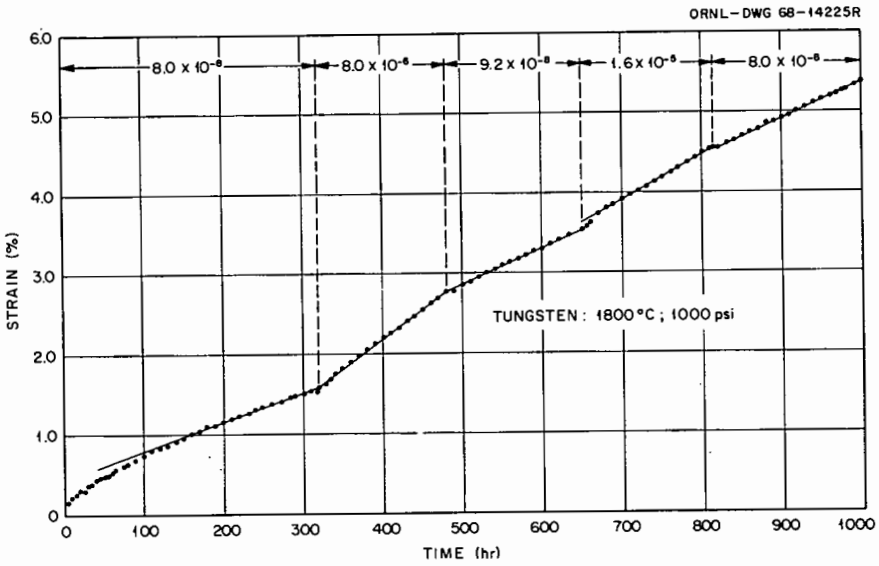

Fig. 15.8. Effect of Pressure Cycles Between Base Pressure and about 10^{-5} torr of Oxygen on the Creep Behavior of Tungsten at 1800°C and 1000 psi.

Long-Time Creep Properties of Tungsten Alloys

H. E. McCoy, Jr. J. O. Stiegler

Comparative Creep-Rupture Properties of W–25% Re Consolidated by Arc-Melting and Powder-Metallurgy Techniques (R. L. Stephenson)

We completed our comparison of the creep-rupture properties of arc-melted and powder-metallurgy W–25% Re sheet. A topical report was issued;[4] the abstract is given below:

The creep-rupture properties of W–25% Re materials consolidated by arc melting (AM) and powder metallurgy (PM) techniques have been compared at 1650 and 2200°C for rupture times up to 1000 hr. At comparable stresses, PM material has a shorter rupture life and a lower rupture ductility than AM material. On the basis of secondary creep rate, PM material is weaker than AM material at 1650°C but stronger at 2200°C. Optical and electron metallography showed that voids form at grain boundaries in both materials. In the PM material, grain boundaries appear to be immobile, and massive growth of voids initiates fracture with very little deformation. In the AM material, grain boundaries appear to be mobile, and fracture seems to be forestalled by their ability to move. The relative creep rates can be explained on the basis of void growth and grain size.

Long-Time Creep and Stress-Rupture Properties of Tungsten-Rhenium Alloys (R. L. Stephenson)

We are continuing our evaluation of the creep and stress-rupture properties of arc-melted W, W–5% Re, W–26% Re, and W–25 at. % Re–30 at. % Mo. Our recent data for time to 1, 2, and 5% strain and rupture for W–26% Re at 1650°C are shown as a function of stress in Fig. 15.9. The stress-rupture data for this alloy at 1400, 1650, 2000, and 2200°C are shown in Fig. 15.10 along with computed curves for the isotherms obtained from the Larson-Miller constant.

Interrupted Creep Tests on Tungsten (J. O. Stiegler, R. L. Stephenson)

We began an examination of mechanisms of creep deformation and fracture by studying the progressive evolution of microstructural features during creep tests. Specimens of a very pure grade of powder-metallurgy W are being tested at 1600°C at stresses of 4500, 6000, 8000, 10,000, and 12,000 psi. These samples are being examined after they have achieved 2, 4, 6, 8, and 10% strain. This particular material was chosen because at room temperature it fractures easily in a brittle manner along grain boundaries, thereby exposing creep cavities for direct examination by conventional electron fractography. Transmission electron microscopy is also being used to study dislocation configurations, particularly the interactions of dislocations and grain boundaries. We believe that information from this program will also be of use in

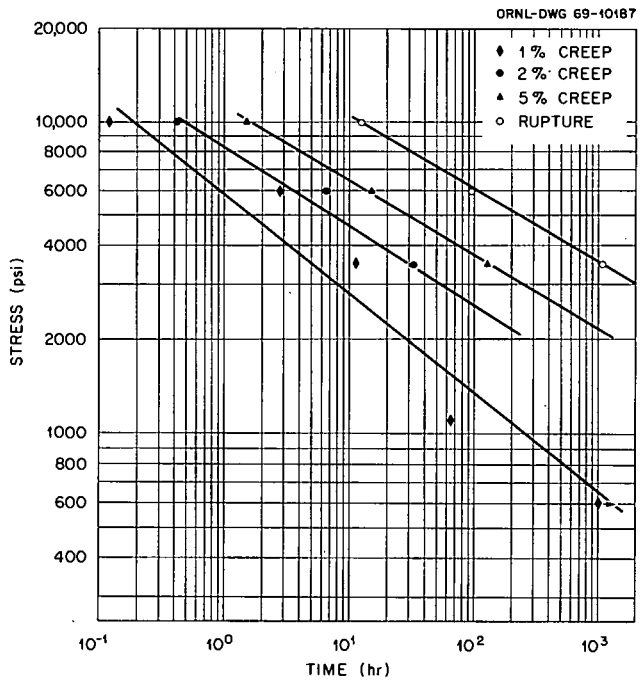

Fig. 15.9. Creep and Stress-Rupture Properties of Arc-Melted W–26% Re at 1650°C.

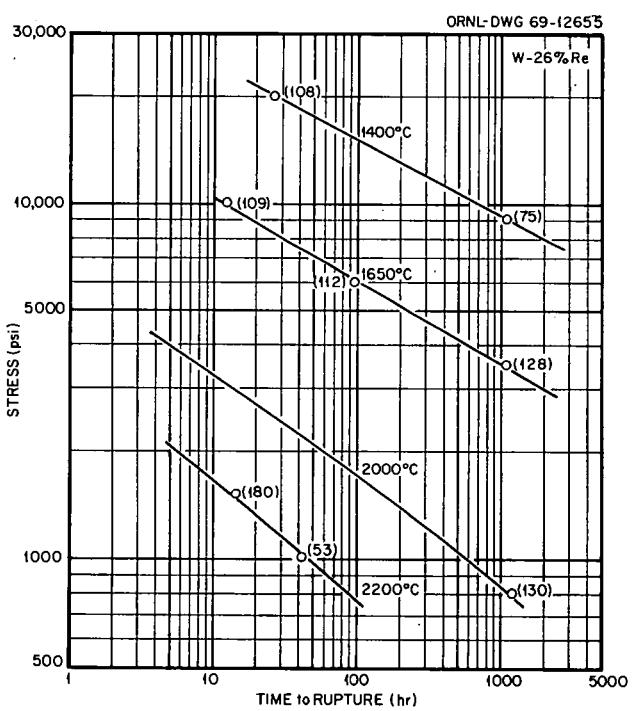

Fig. 15.10. Stress-Rupture Data for Arc-Melted W–26% Re Compared with Isotherms Derived from Larson-Miller Constants.

understanding and interpreting the processes of deformation at high temperatures in other refractory metals.

The creep-rupture properties of this material agree well with those determined by McCoy[5] for high-purity powder-metallurgy W sheet tested at 1650°C. Considerable necking and ductility are observed in tests at 12,000 psi, but at lower stresses failure occurs at lower ductilities by the linking and growth of cracks at grain boundaries. The cracks have the typical wedge appearance at high stresses and are more isolated and rounded at lower stresses. There is, however, no clear line of demarcation between the two types of cracks, at least under examination by optical microscopy.

Fractographic examination of grain boundaries in annealed specimens revealed gas bubbles attached to particles on nearly all interfaces between two grains. Most, but not all, junctions between three grains or four grains are free of these bubbles. The boundaries are very rugged or "mountainous" on a microscale, probably as a result of pinning by particles and bubbles.

During straining, the boundaries tend to straighten between the major pinning points. The gas bubbles change little during the early stages of straining, but as strain accumulates they begin to grow, as flat amoeboid cavities at higher stresses and as regular polyhedral cavities at lower stresses. Specimens fail at low ductility because of the growth and linking of these cavities.

Evaluation of Methods for Joining Tungsten Alloys

G. M. Slaughter

Development of Filler Metals with Low Melting Points (Nancy C. Cole)

The prime objective of this program is to determine the weldability of W with various filler metals that have melting points lower than that of W. Low melting point is of interest because the lower overall energy input minimizes total thermal stresses, recrystallization, and grain growth in the heat-affected zone. A filler metal with low melting point is also useful in fabricating complex structures such as those in

which thin-walled tubes are joined to thicker sections, since there is less danger of melting through the thin-walled tube.

We welded a proprietary "weldable" powder-metallurgy W product[6] with various filler metals with low melting points fabricated by the powder-metallurgy process. The welding conditions and results of a visual examination are shown in Table 15.5. The joint design was a butt weld with a 0.030 × 0.060-in. strip of filler metal wedged between the two 0.060-in.-thick sheets of W base metal. The specimens were cleaned with acetone and alcohol and electropolished before they were welded in an inert-atmosphere chamber purged with very pure Ar. The workpiece was preheated to 150°C, the temperature previously determined to be desirable for welding 1/16-in. W sheet.[7] The current (350 amp) and arc gap (1/16 in.) were kept constant. A travel speed of 12 in./min was used with all the Mo-Re filler metals to obtain full penetration. Since more heat was required for full-penetration welds with the W–25 at. % Re–30 at. % Mo filler metal, the travel speed was reduced to 10 in./min.

Table 15.5. Welding Conditions[a] and Results of Visual Examination for Tungsten Welds Made with Various Filler Metals

Filler Metal	Travel Speed (in./min)	Remarks
Mo–1 wt % Re	12	Good weld, full penetration
Mo–20 wt % Re	12	Poor weld, center-line cracking
Mo–50 wt % Re	12	Good weld, full penetration
W–25 at. % Re–30 at. % Mo	10	Good weld, full penetration

[a]The current and arc gap were kept constant at 350 amp and 1/16 in.

Photomacrographs of the weld are shown in Fig. 15.11. All the welds were free of visually detectable cracks except for the ones made with Mo–20% Re filler metal. Figure 15.11(b) shows cracking at the center line in the left half of the weld made with Mo–20% Re filler metal. Also, the filler metal dropped out of the center section, leaving a weld without filler metal.

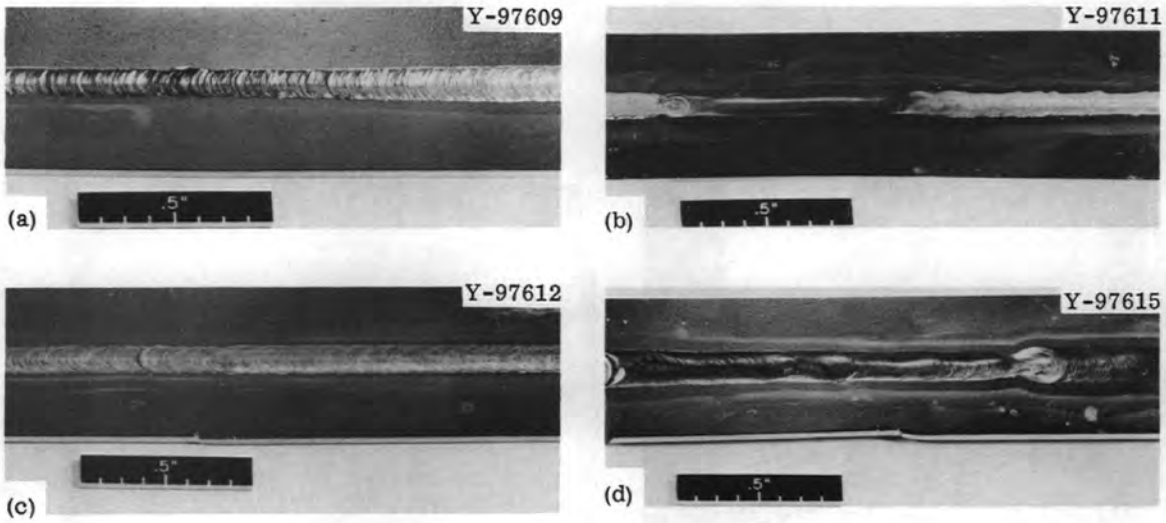

Fig. 15.11. Photomacrographs of Tungsten Welds Made with Various Filler Metals. (a) Mo–1% Re, (b) Mo–20% Re, (c) Mo–50% Re, and (d) W–25 at. % Re–30 at. % Mo.

Figure 15.12 shows photomicrographs of these welds. The welds made with filler metals other than Mo–20% Re are free of cracks. Slight porosity was expected, since both the base metal and filler metal are powder-metallurgy products. Use of arc-cast material, both as base metal and as filler metal, should eliminate the problem of porosity.

We shall determine the bend ductility of these welds and of similar welds that will be made in arc-cast W materials and compare the results. For comparison, we shall also determine the bend ductility of welds in arc-cast W to which no filler metal is added; this information has already been determined[7] for welds in powder-metallurgy W. Other filler metals will be investigated in the future.

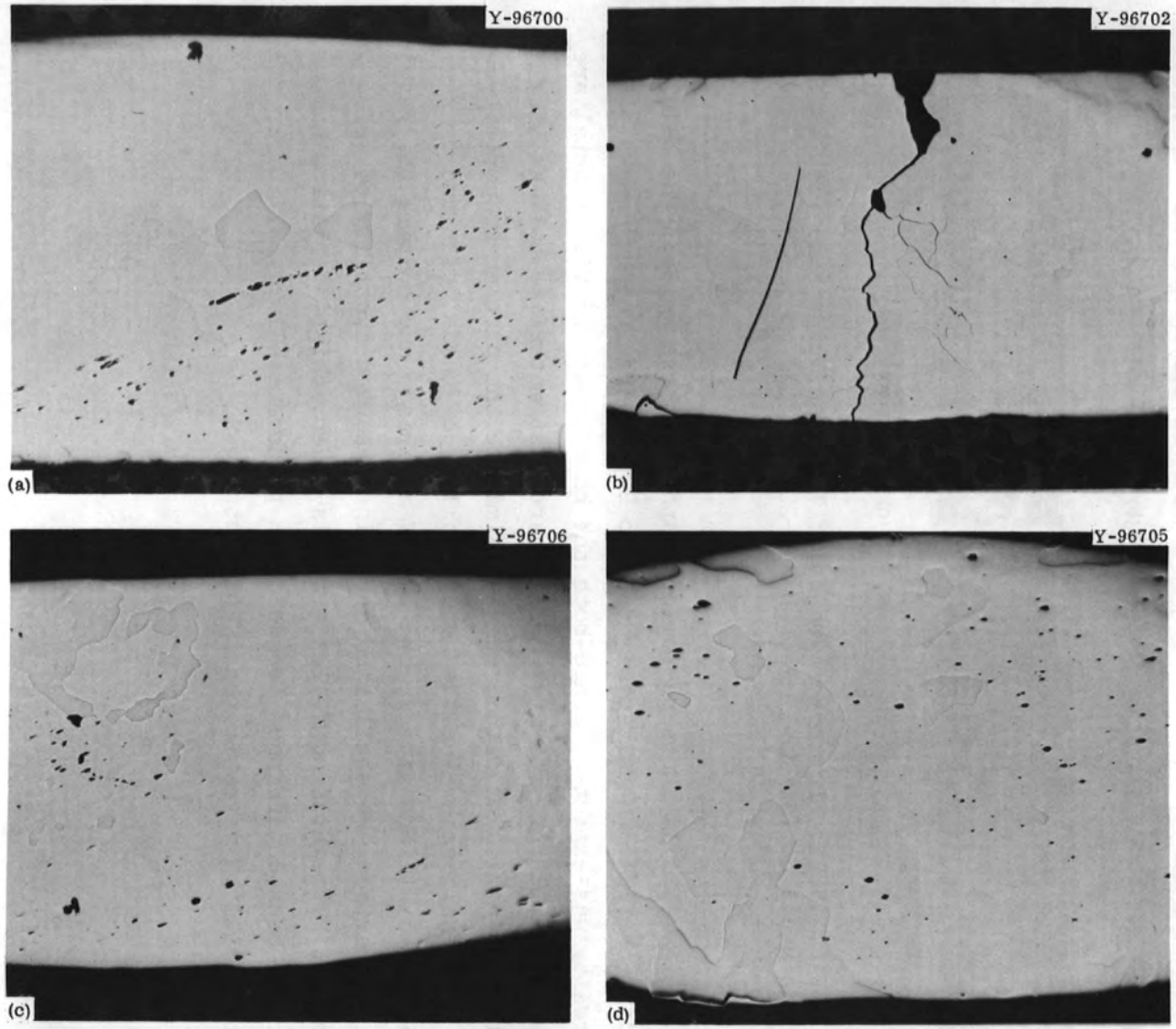

Fig. 15.12. Photomicrographs of Powder-Metallurgy Tungsten Welds Made with Various Powder-Metallurgy Filler Metals. (a) Mo–1% Re, (b) Mo–20% Re, (c) Mo–50% Re, and (d) W–25 at. % Re–30 at. % Mo. 50×. Reduced 30%.

References

1. J. I. Federer, Fuels and Materials Development Program Quart. Progr. Rept. June 30, 1969, ORNL-4440, pp. 148–151.
2. J. I. Federer, Fuels and Materials Development Program Quart. Progr. Rept. Dec. 31, 1968, ORNL-4390, pp. 165–166.
3. H. Inouye, "The Effect of Low-Pressure Oxygen on the Creep Properties of Tungsten and a Tungsten-Molybdenum Alloy," paper presented at 1969 Conference on Vacuum Metallurgy, Pittsburgh, June 16–19, 1969. To be published in the transactions.
4. R. L. Stephenson, Comparative Creep-Rupture Properties of W–25% Re Consolidated by Arc Melting and Powder Metallurgy Techniques, ORNL-TM-2651 (September 1969).
5. H. E. McCoy, Creep Rupture Properties of Tungsten and Tungsten-Base Alloys, ORNL-3992 (August 1966).
6. GE-15, Produced by General Electric Company, Cleveland, Ohio.
7. N. C. Cole, Fuels and Materials Development Program Quart. Progr. Rept. June 30, 1968, ORNL-4330, pp. 295–300.

16. FAST-NEUTRON IRRADIATION EFFECTS ON ELECTRICAL INSULATORS

G. M. Watson[1] G. W. Keilholtz[1]

The purpose of this program is to establish the effects of fast neutrons on the mechanical, physical, and electrical properties of materials suitable for use as electrical insulators in thermionic converters and to evaluate the mechanisms of neutron damage in these materials up to 1100°C.

General Survey of Fast-Neutron Effects on Electrical Insulators

D. A. Dyslin[2] R. E. Moore[1] H. E. Robertson[1]

Silicon Oxynitride

We previously reported[3] that silicon oxynitride (Si_2ON_2) (ref. 4) did not fracture or release N_2 during irradiation at low temperatures. The fast fluences were calculated from analyses of flux monitors included within the assembly. Exposures ranged from 1.6 to 5.5×10^{21} neutrons/cm^2 (> 1 Mev). Irradiation temperatures calculated for each specimen ranged from 70 to 100°C.

Fractional volume changes calculated from dimensional measurements are presented in Table 16.1. The volume changes are very small but clearly show an initial shrinkage followed by expansion upon exposure to very high fluences.

Single-Crystal Materials and Other Advanced Materials

Specimens fabricated from three advanced materials are now being irradiated in the Engineering Test Reactor (ETR) at low temperatures (< 150°C). The advanced materials are (1) synthetic sapphire made by the Czochralski process, (2) high-purity MgO single crystals, and (3) zirconia-doped transparent Y_2O_3 (General Electric). These materials are excellent electrical insulators that may have an advantage over polycrystalline alumina with respect to separation at grain boundaries. Synthetic sapphire and single-crystal MgO do not have grain boundaries,

Table 16.1. Fractional Volume Changes of Specimens of Silicon Oxynitride Irradiated to Temperatures from 70 to 100°C

Fast-Neutron Fluence [neutrons/cm^2 (> 1 Mev)]	Fractional Volume Change (%)
$\times 10^{21}$	
1.6	−0.24
1.7	−0.22
2.8	−0.16
3.0	−0.20
3.3	−0.36
3.4	−0.20
4.7	0.04
4.8	0.06
5.1	0.04
5.2	−0.02
5.5	0.16
5.5	0.06

and Y_2O_3 has a cubic crystal system that precludes separation at grain boundaries caused by anisotropic crystal expansion.

Irradiation of High-Density Commercial Al_2O_3 Products Considered for Thermionic Insulators

D. A. Dyslin[2] R. E. Moore[1] H. E. Robertson[1]

The irradiations of a long-term assembly in the ETR at temperatures from 400 to 1230°C and of an uninstrumented assembly containing four commercial Al_2O_3 products in the Experimental Breeder Reactor-II (EBR-II) at about 800°C were completed. Results from these irradiations are not yet available. Examinations of specimens irradiated in the ETR in a short-term assembly, which is identical to the long-term assembly, were reported previously.[5]

An assembly containing the same four commercial Al_2O_3 products was irradiated at very low temperatures (60 to 90°C) in the ETR over a low fast-fluence range [0.2 to 0.7 $\times 10^{21}$ neutrons/cm^2 (> 1 Mev)] to determine the initial slope of the curves for fractional volume change versus fast fluence. The data are given in Table 16.2. No significant differences are apparent among the four types of Al_2O_3 with respect to fractional volume expansion in this low fluence range. The data are consistent

Table 16.2. Fractional Volume Increases of Specimens of Commercial Al_2O_3 Products Irradiated at Very Low Temperatures (60 to 90°C)

Coors AD-995		Wesgo AL-995		General Electric Opaque Lucalox		General Electric Translucent Lucalox	
Fast-Neutron Fluence [neutrons/cm^2 (> 1 Mev)]	Fractional Volume Increase (%)	Fast-Neutron Fluence [neutrons/cm^2 (> 1 Mev)]	Fractional Volume Increase (%)	Fast-Neutron Fluence [neutrons/cm^2 (> 1 Mev)]	Fractional Volume Increase (%)	Fast-Neutron Fluence [neutrons/cm^2 (> 1 Mev)]	Fractional Volume Increase (%)
$\times 10^{21}$		$\times 10^{21}$		$\times 10^{21}$		$\times 10^{21}$	
0.22	1.0	0.29	0.9	0.20	0.8	0.19	0.9
0.27	0.9	0.36	1.0	0.25	0.8	0.33	1.0
0.38	0.9	0.41	1.1	0.34	1.1	0.43	1.0
0.38	1.0	0.63	1.2	0.40	1.0	0.60	1.3
0.62	1.2	0.70	1.0	0.65	1.2	0.66	1.2
0.67	1.2	0.73	1.2	0.69	1.0	0.68	1.1
				0.72	1.2	0.73	1.2
				0.74	1.1		
				0.74	1.1		

with data previously obtained at somewhat higher temperatures when only Type IV Al_2O_3 (General Electric Translucent Lucalox) was irradiated[6] and with data for a single crystal irradiated at 150°C (ref. 7).

Another assembly was irradiated at very low temperatures (70 to 90°C) to high fast fluences ranging from 1.8 to 5.5 $\times 10^{21}$ neutrons/cm^2 (> 1 Mev). The Al_2O_3 specimens were all of Type IV Al_2O_3. All specimens survived the irradiation in good condition except two specimens from the same capsule that had received fast fluences of 4.5 and 4.6 $\times 10^{21}$ neutrons/cm^2 (> 1 Mev). One of these was chipped on one side, and the other was broken longitudinally into two pieces. Fractional volume increases calculated from dimensional changes of all the irradiated specimens except the broken specimen are given in Table 16.3. The volume expansion at high fluences (3.6 to 5.5 $\times 10^{21}$ neutrons/cm^2) is very much less than was previously observed for the same material irradiated at higher temperatures.[6] Separation at grain boundaries was found to contribute to the volume expansion at higher temperatures. The results of this irradiation illustrate again the temperature sensitivity of neutron damage to Al_2O_3, which has been discussed previously.[5] Additional metallographic and x-ray diffraction examinations are needed to define the damage mechanisms more precisely.

Table 16.3. Fractional Volume Increases of Specimens of Translucent Lucalox Irradiated at Very Low Temperatures (70 to 90°C)

Fast-Neutron Fluence [neutrons/cm^2 (> 1 Mev)]	Fractional Volume Change (%)
$\times 10^{21}$	
1.8	1.5
1.9	1.6
2.5	1.9
2.6	2.0
3.6	1.9
3.7	1.9
4.6	2.2
5.3	2.3
5.4	2.2
5.4	2.3
5.5	2.4

Metal-Clad Al_2O_3 Specimens

D. A. Dyslin[2] R. E. Moore[1] H. E. Robertson[1]

Combinations of insulators and metallic conductors were irradiated in the ETR. The units, which were furnished by other installations, were either trilayers, which are cylindrical shells of insulator material clad on both the inside and outside with metal, or bilayers, which are insulator shells clad only on the outside.

The units furnished by Thermo Electron Engineering Corporation were removed from their capsules and photographed. A side view of trilayer specimen 22S is shown in Fig. 16.1; an end view is shown in Fig. 16.2. The inner layer of metal can be seen to have pulled away from the alumina insulator. Figure 16.3 shows that this also occurred to trilayer 23S, which was exposed to the same conditions. An end view of the bilayer 32S (Fig. 16.4) indicates good condition. Figure 16.5, an end view of bilayer 25S, shows that the alumina layer is chipped and cracked on one side.

The units furnished by the National Aeronautics and Space Administration-Lewis Research Center were returned to them for examination. Units provided by Thermo Electron Engineering Corporation and Fairchild Hiller will be examined, by dimensional measurements and metallography, in the ORNL hot cells.

Fig. 16.1. Thermo Electron Trilayer 22S Exposed to a Fast Fluence of 2.7×10^{21} neutrons/cm^2 (> 1 Mev) at 700°C, Side View. 6×.

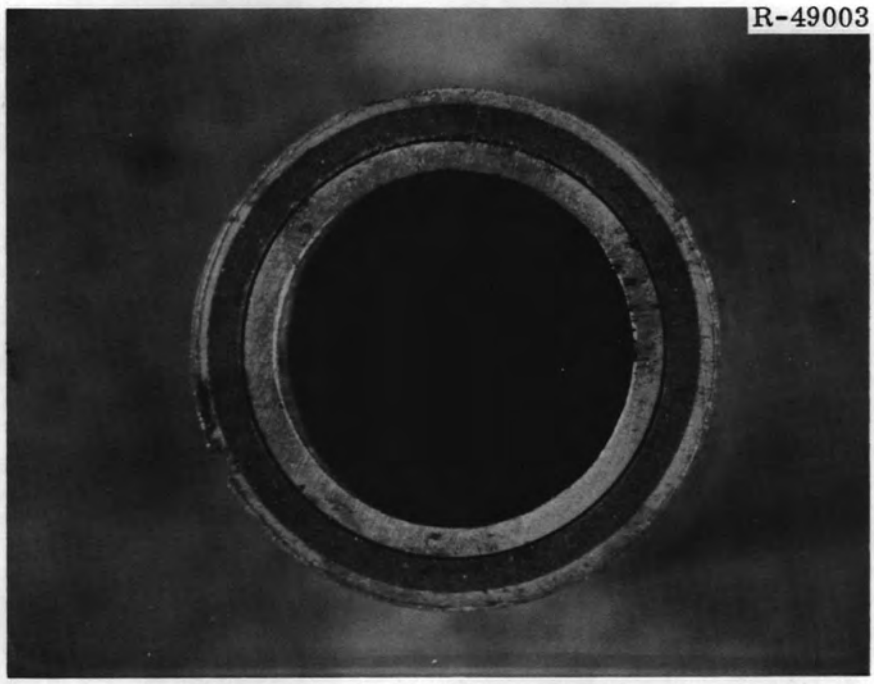

Fig. 16.2. Thermo Electron Trilayer 22S Exposed to a Fast Fluence of 2.7×10^{21} neutrons/cm^2 (> 1 Mev) at 700°C, End View. 6x.

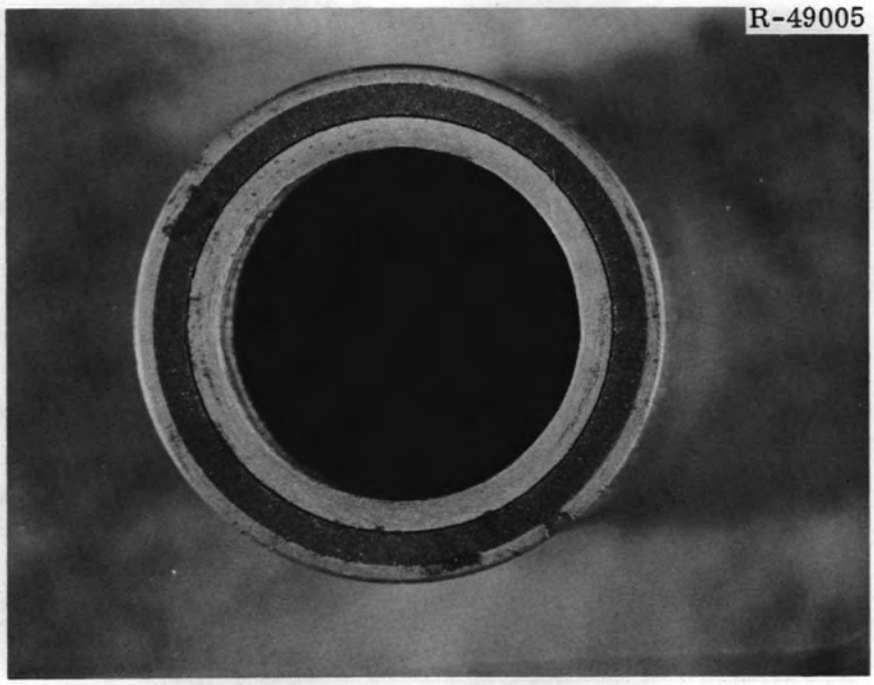

Fig. 16.3. Thermo Electron Trilayer 23S Exposed to a Fast Fluence of 2.7×10^{21} neutrons/cm^2 (> 1 Mev) at 700°C, End View. 6x.

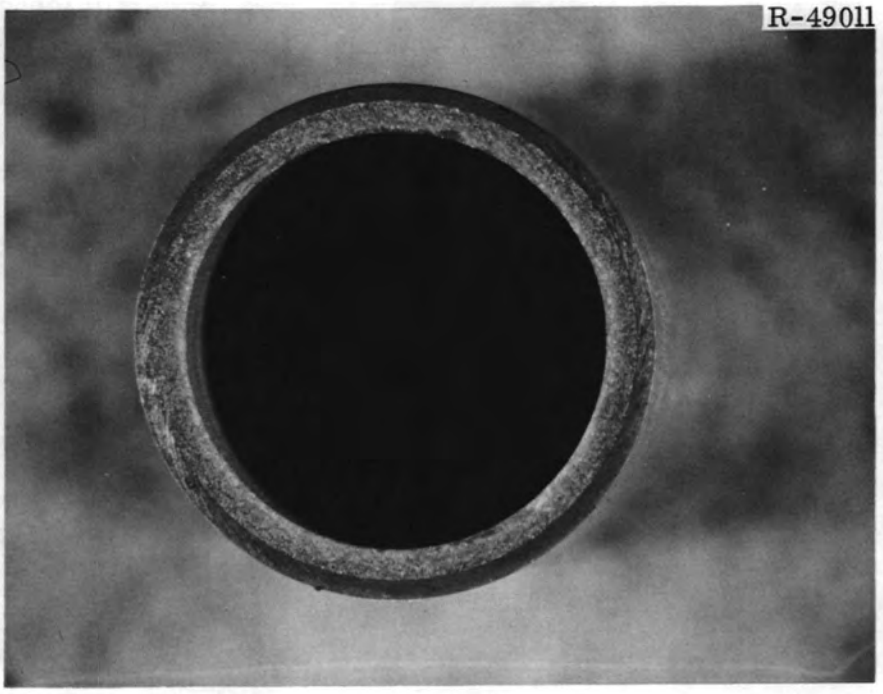

Fig. 16.4. Thermo Electron Bilayer 32S Exposed to a Fast Fluence of 1.3×10^{21} neutrons/cm^2 (> 1 Mev) at 550°C, End View. 6×.

Fig. 16.5. Thermo Electron Bilayer 25S Exposed to a Fast Fluence of 2.4×10^{21} neutrons/cm^2 (> 1 Mev) at 550°C, End View. 6×.

References

1. Reactor Chemistry Division.
2. General Engineering Division.
3. G. W. Keilholtz, R. E. Moore, D. A. Dyslin, and H. E. Robertson, Fuels and Materials Development Program Quart. Progr. Rept. June 30, 1969, ORNL-4440, pp. 115–120.
4. Norton Company, Worcester, Mass.
5. G. W. Keilholtz, R. E. Moore, D. A. Dyslin, and H. E. Robertson, Fuels and Materials Development Program Quart. Progr. Rept. March 31, 1969, ORNL-4420, pp. 123–130.
6. G. W. Keilholtz, R. E. Moore, and D. A. Dyslin, Fuels and Materials Development Program Quart. Progr. Rept. June 30, 1968, ORNL-4330, pp. 159–164.
7. R. S. Wilks, J. A. Desport, and J.A.G. Smith, The Irradiation-Induced Macroscopic Growth of α-Al_2O_3 Single Crystals, AERE-R-5460 (May 1967).

17. CORROSION STUDIES OF ADVANCED REFRACTORY METALS

W. O. Harms J. H. DeVan A. P. Litman

Requirements for auxiliary electricity or ion propulsion for space vehicles necessitate power plants of high efficiency that will operate at high temperatures. For these applications, nuclear power systems have been proposed in which alkali metals are used to transfer heat, drive a turbogenerator, and lubricate rotating components. Accordingly, we are investigating the corrosion properties of candidate alkali metals, primarily Li, K, and Na, under conditions of interest for space applications. Because of the relatively high temperatures (> 1000°C), the investigation is concerned largely with refractory-metal container materials.

Lithium Studies

J. H. DeVan A. P. Litman

Lithium Thermal-Convection Loop Experiments (J. H. DeVan)

We have programmed a series of thermal-convection loop tests to evaluate the mass-transfer characteristics of W alloys in Li at 1350°C. The first of these loops is being fabricated by Thermo-Electron Corporation and is scheduled for delivery in November 1969. The loop and its corrosion inserts are constructed of arc-cast unalloyed W. The tubing for the loop was produced at ORNL by means of the floating-mandrel duplex-billet extrusion process developed by McDonald and Reimann.[1] All joints are being made by the electron-beam process with Mo–50% Re filler metal. A second loop, being fabricated of W–25% Re by Thermo-Electron Corporation, is about 50% complete. The procedures for tubing fabrication and welding for this loop are similar to those used for the W loop.

Lithium Forced-Circulation Loop Experiments (D. L. Clark,[2] C. W. Cunningham,[2] B. Fleischer, W. R. Huntley[2])

Our program of forced-circulation Li loops was designed to gain information on cladding materials for fuel elements and containment materials for Li-cooled power systems. A test loop (FCLLL-1) was assembled,

and a trial run was made.[3] During this test, we noted a gradual failure of the W-Re thermocouples and found that the adjustable radiation shield could not be moved throughout its full range of travel. We investigated these operational troubles and began correcting them this quarter. The original bare-wire and sheathed thermocouples were stripped from the loop, and new thermocouples are being installed.

Sheathed W–3% Re vs W–25% Re Thermocouples. – Our examination[3] of the sheathed thermocouples on FCLLL-1 showed several failures caused by differential thermal expansion at a transition joint used to couple Ta sheathing to stainless steel sheathing. Therefore, we replaced the composite thermocouple sheath with one made entirely of Ta, such as was used on previous loops.[4] Nine of these thermocouples are being installed on FCLLL-1.

Bare-Wire W–3% Re vs W–25% Re Thermocouples. – Our inspection of the 0.005-in.-diam bare-wire thermocouples indicated a number of failures of the spot-welded hot junctions. We studied the variables of the spot-welding process and found that three spot welds about 1/16 in. apart on each wire, as shown in Fig. 17.1, gave the best result. The welds were made at three different power settings starting with 7 wsec nearest the ceramic insulator and increasing to 9 and 11 wsec for consecutive welds. An expansion loop, also shown in Fig. 17.1, was incorporated between the ceramic insulator and the first weld. In spite of these improvements, the spot welds are still quite brittle and must be made as the last assembly operation to minimize breakage.

The brittleness of these spot welds prompted us to investigate other methods for making the thermocouple hot junction. The most promising method we found was to attach the thermocouple wires mechanically to the loop wall by inserting the 0.005-in.-diam wires into a 0.020-in.-diam cylinder of 0.005-in.-thick Ta shim stock and flattening the cylinder onto the wires. The flattened cylinder is then folded back upon itself at the midpoint and flattened again to produce a junction about 0.021 in. thick × 1/16 in. wide × 1/8 in. long. The assembly steps are illustrated in Fig. 17.2. The junction is then fastened to the pipe wall by a 0.002-in.-thick Ta strap that is spot welded to the pipe as shown in

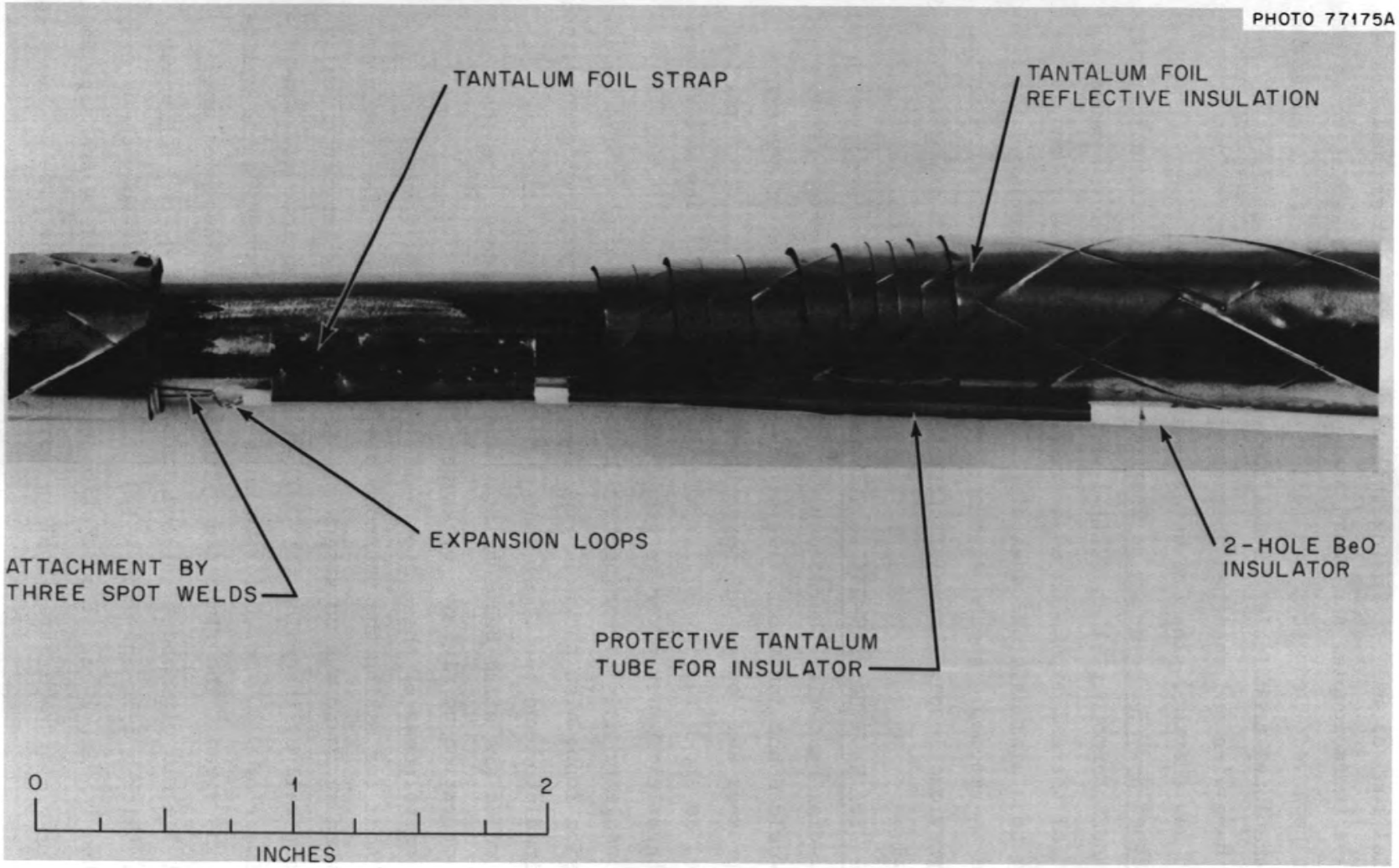

Fig. 17.1. Method of Attaching Bare-Wire Thermocouples to Insulated Piping of FCLLL-1.

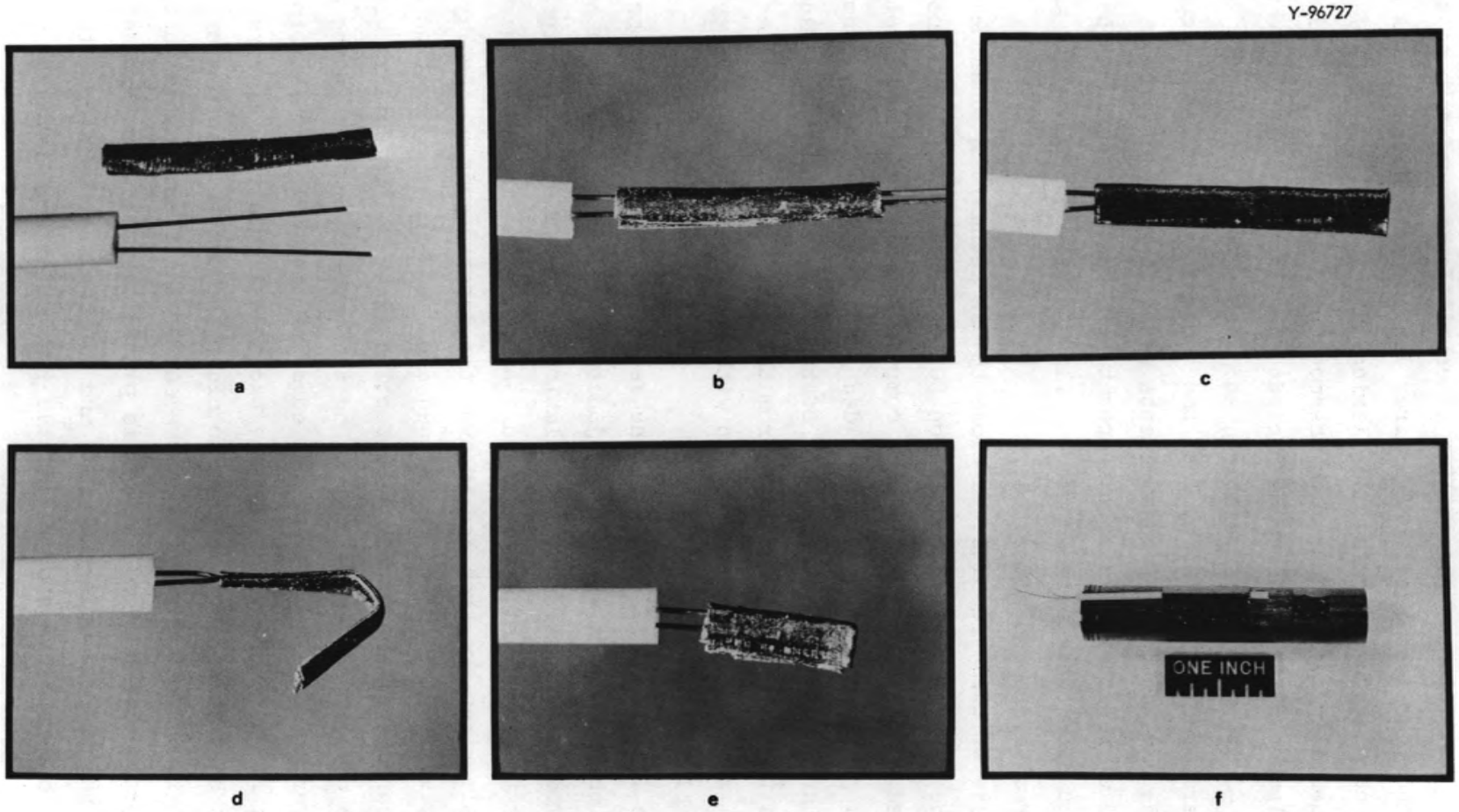

Fig. 17.2. Sequence for Assembly of Mechanical Joint for Bare-Wire Thermocouples.

Fig. 17.2. To avoid any possibility of embrittlement, we make no spot welds on the junction itself. The wires leading into such a joint can withstand considerable bending and flexing.

We thermally cycled four such thermocouples and measured their electrical continuity. The cycle included heating for 1 1/2 hr to about 1275°C, a 45 min hold at temperature, and then a 5 1/2 hr cooling to room temperature. After ten cycles, the thermocouples still had continuity as determined both by measurements of electromotive force at 1275°C and of resistance at room temperature. There appeared to be no significant difference between the ductility of the junctions and associated wires before and after test.

Because of these results, we chose to use mechanical junctions for most of the bare-wire thermocouples on FCLLL-1, but we included enough spot-welded junctions so that we can compare the thermal contact of the mechanical junctions with that of welded junctions located above both thermal insulation and the bare wall of the pipe. We have also made provisions to compare the readings from the bare-wire thermocouples with those from sheathed thermocouples and with those from an optical pyrometer at a blackbody viewing port.

There is little difference in the sequence of assembly for the bare-wire thermocouples whether the junction is made mechanically or welded. Most of the reflective insulation is installed on the piping before the thermocouples are attached. As shown in Fig. 17.1, the thermocouple wires are then led in over the tapered ends of the layers of reflective insulation and positioned along a 2-in.-long section of the bare surface of the pipe. A protective sleeve of Ta foil is wrapped around the ceramic insulator only along the tapered section at the ends of the layers of foil to prevent the edges of the foil from shorting the W-Re wires if any breaks occur in the two-hole insulators. A strap of Ta foil is spot welded to the pipe to clamp the two-hole insulator tightly to it and thereby prevent movement of the thermocouple junction. A small, protective hood of Ta foil is placed over the wire expansion loops and the thermocouple junctions and is then spot welded to the pipe. Finally, about ten layers of reflective insulation are installed over the entire area.

Radiation Shield. — The mechanical interference that prevented the correct positioning of the radiation shield was traced to a vertical section of piping that had moved out of position so that its insulation caught on the shield. We repositioned the line, added a smooth layer of foil to eliminate future interference, and added more counterweight to reduce the amount of torque required to lift the shield.

Effect of Oxygen on Compatibility of Refractory Metals and Alkali Metals

J. H. DeVan

Partitioning of Oxygen Between Potassium and Zirconium (R. L. Klueh)

We previously discussed[5] the use of Zr tabs for determining the O content of K and Na [i.e., the gettering-vacuum-fusion (GVF) method for O analysis]. For this application it was necessary to know the coefficient, κ°, for the equilibrium distribution of O between Zr and K and Zr and Na (i.e., the concentration of O in Zr divided by the concentration of O in the alkali metal). We deduced that κ° was very large and for all practical purposes could be considered infinite. If this were true, it would follow that, when Zr contacts K for 100 hr at 800°C, effectively all of the O originally in the K should be gettered by the Zr. This point could not be verified, however, because no accurate technique was available for determining the O content in K at very low O concentrations.

After we completed our study, we acquired equipment for fast-neutron activation analysis that allows us to analyze low levels of O in K. For a series of GVF analyses, we added O to the K and then determined the O remaining in the K after exposure to Zr for 100 hr at 800°C.

The results are shown in Table 17.1. The concentration of O in the K was reduced to a very low level, in agreement with our previous prediction.[5] A higher concentration of O was detected in tests 5–7 than in tests 8–10 despite the fact that there was more O in the latter capsules before test. This suggests that the atmosphere of our glove box may have been contaminated at the time the K samples were taken from capsules 5–7.

Table 17.1. Oxygen Concentration[a] in Potassium After Exposure to Zirconium for 100 hr at 800°C

Capsule Number	O Added[b] to K as K_2O (ppm)	O in K After Exposure to Zr (ppm)
1	0	< 5[c]
2	0	< 5
3	200	< 5
4	200	< 5
5	400	9[d]
6	400	11[d]
7	550	6[d]
8	600	< 5
9	800	< 5
10	800	< 5

[a]Analyses by fast-neutron activation.

[b]The K contained about 100 ppm O as received.

[c]Limit of detection.

[d]The accuracy at this level is ±100%.

We previously estimated $\kappa°$ to be greater than 2000. The concentration of O in the Zr coupons after test in the materials with the highest initial O content (tests 9 and 10) was about 5000 ppm. If the O concentration in the K after test is assumed to be about 1 ppm, our original conclusion, that $\kappa°$ is greater than 1000, is corroborated.

Penetration of Refractory Metals by Alkali Metals (R. L. Klueh)

During the past five quarters we have reported on the effect of O on the compatibility of the refractory metals Ta and Nb with the liquid alkali metals K, Na, and Li at 600°C. Oxygen affects the compatibility in two ways. First, increasing the O concentration in the K (refs. 6–8) or Na (refs. 7, 9) increases the solubility of the refractory metal in

the liquid. [Increasing the O concentration of Li (ref. 10) has a lesser effect on solubility.] Second, O in the refractory metal can lead to penetration of the refractory metal by the alkali metal. We found penetration in all of the systems tested (i.e., in O-doped Ta and Nb exposed to K, Na, and Li).

To complete our comparison of these systems at 600°C, we are determining the "threshold" O concentrations (that O concentration in the refractory metal above which penetration occurs) for the penetration of Nb and Ta by Li, Na, and K. To do this we are exposing a series of O-doped Nb and Ta specimens to Li, Na, and K.

The Nb-Li series of tests was completed; the results are shown in Table 17.2. Figure 17.3 shows a penetrated specimen that illustrates both intergranular and transgranular attack. From the results, we concluded that the threshold concentrations for intergranular and transgranular penetration of Nb by Li at 600°C are about 400 and 800 ppm O, respectively.

Table 17.2. Depth of Lithium Penetration of Oxygen-Doped Niobium at 600°C[a]

O Concentration (ppm)	Average Depth of Penetration,[b] in.	
	Intergranular	Transgranular
300	0	0
450	0.0007	0
600	0.004	0
900	0.016	0.0002
1100	0.020	0.002
1250	0.020	0.006
1400	0.020	0.007
1650	0.020	0.014

[a]Specimens were exposed simultaneously for 20 hr in a container of type 304 stainless steel.

[b]Specimen was 0.04 in. thick; penetration to 0.02 in. represents complete penetration.

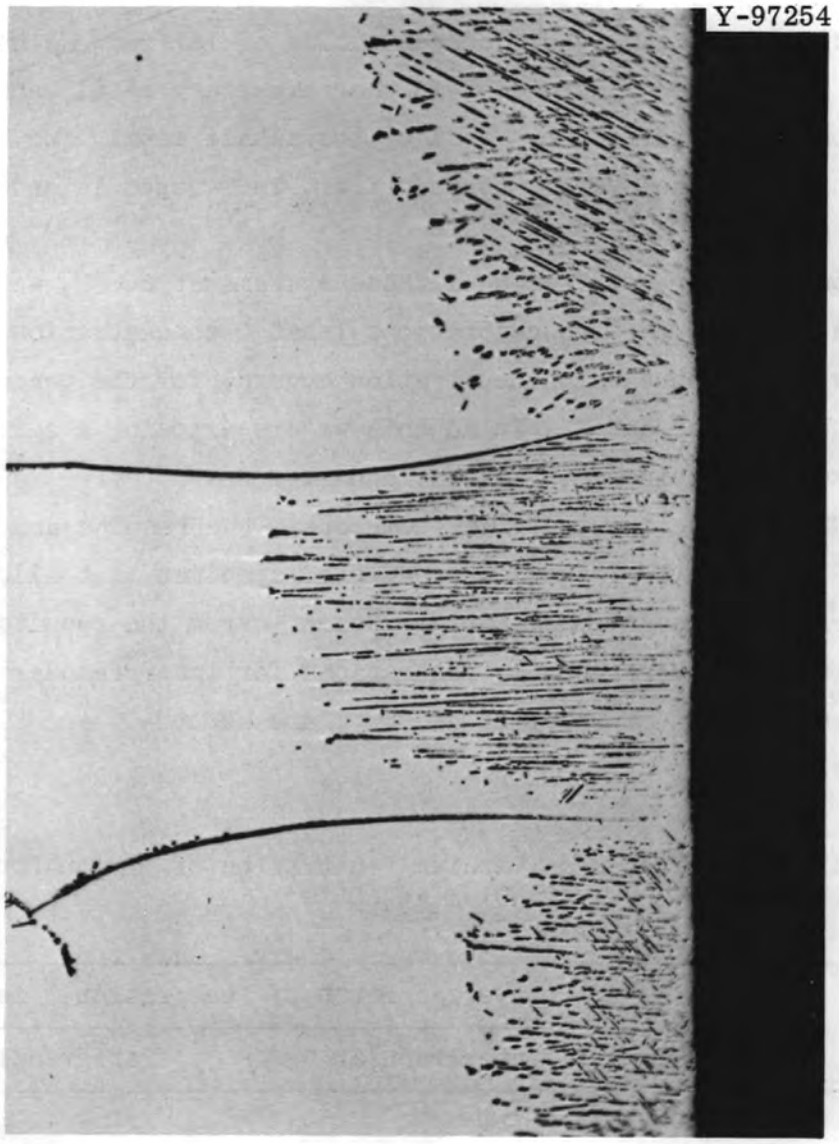

Fig. 17.3. A Tantalum Specimen That Contained 1400 ppm O and Was Exposed to Lithium for 20 hr at 600°C. 200×.

References

1. R. E. McDonald and G. A. Reimann, Floating-Mandrel Extrusion of Tungsten and Tungsten-Alloy Tubing, ORNL-4210 (February 1968).
2. Reactor Division.
3. B. Fleischer, D. L. Clark, and C. W. Cunningham, Fuels and Materials Development Program Quart. Progr. Rept. June 30, 1969, ORNL-4440, pp. 96–108.

4. D. H. Jansen, J. H. DeVan, C. W. Cunningham, L. C. Fuller, and R. E. MacPherson, Niobium–1% Zirconium Boiling-Potassium Forced Circulation Loop Test (FCL-5), ORNL-4301, p. 97 (December 1968).

5. R. L. Klueh, Oxygen Determination and Purification of Liquid Alkali Metals by Zirconium Gettering, ORNL-TM-2473 (March 1969).

6. R. L. Klueh, Fuels and Materials Development Program Quart. Progr. Rept. June 30, 1968, ORNL-4330, pp. 142–146.

7. R. L. Klueh, Fuels and Materials Development Program Quart. Progr. Rept. Sept. 30, 1968, ORNL-4350, pp. 125–126.

8. R. L. Klueh, Fuels and Materials Development Program Quart. Progr. Rept. Dec. 31, 1968, ORNL-4390, pp. 95–97.

9. R. L. Klueh, Fuels and Materials Development Program Quart. Progr. Rept. March 31, 1969, ORNL-4420, pp. 100–103.

10. R. L. Klueh, Fuels and Materials Development Program Quart. Progr. Rept. June 30, 1969, ORNL-4440, pp. 90–92.

PART III

GENERAL REACTOR TECHNOLOGY

FUELS

18. FISSION-GAS RELEASE AND PHYSICAL PROPERTIES OF FUEL MATERIALS DURING IRRADIATION

O. Sisman

The purpose of this work is to measure the variables that control the release of fission gas from highly characterized nuclear fuels and to evaluate these variables in terms of a generalized model for predicting release from operating fuel materials. Thermal diffusivity is measured in-reactor in analogous experiments.

Measurements of Thermal Diffusivity in UO_2 During Irradiation

R. M. Carroll R. B. Perez

During this quarter we have processed 120 different measurements of the temperature response as a function of time of a hollow cylinder of large-grained UO_2 to a stepped change in fission power. The results show an erratic release of stored energy during the first 2 min of response. The impression we have from the data is that a part of the release of stored energy is the result of long-term irradiation and that another component results in a change from one equilibrium level to another.

Because of the erratic nature of the release of stored energy, we have postponed trying to evaluate the amount of stored energy released under various conditions. Instead, we have analyzed the curve for temperature response for the interval between 120 and 600 sec after the initiation of the stepped change in fission power, thus avoiding the erratic effect produced by the stored energy. In this interval, the curve had a single exponential form of the type

$$T_S(t) = A_0 - A_1 e^{-r_1 t} , \tag{18.1}$$

$$T_E(t) = B_0 - B_1 e^{-r_2 t} , \tag{18.2}$$

where T_S and T_E are, respectively, the temperatures of the specimen and of the environment at time t. The terms A_0 and B_0 represent the equilibrium temperature of the specimen and its environment after the temperature rise in the specimen and environment caused by the stepped change of power. The rate constant, r_1 or r_2, is determined by the dependence of the temperature response on time; in the interval between 120 and 600 sec, r_1 equals r_2.

The taped data were processed by computer in each of the 120 cases for the values of A_0, A_1, B_0, B_1, r_1, and r_2. The mechanical operation of the apparatus and of the computer program was excellent. When the same measurements were taken in rapid succession, the values of A_0 and B_0 were reproducible to within 0.05% deviation at 1000°C. These measurements were so sensitive that we could observe the change in the profile of the neutron flux in the reactor within a few hours. This change in profile is an order of magnitude less than our argon-activation flux monitor can detect.

These data were combined with data for the physical constants of the specimen, the specimen holder, and the irradiation conditions into a formula for calculating the thermal diffusivity of the UO_2. This formula includes the nonfission heating which had been determined in a previous experiment.[1] The main purpose of the formula was to make corrections for the influence of the change in the environment of the specimen.

Because both the specimen and the specimen holder are changed in steps from one fission- and nonfission-heating condition to another, each would change temperature in a way dependent on its own physical characteristics. Since both must be moved together, the rate of change of temperature of both depends on heat transfer between specimen and holder as well as their individual physical characteristics. The parameters of Eq. (18.2) were obtained to enable us to make a correction for the interaction.

A computer solution for the thermal diffusivity was obtained by use of the correction formula, but, unfortunately, these corrections were much larger than the values to which they would apply. We are in the unhappy situation of having raw data that give answers that are reproducible and in the approximate range of those obtained from bench tests

while the corrected data give answers that scatter and are an order of magnitude lower than those from bench tests. The correction process is being checked.

Some of the correction process could be avoided if we could use the entire heating curve, including the first 120 sec. Because of the release of stored energy, however, the curves are not reproducible in the initial portion; also, equations of the type used for Eqs. (18.1) and (18.2) cannot be used to fit the entire curve. An equation with two exponents will fit the entire heating curve with reasonable accuracy, but, unfortunately, there are many combinations by which three constants and two exponents can be used to fit a given curve.

We have obtained and processed heating curves that show a reproducibility that implies high precision. The mathematical processes of obtaining values for thermal diffusivity from the data have not worked. We are now investigating whether it is even possible to obtain a unique solution to the equations necessary to separate the stored energy from the initial temperature rise caused by a change of irradiation conditions.

Release of Fission Gas from UO_2

R. M. Carroll R. B. Perez

The release of fission gas from the cylinder of large-grained UO_2 has followed the same pattern previously found in high-density UO_2. The release has decreased slightly as burnup has progressed, likely because of surface changes induced by irradiation. Since the release rate does not change in direct proportion to the amount of fission gas generated, trapping at fission defects is also occurring in the sintered, large-grained UO_2 specimen.

The specimen has now achieved a burnup of 1.7×10^{19} fissions/cm^3 at temperatures up to 1150°C without any evidence of cracking. Since the data for thermal diffusivity have already been obtained, this specimen will now be irradiated in the temperature range where grain growth will occur.

References

1. R. M. Carroll, R. B. Perez, and O. Sisman, Nucl. Sci. Eng. 36, 232–237 (1969).

19. DEVELOPMENT OF FUEL ELEMENT FABRICATION

G. M. Adamson, Jr.

The purpose of these programs is to devise new combinations of materials or new fabrication techniques to advance the technology for fabricating fuel elements and components for research reactors. We are attempting to improve the performance of advanced research reactors, such as the High Flux Isotope Reactor (HFIR) and Advanced Test Reactor (ATR), by developing fuel elements with lower production cost, longer lives, increased safety or reliability, or all three. The studies include factors affecting both fabrication and irradiation performance. We must also develop sufficient knowledge of the processes used for fabricating Al-based dispersion fuel elements so that we can adequately assist commercial fabricators, purchasers, specification writers, and technical inspectors. Other studies are aimed at improving the reliability and reducing the cost of the required nondestructive inspection techniques.

Irradiation Studies

W. R. Martin

Evaluation and Design of Cermet Fuel-Plate Irradiation Experiments
(M. M. Martin, W. K. Crowley[1])

Since the G-12 loop of the Engineering Test Reactor (ETR) was shut down by Idaho Nuclear Corporation upon direction from USAEC-RDT, we are assessing the possibility of performing our planned irradiations for fiscal year 1970 in the HFIR or the Oak Ridge Research Reactor (ORR). The VXF-6 and VXF-19 positions in the HFIR and the F-2 and B-2 positions in the ORR are being considered for irradiation of our test plates. Pertinent characteristics for these positions and for the G-12 loop of the ETR are shown in Table 19.1. In the HFIR, our experiments would be cooled by reactor water, whereas in the ORR they would be contained in a separate loop. Because of the significantly higher operating pressure, the

Table 19.1. Pertinent Conditions of HFIR, ORR, and ETR Facilities for Planned Irradiations

	HFIR	ORR	ETR
Experimental position	VXF-6 or VXF-19	F-2	G-12
Maximum unperturbed thermal-neutron flux, neutrons cm^{-2} sec^{-1}	$4.7–5.9 \times 10^{14}$	2.2×10^{14}	5.7×10^{14}
Average operating pressure, psig	465	150	727
Saturated boiling temperature, °C	237	186	264
Inlet water temperature, °C	49	43	71
Critical heat flux, Btu hr^{-1} ft^{-2}	3.41×10^6	1.64×10^6	5.66×10^6
Wall temperature at critical heat flux, °C	292	237	310
Duration of normal reactor cycle, days	23	49	42
Relative duration (compared to ETR) needed to achieve the same degree of burnup	0.41	1.46	1.00

facilities in the HFIR permit safe operation of our proposed experiments at higher surface temperatures and heat fluxes. Such a thermal environment is desirable since our tests should approximate actual conditions of current and advanced HFIR and ATR cores. Also, our proposed experiments in HFIR can achieve a level of burnup in 23 calendar days (1 cycle) that would require either 82 calendar days in the ORR or 56 calendar days in the ETR. Because of these considerations, we have tentatively selected HFIR for our irradiations. A conceptional design for a miniature fuel element to contain our test plates is in progress.

Status of Irradiation Experiments in ETR (M. M. Martin)

Table 19.2 summarizes the disposition of the irradiation experiments on miniature fuel plates after the shutdown of the G-12 loop. The irradiated and unirradiated samples should be returned to ORNL by the middle of October if the cask is delivered promptly.

The test plates for experiments 70-1 and 70-2 are fabricated and characterized for irradiation.[2] The test plates in experiments 70-2

Table 19.2. Summary of G-12 Loop Experiments for Fiscal Years 1969 and 1970

Experiment Number	Description	Number of Test Plates	Exposure (Mwd)	Status
69-1	Effect of burned U_3O_8 particle size on performance of fuel plates at high burnup. Dispersion clad with type 6061 Al, contains 1.42 g $^{235}U/cm^3$ of core.	4	9995	Exposure completed. Plates being returned to ORNL.
69-2	Effect of high-fired U_3O_8 particle size on performance of fuel plates at high burnup. Dispersion clad with type 6061 Al, contains 1.14 g $^{235}U/cm^3$ of core.	4	9995	Exposure completed. Plates being returned to ORNL.
69-3	Effect of Ni coating on performance of fuel plates clad with types 6061 and 2219 Al. Core contains 1.42 g $^{235}U/cm^3$ as burned U_3O_8.	8	4331	Exposure completed. Plates being returned to ORNL.
70-1	Effect of sol-gel and burned U_3O_8 particle size on performance of fuel plates at low, intermediate, and high burnups. Dispersion clad with type 6061 Al, contains 1.57 g $^{235}U/cm^3$ of core.	8	0	Ready for irradiation. Plates being returned to ORNL.
70-2	Effect of up to 7.4 mg $^{10}B/cm^3$ of core on performance of poison plates clad with type 6061 Al.	6	0	Ready for irradiation. Plates being returned to ORNL.
70-3	Effect of up to 7.4 mg $^{10}B/cm^3$ of core on performance of fuel plates clad with type 6061 Al and containing 1.42 g $^{235}U/cm^3$ of core in the form of burned U_3O_8.	6	0	To be fabricated.
70-4	Effect of cladding-to-core interfacial grain growth on performance of fuel plates clad with types 6061 and 2219 Al. Cores contain 1.14 and 1.30 g $^{235}U/cm^3$ as burned U_3O_8 and UAl_x, respectively.	12	0	To be fabricated.

and 70-3 contain matching loadings of ^{10}B, and those in 69-1 and 70-3 contain identical ^{235}U core concentrations. We shall, of course, note the performance of these test plates in the reactor; in addition, the similarity in their loadings should also permit us to determine the contributions of the $B(n,\alpha)Li$ reaction to swelling of U_3O_8-B_4C-Al dispersions.

The only experiments that remain to be fabricated (70-3 and 70-4) are 18 test plates that contain B_4C plus burned U_3O_8, burned U_3O_8, and arc-cast UAl_x dispersed in Al. Table 19.3 lists their core compositions and loadings of ^{235}U and ^{10}B. Before the G-12 loop was shut down, we prepared the fuel, poison, and matrix powders and pressed the compacts for experiments 70-3 and 70-4. Table 19.4 records the characteristics determined for these core components. Idaho Nuclear Corporation supplied the UAl_x powder for the bonding experiment. We will not complete the fabrication of these plates, however, until the exact irradiation position in HFIR is selected and approved.

The specifications for both the HFIR and ATR require that the components of the fuel plates be metallurgically bonded. Acceptable bonding is defined as no visible separation between the core and cladding with grain growth evenly distributed across a minimum of 50% of the interface length. In experiment 70-4, we plan to compare the in-reactor performance of test plates clad with types 6061 and 2219 Al with low, intermediate, and high degrees of interfacial grain growth. The fuel compositions to be clad with both types of cladding are 42 wt % burned U_3O_8 (1.14 g $^{235}U/cm^3$)-Al and 52 wt % arc-cast UAl_x (1.30 g $^{235}U/cm^3$)-Al. The former simulates the current fissile concentration of the fuel plates for the HFIR outer annulus while the latter represents the reference fuel plate for the ATR. Irradiation swelling data at exposures of 2 to 2.5 fissions/cm^3 are of interest if ATR is to go to an extended reactor cycle. We are developing an experiment to examine both UAl_x and U_3O_8 to be irradiated in HFIR to establish the irradiation behavior of plates at this level of burnup. This experiment appears to be ideally suited for HFIR.

Table 19.3. Compositions for Irradiation Experiments 70-3 and 70-4

Experiment Number	Composition Number	Core Material[a]	^{235}U Content (g)	^{10}B Content (mg)
70-3	3	Al + 49.5% U_3O_8	1.07	0.00
	4	Al + 49.58% U_3O_8 + 0.39% B_4C	1.07	1.47
	5	Al + 49.59% U_3O_8 + 0.58% B_4C	1.07	2.21
	6	Al + 49.60% U_3O_8 + 0.78% B_4C	1.07	2.97
	7	Al + 49.62% U_3O_8 + 1.31% B_4C	1.07	4.97
	8	Al + 49.63% U_3O_8 + 1.49% B_4C	1.07	5.66
70-4	1	Al + 42.33% U_3O_8	0.88	0.00
	2	Al + 52.14% UAl_x	0.98	0.00

[a]Experiment 70-3: cores clad with type 6061 Al alloy; experiment 70-4: cores clad with types 6061 and 2219 Al alloys.

Table 19.4. Characterization of Core Components for Experiments 70-3 and 70-4

	Core Materials			
	Burned U_3O_8	Arc-Cast UAl_x	B_4C	Matrix Al
Powder blend designations	PB-5	PB-26	HER	G-12-3
Assay, g U or g B per g sample	0.8430	0.7192	0.7520	a
Enrichment, g ^{235}U or g ^{10}B per g U or B	0.9316	0.9320	0.1836	a
Toluene density, g/cm^3	7.647	6.631	2.513	2.708
Surface area, m^2/g	0.36	0.09	a	a
Distribution of particle sizes, wt %				
−100 +140 mesh	0.0	31.5	0.0	0.0
−140 +170 mesh	0.0	17.3	0.0	0.0
−170 +200 mesh	19.7	13.5	0.0	Trace
−200 +230 mesh	17.5	9.2	0.0	0.1
−230 +270 mesh	17.6	8.6	0.0	1.6
−270 +325 mesh	19.0	14.9	Trace	6.4
−325	26.2	5.0	100.0	91.8

[a]Not determined.

Correlation of Cermet Swelling with Fabrication Voids (A. E. Richt)

Voids in the cores of dispersion fuels after fabrication are thought to be beneficial in reducing swelling of Al-based fuel plates during irradiation. We previously reported[3] that differences in the swelling behavior of six miniature fuel plates irradiated in the G-12 loop of the ETR could be explained by differences in their initial void content. We recently reviewed some results of other tests in the G-12 loop to see if differences in the swelling behavior of other Al-based fuel plates could also be attributed to differences in the void content.[4] We calculated the amount of swelling that should have occurred in these plates by assuming that the fuel cores swelled 6.3% for every 10^{21} fissions/cm^3 and that all the voids initially present in the fuel core could be utilized to accommodate this swelling. As shown in Fig. 19.1, the swelling

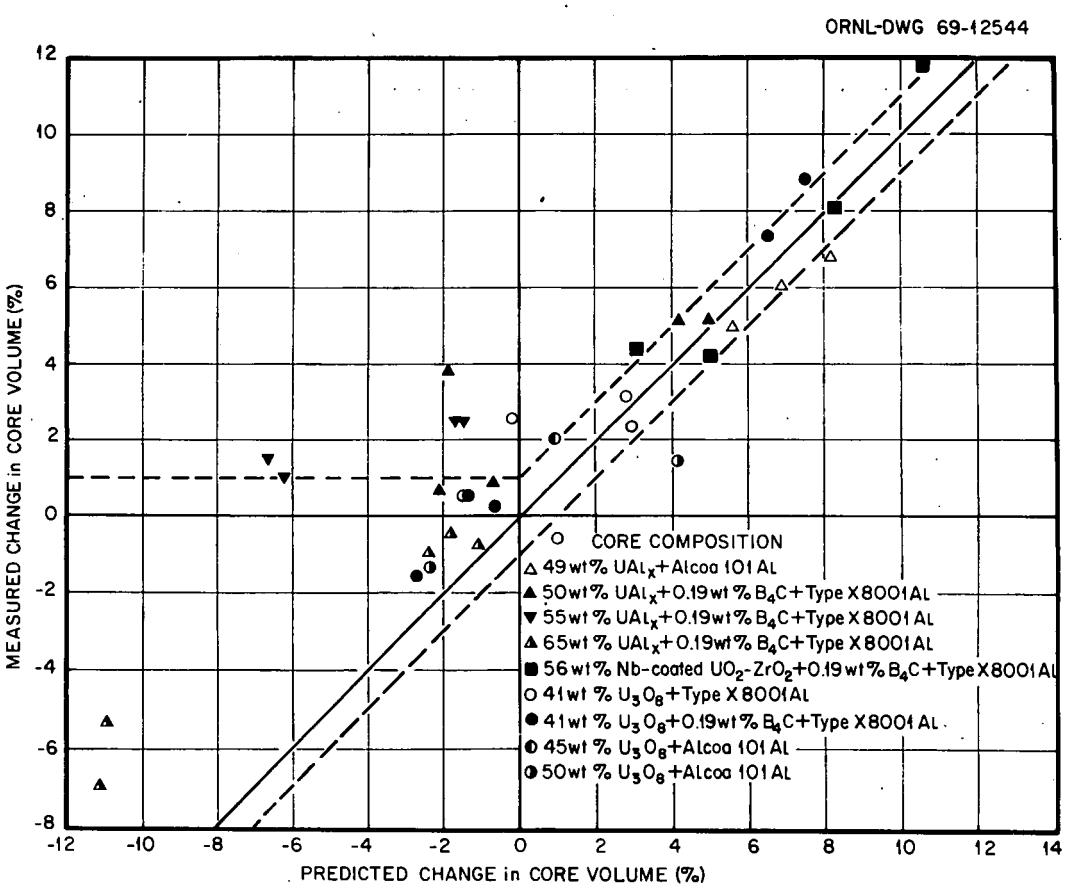

Fig. 19.1. Comparison of Calculated and Measured Changes in Core Volume of Al-Based Dispersion Fuel Plates.

values calculated for each specimen agree quite well with the measured changes in core volume for those irradiation conditions under which the predicted swelling is positive. Consequently, it appears that the differences in the swelling of these fuel plates primarily result from differences in the initial void content of the fuel cores and not from differences in loading or type of dispersion (i.e., U_3O_8, UAl_x, Nb-coated UO_2-ZrO_2). More importantly, these data indicate that one can predict with reasonable accuracy (within about ±1%) the amount of swelling that will occur during irradiation if he knows the initial void content of the dispersion core and the burnup which the plate will receive.

Refractory-Metal Cermet Fuels (M. M. Martin, A. E. Richt)

The AEC terminated the General Electric (Cincinnati) program entitled "Refractory-Metal Fuel Element Material Research." Under direction from AEC, ORNL is performing the postirradiation examination and evaluation of experiment ORRF-5 from that program. The objective of this experiment is to determine the effectiveness of a built-in plenum region in reducing swelling of W-UO_2 and W-UO_2-ThO_2 fuel specimens that contain 3 to 18% void volume in the core. The specimens were scheduled to operate at 1500 to 1650°C and incur a burnup of 2×10^{20} fissions/cm^3 of core.

For experiment ORRF-5, only eight clad fuel specimens were irradiated in the F-2 facility of the ORR. Figure 19.2 illustrates the longitudinal cross section of each of the specimens and gives their core composition and total internal void content in volume percent. The annular fuel core is about 1.19 cm in outside diameter, 0.45 cm in inside diameter, and 3.8 cm long and is clad on both circumferential surfaces and ends with 0.038-cm-thick W-Re-Mo cladding. The overall length of the specimens varied from 5.08 to 6.65 cm depending on the length of the end plenum. Specimen 554-14 contains eight 1.1-mm-diam holes drilled longitudinally into the core to a depth of 2.54 cm; these holes account for 26% of the total 19 vol % internal void content.

The fabrication procedures for the test specimens are reported elsewhere.[5] In general, the essential processing steps are (1) preparation of a fuel agglomerate from enriched UO_2, depleted UO_2, and (in six specimens) ThO_2, (2) blending of the fuel agglomerate with W powder,

ORNL-DWG 69-10890

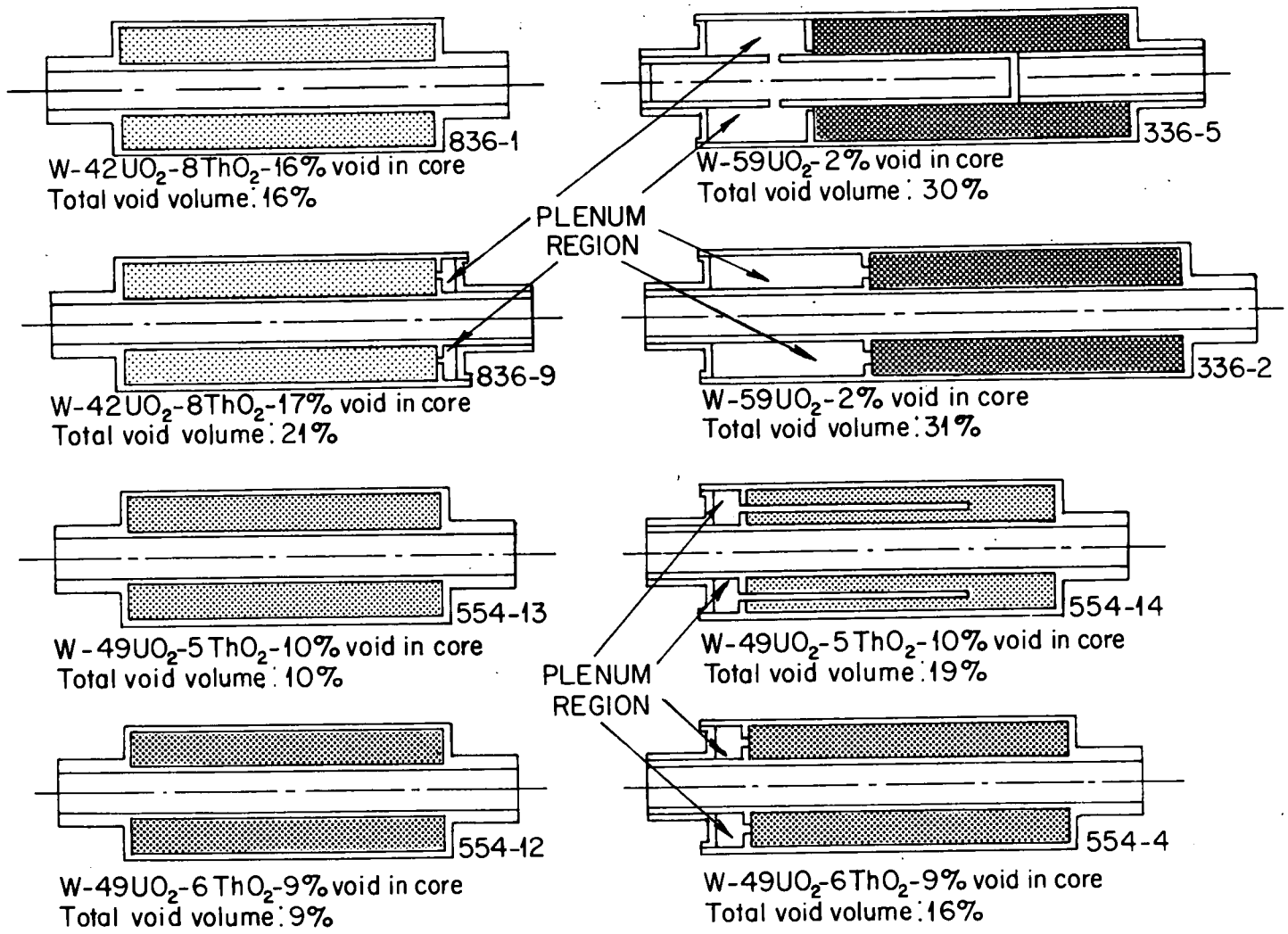

Fig. 19.2. Longitudinal Cross Section of ORRF-5 Test Specimens Showing Integral Plenum Region. Compositions shown are volume percentages.

(3) pressing in a mechanical die, (4) sintering to achieve stoichiometric UO_2, (5) machining, (6) hot autoclaving for dimensional stability, (7) machining to size, (8) cleaning and vacuum outgassing, and (9) hot pressure bonding. Table 19.5 tabulates the detailed core composition, theoretical core density, and ^{235}U content of each specimen.

Changes from their standard composition and fabrication procedure allowed General Electric to produce the three levels of void concentration of about 2, 9, and 16 vol % shown in Fig. 19.2. For example, the high-density specimens of the 336 composition were clad by standard pressure bonding of 700 kg/cm^2 at 1750°C for 3 hr. The fuel agglomerates of UO_2 for this composition were also fired at the standard temperature of 750°C. On the other hand, addition of ThO_2 to UO_2 and firing the resultant fuel agglomerate at 1600°C helped produce the lower density of the specimens from the 554 and 836 compositions. The cores of intermediate density from the 554 composition (about 5 vol % ThO_2) were bonded at a reduced pressure of 350 kg/cm^2. Bonding at 1650°C and 315 kg/cm^2 (for the specimens from the 836 composition, which contained about 8 vol % ThO_2) produced the lowest core density.

Irradiation testing of the specimens began February 18, 1969, and was terminated on July 31, 1969, when fission-product activity was detected in the coolant gas. The specimens operated for about 3400 hr at temperatures above 1250°C and achieved burnups estimated at about 1.5×10^{20} fissions/cm^3. After a short decay period, the test assembly was transferred to the hot cells, where disassembly of the experiment was started on September 2, 1969. Except for sampling of fission gas and sectioning for burnup analysis and metallographic examinations, all phases of the postirradiation examination program were completed, and results are summarized below.

We observed nothing unusual in disassembly of the test assembly; the specimen coolant tubes appeared to be free of obstruction or blockage, and all 16 thermocouples appeared to be in excellent physical condition. The overall appearance of the test specimens after irradiation is shown in Fig. 19.3. In general, the specimens appeared to be in good condition. Swelling of the fuel core is apparent in the slight barrel-like shape of some of the specimens. The cladding over the fueled region of all

Table 19.5. Cermet Composition, Theoretical Density, and ^{235}U Content of ORRF-5 Test Specimens

Composition Number	Specimen Number	Composition of Cermet, wt %		Composition of Fuel Agglomerate, wt %			Theoretical Core Density (g/cm^3)	Total ^{235}U Content (g)
		W Matrix	Fuel Agglomerate	UO_2 Enriched 0.7005 g ^{235}U/g U	UO_2 Enriched 0.0020 g ^{235}U/g U	ThO_2		
336	2	54.00	46.00	4.49	95.51		14.296	0.673
	5							0.668
554	4	54.22	45.78	6.92	83.88	9.20	14.238	0.954
	12							0.958
	13							0.944
	14							0.897
836	1	54.36	45.64	9.86	74.71	15.43	14.200	1.223
	9							1.212

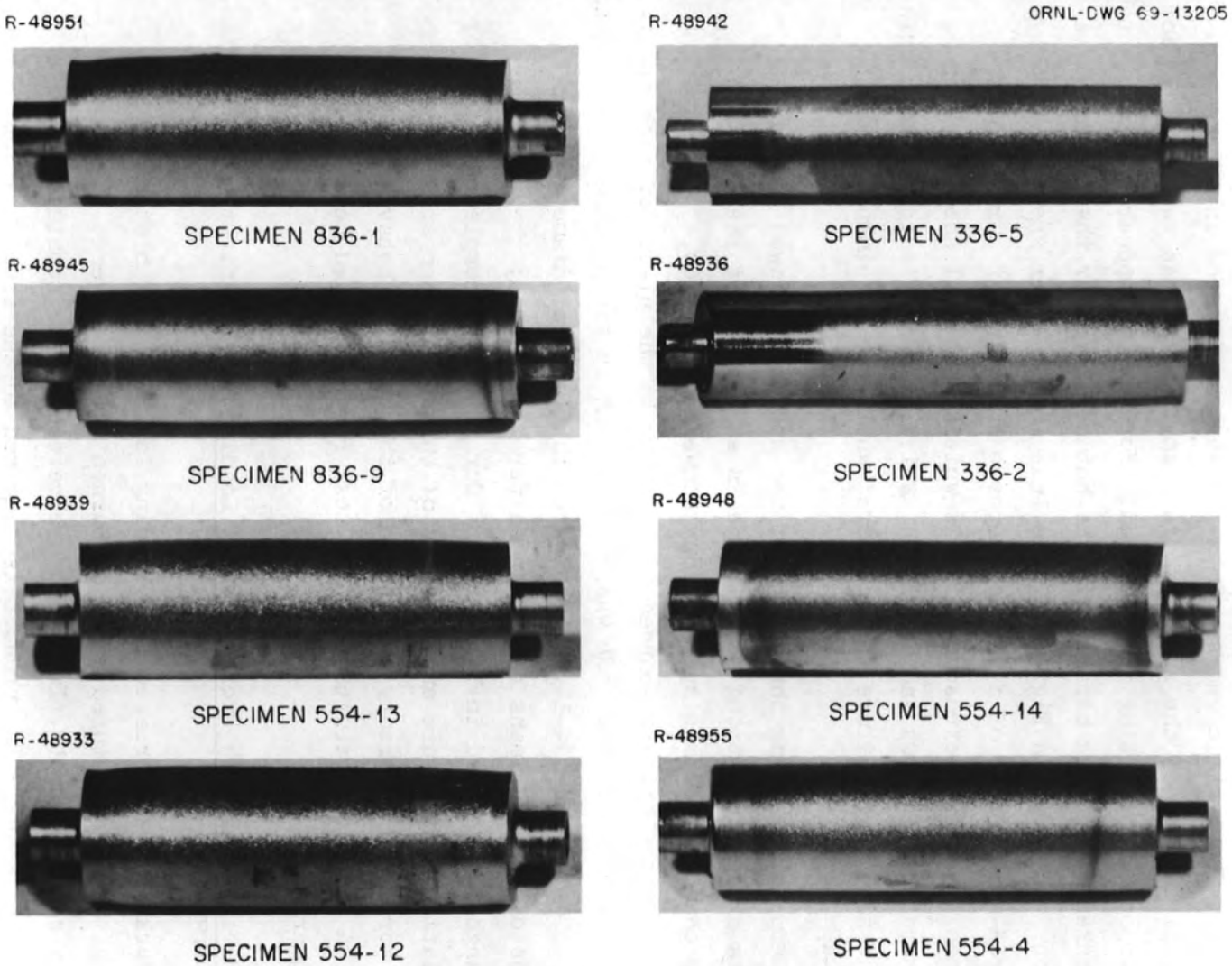

Fig. 19.3. Postirradiation Photographs of Fuel Specimens From the ORRF-5 Irradiation Test Program. Specimen orientation is the same as shown schematically in Fig. 19.2.

specimens had an etched or frosted appearance, while that over the plenum regions was bright and shiny.

Helium leak testing revealed that two specimens had cladding penetrations. The leak in one specimen (836-9) was located in a tack weld at the plenum end of the sample where a small metal tab was attached for the purpose of orienting the specimen. However, it appears that this tab was broken off during handling in the hot cells rather than during irradiation. As shown in Fig. 19.4, the leak in the other specimen (836-1) occurred at the site of a whitish deposit on the outer surface of the specimen. Gamma spectroscopy of this whitish material showed a high concentration of ^{137}Cs and $^{95}Zr/^{95}Nb$, which strongly indicates that this was the site of a failure that occurred while the specimen was in the reactor.

Gamma scans along the length of the specimens showed no unusual effects except for strong activity peaks at the end of the specimen plenum chambers. Gamma spectroscopy showed ^{131}I, ^{134}Cs, ^{136}Cs, and ^{137}Cs to be the primary sources of activity in the plenum of each specimen; however, some $^{95}Zr/^{95}Nb$ was also present in the plenums of specimens 554-4, 554-13, and 554-14. We compared the lengths, diameters, and volumes of the specimens before and after irradiation; the percentage of change is recorded in Table 19.6. Our lack of a complete history of irradiation temperature and analysis of burnup for each specimen prevents more than a cursory evaluation of the specimen behavior at this time. A complete evaluation of the test results should be available next quarter.

HFIR Fuel Plates with Increased Fuel Loading (R. W. Knight, M. M. Martin, J. H. Erwin)

Work on the increased fuel loading for HFIR fuel plates[6] is continuing. We manufactured 25 kg of burned U_3O_8, delivered 15 kg of it to Metals and Controls, Inc., and are retaining the remainder at ORNL for further study. The product is compared to the specification in Table 19.7. The specification was exceeded only for impurities.

The process and control procedure submitted by Metals and Controls, Inc., for manufacturing and evaluating the plates with increased loading

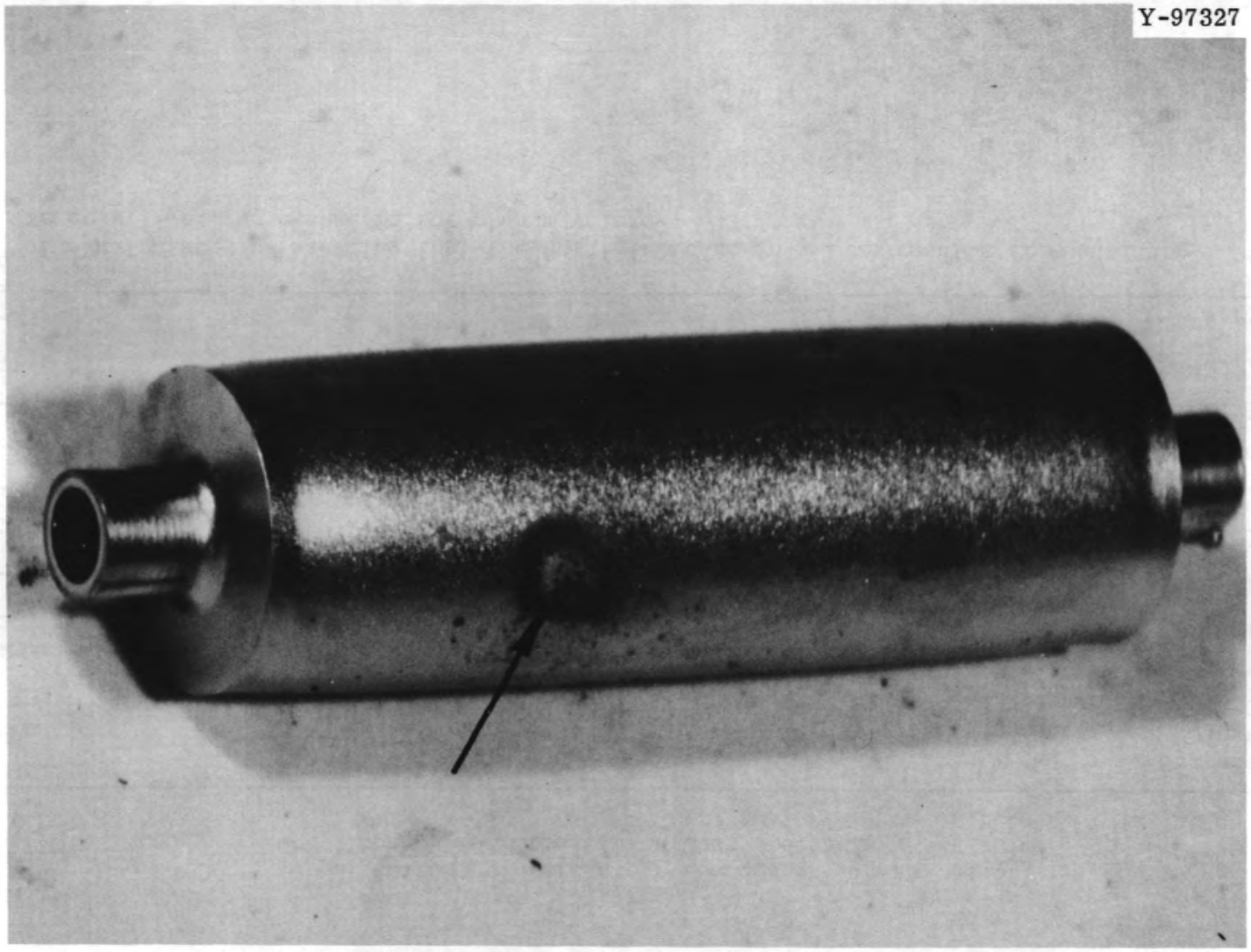

Fig. 19.4. Suspected Failure Area on Specimen 836-1. Approximately 2×.

Table 19.6. Summary of Percentage Changes in Dimensions of the ORRF-5 Irradiation Test Specimens

Specimen Number	Maximum Increase in Outside Diameter (%)	Maximum Decrease in Inside Diameter (%)	Increase in Length (%)	Total Increase in Volume (%)	Increase in Volume of Fuel Core[a] (%)
336-2	3.6	4.5	0.45	4.83	8.95
336-5	1.3	2.5	0.44	2.05	3.76
554-4	2.7	2.3	0.39	4.40	6.33
554-12	6.7	4.7	0.78	12.95	17.12
554-13	4.8	2.7	0.51	8.63	11.44
554-14	1.7	1.6	0.45	2.88	4.23
836-1	5.0	6.2	0.67	9.18	12.21
836-9	3.2	2.1	0.30	4.35	6.12

[a]Value calculated by assuming that the total increase in volume results from swelling in the fuel core only (i.e., no change in the plenum volume).

Table 19.7. Enriched, Burned-Oxide Powder Blend[a] Compared to Specifications

Property	Specification	Product
Total U, wt %	84.5 ± 0.5	84.41
Isotopic U, wt % total U		
^{234}U		1.00
^{235}U	> 93	93.16
^{236}U		0.41
^{238}U		5.43
Impurities, ppm		
Al	30	10
B	1	0.2
Ba	10	< 2
Be	3	< 0.01
Ca	50	30
Cd	3	< 0.1
Co	3	2
Cu	50	10
Cr	200	60
Fe		350 } 520
Ni		110
Li	1	< 0.2
Mg	100	5
Mn	5	6
Na	5	4
K	20	< 6
P	100	< 100
Si	100	200
V	3	< 1
F	10	3.0
Mo	20	60
Sn	10	< 1
W	100	< 100
Zn	20	< 10
Density, g/cm^3	7.65 ± 0.15	7.62
Surface area, m^2/g		0.309
Distribution of particle sizes, wt %		
+170	< 1	0
−170 +325	> 89	96
−325	< 10	4

[a]Batch number 31-5009; requisition number 450003.

was approved. The plates with an increased loading of oxide made according to present HFIR specifications will be fabricated and evaluated first. The burned oxide plates, with both standard and increased loading, will be scheduled in the next quarter.

Technical Assistance for Commercial and Manufacturing Problems

W. R. Martin

Use of ZrO_2 to Generate Fabrication Voids in Composite Plates (J. H. Erwin, M. M. Martin, R. W. Knight)

We showed[7] that ZrO_2 added to Al as a dispersoid will result in additional fabrication voids and that the number of voids is dependent upon the concentration of the dispersoid. Our initial intent was to use this approach to reduce the amount of swelling that might be expected in an inner annulus of the advanced HFIR element because of the He from the $^{10}B(n,\alpha)^{7}Li$ reaction. However, it appears that this procedure may also provide a reduction in rejections for bond defects. Over half of the total rejections of HFIR fuel plates are for bond defects, most of which are only on the filler side of the plate. We speculate that the addition of fine voids to the filler, which is of a much higher density than the fuel core, would provide sites for the gases that cause blistering and would reduce the rejection rate.

When complex miniature plates containing layered cores of both filler material and fuel without the ZrO_2 addition were rolled, they blistered; similarly rolled plates containing 50 wt % ZrO_2 (3% fabrication voids) in the filler side did not blister. We recognize the inherent inconsistency of predictions of blistering and do not consider these results conclusive. However, we consider this approach to be reasonable; and, if it is successful, it could make the largest single improvement in the rejection rate for HFIR fuel plates.

We have asked the reactor operators to estimate the influence that ZrO_2 additions would have on the operation of the reactor and to establish the maximum level of Hf that can be tolerated as an impurity.

Twenty-four full-size outer-annulus plates containing up to 50 wt % ZrO_2 in the filler will be fabricated for the HFIR to determine the influence of this dispersoid on the fabricability of full-size plates and the amenability to inspection by ultrasonics and x-ray attenuation and to gather more data on the frequency and location of blisters.

Fabrication Behavior of Plates That Contain Shaped Cores (J. H. Erwin)

Shaped cores are used commercially to minimize the consequence of dogboning, but occasionally other problems arise because of these cores. Using fuel plates that contain shaped powder-metallurgy cores and simulated cores of like geometry fabricated from wrought type 2219 Al, similar to those described elsewhere in this report,[8] we are characterizing the behavior of the cores during hot and cold rolling.

Radiographic and physical measurements on the core and plate after each pass are being used to characterize the deformation. Although our study is not complete (the rolling has been finished through the fifth hot-working pass), we have observed the following from our results to date.

1. During the first two passes of 15% reduction in area per pass, the misfit space within the frame cavity is filling up with core, but the powder-metallurgy core undergoes little densification.

2. On the second, third, and fourth passes, the powder-metallurgy cores appear to densify.

3. After the third pass, tapered or shaped cores spread or elongate less than the rectangular cores (most of the difference appears to be in spread). It is possible that the tapered cores may be more dense than the rectangular cores. Preliminary analyses indicate that the difference after five passes may be equivalent to 1% reduction in fabrication voids for tapered cores.

4. Tapered cores have not cracked thus far, but radiographs between passes show the small gap between the end of the core and the frame that we discovered last year in our high-speed motion pictures of dogboning.

Susceptibility to Blistering of Fuel Plates That Contain Shaped Fuel Cores (J. H. Erwin)

We previously reported[9] no apparent blistering of type 6061 Al fuel plates as a result of poor fit between 46 wt % U_3O_8-Al powder-metal compacts and the frame. Fuel cores 5% undersize in thickness, width, or length did not blister during the final anneal of the 0.050-in.-thick rolled plate. Later we reported[10] profuse blistering of plates containing shaped simulated cores of wrought types 6061 and 2219 Al rolled in type 6061 Al cladding. We were in error in stating that the size of the blisters was reduced by a high reduction rate; the blister size was reduced when the mill passes were 10% rather than the normal 24%.

During this reporting period, we determined the effect of poor core fit upon the formation of blisters when the simulated cores were shaped rather than rectangular. Standard double-cavity billets of Alclad type 6061 Al for the HFIR outer annulus were loaded with a 46 wt % U_3O_8-Al (U depleted in ^{235}U) powder-metal compact and a simulated core of like geometry fabricated from wrought type 2219 Al. Before assembly, the U-bearing cores were degassed for 2 hr at 500°C in a vacuum furnace; the simulated cores of type 2219 Al, the frames, and cover plates were chemically cleaned with Oakite 160. Thirty billets were rolled according to the present HFIR production schedule. These consisted of ten duplicate billets and three different core geometries: (1) rectangular cores with 3.3% cavity overfill, (2) cores with 1/8-in.-radius chamfer on four edges (leading and trailing ends) and with 1% cavity underfill, and (3) cores with 1/2-in.-radius chamfer on the four edges and 5.3% underfill.

Inspection of the fabricated plate, cold rolled to 0.050-in. thickness and annealed 2 hr at 500°C, revealed no blisters in the U_3O_8-bearing cores while the majority of the simulated cores of type 2219 Al blistered, as shown in Table 19.8.

From both these and the earlier data[9] it appears that high-density cores, such as those simulated by wrought types 6061 and 2219 Al, will result in blistered plates more readily than lower density powder-metallurgy cores. In the earlier study of the fit of frame to cavity, using powder-metallurgy cores, we found no blistering for the range of

Table 19.8. Blistering in Fuel Plates[a] Containing Shaped U_3O_8-Al and Simulated Fuel Cores

Plate Description	Number of Cores Rolled	Number of Plates Blistered	
		One End	Both Ends
Rectangular cores with 3.3% overfilled cavity			
46 wt % U_3O_8 and Al powder	10	0	0
Wrought type 2219 Al	10	3	4
1/8-in. chamfer on leading and trailing edges			
46 wt % U_3O_8 and Al powder	10	0	0
Wrought type 2219 Al	10	1	9
1/2-in. chamfer on leading and trailing edges			
46 wt % U_3O_8 and Al powder	10	0	0
Wrought type 2219 Al	10	0	10

[a]Billets were standard HFIR Alclad type 6061 Al fabricated into plate according to standard HFIR procedure.

misfits examined. In the current study, the largest taper on the wrought cores resulted in a higher rate of blistering when we consider the total plate surface. From these data, it appears that the powder-metallurgy compact is a factor in the blistering of fuel plates during rolling, either due to compact density or compositional variables such as Al_2O_3 dispersion.

Factors That Affect the Oakite Cleaning Process (J. H. Erwin)

Our investigation of the Oakite 160-HNO_3 chemical cleaning process used to ensure satisfactory interfacial grain growth during roll bonding is continuing in an effort to determine the limitations of the standard procedure.

The concentration of the Oakite 160 solution was reduced from the 10% previously established as the standard to 5 and 2.5% with no effect on the cleaning potential of new solutions. Interfacial grain growth along the bond lines of type 6061 Al after rolling remained about 85%.

We have not yet established the effect of the dilute concentrations on the lifetime of the solutions.

Variations in temperature from 55 to 82°C compared to the 74°C standard have not changed the cleaning results significantly.

Time intervals between cleaning and rolling have been cursorily examined for times up to two weeks; again, no significant effects were noted on the interfacial grain growth after rolling.

The shelf life of the solution appears to be at least greater than a few months. In fact, we have yet to see an inhibiting effect of shelf life, although there certainly must be a point at which the solution will deteriorate.

To date, we have noted one variable that does inhibit the cleaning. The lifetime of the solution is dependent upon the amount of Al cleaned. We have seen interfacial grain growth reduced to 75% on roll-bonded sheets when a large amount of material has been cleaned. The rate of deterioration appears to be controlled by the weight of Al dissolved in the cleaning solution. We are now attempting to establish from both our results and the experience at Metals and Controls, Inc., the tolerable level of Al in solution. This tolerance appears to be the factor to use for quality control.

A sludge that tends to precipitate from the cleaning solution onto the floor of the tank must be removed from the cleaning tank because it will clog drains up to 1.5 in. in diameter unless they are flushed regularly with a large volume of water.

Evaluation of Surface Chemistry on Some Chemically Cleaned Plates (R. W. Knight)

On one occasion, etching with Oakite 160 resulted in a very uneven plate thickness,[11] as shown in Fig. 19.5. Two 1/4-in. plates of type 6061-T6 Al, purchased from the same vendor, etched preferentially after heat treatment at 500°C for 1 hr. An analysis of the unetched areas protruding above the etched metal showed the inhibiting contaminant to be Ni. Whether the Ni is there as a compound or free Ni is not known. When the Al was etched as received with no intervening heat treatment, no problems were encountered. We postulate that the plates

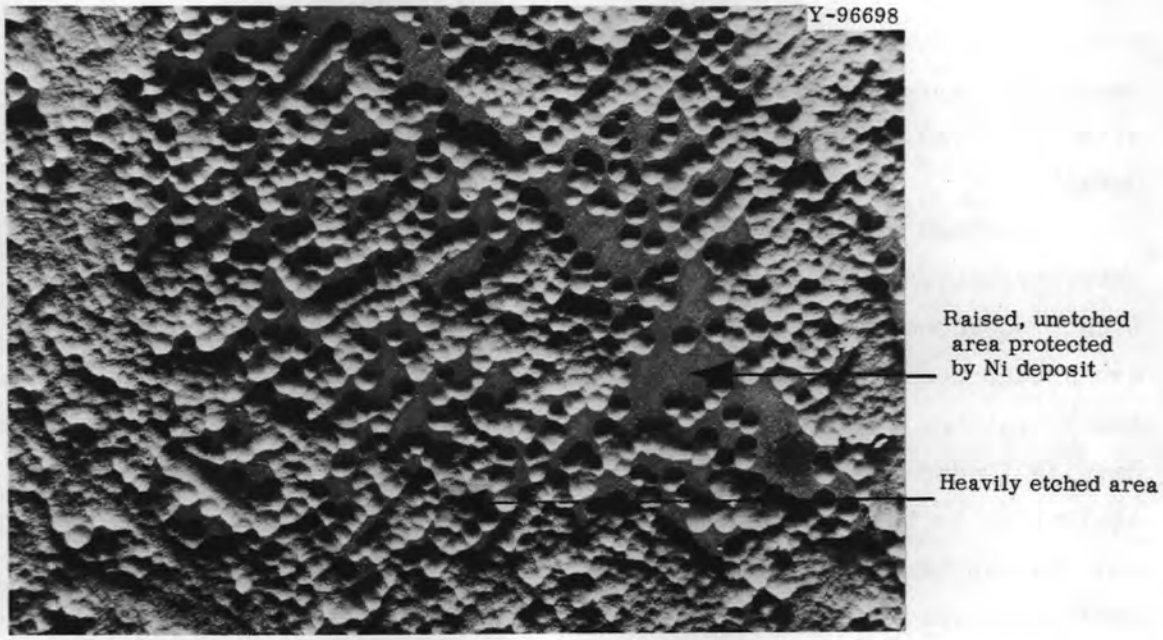

Fig. 19.5. Nonuniform Etching of Heat-Treated Type 6061 Aluminum With Nickel Contaminant.

were exposed to a soluble Ni compound that was reduced during heat treatment so that the inhibiting Ni was left diffused on the surface of the plate.

Fabrication Development

W. R. Martin

Deformation Characteristics of U_3O_8-Al and UAl_x-Al Dispersion Fuel Plates with Increased Loadings (M. M. Martin)

We showed[12] that many factors influence the formation of the localized core thickening (a dogbone shape) in Al-based fuel plates. The judicious selection of materials, plate design, and roll-cladding procedures can reduce, if not entirely eliminate, the formation of a dogbone. The effect of the initial density of the fuel dispersion on the formation of a dogbone is unknown, however. This factor may be of major importance to the fabricator, since it can be controlled easily. For example, fuel compacts with a large initial void content may densify during the first few passes through the rolling mill instead of forming

a dogbone. That could reduce the dogboning in final fuel plates. However, any changes in core density must be carefully evaluated for their effects on radiation damage, since this problem increases with increasing density.[13]

To determine the effect of initial compact density on the deformation characteristics of Al-based fuel plates, we are investigating the formation of dogbone and the final void content of U_3O_8-Al and UAl_x-Al dispersions that contain about 41 vol % of the fuel compound. The dispersoid concentrations are 71.6 wt % U_3O_8 and 67.2 wt % UAl_x and are the most heavily loaded fuels to be fabricated at ORNL. The UAl_x loading is equivalent to the 7F element design for the ATR. The two fuel compounds and the matrix Al were similar to previous batches, and their U assay, toluene density, and distribution of particle sizes compare favorably with HFIR and ATR core materials.

The dispersions were fabricated by conventional powder-metallurgy techniques and then clad with type 6061 Al by roll bonding at 490°C. To achieve various concentrations of voids, we chose compact pressing pressures of 20, 30, and 50 tsi and compact degassing temperatures of 25 (as pressed), 400, 500, and 600°C. All compacts that would subsequently be degassed were pressed at 30 tsi.

Table 19.9 records the average concentrations of dispersoid and voids in the compacts prepared for the investigation. The values given in Table 19.9 are calculated from the toluene density of the U_3O_8, UAl_x, and 101 Al powders, the weight of the components in the compacts, and the geometric volume of the compacts. As pressed, the U_3O_8- and UAl_x-bearing compacts had comparable void contents at each of the three pressing pressures. As expected, the compacts pressed at 50 tsi are considerably more dense than those pressed at 30 tsi, which, in turn, are more dense than those pressed at 20 tsi.

Selected compacts were degassed at less than 0.05 torr for 1 hr at temperature. A comparison of pressed to degassed void contents in Table 19.9 shows that the U_3O_8-Al compacts grew about 1.5 vol % regardless of the degassing temperatures of 400, 500, and 600°C. Compacts that contained UAl_x, however, grew only 0.7 vol % at 400°C but essentially doubled their void content at 500°C. We believe the small degree of

Table 19.9. Effect of Pressing Pressure and Degassing Temperature on the Void Contents of 71.6 wt % U_3O_8-Al and 67.2 wt % UAl_x-Al Compacts[a]

Pressing Pressure[b] (tsi)	Degassing Temperature[c] (°C)	Concentration,[d] vol %	
		Dispersoid	Voids
	High-Fired U_3O_8-Al Compacts		
20	None	39.0	13.5
30	None	40.8	9.7
50	None	42.2	6.7
30	400	40.1	11.2
30	500	40.2	11.2
30	600	40.2	11.1
	Arc-Cast UAl_x-Al Compacts		
20	None	40.9	13.8
30	None	43.1	9.2
50	None	44.7	5.8
30	400	42.8	9.9
30	500	39.0	17.9

[a]Compact dimensions: 0.73 in. long by 0.96 in. wide by 0.15 in. thick.

[b]Pressure applied for 6 sec.

[c]Compacts degassed for 1 hr at less than 0.05 torr.

[d]Each value represents average from four compacts. Maximal dispersoid concentration and void content ranges were ±0.1 and ±0.2 vol %, respectively.

swelling in the U_3O_8 compacts at 400, 500, and 600°C and in the UAl_x compacts at 400°C resulted from the evolution of adsorbed gases that caused separation at grain boundaries and powder surfaces.[14] Undoubtedly, the transformation of the UAl_x, induced by diffusion,[15] caused the large change in volume observed at 500°C. All swelling observed agrees with values predicted from our earlier work.[14] We would expect more growth at 600°C, but the UAl_x-Al compacts we intended to degas at 600°C melted during the degassing treatment when the furnace thermocouple failed.

From a practical viewpoint, we eliminated from this investigation the 600°C treatment on UAl_x-bearing compacts.

We are rolling four identical compacts for each combination of pressing pressure and degassing temperature. Each group of compacts was assembled into a single rolling billet and then roll bonded simultaneously into four fuel plates. Their hot reductions in thickness per pass in chronological sequence are 15, 15, 25, 25, 25, 25, 20, and 10%. Before each hot pass, the billets are rotated 180° about their longitudinal and transverse axes and reheated to rolling temperature. At the completion of hot rolling, the plates are cold rolled to 20% reduction in thickness and annealed at 490°C.

After each hot-rolling pass and each cold-rolling mill setting, the billets are being analyzed for dogboning by x-ray attenuation. Typical results through six hot passes for the U_3O_8-Al dispersions pressed at 30 tsi and degassed at 500°C are shown in Fig. 19.6. To date, all the

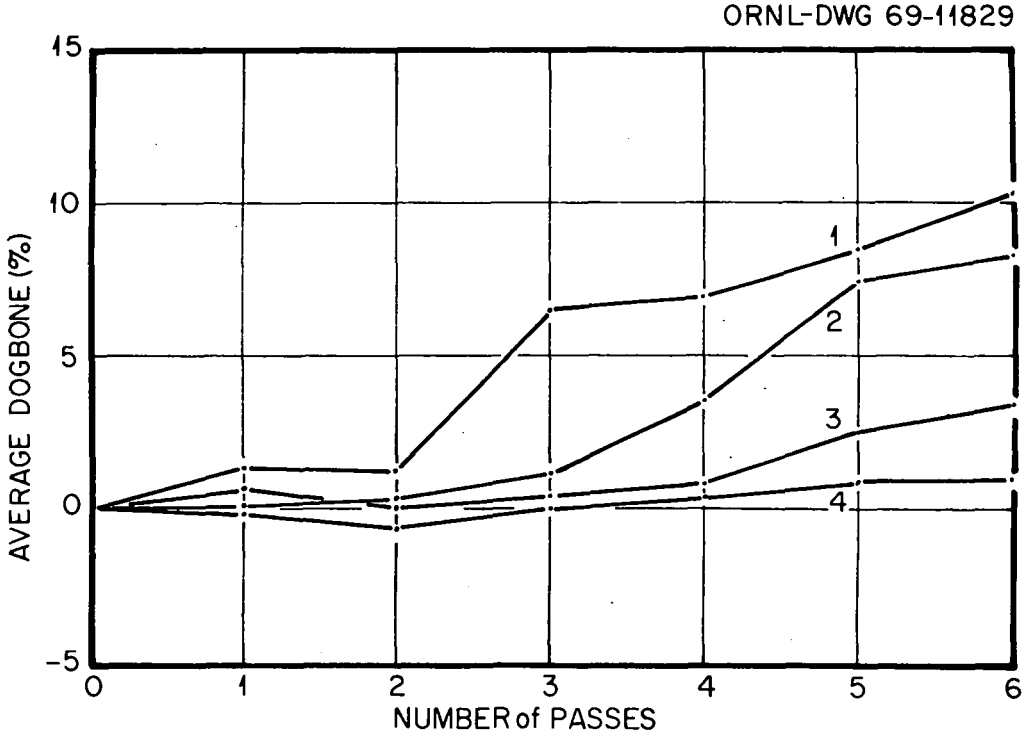

Fig. 19.6. Dogboning of Four 71.6% U_3O_8-Al Cores Within Type 6061 Al Frames and Cover Plates During Rolling at 490°C. Compacts were pressed at 30 tsi and then degassed at 500°C. Dogboning determined for unnumbered core end by x-ray attenuation techniques.

plates have been rolled through the eighth pass, and we are analyzing the data. We anticipate that the investigation will be completed before the next reporting period.

After the plates are rolled and blister annealed, the density of the clad dispersions will be obtained by conventional pycnometer techniques and from the density of the type 6061 Al cladding. Density will be measured again after cold rolling and annealing. From the theoretical density of the dispersions, we can then calculate their void content.

Development of Nondestructive Inspection Techniques

R. W. McClung

Radiographic Densitometry (B. E. Foster, S. D. Snyder)

We have completed our extensive study of the qualitative and quantitative capabilities and limitations of radiography and densitometry for detecting and measuring fuel inhomogeneity in dispersion-core fuel plates.[16] We investigated variables such as x-ray energy, exposure time, distance between film and focal spot, x-ray scattering, film processing, safelight exposure, densitometer aperture size, and repeatability. We found that by radiographing a step wedge on the same film with the fuel plate, assuming nominal fuel loading, and obtaining a separate calibration on each radiograph, comparative values of fuel homogeneity could be made without exercising extremely close control of x-ray energy, exposure times, and film processing. This mild relaxation is possible since the step wedge keeps such variations insignificant compared to the inaccuracy of ±0.02 in measuring film density due to the inherent limitation of the densitometer. This causes a ±5% uncertainty in the resultant data for inhomogeneity at the reference film density of about 1.0 and x-ray energy of 100 kilovolts constant potential (kvcp). Of course, care must be exercised to minimize local variations in the intensity of the x-ray beam and film processing.

We found that exposure of film to safelights before exposure to x rays had less effect on film density than exposure to safelights after exposure to x rays. Film exposure of 30 min to red safelights

produced a density change equivalent to only 6% inhomogeneity, but the same exposure to amber safelights caused a density change equivalent to 70% inhomogeneity. This would be particularly troublesome for nonuniform exposure across the film. We recommend use of red rather than amber safelights for quantitative radiography-densitometry.

Densitometric measurements were made on ten different areas 2 in. long by 0.078 in. wide of a radiograph of a HFIR fuel plate. All radiographic variables had been carefully controlled. Using an Al step wedge for control, we determined the thicknesses of Al for equivalent film density on each of these areas. Sample area 3 was selected as the standard or base, and the percentage difference of the other nine areas from this base was calculated. These data are shown in Table 19.10 along with the values obtained from x-ray attenuation scanning of these same sample areas. The data from densitometry agree fairly well with those from x-ray attenuation scanning, and, with one exception, are within the ±5% uncertainty due to the inherent inaccuracy of ±0.02 of the densitometer.

Table 19.10. Comparative Values of Fuel Inhomogeneity As Determined by Radiography and X-Ray Attenuation Scanning

Sample	Densitometry		X-Ray Attenuation Scanning
	Equivalent Thickness of Al (in.)	Deviation of Al Thickness From Sample 3 (%)	Deviation of U Content From Sample 3 (%)
1	0.140	−30	−33
2	0.173	−14	−14
3	0.201		
4	0.221	+10	+10
5	0.233	+16	+19
6	0.248	+23	+25
7	0.258	+28	+27
8	0.255	+27	+26
9	0.252	+27	+23
10	0.250	+24	+16

Effect of Variations in Fuel Particle Size on X-Ray Attenuation
(B. E. Foster, S. D. Snyder, M. M. Martin)

We began a program for systematically checking the effect of the size and surface area of particles on the calibration curve for x-ray attenuation for both high-fired and burned-U_3O_8 powders in fuel plates. This program may allow us to evaluate the probable bias between the existing calibration curve and calibration curves produced by well-defined particle sizes and provide a check on the consistency of a particle-size recipe for batch blending. The study also offers the potential for establishing calibration curves without analytical chemistry. The 52 plates fabricated for this program have flat cores and are similar in size to irradiation test plates. They match the present HFIR plates in rolling schedule, ratio of Al:U per unit of volume through the plate, filler and cladding materials, and finished thickness. The variables are type of oxide, oxide loading, and oxide particle distribution.

After sampling, the as-received oxides were separated into known mesh fractions. To separate the powders we sieved as many as six times on standard screens and a Ro-Tap Shaker. Preparation of the blends to match the desired distribution of particle sizes required only recombining the desired proportion of each separated fraction. Characteristics of all of the prepared materials are tabulated in Table 19.11. Note that the values for surface area and toluene density appear to be independent of the particle size but differ for the two types of U_3O_8. We conclude that the values for surface area reflect principally the surface roughness of the powders and that the differences in toluene density indicate the amount of porosity within the particles. The variations among the toluene densities for the various blends of either high-fired or burned U_3O_8 are real but are not believed to affect the fabricability of the clad fuel dispersion.

Using the appropriate particles, we have pressed and degassed 52 duplex compacts. Each compact is a rectangular parallelopiped, 0.734 in. long by 0.964 in. wide by 0.268 in. thick, consisting of two integrally mating sections: (1) a fuel section of 30 wt % U_3O_8-Al that varies in thickness to permit the desired loading of 1.0, 1.5, 2.0, and 2.5 g U,

Table 19.11. Characterization of Uranium Oxides

Powder Blend Designation	Specified Range of Particle Sizes		Surface Area (m^2/g)	Toluene Density (g/cm^3)	U Content (wt %)	Particle Size[a]	
	Mesh	μm				Major Range (μm)	Fines < 44 μm (wt %)
			High-Fired U_3O_8 (Batch 30-2627)				
PB-12	−170 +200	88–74	0.052	8.129	84.68	105–62	2
PB-13	−200 +230	74–62	0.040	8.176	84.66	88–62	3
PB-14	−230 +270	62–53	0.047	8.141	84.66	88–53	2
PB-15	−270 +325	53–44	0.052	8.119	84.66	74–44	8
PB-16	−325	< 44	0.051	8.209	84.71	62–0	55
PB-17	b	b	0.051	8.230	84.66	88–0	10
PB-18	c	c	0.049	8.195	84.68	88–0	9
			Burned U_3O_8 (Batch 30-2628)				
PB-19	−170 +200	88–74	0.227	7.641	84.73	105–62	7
PB-20	−200 +230	74–62	0.205	7.678	84.79	88–53	7
PB-21	−230 +270	62–53	0.245	7.646	84.73	88–53	4
PB-22	−270 +325	53–44	0.303	7.658	84.75	74–44	8
PB-23	−325	< 44	0.269	7.633	84.72	53–0	30
PB-24	b	b	0.268	7.662	84.71	88–0	13
PB-25	c	c	0.256	7.654	84.75	88–0	10

[a]From Coulter Counter analysis.

[b]As received from Y-12 plant; > 90 wt % −170 +325 mesh particles.

[c]Blend of separated size fractions; > 90 wt % −170 +325 mesh particles.

and (2) a complementary section of Al filler. Table 19.12 summarizes the void content of the fuel and filler sections. As expected, the fuel sections of burned U_3O_8 in Al contained about 2.5 vol % more voids than those with high-fired U_3O_8. For each type of fuel dispersion, the four fuel loadings (four thicknesses of fuel section) as well as the seven distributions of U_3O_8 particle sizes gave identical void concentrations.

Table 19.12. Void Content of Degassed Compacts[a]

Composition	Number of Compacts	Average Void Concentration (vol %)	Estimate of Standard Deviation	
			Value (vol %)	Degrees of Freedom
Fueled section				
30.16% high-fired U_3O_8 + Al	26	4.14	0.230	25
30.03% burned U_3O_8 + Al	26	6.69	0.322	25
Filler section, Alcoa 101 Al	5	2.69	0.070	4

[a]Compacts pressed at 30 tsi, then degassed for 1 hr at 500°C.

The compacts have been clad with type 6061 Al, alclad with type 1100 Al, and rolled into the desired plates but have not been fully evaluated in plate form.

Studies of Joining and Assembly

G. M. Slaughter

Joining Fuel Plates to Side Plates (W. J. Werner)

The data from our systematic investigation of the effects of variations in electron-beam welding conditions on weld penetration and geometry are being analyzed statistically. These analyses should be completed next quarter.

We were unable to extend our study during this reporting period because a transformer in the power supply for the electron-beam welder failed and we were unable to obtain a replacement part. A new part has now been shipped.

Construction of Prototype Element (W. J. Werner, R. W. Knight)

The removable extension to our low-voltage electron-beam welding chamber was received and installed (Fig. 19.7). We checked the system for leaks and found that, with the existing pumping facility, we were

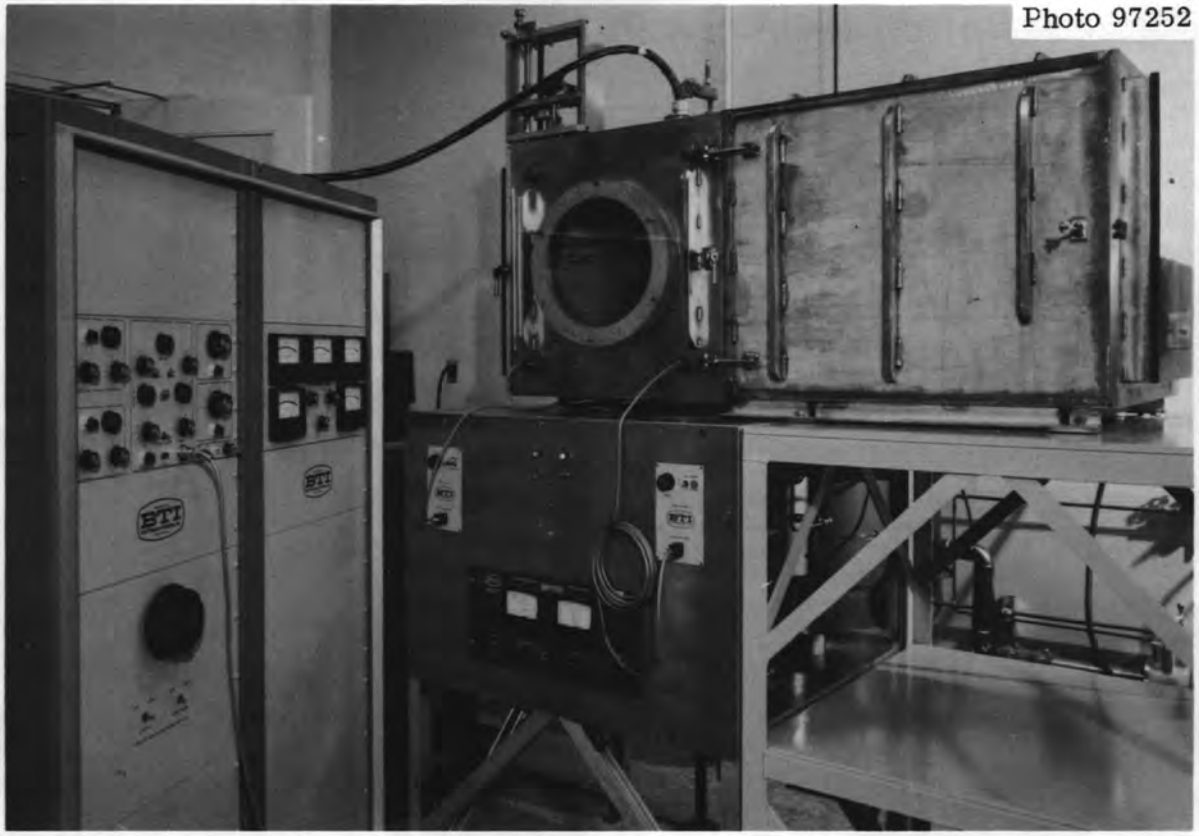

Fig. 19.7. Low-Voltage Electron-Beam Welder with Extension for Fabricating Aluminum Fuel Elements.

readily able to achieve a vacuum of 4×10^{-6} torr. Since much outgassing will probably occur during the welding of a HFIR element, provisions were made to attach an additional diffusion pump to the extension. The drawings for the rotating mechanism were changed slightly to accommodate various lengths of HFIR fuel elements. We anticipate that construction of this piece of hardware will be completed during this reporting period.

References

1. Plant and Equipment Division.
2. M. M. Martin and J. H. Erwin, Fuels and Materials Development Program Quart. Progr. Rept. June 30, 1969, ORNL-4440, pp. 208–209.
3. A. E. Richt and M. M. Martin, Fuels and Materials Development Program Quart. Progr. Rept. Dec. 31, 1969, ORNL-4390, pp. 251–258.

4. V. A. Walker et al., ATR Fuel Materials Development Irradiation Results — Part II, IDO-17157, June 1966.

5. AEC Fuels and Materials Development Program, Eighth Annual Report, GEMP-1011, pp. 131–134, (Feb. 28. 1969). Classified.

6. R. W. Knight, M. M. Martin, and J. H. Erwin, Fuels and Materials Development Program Quart. Progr. Rept. June 30, 1969, ORNL-4440, pp. 200–202.

7. M. M. Martin and J. H. Erwin, Fuels and Materials Development Program Quart. Progr. Rept. June 30, 1969, ORNL-4440, pp. 195–196.

8. J. H. Erwin, "Susceptibility to Blistering of Fuel Plates That Contain Shaped Fuel Cores," pp. 230–231, this report.

9. J. H. Erwin, Fuels and Materials Development Program Quart. Progr. Rept. Sept. 30, 1968, ORNL-4350, pp. 6–10.

10. J. H. Erwin, Fuels and Materials Development Program Quart. Progr. Rept. June 30, 1969, ORNL-4440, pp. 198–200.

11. J. H. Erwin, Fuels and Materials Development Program Quart. Progr. Rept. June 30, 1969, ORNL-4440, pp. 197–198.

12. J. H. Erwin, W. R. Martin, and R. W. Knight, Fuels and Materials Development Program Quart. Progr. Rept. Dec. 31, 1968, ORNL-4390, pp. 223–234.

13. M. M. Martin and A. E. Richt, Trans. Am. Nucl. Soc. 12, 98 (1969).

14. A. K. Chakraborty, Fuels and Materials Development Program Quart. Progr. Rept. June 30, 1968, ORNL-4330, pp. 317–320.

15. J. L. Gregg, R. S. Crouse, and W. J. Werner, Swelling of UAl_3-Al Compacts, ORNL-4056 (1967).

16. B. E. Foster, S. D. Snyder, and R. W. McClung, Fuels and Materials Development Program Quart. Progr. Rept. Dec. 31, 1968, ORNL-4390, pp. 261–266.

20. TECHNICAL ASSISTANCE IN PROCUREMENT OF FUEL ELEMENTS

G. M. Adamson, Jr. W. R. Martin

The purpose of this program is to provide technical assistance and inspection surveillance to the AEC-RDT in its effort to procure fuel and neutron-absorber components from commercial sources for AEC-owned research reactors. Through this program, immediate technical help can be made available to analyze and solve problems as they arise in manufacturing plants of commercial vendors.

Technical Assistance in Solving Pressing Manufacturing and Inspection Problems

R. W. Knight

Representatives of the National Lead Company visited ORNL to review recent developments in the manufacture of fuel elements. We discussed causes and control of nonuniform deformation (dogboning), manufacturing of UAl_x, procedures for use of unclad type 6061 Al in fuel plates, and the production of fuel elements for the High Flux Isotope Reactor.

CLADDING AND OTHER STRUCTURAL MATERIALS

21. BEHAVIOR OF REFRACTORY MATERIALS UNDER IRRADIATION

G. M. Watson[1] G. W. Keilholtz[1]

The purpose of this program is to evaluate the effects of high fast-neutron fluences at temperatures up to 1100°C on the properties of refractory nuclear materials for both space and civilian power reactors. The investigation of carbides, nitrides, and silicides of refractory metals is nearly complete. The present program has two major objectives: (1) the determination of the effects of He gas produced by fast neutrons in depleted UN fuels, and (2) investigation of the effects of fast neutrons on materials considered for control of reactivity in fast-flux reactors.

Irradiation Damage to Nonfissionable Refractory Materials

D. A. Dyslin[2] R. E. Moore[1] H. E. Robertson[1]

Refractory Metal Carbides

Results of irradiations of carbides of Ti, Zr, Ta, Nb, and W at intermediate and high temperatures were reported previously.[3–5] Results of a low-temperature irradiation at low fluences are reported below. A high-fluence irradiation at low temperatures is still continuing in the Engineering Test Reactor (ETR). Results of annealing experiments conducted out-of-reactor are now available and have contributed to our understanding of mechanisms of neutron damage.

Low-Temperature Irradiation of Carbides. – Two uninstrumented assemblies containing carbides were irradiated at low temperatures in the J-12 position of the ETR. Calculated temperatures of the specimens of each type of carbide from the lowest to the highest rate of gamma-heat generation are as follows: TiC, 65 to 100°C; ZrC, 65 to 90°C; TaC, 80 to 120°C; NbC, 70 to 100°C; and WC, 90 to 130°C. Results from the short-term assembly are reported below. The long-term assembly of the pair is still undergoing irradiation.

The fractional volume expansions of specimens irradiated in the short-term assembly are given in Table 21.1. Initial slopes of the curves for fractional volume change (i.e., $\Delta V/V$, or change in volume divided by original volume) versus fast fluence were obtained from plots of these data and are as follows: TiC, 0.24; ZrC, 0.22; TaC, 0.15; NbC, 0.14; and WC, 0.24.

Half of the specimens of each type of carbide were made by slip casting and half by explosion pressing. There were no significant differences in $\Delta V/V$ between specimens made by the two methods.

Out-of-Reactor Annealing Experiments. — Specimens of carbides that were irradiated at intermediate temperatures in previous experiments were annealed out-of-reactor at increasingly higher temperatures. The annealing was continued at each temperature until no further changes in dimensions could be detected. This took no more than 24 hr in most cases, but the specimens were annealed longer to be certain that the dimensions were stable.

Figures 21.1 and 21.2 show the annealing results for TiC and ZrC. In each case there was a rapid reduction in the fractional volume increase followed by a leveling off when the annealing temperature was increased to 900 to 950°C. Titanium carbide shrank only slightly more between 950 and 1100°C, but the explosion-pressed ZrC specimen shrank considerably at 1100°C. The expansion of the slip-cast specimen at annealing temperatures above 900°C was unexpected, and we cannot yet explain it.

The volume increase at the point at which leveling off occurs may represent the contribution of defect clusters to the overall volume expansion. Accordingly, the shrinkage down to the leveling-off point would represent the contribution of the easily annealed single displacements. Annealing of clusters is assumed to be a sintering process, which requires very high temperatures.

Mechanism of Neutron Damage to Carbides at Irradiation Temperatures up to 1100°C. — Using more recent information, we recalculated the irradiation temperatures of the intermediate-temperature experiments reported previously.[4] Volume increase of the carbides over both the intermediate- and high-temperature ranges are given in Fig. 21.3 with the recalculated temperatures. The data for both temperature ranges indicate an initial

Table 21.1. Fractional Volume Increase of Refractory-Metal Carbides Irradiated at Low Temperatures

TiC		ZrC		TaC		NbC		WC	
Fast Fluence [neutrons/cm^2 (> 1 Mev)]	Fractional Volume Increase	Fast Fluence [neutrons/cm^2 (> 1 Mev)]	Fractional Volume Increase	Fast Fluence [neutrons/cm^2 (> 1 Mev)]	Fractional Volume Increase	Fast Fluence [neutrons/cm^2 (> 1 Mev)]	Fractional Volume Increase	Fast Fluence [neutrons/cm^2 (> 1 Mev)]	Fractional Volume Increase
$\times 10^{21}$		$\times 10^{21}$		$\times 10^{21}$		$\times 10^{21}$		$\times 10^{21}$	
0.14	0.016	0.12	0.017	0.16	0.020	0.18	0.016	0.13	0.009
0.24	0.017	0.27	0.021	0.25	0.025	0.31	0.019	0.29	0.009
0.33	0.018	0.30	0.021	0.34	0.027	0.36	0.021	0.32	0.008
0.44	0.018	0.51	0.020	0.50	0.028	0.48	0.025	0.46	0.006
0.47	0.019	0.52	0.021	0.53	0.027	0.55	0.020	0.50	0.008
0.58	0.021	0.62	0.022	0.63	0.032	0.65	0.024	0.60	0.007
0.70	0.021	0.68	0.025	0.73	0.030	0.67	0.026	0.71	0.007
0.74	0.020	0.72	0.021			0.73	0.026	0.73	0.006

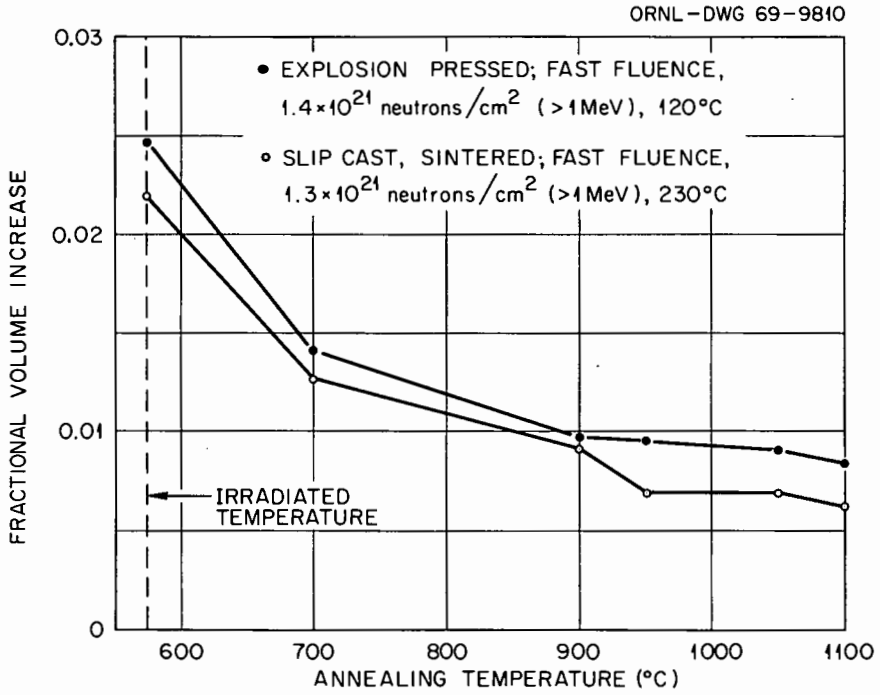

Fig. 21.1. Volume Increase of Irradiated Titanium Carbide After Annealing Out-of-Reactor at Various Temperatures.

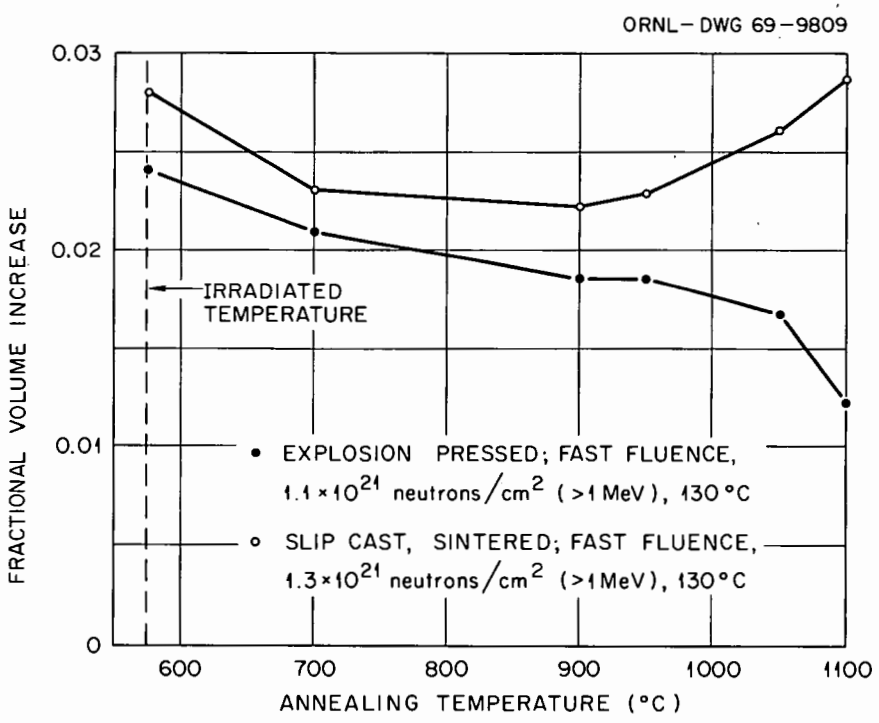

Fig. 21.2. Volume Increase of Irradiated Zirconium Carbide After Annealing Out-of-Reactor at Various Temperatures.

ORNL-DWG 68-12062R

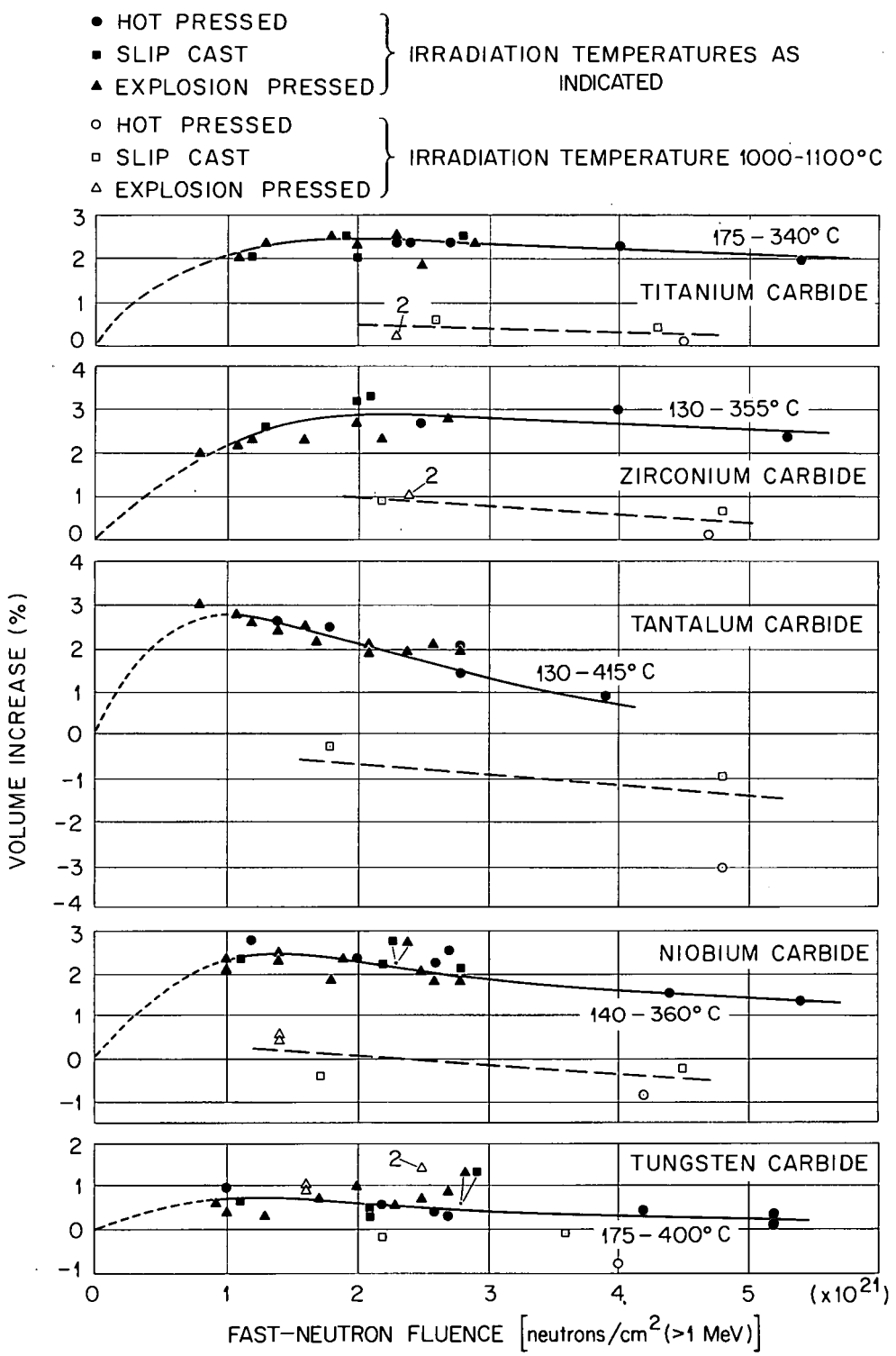

Fig. 21.3. Volume Increase of Carbides of Titanium, Zirconium, Tantalum, Niobium, and Tungsten Irradiated Over Two Temperature Ranges.

saturation of the volume increase at fast fluences below 2×10^{21} neutrons/cm^2 (> 1 Mev). Shrinkage begins to occur at higher fluences.

The work of Thorne, Howard, and Hope[6] on cubic SiC inspired us to develop a damage mechanism based on irradiation annealing. These authors reported evidence of irradiation annealing as well as thermal annealing. The mechanism outlined below explains the initial saturation effect for carbides.

We attribute the shrinkage that occurs in the refractory-metal carbides at high fluences to secondary effects that become significant only after the initial saturation has occurred. These effects are discussed later.

The mechanism is based on the assumptions (1) that single displacements and small clusters are produced in an atomic cascade when a fast neutron collides with an atomic nucleus, and (2) that subsequent cascades can cause both single displaced atoms and atoms in clusters to return to regular lattice sites. The applicable rate equations are

$$\frac{dn_A}{d\Phi t} = K_1 f n_c - K_2 n_A \ , \tag{21.1}$$

and

$$\frac{dn_B}{d\Phi t} = K_1 g n_c - K_3 n_B \ , \tag{21.2}$$

where K_1, K_2, and K_3 are rate constants, n_A is the number of single displacements, n_B is the number of atoms in clusters, and n_c is the number of atoms that occupy regular lattice sites. The coefficients, f and g, are, respectively, the fractions of single displacements and atoms in clusters produced per cascade. It is obvious that $f + g = 1$. The fast fluence is (Φt), the product of fast flux and time. Thermal annealing, whether it occurs only as a result of disruption of atoms in the region of a cascade or as a general consequence of the temperature of the specimen, is rapid as compared with the rate at which displacements are produced. Consequently, there is no need to consider the fast flux and time as separate variables.

If V_F is the volume of a specimen after irradiation, then

$$V_F = n_A v_A + n_B v_B + n_C v_C \ , \tag{21.3}$$

where v_A, v_B, and v_C represent the volumes per atom for each type of atom in the specimen. The original volume of a specimen is the product of the total number of atoms, n_T, and v_C. Therefore,

$$\frac{V_F - n_T v_C}{n_T v_C} = \Delta V/V = n_A/n_T(v_A/v_C) + n_B/n_T(v_B/v_C) + n_C/n_T - 1 \ . \tag{21.4}$$

Inserting the solutions for Eqs. (21.1) and (21.2) into Eq. (21.4) results in a final equation for the volume increase of a specimen:

$$\begin{aligned} \Delta V/V = {} & (v_A/v_C - 1)[p_A + C'_a e^{D(\Phi t)} + C''_a e^{E(\Phi t)}] \\ & \text{(contribution of single displacements)} \\ & + (v_B/v_C - 1)[p_B + C'_b e^{F(\Phi t)} + C''_b e^{G(\Phi t)}] \ . \\ & \text{(contribution of clusters)} \end{aligned} \tag{21.5}$$

The constants D, E, F, and G can be shown to be negative. Therefore, as (Φt) is increased to approach infinity, the fractional volume expansion approaches a saturation value as follows:

$$\lim_{(\Phi t) \to \infty} \Delta V/V = (v_A/v_C - 1)p_A + (v_B/v_C - 1)p_B \ , \tag{21.6}$$

which is

$$\begin{aligned} \lim_{(\Phi t) \to \infty} \Delta V/V = {} & (v_A/v_C - 1)\left(\frac{K_1 K_3 f}{K_1 K_3 f + K_1 K_2 g + K_2 K_3}\right) \\ & \text{(contribution of single displacements)} \\ & + (v_B/v_C - 1)\left(\frac{K_1 K_2 g}{K_1 K_3 f + K_1 K_2 g + K_2 K_3}\right) \ . \\ & \text{(contribution of clusters)} \end{aligned} \tag{21.7}$$

The initial slope at the beginning of irradiation is represented by

$$\left[\frac{d(\Delta V/V)}{d(\Phi t)}\right]_{\Phi t \to 0} = (v_A/v_C - 1)(DC_a' + EC_a'')$$

(contribution of single displacements)

$$+ (v_B/v_C - 1)(FC_b' + GC_b'') ,$$

(contribution of clusters) (21.8)

which reduces to

$$\left[\frac{d(\Delta V/V)}{d(\Phi t)}\right]_{\Phi t \to 0} = (v_A/v_C - 1)K_1 f + (v_B/v_C - 1)K_1 g . \qquad (21.9)$$

The saturation value of $\Delta V/V$ [Eq. (21.7)] and the initial slope for $\Phi t \to 0$ [Eq. (21.9)] can be easily obtained from external dimensional measurements of irradiated specimens if there is no separation at grain boundaries. Determination of the specific contributions of single displacements and clusters is more difficult. Measurements of the lattice parameter can give this if the assumption is valid that single displacements are the sole cause of changes in the lattice parameter. Another approach to the problem is through postirradiation thermal annealing. If clusters do not anneal out at temperatures much below the sintering temperature of the material, annealing curves should show the point at which the volume contribution of single displacements disappears.

The effect of irradiation temperature on the saturation value of $\Delta V/V$ can be predicted by examining the components of the rate constants. Each is proportional to the average cross section for scattering of neutrons of the material, $\bar{\sigma}_s$, and to the average number of atoms displaced in cascades, N_c. The latter is a function of the neutron energy. The rate constants may be represented then as $K_1 = \bar{\sigma}_s N_c x$, $K_2 = \bar{\sigma}_s N_c y$, and $K_3 = \bar{\sigma}_s N_c z$. The factor x is the fraction of N_c that does not immediately return to regular lattice sites following a cascade. An increase in irradiation temperature would, of course, result in a decrease in x and, hence, in K_1. The factors y and z are each at least related to $1 - x$ and would increase with an increase in irradiation temperature. The saturation value of $\Delta V/V$ [see Eq. (21.7)] should, therefore, decrease

with increasing temperature, since K_1 decreases and K_2 and K_3 increase. This is in accordance with the experimental results for carbides.

Thorne et al.[6] found that the changes in lattice parameter for SiC were equivalent to its changes in external dimensions under all conditions. If this indicates that single displacements cause almost all of the damage, then $f \cong 1$ and $g \cong 0$ for SiC. A significant fraction of the displacements of the refractory-metal carbides must be present in clusters, however, since their increases in dimensions greatly exceed their increases in lattice parameters. The fraction in clusters, g, is probably greater in ZrC than in TiC, since thermal annealing after irradiation has a greater shrinkage effect on TiC than on ZrC. Two factors that could be responsible for the increase in g from Si to Ti to Zr could be the increase in masses of the atoms or the increase in the ratios between the atomic radii of the different metals and C.

There are several secondary effects that may account for the shrinkage below the saturation levels at very high fast fluences. Transmutations are likely to have an effect in TaC and NbC. We are planning to irradiate carbides in the Experimental Breeder Reactor-II (EBR-II), which has an almost pure fast flux, to evaluate the importance of slow-neutron transmutations. Another likely secondary effect is densification caused by elimination of small voids. Equation (21.5) does not take into consideration any void space within a specimen. If void space is considered, the fractional volume expansion can be expressed as

$$\Delta V/V = (\Delta V/V)_s + (\Delta V/V)_v \ , \qquad (21.10)$$

where $(\Delta V/V)_s$ represents the solid expansion [Eq. (21.5)] and $(\Delta V/V)_v$ represents the void expansion. The void expansion may have a positive value for materials in which transmutations produce gases or in which there is separation at grain boundaries. Otherwise, it will have a negative value because small voids within the lattice will slowly be filled by atoms that have been moved from their previous positions after being struck by other atoms in a cascade.

The improvement in stability with respect to gross fracturing at high temperatures as compared with that at low temperatures is assumed to be a consequence of the reduced number of atoms displaced at high

temperatures. The greater thermal stability of the displacements in specimens irradiated at high temperatures is either not significant or is masked by the fact that there are fewer of them. Displacements, singly or in clusters, apparently embrittle or weaken the structure and contribute to propagation of fractures. There is some reason to believe that clusters have a greater effect in producing gross fracturing than single displacements. For example, ZrC irradiated at intermediate temperatures was damaged much more than TiC, which, according to evidence gained by annealing studies and measurements of the lattice parameter, contains a smaller fraction of its displacements in clusters.

Since the damage mechanism predicts saturation with a constant ratio of displacements and clusters, it seems possible that some carbides would have a useful life as high-temperature components in fast reactors very much beyond the highest fast fluences achieved in our experiments. Materials for such long-term applications should have very low neutron-absorption cross sections for fast neutrons and should be of high purity. A low ratio of clusters to single displacements (g:f) may also be desirable.

Effects of Irradiation on LMFBR Fuels

D. A. Dyslin[2] R. E. Moore[1] H. E. Robertson[1]

Effects of Helium Gas Produced by Fast Neutrons in Depleted UN

Fuels that contain N are being considered for use in fast breeder reactors. An understanding of the effects of gas generation within nitride fuels would aid in their development. In addition to Xe and Kr fission products, nitride fuels also produce He gas through the $^{14}N(n,\alpha)^{11}B$ fast-neutron reaction. The effects of the generation of He alone (i.e., without the generation of fission gases) are being evaluated in irradiations of depleted fuel.

A high-temperature (1000°C) instrumented assembly and a low-temperature (about 150°C) uninstrumented assembly, both of which contain specimens of depleted nitride fuel, were prepared for irradiation in the ETR. The specimens, which are nominally 0.25 in. in diameter by 0.4 in. long, are of three types: UN, $U^{15}N$, and UN-UC (50-50 mole %). The

low-temperature assembly is now undergoing irradiation. The expected range of exposure is 0.5 to 2.0×10^{21} neutrons/cm^2 (> 1 Mev). The high-temperature assembly required modification before it could be inserted into the ETR. After modification, it will be irradiated to the same range of fluences as the low-temperature assembly will have received.

Postirradiation examinations will include He analysis of capsules of the assemblies, dimensional measurements, metallography, and electron microscopy. Comparisons of the property changes of depleted UN and depleted $U^{15}N$ will directly measure the effect of the (n,α) reaction, since this reaction does not occur in $U^{15}N$. The specimen arrangements in the two capsule assemblies were planned so that gas analyses will provide information on He release from both UN and UN-UC (50-50 mole %).

Fast-Neutron Effects on Materials for Neutron Absorption in Fast Reactors

Assemblies are being designed and specimens are being prepared for irradiation of fast-neutron absorbers in a blanket facility in row 8 of the EBR-II. Two types of B_4C specimens with different ratios of B:C will each be irradiated at 400 and at 750°C. The He gas released at each of the two temperatures by each type of B_4C will be measured and analyzed. Specimens of Ta metal, TaC, and other neutron absorbers will be irradiated at 400 and 750°C in other assemblies. Dispersions of Ta metal and B_4C will be irradiated in a subsequent series of experiments.

References

1. Reactor Chemistry Division.
2. General Engineering Division.
3. G. W. Keilholtz, R. E. Moore, and D. A. Dyslin, Fuels and Materials Development Program Quart. Progr. Rept. Dec. 31, 1968, ORNL-4390, pp. 113–114.
4. G. W. Keilholtz, R. E. Moore, and M. F. Osborne, Nucl. Appl. 4, 330 (1968).
5. G. W. Keilholtz and R. E. Moore, Trans. Am. Nucl. Soc. 12(1), 101 (1969).
6. R. P. Thorne, V. C. Howard, and B. Hope, Proc. Brit. Ceram. Soc. 7, 449 (1967).

22. JOINING RESEARCH ON NUCLEAR MATERIALS

J. R. Weir, Jr. G. M. Slaughter

The purpose of this program is to gather the fundamental and applied data needed to understand the weldability of materials that are either being considered or are currently used for nuclear applications. Fundamental studies are concerned with the effects of minor constituents on the behavior of weldments. We are especially interested in the austenitic stainless steels and the alloys that are rich in Ni, such as Incoloy 800 and Inconel 600. In addition, a modest program concerned with the influence of weld defects will provide reference results in this much-talked-about but little-investigated field.

As a result of this broad-based program, we plan to develop modifications in both alloy composition and procedures needed to improve the quality of weldments used in the various activities of the Commission.

The Effect of Minor Variations in Chemical Composition on Weldability

Our continuing investigation of the effect of minor variations in those elements usually present in small quantities in structural materials has included Incoloy 800, Inconel 600, and stainless steel.

Weldability of 18% Cr–8% Ni Class of Stainless Steel (D. A. Canonico, W. J. Werner)

We are continuing our basic studies concerning the influence of chemical composition and welding variables on the amount and distribution of ferrite in weld metal.

We obtained from a vendor electrodes for shielded metal-arc welding that provide weld metal containing nominally 0, 2, 5, 7, 10, and 15% ferrite. These electrodes were used with an automatic welding head to deposit beads on 1/2-in.-thick type 304 stainless steel plate under controlled welding conditions of current, voltage, and travel speed. The conditions, selected to provide heat input ranges from 10,000 to

60,000 J/in., were achieved primarily by changing travel speed. However, we have also investigated the effects of variations in current and voltage at a given travel speed. The weld specimens are being investigated metallographically.

Effect of Minor Elements on the Hot Ductility of Inconel 600
(D. A. Canonico, W. J. Werner)

We are studying the microstructures of simulated heat-affected zones in alloys of the Inconel 600 type as a function of minor differences in composition.[1] Table 22.1 lists the chemical analyses of the 15 compositions investigated. Both the fracture area and the unaffected base metal of the alloys were investigated metallographically this quarter.

The microstructures in the fracture area resulted from material that was heated to the temperature at which the ductility for that particular composition was zero. Hence, the microstructures are representative of the zero-ductility temperature (ZDT) and are not necessarily the same for the various specimens. The base-metal results in all instances reflect only the effect of an earlier anneal at 1180°C and are altered by the subsequent thermal excursion experienced by the metal in the fracture area.

In Fig. 22.1 are photomicrographs of unaffected base metal from alloy 600-1 (essentially a Ni-Cr-Fe ternary) and from the nominal composition of Inconel 600 (alloy 600-2). The addition of C, Si, Mn, and Cu resulted in a much finer grain size. This difference in grain size is maintained at the ZDT for these alloys.

The next series of alloys, 600-3 through 600-5, were designed to investigate the effect of increasing S content on the properties of the nominal Inconel 600 composition. Increasing S resulted in a decrease in both the ZDT and the ductility of the alloy "on heating" and "on cooling."[2] A probable reason for the differences in the properties of the three compositions is seen in Fig. 22.2. Increasing S content resulted in some liquation at the grain boundaries in the alloys with low S (alloy 600-3) and in gross liquation in the alloy (alloy 600-5) with highest S (0.012%).

Table 22.1. Nominal and Actual Compositions of the Inconel 600 Hot-Ductility Specimens

Alloy Designation	Composition (wt %)														Composition (ppm)	
	Ni	Cr	Fe	C	H_2	N_2	O_2	S	P	Si	Al	Mn	Cu	Ti	B	Pb
600-1	75.2	15.9	8.13	0.004	0.0011	0.0004	0.019	0.003	0.001	0.01	< 0.05	0.007	< 0.01	< 0.01	1	< 2
600-2	75.6	16.1	8.55	0.028	0.0002	0.0010	0.0081	0.002	0.002	0.2	< 0.05	0.11	0.026	< 0.01	1	< 2
600-3	75.2	16.0	8.40	0.028	< 0.0001	0.0004	0.0005	0.006	0.001	0.2	< 0.05	0.11	0.022	< 0.01	1	< 2
600-4	74.7	15.5	8.04	0.025	0.0002	0.0005	0.0025	0.010	0.002	0.2	< 0.05	0.15	0.029	< 0.01	2	< 2
600-5	74.5	15.7	8.32	0.026	0.0005	0.0010	0.0061	0.012	0.002	0.2	< 0.05	0.12	0.18	< 0.01	< 0.2	< 2
600-6	70.9	15.9	12.1	0.027	0.0008	0.0013	0.0079	< 0.002	0.006	0.2	< 0.05	0.23	0.021	< 0.01	0.3	< 2
600-7	73.7	15.8	9.33	0.026	0.0029	0.0018	0.017	< 0.002	0.011	0.2	< 0.05	0.20	0.021	< 0.01	0.3	< 2
600-8	72.6	15.9	10.4	0.023	0.0025	0.0028	0.082	< 0.002	0.015	0.3	< 0.05	0.17	0.018	< 0.01	0.3	< 2
600-9	72.6	16.2	11.4	0.034	0.0021	0.0016	0.0075	0.003	0.004	0.2	< 0.05	0.16	0.024	< 0.01	0.4	< 2
600-10	72.3	16.2	11.5	0.026	0.0029	0.0011	0.018	0.003	0.006	0.2	< 0.05	0.17	0.023	< 0.01	0.7	< 2
600-11	73.7	16.1	8.98	0.026	0.0019	0.0007	0.0079	0.006	0.008	0.2	< 0.05	0.17	0.018	< 0.01	0.2	< 2
600-12	75.6	16.2	8.28	0.033	0.0009	0.0015	0.0086	0.009	0.002	0.2	< 0.05	0.32	0.021	< 0.01	0.2	< 2
600-13	75.4	15.9	8.11	0.022	0.0012	0.0015	0.012	0.009	0.002	0.2	< 0.05	0.48	0.024	< 0.01	0.4	< 2
600-14	75.2	16.0	9.05	0.026	0.0002	0.0013	0.016	0.009	0.002	0.2	< 0.05	0.84	0.029	< 0.01	0.4	< 2
600-15	72.5	16.6	11.3	0.026	0.0005	0.0008	0.011	0.008	0.007	0.2	< 0.05	0.80	0.022	< 0.01	0.5	< 2

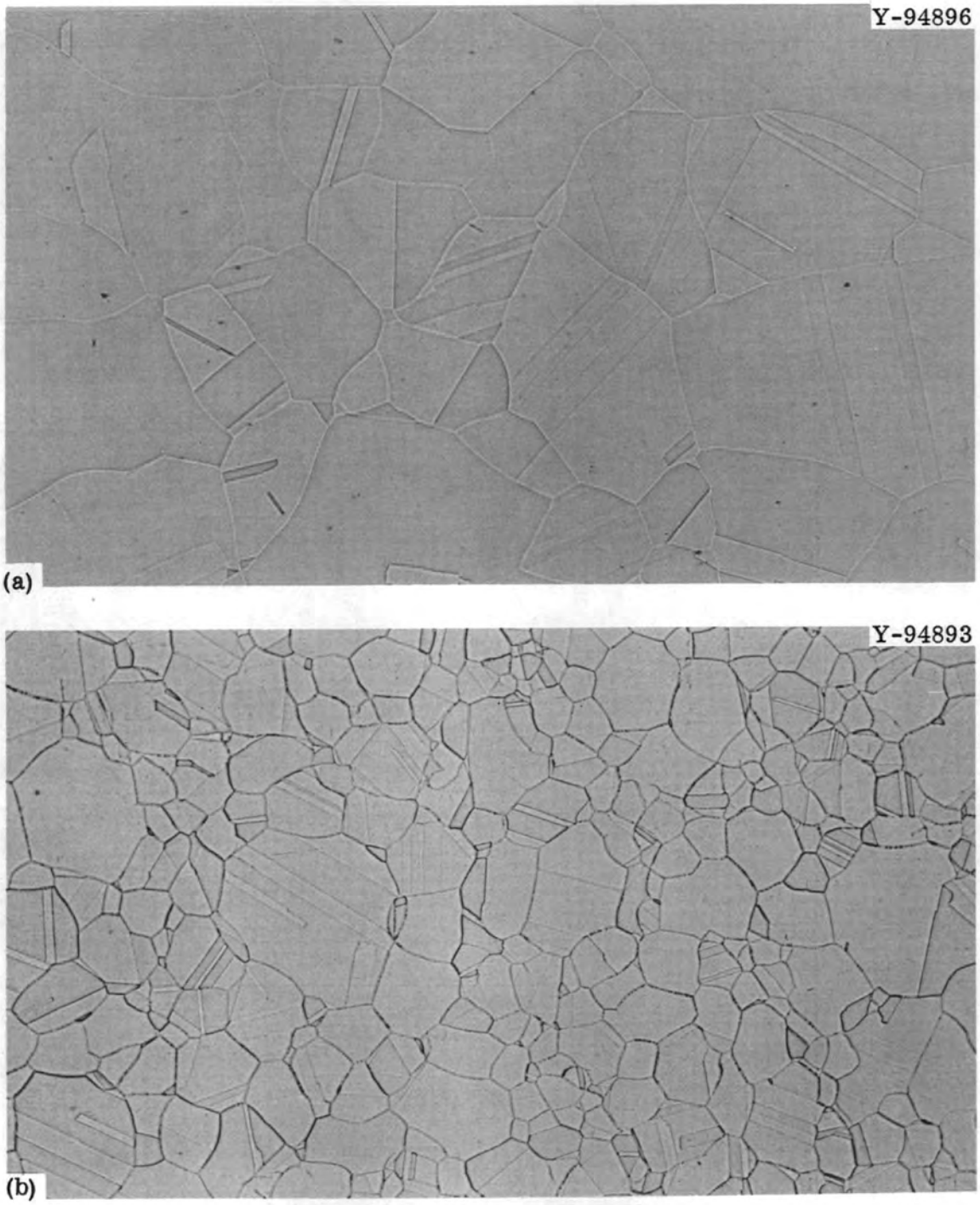

Fig. 22.1. Photomicrographs Showing the Gross Difference in Grain Size Between (a) the Ni-Cr-Fe Ternary Composition (Alloy 600-1) and (b) the Nominal Inconel 600 Composition (Alloy 600-2). Both alloys were annealed at 1180°C. 100×.

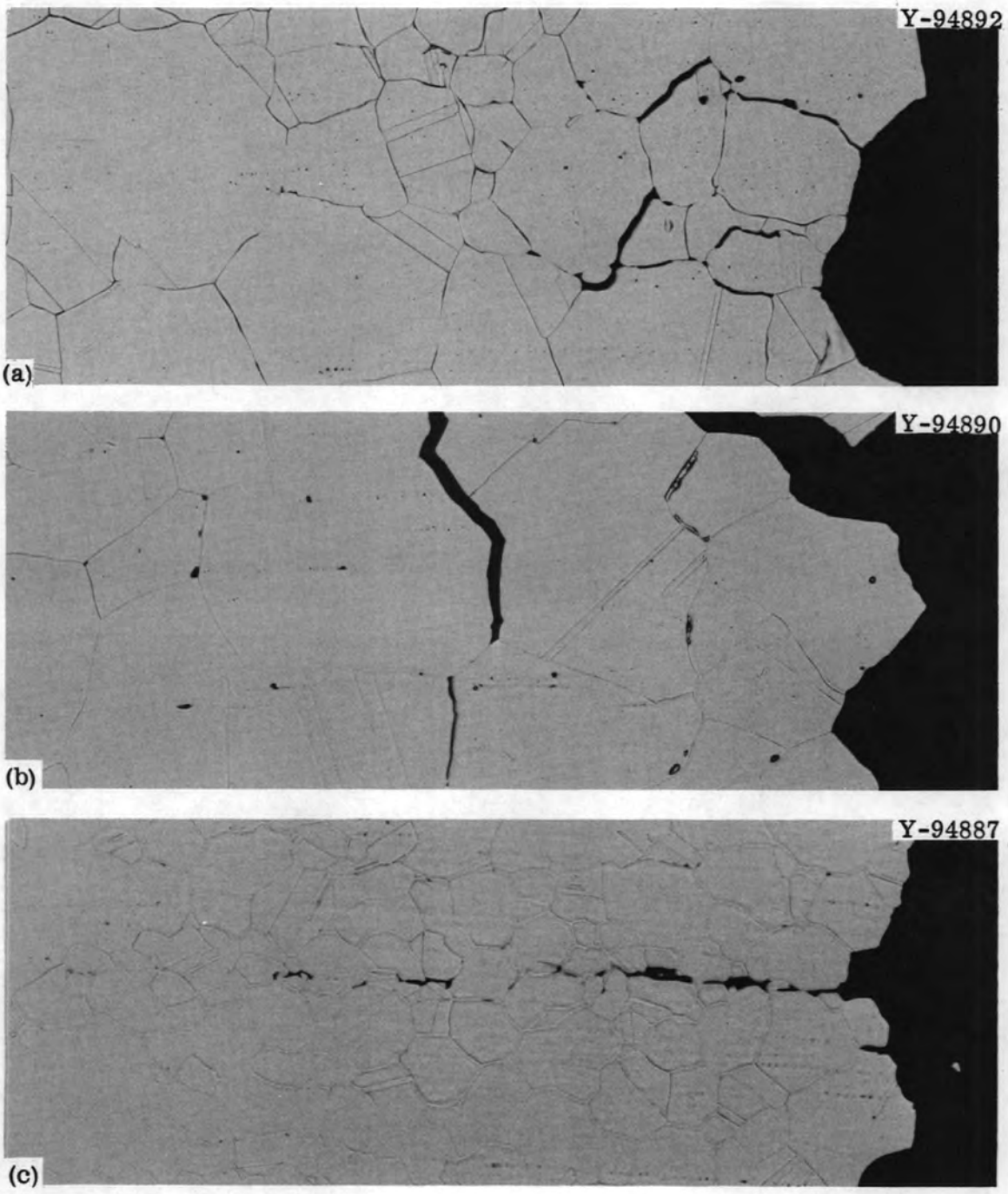

Fig. 22.2. Photomicrographs of the Fractured Regions of the Specimens for Tests of Zero-Ductility Temperature. Note the tendency toward gross liquation as the sulfur content is increased. 100×. (a) Alloy 600-3: 0.006% S, ZDT = 1338°C. (b) Alloy 600-4: 0.010% S, ZDT = 1330°C. (c) Alloy 600-5: 0.012% S, ZDT = 1300°C.

The laminar distribution of S is also readily apparent in photomicrographs of the unaffected base metal. Moreover, the presence of S has resulted in areas of large grains so that the alloy with high S content has many locations in which the grain size is equal to that seen in the pure ternary (Fig. 22.1). Figure 22.3 shows the microstructures of the unaffected base metals (that is, samples that were not later subjected to a welding thermal cycle).

The effect of 0.006 to 0.015% P was investigated with alloys 600-6 through 600-8. Phosphorus does not appear to have a deleterious effect. The fracture behavior at the ZDT is similar to that of the nominal alloy (alloy 600-2). This similarity is also evident in the microstructures of the unaffected base metal, for there was no discernable difference between the alloy with no P addition (0.002% P) and alloys with varying additions of P.

When both P and S are added (alloys 600-9, 600-10, and 600-11), S appears to dominate, and its effect on grain coarsening and banding is evident. In Fig. 22.4 are photomicrographs of the unaffected base metal from alloy 600-9 (0.003% S and 0.004% P) and alloy 600-11 (0.006% S and 0.008% P).

Increasing the Mn content from 0.11 to 0.84% in the presence of nominally 0.010% S had no apparent effect on the microstructure of the base metal or on fracture morphology at the ZDT. The grain size of the alloy high in Mn (alloy 600-14) is similar to that of the ternary alloy (alloy 600-1). However, the addition of 0.007% P to the nominal alloy containing Mn and S (alloy 600-14) resulted in a considerable refinement of the grain size. This difference is shown in the photomicrographs in Fig. 22.5. This refinement in grain size is in contrast to the results seen in Fig. 22.4, where the effect of S was dominant. An association between the Mn and S is indicated. This would make the effect of S innocuous and promote the dominance of the effect of P as in alloy 600-15.

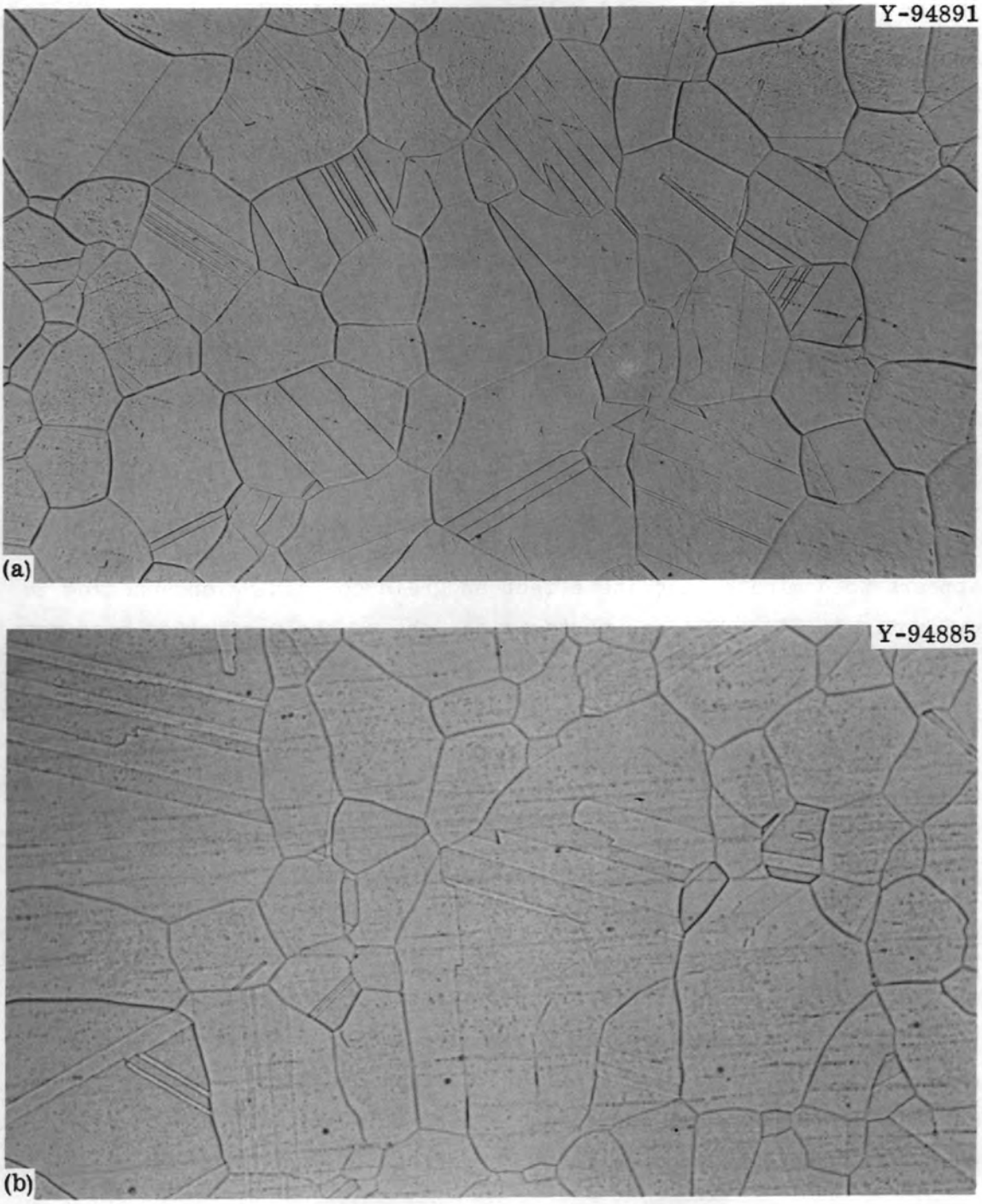

Fig. 22.3. Photomicrographs Showing the Effect of Increased Sulfur Content on the Microstructures of the Unaffected Base Metal. 100×. (a) Alloy 600-3: 0.006% S. (b) Alloy 600-5: 0.012% S.

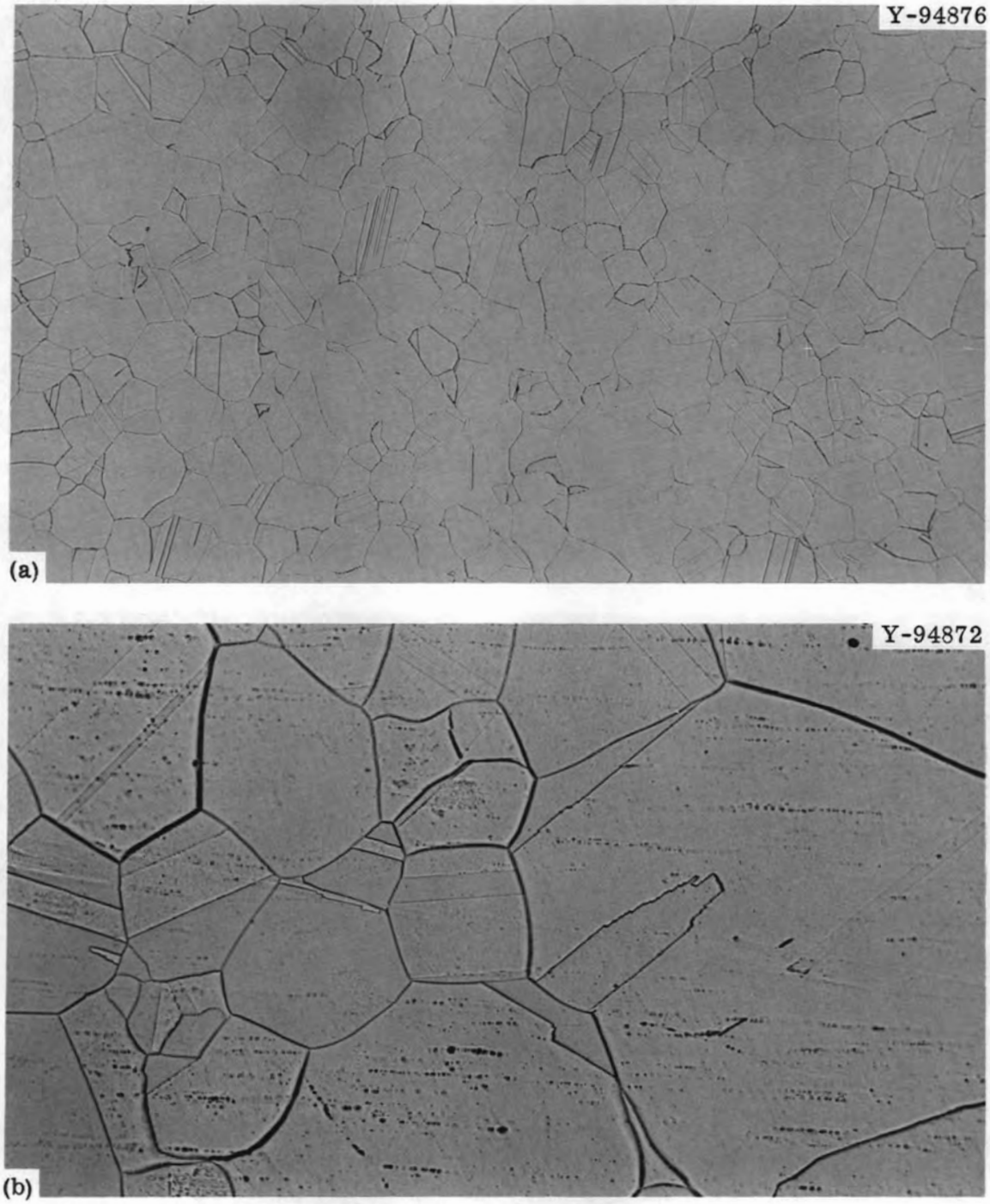

Fig. 22.4. Photomicrographs of Inconel 600-Type Alloys Containing Both Sulfur and Phosphorus. The effects on grain coarsening and banding are evident in the lower photomicrograph. 100×. (a) Alloy 600-9: 0.003% S and 0.004% P. (b) Alloy 600-11: 0.006% S and 0.008% P.

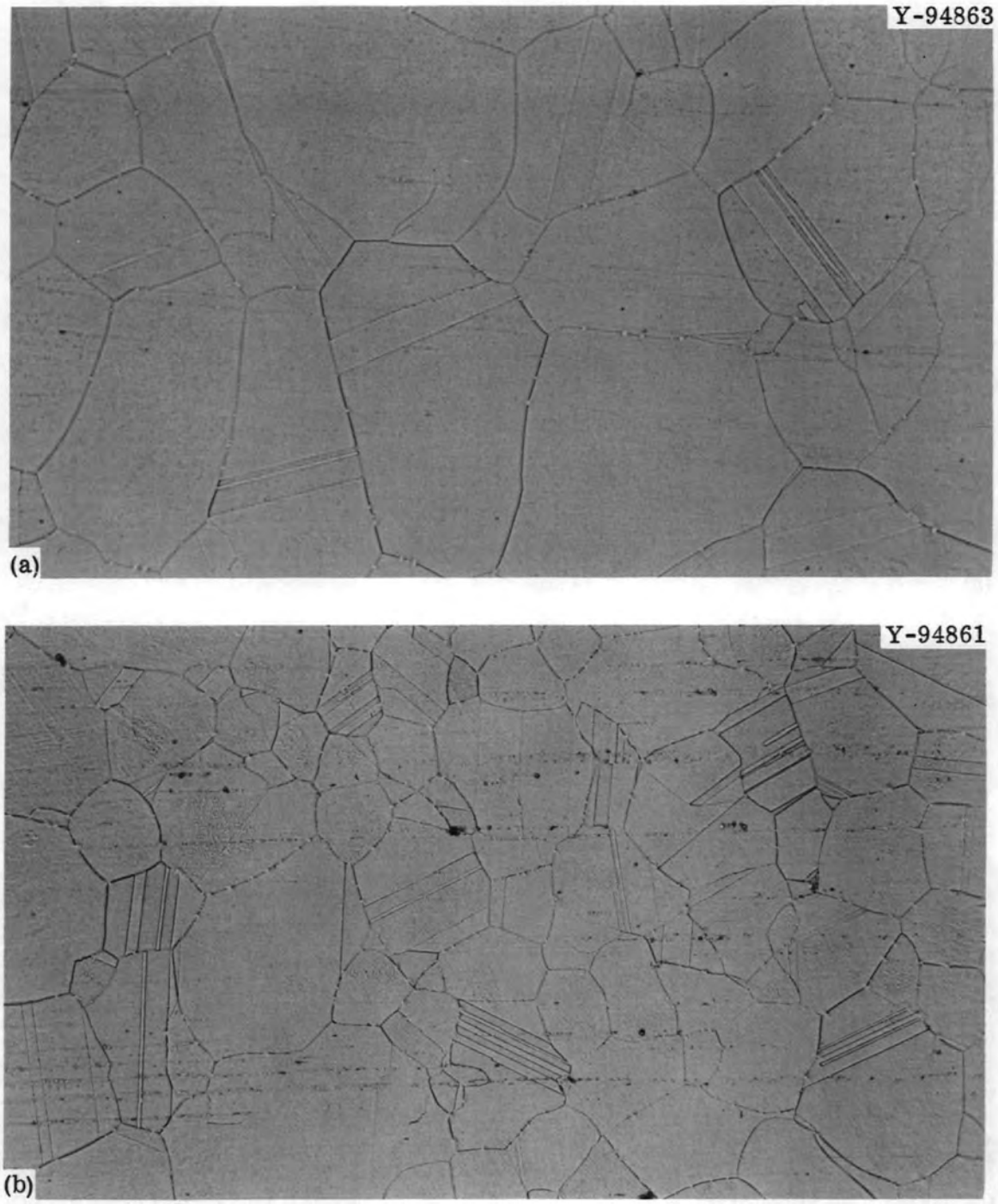

Fig. 22.5. Photomicrographs of Alloys Containing Nominally 0.010% S and 0.80% Mn With and Without Added Phosphorus. Note the reduction in grain size that accompanies the phosphorus addition. 100×. (a) Alloy 600-14: 0.009% S, 0.84% Mn, and 0.002% P. (b) Alloy 600-15: 0.008% S, 0.80% Mn, and 0.007% P.

The Effect of Defects on the Mechanical Properties of Weldments

G. M. Slaughter

Electron-Beam Welds in Inconel 600 (C. D. Lundin[3])

The electron-beam welds made in Inconel 600 specimens[4] at beam angles of 90 and 45° were machined and radiographed. Eight tensile specimens were obtained from each test plate. Discontinuity indications were obtained in each specimen, but most of the discontinuities were in the welds made with a beam angle of 45°. Short-time stress-rupture strength will be tested with the Gleeble hot-ductility machine in an effort to evaluate the effect of the discontinuities. We will also determine tensile strength at room temperature.

The fracture surfaces of the discontinuities excised from the electron-beam welds were recorded by scanning electron photomicrographs. These fractographs are being analyzed, and the fracture characteristics of these welds will be compared with the fracture characteristics of welds in other Ni-base alloys.

References

1. D. A. Canonico and W. J. Werner, Fuels and Materials Development Program Quart. Progr. Rept. June 30, 1969, ORNL-4440, pp. 161–165.
2. D. A. Canonico and W. J. Werner, Fuels and Materials Development Program Quart. Progr. Rept. Dec. 31, 1968, ORNL-4390, pp. 190–192.
3. Consultant from the University of Tennessee.
4. C. D. Lundin, Fuels and Materials Development Program Quart. Progr. Rept. Sept. 30, 1968, ORNL-4350, pp. 256–259.

23. NONDESTRUCTIVE TESTING

W. O. Harms R. W. McClung

Our task is to develop new and improved methods of nondestructively testing reactor materials and components. We are studying various physical phenomena, developing instruments and other equipment, devising techniques, and designing and fabricating reference standards. Among the methods being studied for both normal and remote inspection are electromagnetics (with major emphasis on eddy currents), ultrasonics, penetrating radiation, and holography.

Electromagnetic Inspection Methods (Eddy Currents)

Solutions for Electromagnetic Induction Problems (C. V. Dodd, W. E. Deeds,[1] J. W. Luquire,[1] C. C. Cheng[2])

We continued research and development on both analytical and empirical bases. We derived the equations for the solution of electromagnetic induction problems for a number of additional configurations of coil and conductor. These include those for a coil between a number of conducting plates and for a coil encircling two concentric, spherical shells. The answer to the former case is in terms of an infinite integral, and that for the latter case is in terms of an infinite sum. Both cases are sufficiently general to allow the solution of a considerable number of different problems of electromagnetic induction. We derived equations for physical phenomena such as the coil impedance, the power dissipated in the various conductors, the time-averaged electromagnetic force, the voltage induced, and the effect of a defect. These equations can be evaluated by means of a digital computer.

We are continuing to study the problem of a defect in a conductor. This problem requires the solution of the vector Helmholtz equation with very difficult boundary conditions. We have derived a more general reciprocity theorem and increased the accuracy of the expression for the defect, but we still have not achieved the desired accuracy in the solution.

We studied the use of a time-sharing computer for the analysis of eddy-current problems; the abstract appears below:[3]

> A technique was developed for quick and accurate calculation of eddy current probe coil problems. A set of integral equations was derived for describing various eddy current phenomena such as coil impedance, voltage induced in coils and the effect of material defects. These integral equations can be numerically evaluated for various coil and conductor parameters. By using a time-sharing computer to perform this operation, the designer can quickly achieve accurate answers to eddy current coil problems.

We also devised computer programs for some eddy-current problems; the abstract of our report appears below:[4]

> This report contains computer programs for solving some eddy-current problems frequently encountered in nondestructive testing. Operating instructions and examples are given for each program. These programs are written in BASIC language and may be used on a time-sharing computer. Various eddy-current tests can be quickly and accurately designed by utilizing these programs.

Ultrasonic Inspection Methods

Optical Visualization of Ultrasound (H. L. Whaley, Jr., K. V. Cook)

We made several improvements in the optical system in preparation for our study of weld samples with the schlieren apparatus. We devised a method for simultaneously mounting two light sources on the optical bench in such a way that a minimum of realignment is necessary to switch from one to the other. This allows us to use a rapidly pulsed light source when maximum intensity is not essential and to use one that flashes only about once per second but that has very high intensity whenever maximum sensitivity is required. Since the high-intensity source flashes only once per second, a problem of lack of visual persistence occurs for the operator. One step taken to counter this problem was the rewiring of an incandescent bulb (built into the pulsed light source for alignment

purposes) to produce a continuous background of adjustable intensity on the television monitor. A long-persistence picture tube installed in the television monitor also proved to be a major improvement. Because of these improvements, routine use of the system with the high-intensity pulsed source is now practical.

We were successful in recording visual sequences from the television monitor with both a video tape recorder and on motion picture films for educational and illustrative purposes.

Frequency Analysis (H. L. Whaley, Jr., K. V. Cook)

We are investigating variations in frequency spectra of ultrasonic pulses reflected from flat, circular reflectors located on the extended axis of a transducer immersed in water. Among the variables being considered are the distance from the source to the reflector, the relative diameters of the source and reflector, the relative dimensions of the diameter of the reflector and the ultrasonic wavelength, and the angular orientation of the reflector with respect to the axis of the source. The reflecting surfaces are the flat, polished ends of a number of brass, Cu, and Al rods ranging in diameter from 7.1 mm (0.281 in.) to 0.79 mm (0.031 in.). Several different materials were selected because of the possibility that some of the effects might depend on specific acoustic impedance.

So that we might change the angle of incidence without changing the water path or moving the center of the reflecting rod off the source axis, we designed and fabricated a mechanical apparatus to rotate the rod about a diameter in the plane of its flat end. Mechanical positioning must be very precise and reproducible if results are to be reproducible, especially when the water path is small enough that the reflector is inside the "near field" of the transducer.

Initial experiments were performed with a nominal 2.25-MHz, 1.9-cm-diam (0.75 in.) transducer at two different distances from the reflector; one of these positions was inside the near field. The transducer is excited by shock to produce a spectrum from about 0.5 to 4.0 MHz. Significant variations were observed in the frequency spectrum of the reflected pulse as a function of reflector size and angular orientation.

These variations are quite reproducible. We believe that these effects are due to a number of interacting phenomena, and we are devising both experimental and theoretical approaches to separate them. We are also investigating analytical approaches that might be applicable to the problem.

Fabrication of Reference Notches (H. L. Whaley, Jr., K. V. Cook)

We are continuing work on the problems encountered in inspecting tubing by ultrasonic methods. A major problem is the fabrication of reference notches that can be used as realistic standards for calibration. Since electro-discharge machining (EDM) appears to be a reliable method for making both inner- and outer-surface notches, we are continuing our studies of notch fabrication. As we encounter new alloys, we are generating appropriate reference curves for both longitudinal and transverse notches.

We have assembled a 6-in. lathe system for making silicone rubber replicas of the complete inner surface of notched standards for tubing. The lathe spins the tube while the rubber hardens.

We can now machine transverse notches inside 0.200-in.-ID tubing as much as 7 in. from the end of the tube. Calibration on the long transverse cutting arm is excellent; however, several modifications were necessary in the procedural details for making transverse notches this far from the end. A motor and dither-weight assembly was designed, tuned, and attached to the cutting system to vibrate the tool so that it would not become welded to the workpiece. We are making increased use of Ta shims for the cutting tool because they wear less rapidly than brass shims and produce notches with straighter sides. We have planned additional work to further improve the characteristics of the machined notch.

We cooperated with the Plant and Equipment Division of ORNL to design an EDM device that is being fabricated to operate in an environmental chamber. This system will be used to study the effect of temperature on microcracking generated during electro-discharge machining of reference notches in W- and Mo-based alloys.

Penetrating-Radiation Inspection Methods

X-Ray Attenuation (B. E. Foster, S. D. Snyder)

During the past several years we successfully used penetrating radiation for determining the homogeneity of reactor fuels and other materials with high atomic numbers and for determining the thickness of coatings of C on microspheres of nuclear fuels. But we had not used this method for measuring the homogeneity of materials with low atomic numbers, such as graphite. Since most previous determinations of the homogeneity of graphite were made by radiography on a qualitative basis, we felt that a limited study to determine the quantitative sensitivity of our x-ray attenuation equipment would be valuable.

We obtained two 1 1/4-in.-thick blocks of graphite, one 8 1/2 × 3 1/4 in. and the other 8 1/2 × 1 1/4 in. Each block had a series of five 1/8-in.-diam and five 1/16-in.-diam flat-bottomed holes drilled to depths of about 0.050, 0.100, 0.150, 0.200, or 0.250 in. Since we did not have graphite standards of known density and thickness, we related the attenuation measurements to equivalent changes in the thickness of Al. The x-ray energy conditions were 50 kvcp (kilovolts constant potential) at 2.5 ma with a 0.078-in.-diam beam. We did not try to optimize the x-ray energy for best sensitivity, but rather used the conditions for which we already had data on attenuation in Al. The sensitivity to thickness change for the 1/8-in.-diam holes was about 1% per division of the recorder chart. Since the 1/16-in.-diam holes are smaller than the diameter of the beam, no valid correlation between thickness and attenuation could be made. Table 23.1 compares the percent deviation from the nominal thickness of the graphite under the 1/8-in.-diam holes as predicted by the x-ray attenuation method and as determined by direct dimensional measurements.

Since the x-ray attenuation method is sensitive to both thickness and density, the differences between the attenuation and dimensional methods are attributed to variations in the density of the graphite under the holes. This was especially true for the 8 1/2 × 1 1/4 in. block,

Table 23.1. Comparison of Graphite Thickness as Determined by X-Ray Attenuation and Direct Dimensional Measurement

Approximate Depth of Hole (in.)	Deviation from Nominal Thickness, %	
	Predicted by X-Ray Attenuation	Direct Dimensional Measurement
8 1/2- × 3 1/4- × 1 1/4-in.-thick Graphite Block		
0.250	−19.52	−19.98
0.200	−16.41	−16.20
0.150	−11.98	−12.04
0.100	−7.39	−7.84
0.050	−3.95	−3.81
8 1/2- × 1 1/4- × 1 1/4-in.-thick Graphite Block		
0.250	−17.55	−20.02
0.200	−13.60	−16.14
0.150	−11.07	−11.83
0.100	−7.59	−8.11
0.050	−5.30	−4.15

since a visual observation showed many laminations running perpendicular to the direction of the x-ray beam.

This brief study shows that a sensitivity to changes in thickness or density in graphite of about 0.5% are readily detected. (Reading the strip-chart trace to 0.5 divisions is quite practical.) With optimization of the x-ray energy and suitable standards, even greater sensitivity can be achieved.

Radiation Scattering (B. E. Foster, S. D. Snyder)

Our investigation of the use of Compton scattered radiation for measuring the thickness of coatings or claddings on reactor components have continued after repairs to both the single-channel and 1600-channel analyzers. There was also some delay in replacing the radiation detector that was inadvertently broken.

The radiation source initially used was 1/2 curie of ^{241}Am. As a specimen for the initial studies we used a fuel plate clad with about 0.010 in. of Al and with a flat core dispersion of U_3O_8 in Al. However, the count rate of the scattered radiation from both the cladding and core material varied with successive measurements with about ±1% uncertainty. This variation in count rate could have been caused by inhomogeneity within the core material as well as by radiation being scattered to the detector from the table under the specimen.

Figure 23.1 is a schematic diagram of the experimental setup. The radiation beam is collimated to 3/8 in. in diameter and impinges on the surface of the specimen at an angle of 40° from the normal. Changes in the thickness of the cladding can be simulated by laying Al foils of different thicknesses (0.00025 to 0.003 in.) on the specimen surface

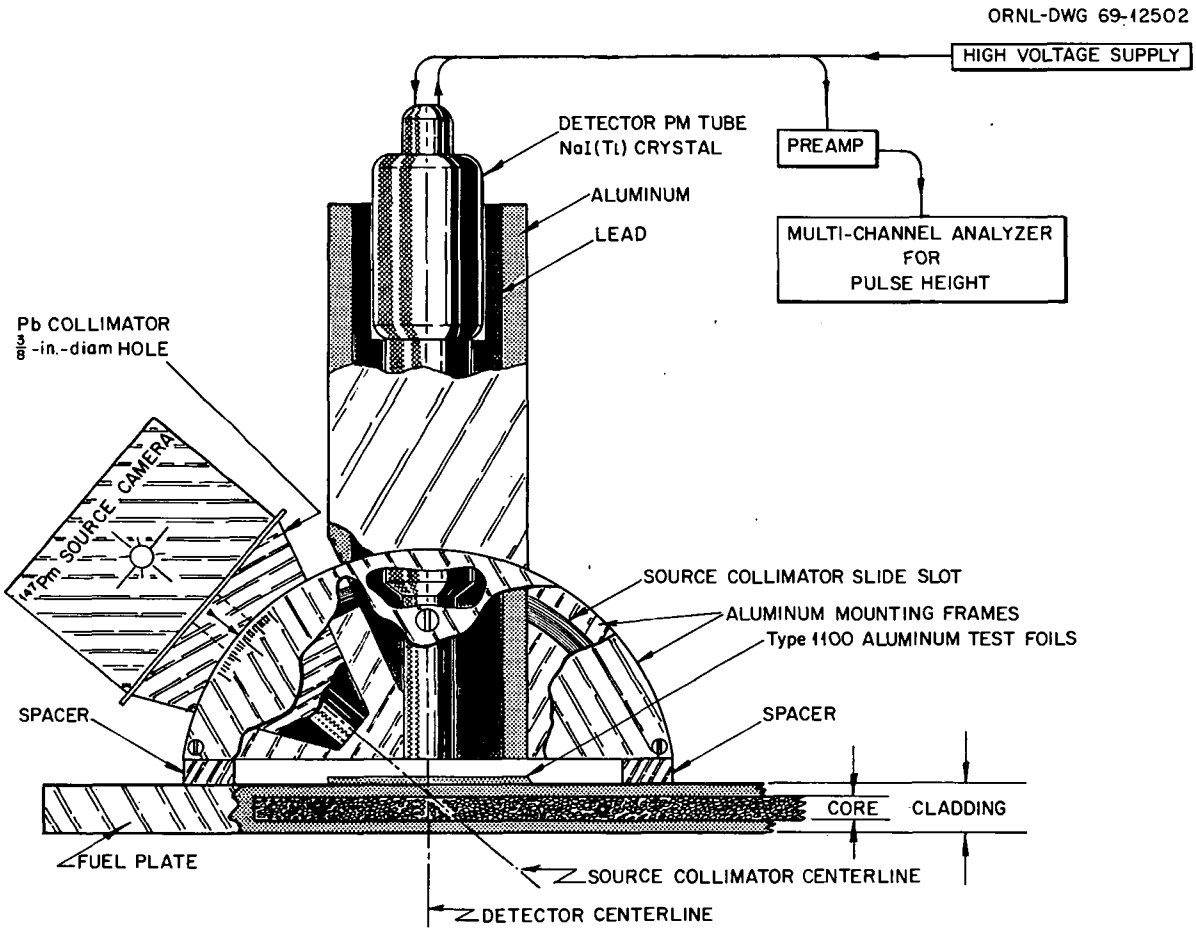

Fig. 23.1. Schematic Diagram of Device for Studying Radiation-Scattering Methods for Determining Cladding Thickness.

beneath the detector. The data are accumulated as count rate in the 1600-channel analyzer, which is calibrated for spectral energy of 0.5 kev per channel. A feature of the analyzer is the "Region-of-Interest," which allows selection of any portion of the energy spectrum and provides digital printout of the integral count within that area. The analyzer is also divided into eight groups of 200 channels each that can be used in parallel to allow eight consecutive samples of count rate for a single foil thickness. The average of the values from the "Region-of-Interest" for these eight readings can be used as one datum point for subsequent calibration curves of count rate versus cladding thickness. We are investigating the use of ^{147}Pm (about 50 curies) as a radiation source. Perhaps the lower energy (38 kev) and much greater intensity will reduce the fluctuations in count rate experienced with the ^{241}Am source.

If the present experimental arrangement has sufficient sensitivity to a given change in cladding thickness, we will then be able to continue our parametric study of the scattering angles and associated energies for reactor materials.

References

1. Consultant from the University of Tennessee.
2. Consultant from Northwestern College, Orange City, Iowa.
3. C. V. Dodd, W. E. Deeds, J. W. Luquire, and W. G. Spoeri, Mater. Evaluation 27(7), 165–168 (July 1969).
4. J. W. Luquire, W. E. Deeds, C. V. Dodd, and W. G. Spoeri, Computer Programs for Some Eddy Current Problems, ORNL-TM-2501 (August 1969).

24. IMPROVEMENT OF HASTELLOY N AND RELATED COMPOSITIONS

J. R. Weir, Jr. H. E. McCoy, Jr.

This program is aimed at defining and understanding the metallurgical variables that affect the engineering performance of Ni-based structural alloys in reactor environments. Such alloys have been shown to have reduced stress-rupture properties and greatly reduced fracture strain after exposure to thermal-neutron fluences. Our work has concentrated on Hastelloy N. We have found that small additions of Ti, Zr, Hf, and Nb effectively reduce the deterioration of properties caused by irradiation. The end products sought by this program are a better understanding of the factors important to controlling irradiation damage in Ni-based alloys and development of a modified Hastelloy N with improved resistance to irradiation damage.

Mechanical Properties of Hastelloy N and Related Compositions

Aging of Ti-Modified Hastelloy N (C. E. Sessions)

The creep behavior of four Ti-modified alloys was measured at 40,000 psi and 650°C after aging 3000 hr at 650 and 760°C. The rupture life and ductility increased with Ti content when tested in the solution-annealed condition. The influence of aging treatment on the creep properties is shown in Figs. 24.1 and 24.2.

For the three lower levels of Ti, aging at 760°C reduced the rupture life and increased the creep rate. Aging at 650°C generally increased the rupture life. Although the rate of creep deformation was increased over that of the solution-annealed material it was lower than that found after aging at 760°C. The most significant test results, however, were that the 1.2% Ti heat showed no change in its creep rate as a result of the aging process and that the rupture life of this heat was slightly increased for each heat treatment plotted in Fig. 24.1.

The trends in creep elongation for these same treatments are shown in Fig. 24.2. For each heat treatment the ductility increased with Ti content. Aging at 650°C significantly improved the ductility, whereas

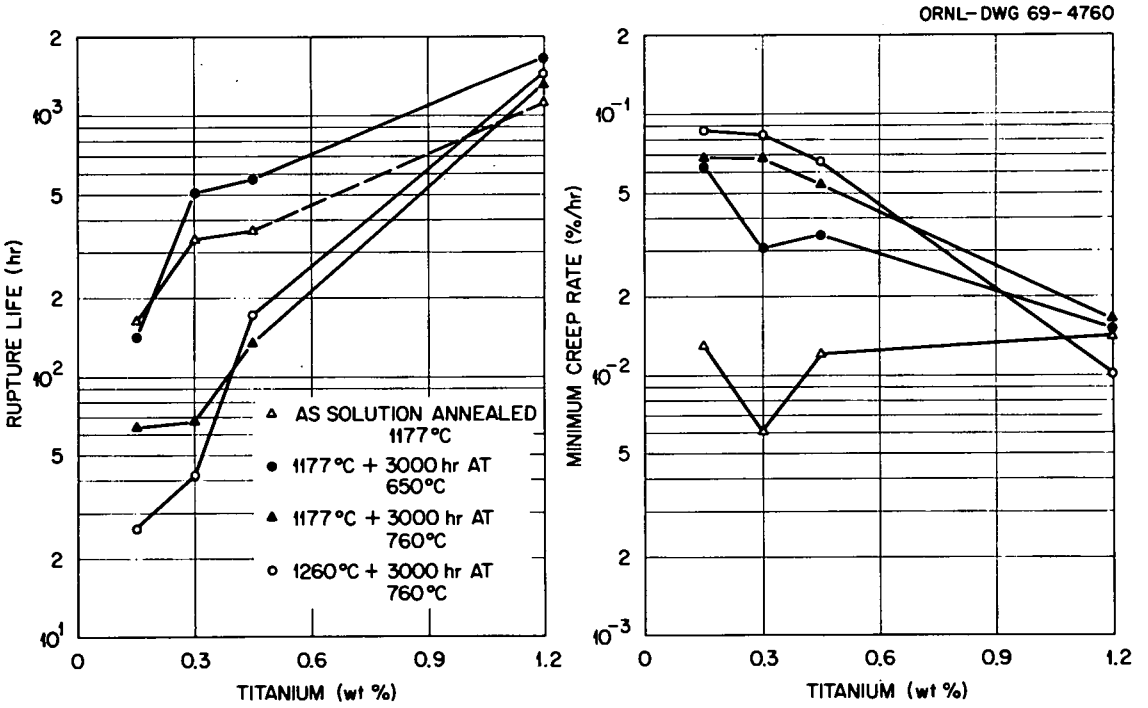

Fig. 24.1. Variation in Rupture Life and Creep Rate with Titanium Content and Aging Treatment for Creep Test of Modified Hastelloy N at 40,000 psi and 650°C.

annealing at 1260°C and aging at 760°C gave the lowest creep ductility of all the treatments investigated. However, these lower ductility values are not appreciably different from that obtained for the samples annealed at 1260°C in the annealed condition (not plotted).

The heat with 1.2% Ti deteriorated only slightly in creep-rupture properties after 3000 hr at 650 or 760°C, whereas alloys with lower levels of Ti have higher creep rates and reduced rupture lives after aging – particularly after aging at 760°C. The good creep behavior of this heat with higher Ti content corresponds to a favorable distribution of the MC type of carbide[1] in the microstructure.

Statistical Treatment of Aging Data for Hastelloy N (Claudia S. Lever,[2] C. E. Sessions)

Analysis of Variance. – We previously discussed[3] the procedures for analysis of variance for testing the changes in tensile properties after aging as a function of the variables in the aging program. The analysis

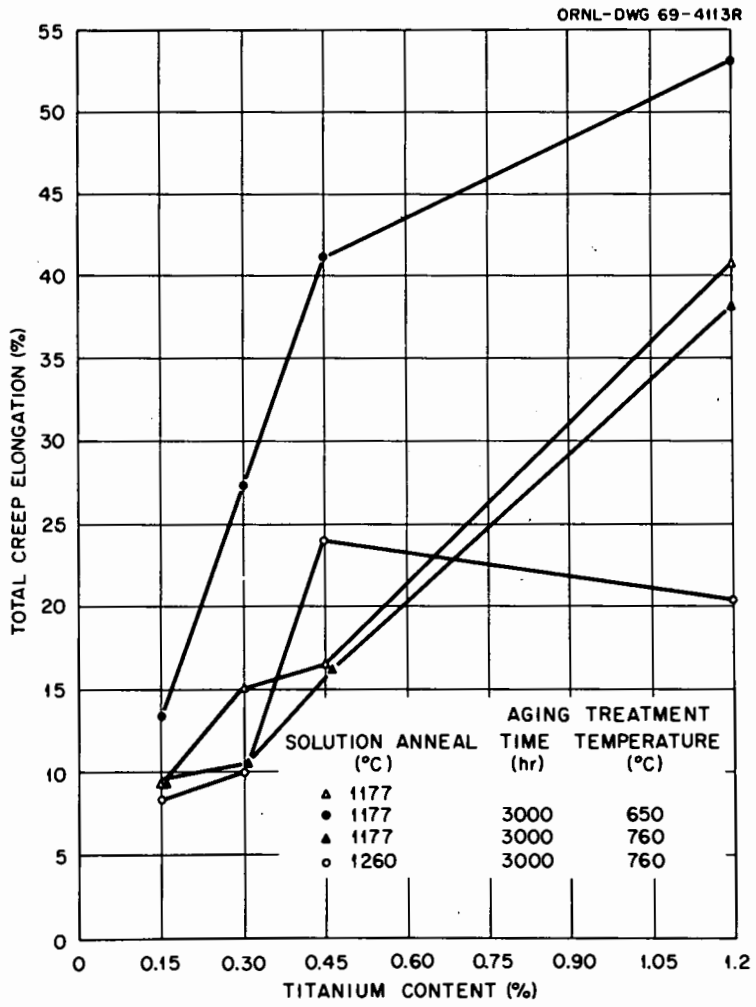

Fig. 24.2. Ductility of Aged Titanium-Modified Hastelloy N After Creep at 40,000 psi and 650°C.

of variance (Table 24.1) was calculated from the measurements made on 72 samples after aging 1500, 3000, and 10,000 hr at 650 and 760°C.

All of the main, single variables had significant effects except that aging more than 1500 hr did not affect the yield strength. Since many of the second-order interactions are significant, the tensile response depends on at least two variables. For instance, we must define the preage treatment to specify the influence of Ti content.

The third-order interactions were not significant in most cases and, thus, could be used with the four duplicate test results to estimate the error variation. This variation was then used to establish a basis for comparing the main effects and second-order interactions.

Table 24.1. Analysis of Variance for Changes in Tensile Properties

Variable	Strength		Elongation		Reduction of Area
	Yield	Ultimate Tensile	Uniform	Total	
	Effects of Single Variables				
Ti content	S[a]	S	S	S	S
Preage treatment	S	S	S	S	S
Time at temperature	NS[b]	S	S	S	S
Aging temperature	S	S	S	S	S
	Effects of Interactions				
Ti content and preage	S	S	S	S	S
Ti content and time	NS	S	NS	NS	NS
Ti content and temperature	S	NS	S	S	S
Preage and time	S	NS	NS	NS	NS
Preage and temperature	S	S	S	S	S
Time and temperature	S	NS	S	S	S
Ti content, preage, and time	NS	S	NS	NS	NS
Ti content, preage, and temperature	NS	S	S	S	NS
Ti content, time, and temperature	NS	S	S	NS	NS
Preage, time, and temperature	NS	NS	NS	NS	NS

[a]An S means that the variable significantly affected the tensile property.

[b]NS indicates that the effect was not significant.

Regression Analysis. — We used a regression model to fit the data on tensile properties as functions of aging time, temperature, and Ti content for a given pretest annealing condition. We used a model of the form

$$E(y) = \beta_0 + \beta_1 x_1 + \beta_{11} x_1^2 + \beta_{111} x_1^3 + \beta_2 x_2 + \beta_{21} x_2^2 + \beta_3 x_3 + \beta_{12} x_1 x_2 + \beta_{13} x_1 x_3 + \beta_{23} x_2 x_3 + \beta_{123} x_1 x_2 x_3 , \quad (24.1)$$

where E(y) is the expected value (predicted value) and x_1, x_2, and x_3 are the variables time, temperature, and Ti content. By using a least squares procedure, we minimized the residual sum of squares in this linear regression model between E(y) and the observed data for each tensile property. By considering other models with various terms omitted, we obtained the best equation to describe the experimental data with the minimum variance. Fifteen equations were obtained, describing the five tensile properties for the three pretest heat treatments.

The main difference in the models that were selected based on our fitting criteria is that the properties after a solution anneal at 1260°C required the inclusion of a cubic term (i.e., x_1^3) to fit the data, while this term was not required to fit the data for a solution anneal at 1177°C or for a solution anneal at 1177°C plus 10% prestrain (i.e., a quadratic dependence on Ti content, whereas the data for 1260°C follow a cubic dependence on Ti content).

Figure 24.3 is a plot of the fitted equations for yield strength and total elongation at 650°C for samples solution annealed 1 hr at 1177°C. All data for a given preage treatment were used to determine the coefficients in the regression equation; thus, the curves plotted are defined by a least squares fit of 24 points. The fit of the equation to the four experimental points for a given time of aging is better for the yield strength than for the elongation. The equations plotted are as follows:

$$\text{Yield strength} = 67.166 - 47.281x_1 + 32.1x_1^2 - 0.709x_2 + 0.0414x_2^2 - 3.426x_3 - 0.3362x_1x_2 + 1.423x_1x_3 + 0.0038x_2x_3 \quad (24.2)$$

and

$$\text{Total elongation} = 139.2 - 0.1455x_1 - 34.608x_1^2 - 8.70x_2 + 0.449x_2^2 - 16.66x_3 + 0.449x_1x_2 + 9.713x_1x_3 + 0.383x_2x_3 \quad (24.3)$$

where

x_1 = Ti content of $0.15 \leq x_1 \leq 1.2$,

x_2 = aging time of $1.5 \leq x_2 \leq 10.0$, and

x_3 = aging temperature of $6.5 \leq x_3 \leq 7.6$.

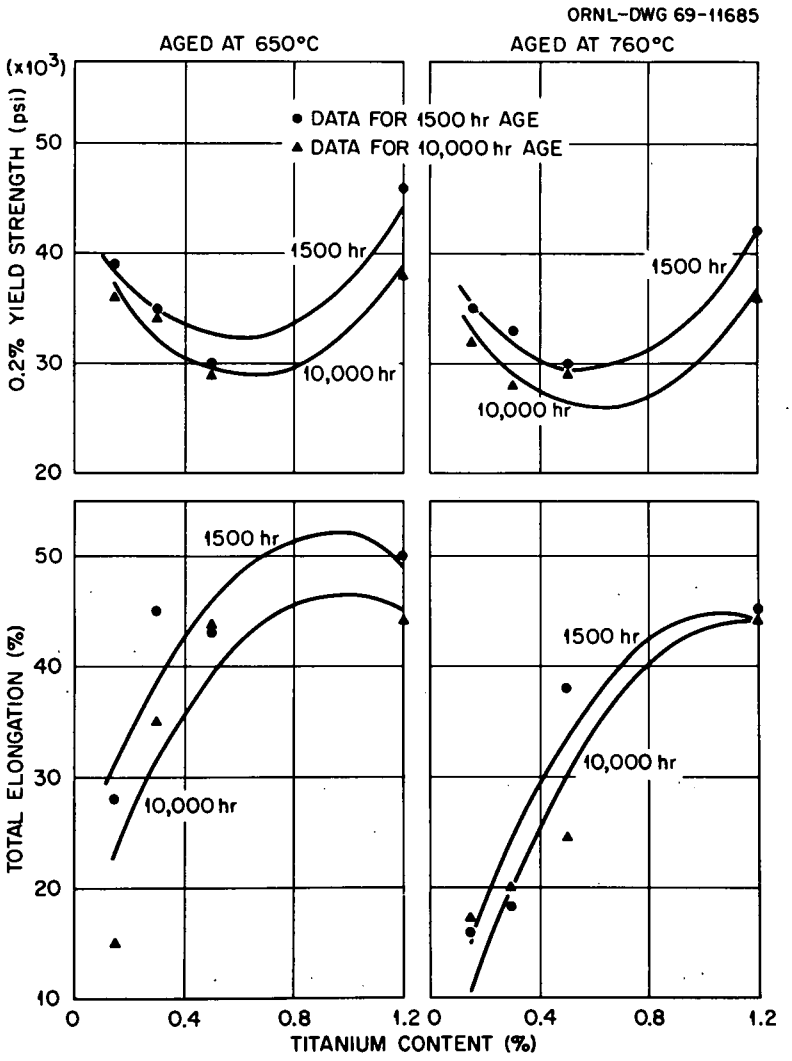

Fig. 24.3. Tensile Strength and Ductility of Modified Hastelloy N at 650°C as Fitted by Regression Model as a Function of Titanium Content and Aging Time.

These equations indicate clearly the increase in ductility with Ti content, the small decrease in strength and ductility with aging time, the significant lowering of ductility after aging at 760°C, and a predicted minimum in strength and maximum in ductility between 0.5 and 1.2% Ti.

Development of a Modified Hastelloy N (C. E. Sessions, R. E. Gehlbach)

Our work has concentrated in the areas of determining the optimum composition and gaining further experience with these modified Hastelloy N alloys through commercial vendors. Our previous studies[4] indicated that

certain alloys containing additions of Ti, Hf, Nb, and Y had good mechanical properties after being irradiated at 760°C. Additional samples were tested, and this general finding still holds true. The fracture strains of several of the more attractive alloys are shown in Fig. 24.4.

Our rather fragmentary results show that certain alloys have good properties and that these alloys have the MC type of carbide. Our results indicate that Ti, Nb, and Hf favor the formation of the desired carbide and that Si promotes the formation of the less desirable M_6C type of carbide. We have melted about thirty alloys that contain various concentrations of these four elements. These alloys are included in all phases of our work and should enable us to select an optimum composition.

Our experience with alloys containing Ti ($5/lb) and Nb ($20/lb) and the low costs of these elements make it desirable that we utilize these elements in our alloy in preference to Hf (about $100/lb) or Y (about $300/lb). We have demonstrated that alloys containing up to 1.2% Ti and 2% Nb have good weldability. Our studies of postirradiation mechanical properties leave some doubt as to whether Nb alone can produce the desired properties. Additions of Ti alone can produce good properties, but the exact level required is not clear.

Because of the potential importance of the Ti-modified alloys, let us look briefly at the available data. Several alloys that contain about 1% Ti were obtained from various sources and included in our program. The compositions of these alloys are given in Table 24.2, and the postirradiation creep results are summarized in Table 24.3. These results are plotted in Figs. 24.5–24.7 and compared with the properties of irradiated standard Hastelloy N and unirradiated modified alloys. These results lead to several important observations.

1. Alloy 21 behaves much like standard Hastelloy N. This alloy was prepared by remelting standard Hastelloy N, and most of the Ti likely ended up as oxide. The high Mo and Si contents of this alloy should have resulted in the formation of the M_6C type of carbide, and the properties would be expected to be equivalent to those of standard Hastelloy N.

2. Alloys 75 and 76 have excellent properties under all conditions tested.

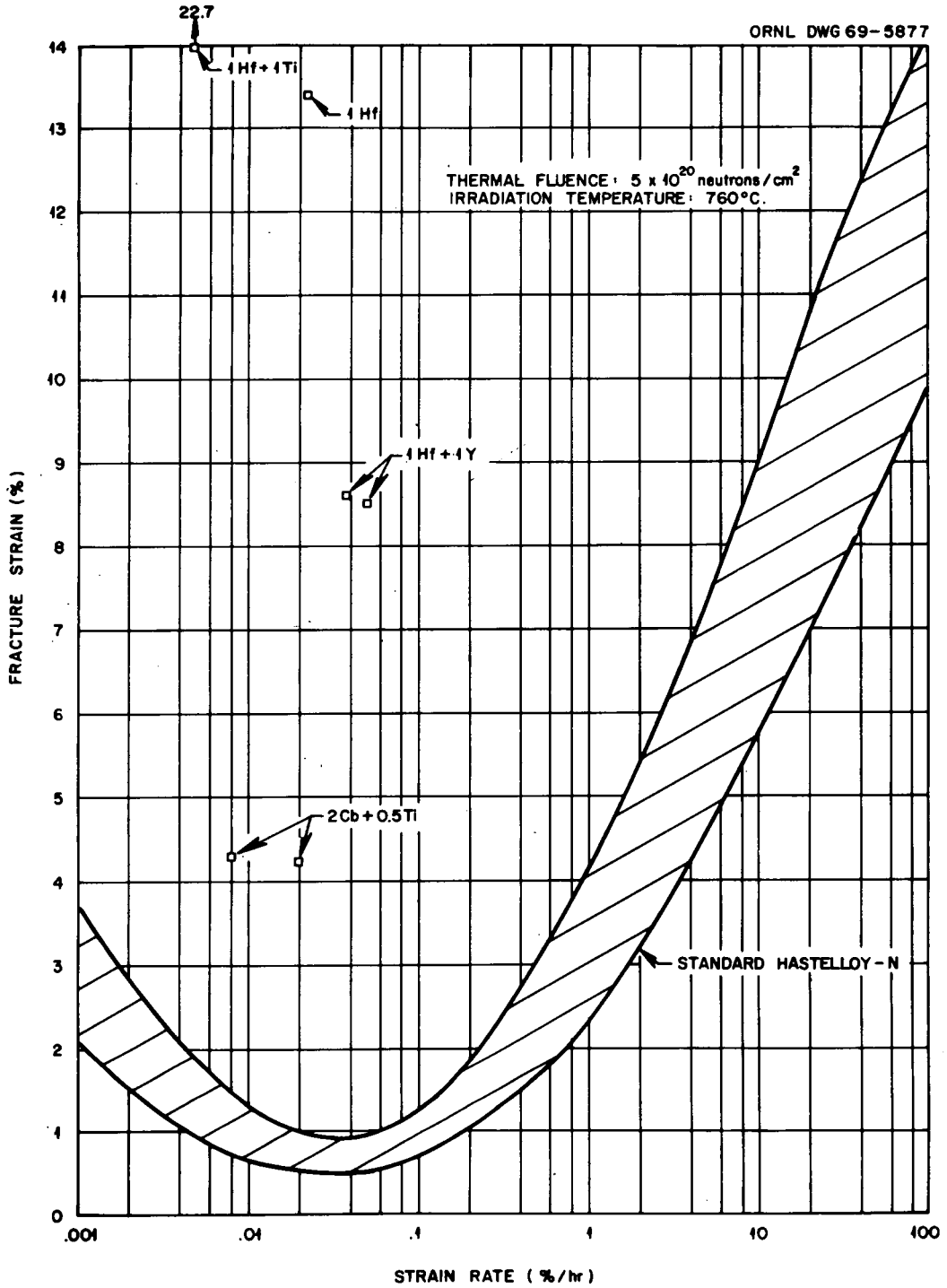

Fig. 24.4. Postirradiation Fracture Strains of Several Compositions of Modified Hastelloy N. All samples were irradiated at 760°C and tested at 650°C. The base composition was Ni–12% Mo–7% Cr–0.2% Mn–0.05% C. (The alloy containing 1% Hf and 1% Ti also contained 4% Fe and 0.1% Si; neither of these elements is thought to be critical.)

Table 24.2. Chemical Analyses of Several Heats of Modified Hastelloy N

Alloy Number	Melt Size (lb)	Origin of Melt[a]	Composition, wt %						
			Mo	Cr	Fe	Mn	Si	Ti	C
21	2	A	16.0	7.0	3.3	0.5	0.5	1	0.038
107	2	A	11.6	6.6	0.082	0.19	< 0.005	1.04	0.05
75	2	A	11.8	7.9	< 0.05	0.2	0	1	0.062
76	2	A	11.8	7.9	< 0.05	0.2	0	1	0.117
67-552	100	B	11.9	7.0	0.02	0.11	0.01	0.84	0.01
67-570	100	B	11.7	7.0	0.02	0.12	0.02	0.92	0.028
67-549	100	B	11.7	7.0	0.03	0.13	0.02	0.93	0.08
67-551	100	B	12.2	7.0	0.02	0.12	0.02	1.1	0.028
67-548	100	B	12.0	7.1	0.04	0.12	0.03	1.1	0.102

[a]A = ORNL; B = Materials Systems Division, Union Carbide Corporation.

3. Alloy 107 has about the same composition as alloy 75, but the single sample of alloy 107 that we tested had poor properties.

4. Alloys 67-552, 67-570, and 67-549 all contain about 0.9% Ti and from 0.01 to 0.08% C. Tests on all three heats – except for a single test on heat 67-549 at 25,000 psi – showed poor properties.

5. Alloys 67-551 and 67-548 contain 1.2% Ti and have C levels of 0.028 and 0.102%, respectively. Again, only the specimens of the higher heat with higher C content that were tested at 25,000 psi had good properties.

Thus the apparent inconsistencies of these results point to the complexity of the processes with which we are dealing. All of these alloys have nominal compositions of 1% Ti, but the properties are quite different. Subtle changes in chemistry, differences in melting practice, and small variations in fabrication may all contribute to the observed differences in properties.

Our experience with commercial vendors has been rather limited because we lack funds to purchase large quantities of material. Since

Table 24.3. Postirradiation[a] Creep Properties at 650°C for Several Modified Alloys of Hastelloy N

Alloy Number	Test Number	Stress (psi)	Rupture Life (hr)	Minimum Creep Rate (%/hr)	Fracture Strain (%)
21	853	40,000	67.2	0.0089	0.92
	819	27,000	414.6	0.0024	1.68
75	888	47,000	248.1	0.0442	13.1
	855	35,000	2669.2	0.0061	23.6
76	889	47,000	276.0	0.0540	19.6
	852	35,000	2688.4	0.0059	22.0
107	784	30,000	49.4	0.0238	1.58
67-552	633	15,000	2.5	0.0085	0.04
	630	21,500	0.5	0.20	0.56
	618	27,000	0.1	1.66	0.17
	681	25,000	59.0	0.0156	1.44
67-570	863	27,000	0.1		0.18
	887	21,500	0.25	0.20	0.07
	680	25,000	0.1		0.62
67-549	825	25,000	3117.6	0.0017	7.3
	850	35,000	1.0	0.071	0.47
	672	30,000	0		
67-551	861	35,000	0		
	685	25,000	0.2	1.22	0.32
67-548	835	40,000	0.4	0.50	0.50
	824	25,000	2283.4	0.0030	7.84
	686	25,000	1437.2	0.0042	7.51

[a]All samples irradiated at 760°C to a thermal fluence of 3×10^{20} neutrons/cm^2.

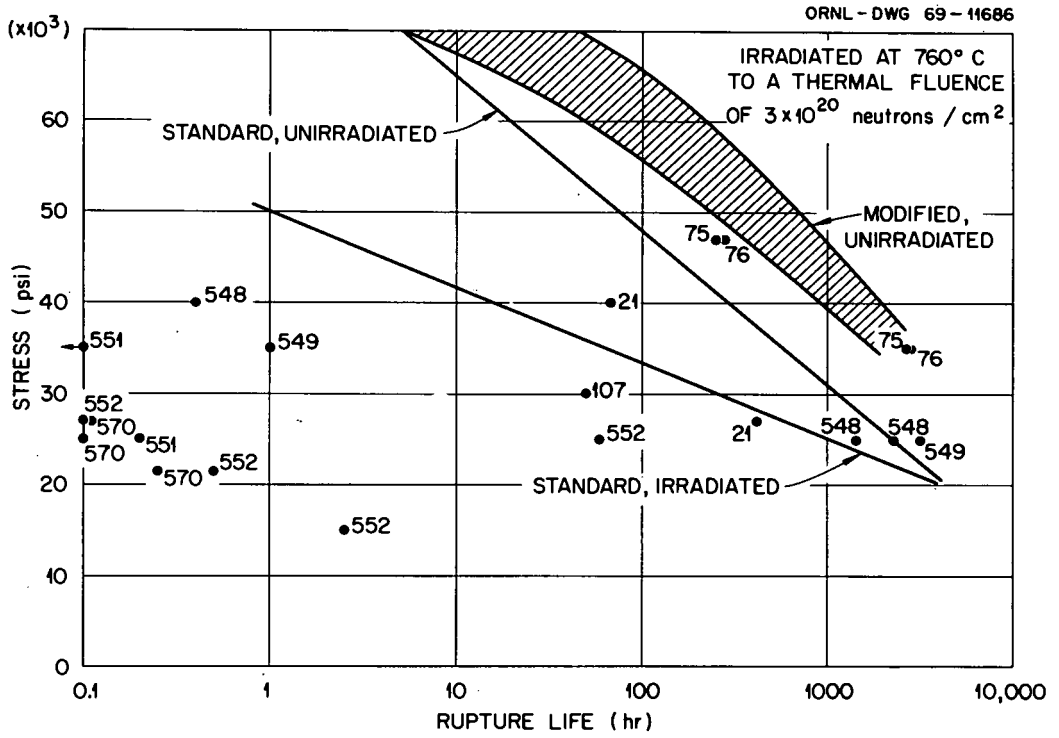

Fig. 24.5. Stress-Rupture Properties of Several Heats of Titanium-Modified Hastelloy N at 650°C. (See Table 24.2 for compositions.)

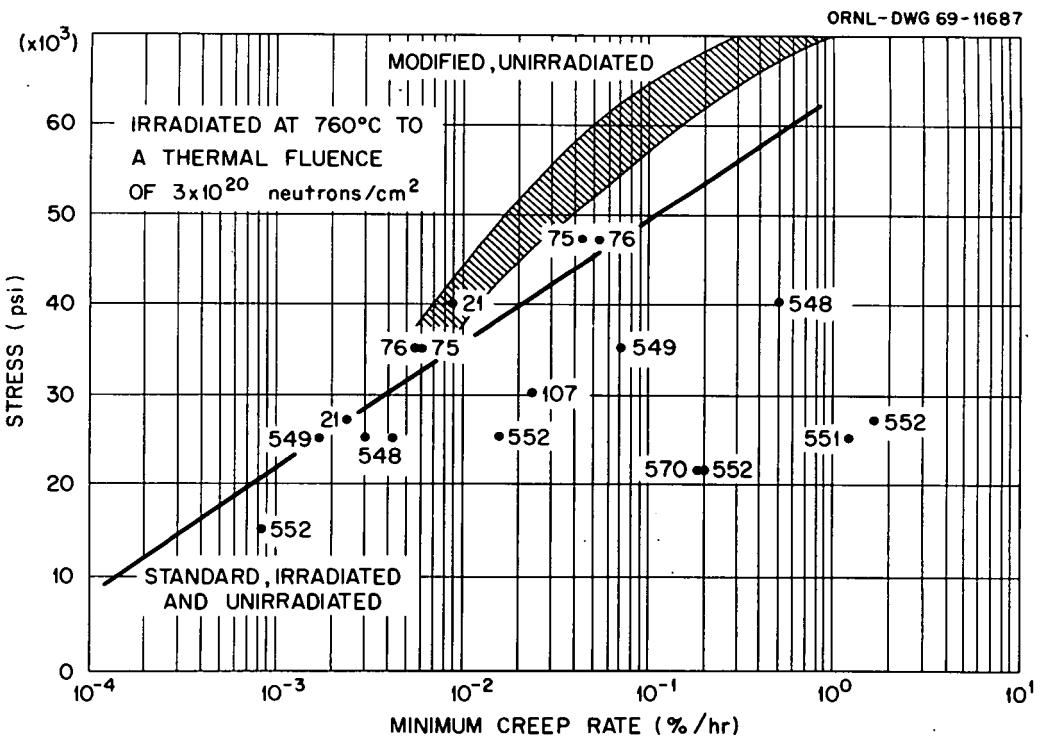

Fig. 24.6. Creep-Rupture Properties of Several Heats of Titanium-Modified Hastelloy N at 650°C. (See Table 24.2 for compositions.)

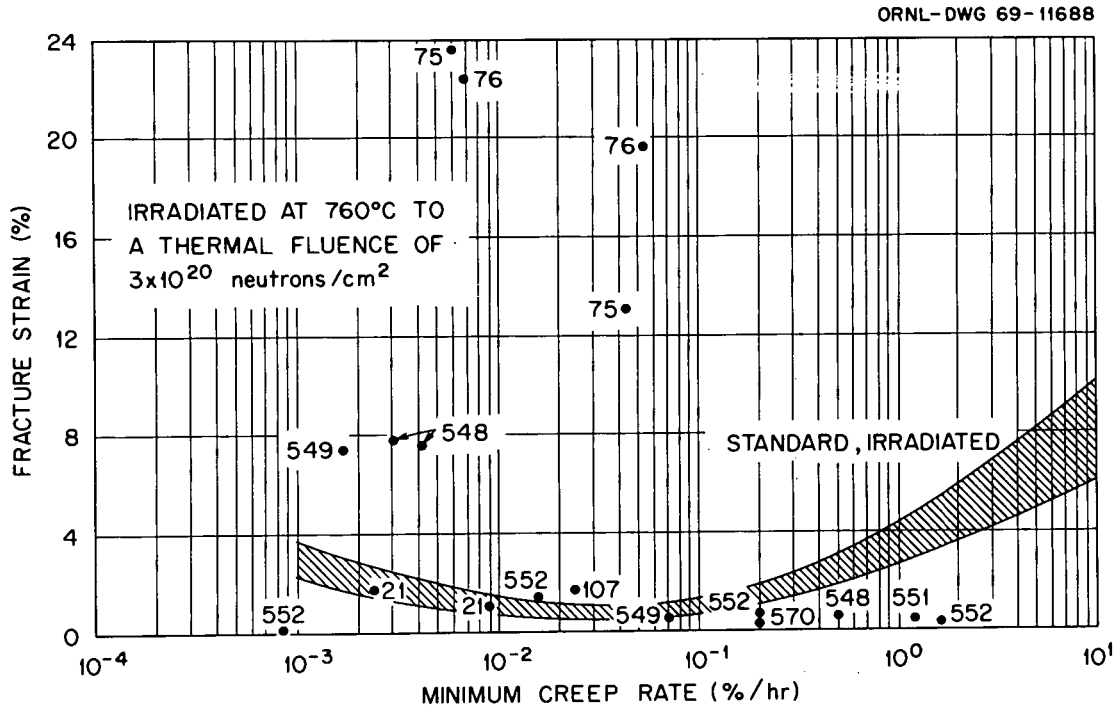

Fig. 24.7. Fracture of Several Heats of Titanium-Modified Hastelloy N at 650°C. (See Table 24.2 for compositions.)

we began our program, a new melting process has gained favor with several vendors. This process, called the electro-slag remelting (ESR) process, remelts an electrode under a pool of molten slag. This slag protects the melt from the air, but likely introduces another set of impurities from the slag. In vacuum-melting practice, this remelting takes place under vacuum. The claimed advantages of the ESR process are smoother ingot surfaces and some improvements in physical properties and weldability. We purchased two small (100-lb) melts made by the ESR process to examine their properties. The compositions of the alloys are given in Table 24.4; one alloy contained a nominal 0.5% Ti and the other alloy did not contain any added Ti. The Mo concentration was on the high side of our specification, and the Si content was from 0.4 to 0.5%. Photomicrographs of the two alloys are shown in Figs. 24.8 and 24.9. The composition was such that both alloys contained stringers of the M_6C type of carbide, just as we noted in standard Hastelloy N. Thus, it is likely that these alloys will not have good postirradiation properties. An experiment

Table 24.4. Chemical Analysis of Electro-Slag Remelted Heats

Heat Number	Source[a]	Concentration, wt %											ppm			
		Mo	Cr	Fe	Mn	C	Si	P	S	Cu	Co	Ti	B	N	O	H
68-688	A	10.0	7.91	4.98	0.52	0.079	0.38	0.042	< 0.002	0.023	0.08	0.013	2	8	8	3
	B	13.8	7.8	5.0	0.50	0.077	0.39	0.002	0.003	0.025	0.07	0.02				
68-689	A	12.6	7.69	4.84	0.47	0.081	0.53	0.010	< 0.002	0.020	0.075	0.36	2	11	12	3
	B	13.9	7.64	4.8	0.47	0.078	0.52	0.001	0.003	0.03	0.07	0.45				

[a]A = ORNL; B = vendor.

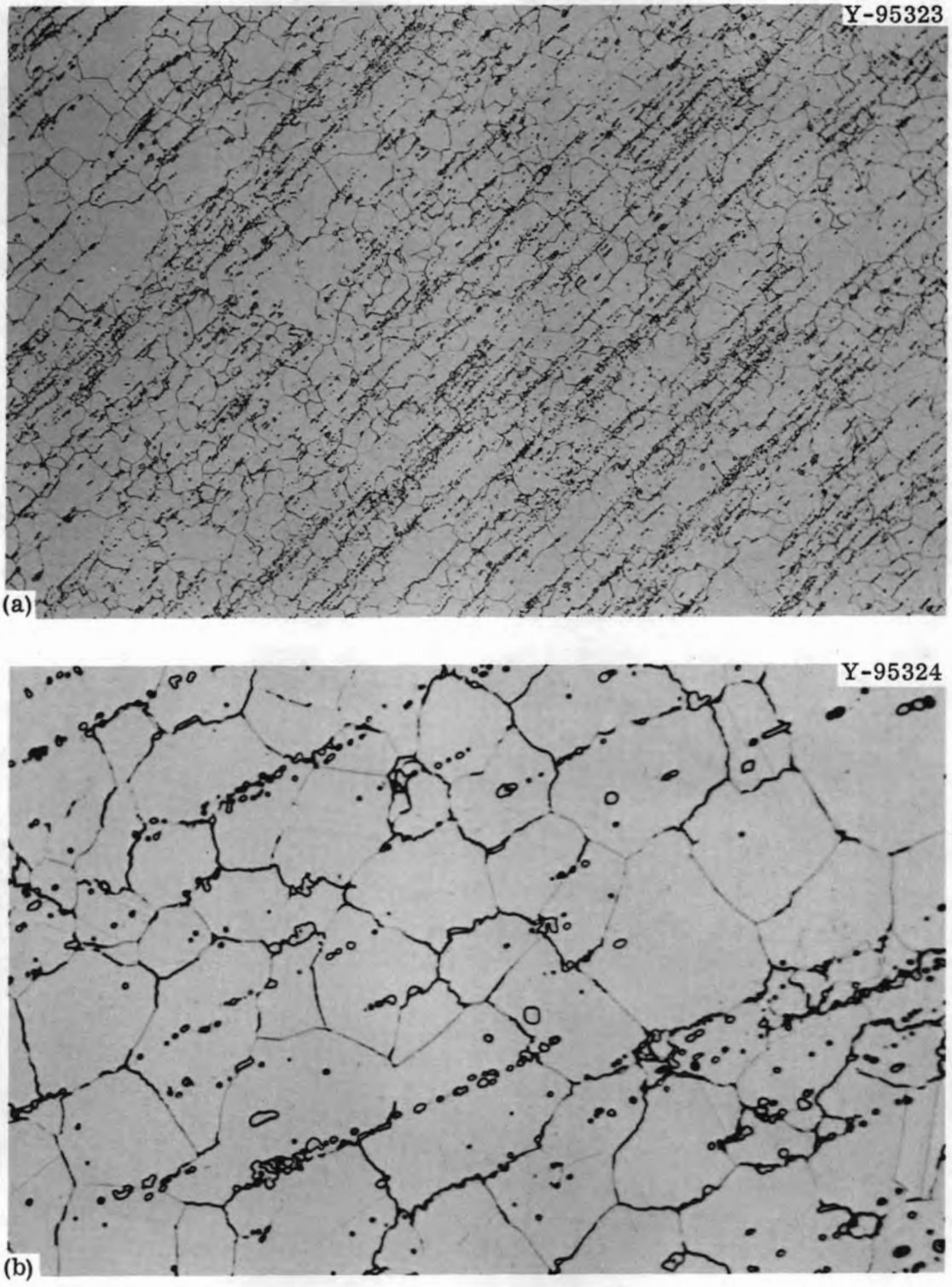

Fig. 24.8. Photomicrographs of Electro-Slag Remelted Alloy 68-688 After 1-hr Anneal at 1177°C. Longitudinal section. (a) 100×. (b) 500×. Etchant: glyceria regia.

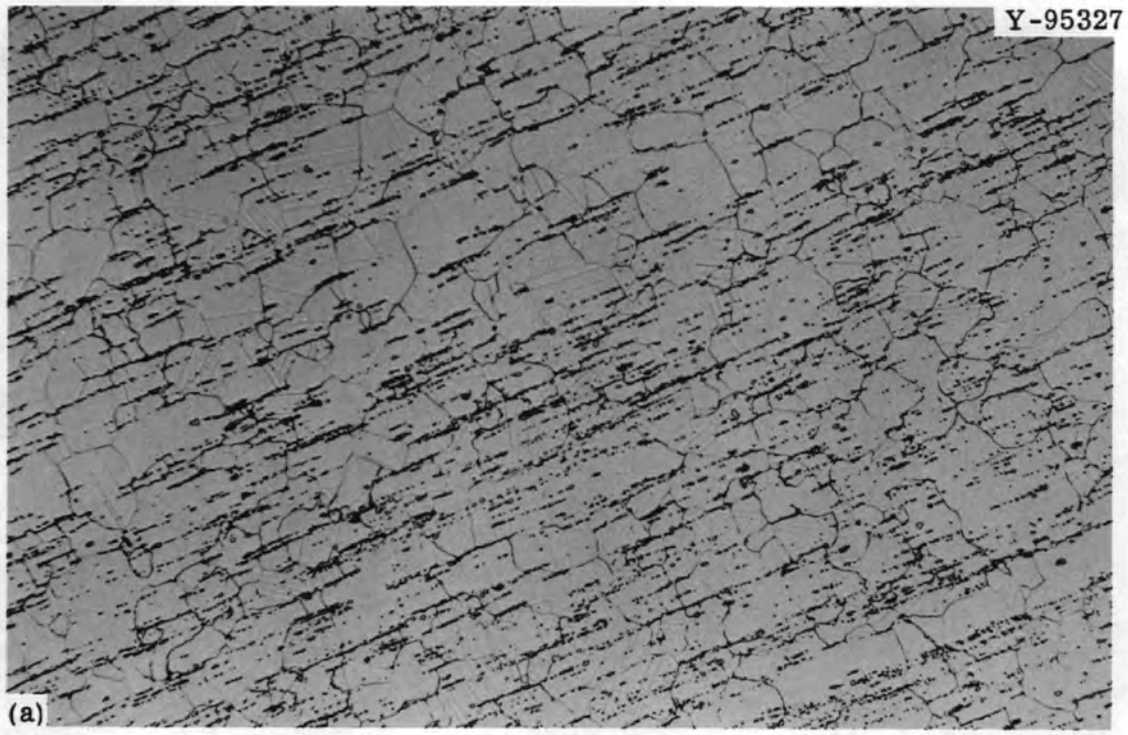

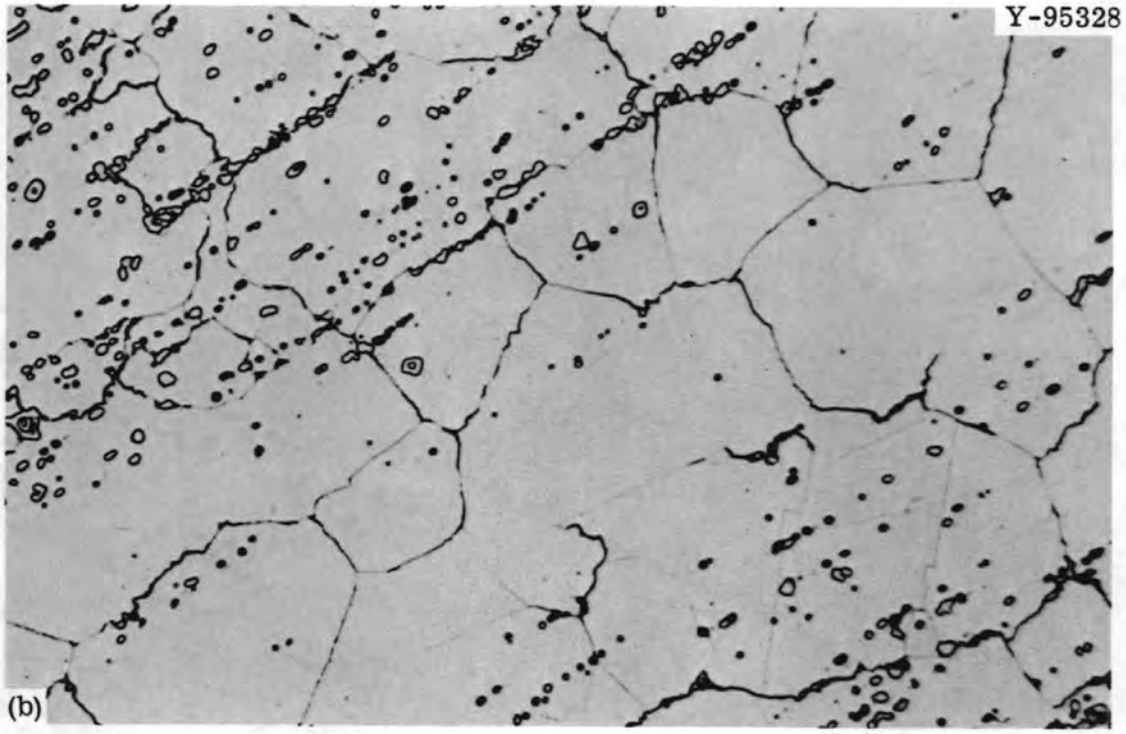

Fig. 24.9. Photomicrographs of Electro-Slag Remelted Alloy 68-689 After 1-hr Anneal at 1177°C. Longitudinal section. (a) 100×. (b) 500×. Etchant: glyceria regia.

that contains some of these alloys will be removed from the Oak Ridge Research Reactor in October 1969.

The ESR alloys were fabricated into 1/2-in.-thick plates about 6 in. wide × 12 in. long. High-restraint welds were made by welding the individual plates to a strongback of carbon steel. Wire fabricated from the same heat was used as filler metal, and the material welded very well.

Several tests were made of the mechanical properties of the ESR heats. The results of tensile tests are summarized in Figs. 24.10 and 24.11; the tensile strengths are equal to each other and equivalent to those of standard Hastelloy N. The vacuum-melted modified alloy generally has lower tensile strength but much better tensile ductility, especially at room temperature. The ESR heats and the standard alloy have comparable fracture strains at low temperatures. At 650°C, the ductility ranges from the highest of 47% for the vacuum-melted heat to the lowest of 32% for the Ti-modified ESR heat.

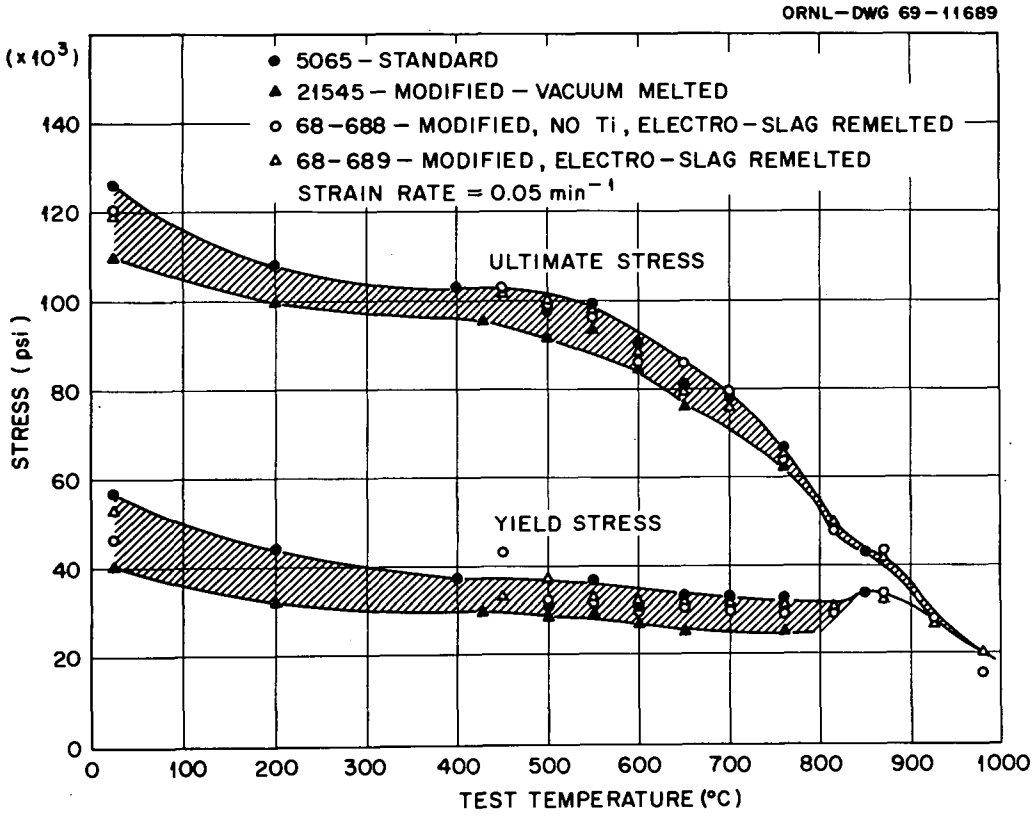

Fig. 24.10. Tensile Properties of Several Modified Compositions of Hastelloy N.

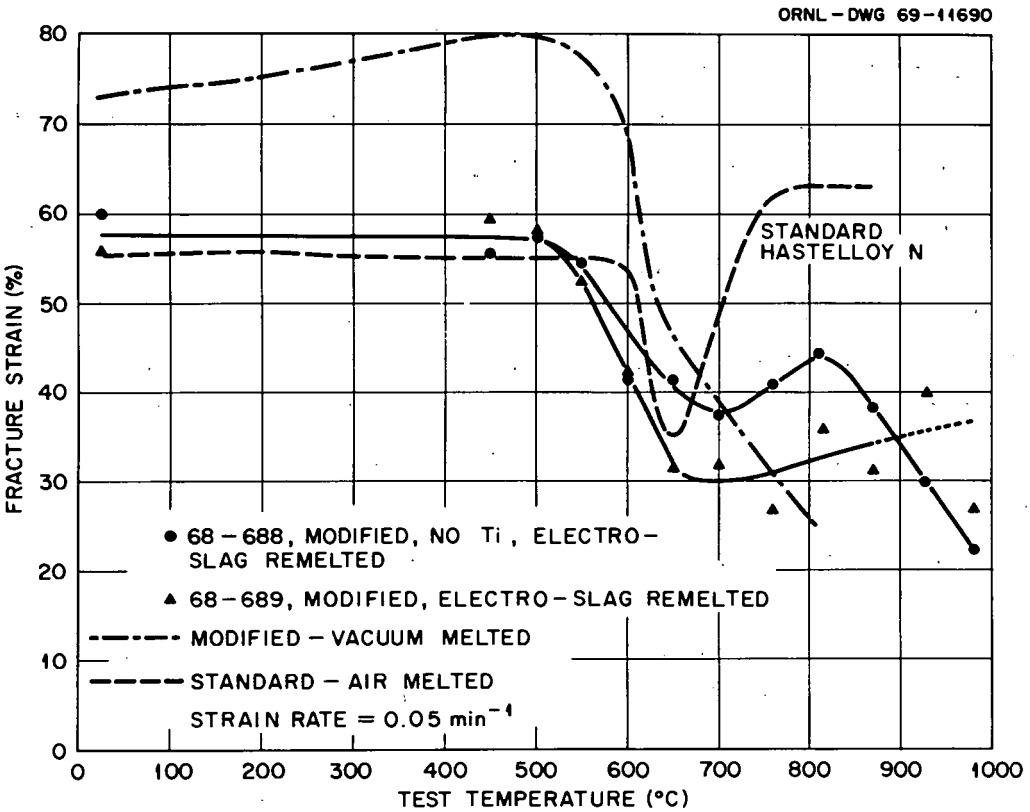

Fig. 24.11. Fracture Strains of Several Modified Compositions of Hastelloy N.

Stress-rupture tests at 650°C show that the ESR alloys resist rupture at a given stress level about as long as the standard alloy, but not nearly as long as the vacuum-melted Ti-modified alloy (Fig. 24.12). Two tests on stress-relieved ESR welds show that the rupture lives of the welds are equivalent to those of the base metal. The creep rates from these tests show that the ESR melts have better creep strength than standard Hastelloy N, but lower strength than the vacuum-melted modified alloy (Fig. 24.13).

Thus the ESR alloys have acceptable properties in the unirradiated condition, but the unavoidable presence of high Si (from the slag) probably will produce a carbide structure that is not conducive to good postirradiation properties.

Allvac Metals Company made two small melts that have nominal compositions equivalent to two ORNL alloys that had excellent postirradiation properties. One alloy had additions of 1% Ti and 1% Hf; a 50-lb heat

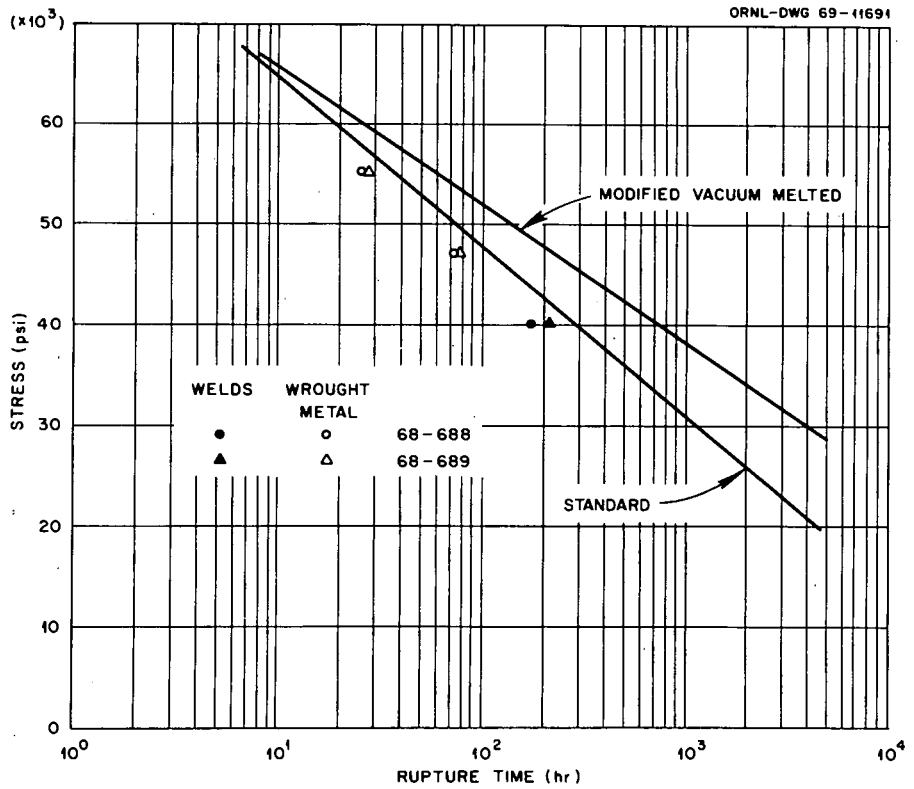

Fig. 24.12. A Comparison of the Stress-Rupture Properties of Electro-Slag Remelted Alloys with Other Compositions of Hastelloy N Alloys at 650°C.

was melted and fabricated without problem. A second melt contained 0.5% Ti and 2% Nb and required frequent grinding to remove cracks that developed during fabrication. These alloys will be included in all phases of our program.

Electron Microscopy of Hastelloy N (R. E. Gehlbach, C. E. Sessions)

We are continuing our studies of the role of the elements Ti, Nb, Hf, and Si on precipitation in modified Hastelloy N. As previously reported,[5] additions of Ti, Nb, and Hf cause the precipitation of the MC type of carbides rather than the M_2C type that is found in the modified alloy when these elements are not present. Additions of Si shift the type of carbides from M_2C to M_6C and possibly from MC to M_2C. The MC type of carbides are finer than either the M_2C or M_6C, and, in view of their morphologies and distribution, we feel that they are responsible

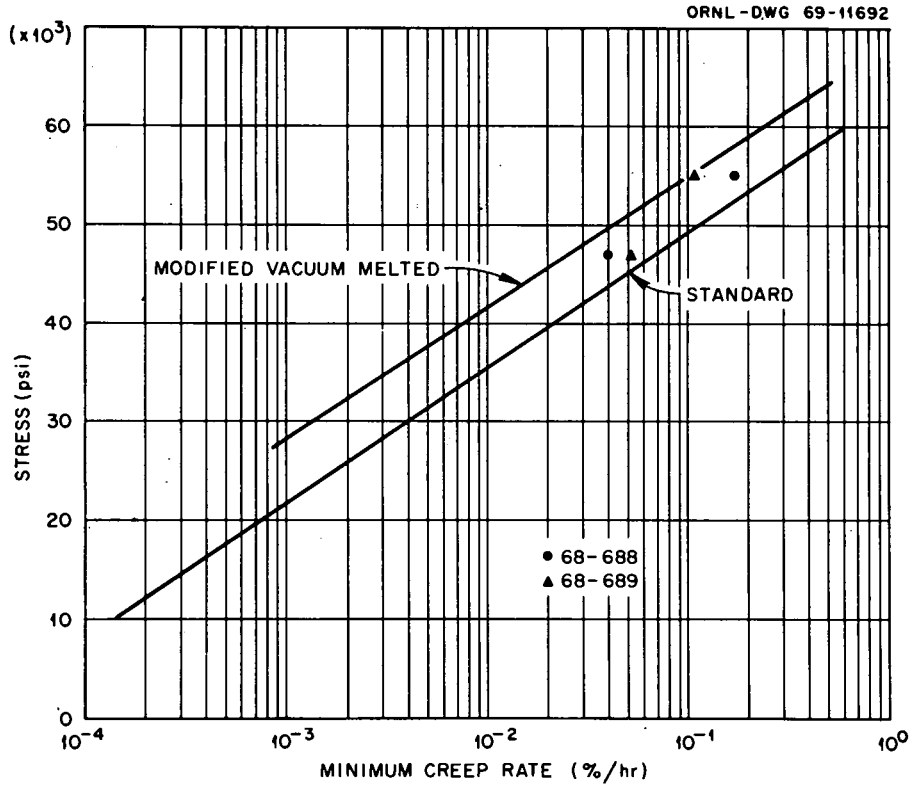

Fig. 24.13. A Comparison of the Creep Properties of Electro-Slag Remelted Alloys with Other Compositions of Hastelloy N Alloys at 650°C.

for the superior postirradiation properties of some modified alloys, particularly after irradiation at temperatures above 700°C.

The morphologies of the MC-type precipitates in the Ti-modified alloys are different when they are precipitated at grain boundaries than they are when they are precipitated in the matrix. Carbides at the grain boundaries are generally shaped like platelets, about 1 μm in diameter and ≤ 0.3 μm thick. The boundaries are quite rough because the particles usually do not follow the direction of the grain boundary. In alloys containing 0.5% Ti or more, a considerable amount of precipitation extends 1 to 2 μm into the matrix. Matrix precipitation is generally composed of very fine particles (≤ 200 A) on thin films that form at stacking faults, as shown in Fig. 24.14. Stacking faults are not observed when this matrix precipitate does not form.

Precipitation at stacking faults is nucleated at primary MC-type particles that are not put into solid solution during the initial

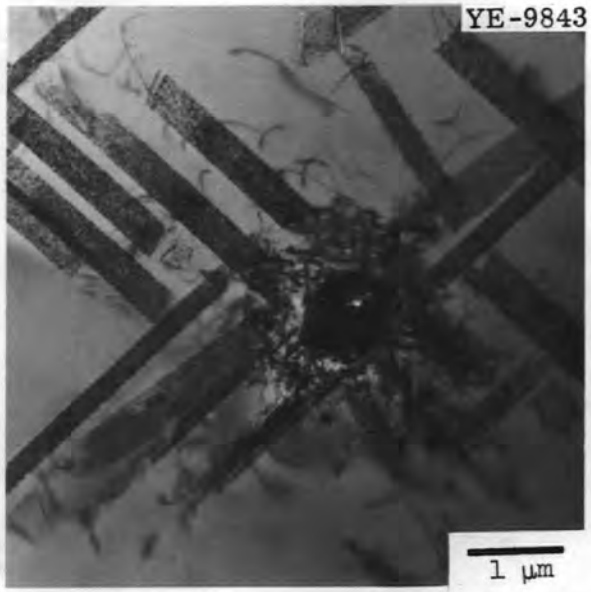

Fig. 24.14. Precipitation of (Mo, Cr, Ti)C on Stacking Faults Nucleated Around Primary MC-Type Particle. Hastelloy N containing 0.5% Ti (ORNL heat 196) annealed at 1177°C and aged 1500 hr at 650°C. 10,000×.

annealing. Dislocations produced around these particles by thermally induced stresses provide sites for initial precipitation. The faults grow by a process of climb of the partial dislocation bounding the sheet of precipitate. The diameter of these sheets is often 6 to 8 μm, depending on the history of the specimen.

The amount and extent of this type of precipitate is sensitive to both annealing and aging temperatures. Much greater amounts are formed on aging after annealing at 1260°C rather than the usual 1177°C. More primary particles are put into solution at the higher temperature; thus, more supersaturation exists and enhances precipitation at stacking faults. Subsequent aging temperatures also affect the extent and amount of this precipitate; higher temperatures (760°C rather than 650°C) produce more extensive precipitation.

The precipitation of the MC type of carbides in an alloy modified with 1% Ti and 1% Hf is different from that in alloys modified with Ti only. The carbides formed are HfC and TiC. As expected, more HfC than TiC is formed since Hf is a stronger former of the MC type of precipitate than Ti. The carbides in the grain boundaries are quite thin and somewhat finer than in the Ti-modified alloys. A more marked difference

is that very little precipitation is observed at stacking faults. Most matrix precipitates are in the form of platelets ≤ 0.5 μm in diameter, as shown in Fig. 24.15.

Fig. 24.15. Microstructure of Hastelloy N Containing 1% Ti and 1% Hf (ORNL heat 184) After Aging 128 hr at 760°C. The carbides are of the MC type (HfC and TiC). 10,000×.

As previously reported,[5] Ti in concentrations of > 0.5% or in combination with other elements that are strong formers of the MC type of carbides is necessary to stabilize the MC rather than the M_2C type of carbides at 760°C. The modified alloys that contain sufficient quantities of Ti, Hf, or Nb to give this stability at 760°C have very good properties after irradiation at temperatures above 700°C (ref. 6). Figure 24.16 shows the microstructure of an alloy containing 1% Ti, 1% Hf, and 0.2% Si after irradiation at 760°C. The specimen was taken from an unstressed portion of a creep sample with more than 5% reduction in area when the test was discontinued after nearly 2200 hr at 27,000 psi.

We believe that superior postirradiation properties result from favorable distributions of precipitates that can be attained with the MC type of carbides. We are now irradiating alloys with several types of microstructures to evaluate their resistance to irradiation damage at

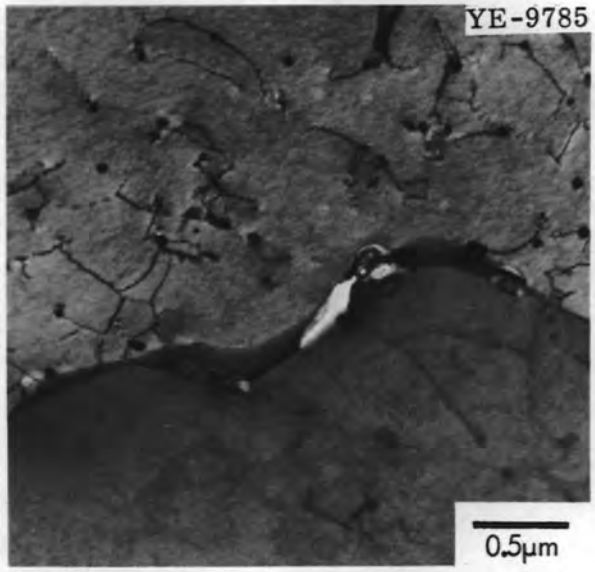

Fig. 24.16. Microstructure of Hastelloy N Containing 1% Ti, 1% Hf, and 0.2% Si (ORNL heat 184) Irradiated More Than 1000 hr at 760°C, Creep Tested 2150 hr at 650°C and 27,000 psi to More Than 5% Reduction in Area Before Test was Discontinued. Specimen was taken from unstressed portion of sample. 25,000×.

high temperatures. We can achieve stability of the MC type of carbides by adding 1% Ti, although 0.5% Ti is not sufficient; 1% Hf, with or without Ti, is sufficient to stabilize these carbides even with 0.2% Si in the alloy. Since Si promotes the formation of the M_2C and M_6C types of carbides, it is likely that considerably less Hf would be needed for alloys with lower Si concentrations. The role of Nb is not clear at this time; but, at least when used in combination with Ti, it is effective in stabilizing the MC type of carbides and gives very good resistance to irradiation damage.

References

1. The symbol M here signifies the metal content of a carbide precipitate.
2. Mathematics Division.
3. C. E. Sessions and C. S. Lever, Fuels and Materials Development Program Quart. Progr. Rept. March 31, 1969, ORNL-4420, pp. 144–147.

4. C. E. Sessions, H. E. McCoy, and R. E. Gehlbach, Fuels and Materials Development Program Quart. Progr. Rept. Sept. 30, 1968, ORNL-4350, pp. 163–173.

5. R. E. Gehlbach and S. W. Cook, Fuels and Materials Development Program Quart. Progr. Rept. March 31, 1969, ORNL-4420, pp. 162–168.

6. C. E. Sessions and R. E. Gehlbach, "Development of a Modified Hastelloy N," pp. 279–291, this report.

25. ADVANCED MATERIALS FOR STEAM GENERATORS

P. Patriarca G. M. Slaughter

The purpose of this program is to determine the corrosion resistance of welds in several high-temperature alloys being considered for use in steam generators for advanced High-Temperature Gas-Cooled Reactors. We need to know how well these weldments will resist both general and preferential corrosion in steam at 595 to 760°C.

The program includes four areas of investigation: (1) general corrosion (formation of a uniform scale) at 595 and 650°C, including an evaluation of the general weldability of various combinations of base and filler metals; (2) general corrosion at 705 to 760°C; (3) preferential corrosion (e.g., oxidation at the fusion line, pitting, and stress-corrosion cracking); and (4) mechanical properties.

Program History

We are investigating general and preferential steam corrosion of weldments between similar and dissimilar metals of interest for advanced steam generators.[1] The structural materials used in conventional steam generators are included in these tests for comparison. The corrosive environment is dynamic, superheated steam at 595 to 760°C, a pressure of 900 psi, and a velocity of 5 ft/sec. While similar studies have been made on several wrought materials for steam generators,[2,3] the behavior of welds with their inherent compositional variations — particularly in welds between dissimilar metals — has been essentially neglected.

Our subcontractor, Southern Nuclear Engineering Company, has exposed the materials 6000 hr at 595 and 650°C to steam of good commercial quality, provided from a steam-generator superheater at the Bartow Plant of the Florida Power Corporation, in the corrosion loop shown in Fig. 25.1. Figure 25.2 illustrates the procedures for chemical control of the water and steam at the Bartow Plant. Table 25.1 lists the

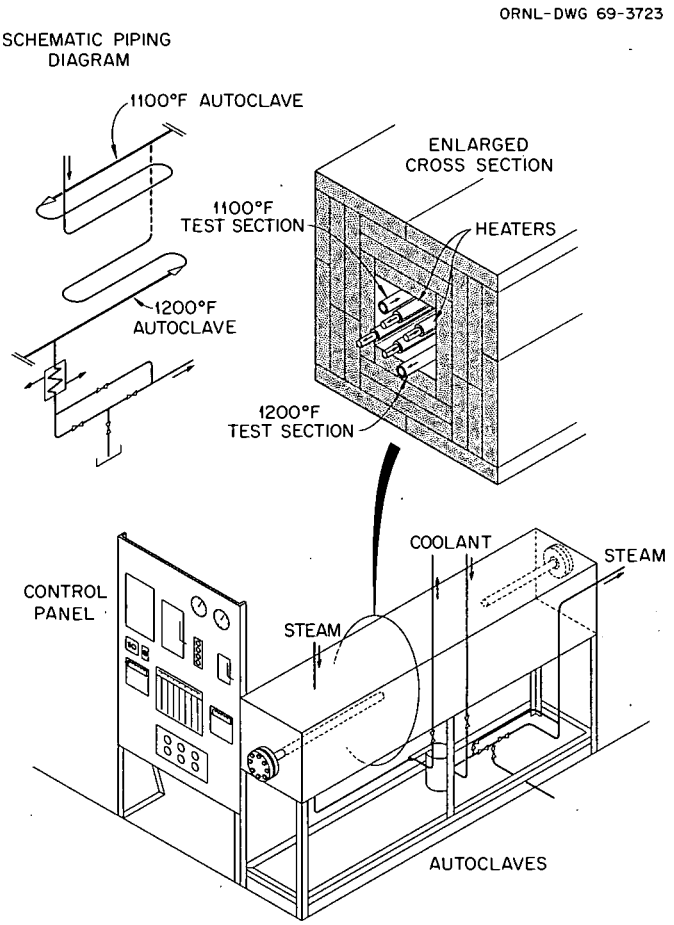

Fig. 25.1. Schematic Drawings of the ORNL-Southern Nuclear Engineering Company Loop for Testing Corrosion of Advanced Materials by Steam at 595 and 650°C (1100 and 1200°F). Useful space in autoclaves is 1.9 in. in diameter and 6 ft long.

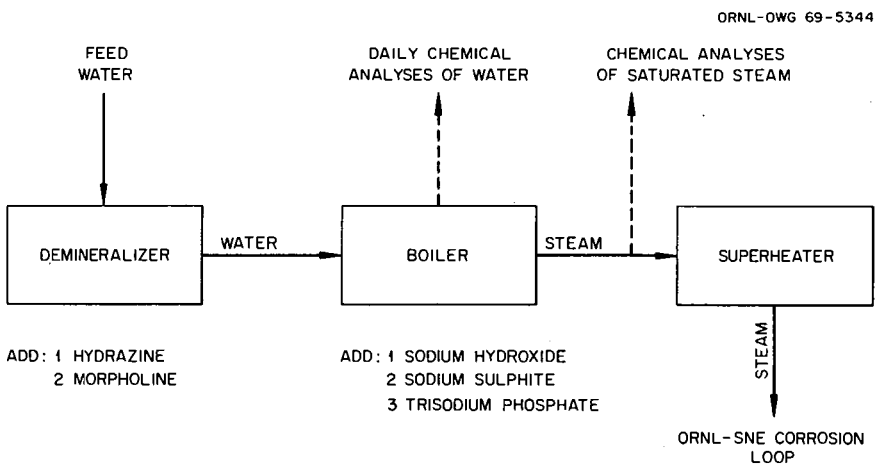

Fig. 25.2. Water and Steam Control at Bartow Plant, Florida Power Corporation.

Table 25.1. Allowable Ranges of Impurities and Random Chemical Analyses of Boiler Water and Saturated Steam at the Bartow Plant of the Florida Power Corporation

	Allowable Range		Chemical Analyses[a]				
			Boiler Water			Saturated Steam	
	Boiler Water	Saturated Steam	Sample 1	Sample 2	Sample 3	Sample 1	Sample 2
pH	10.1–10.7	8.8–9.0	10.7	10.7	10.3	8.8	8.9
Chemical impurities, ppm							
Na_2SO_3	0.6–1.0		1.0	0.6	0.7		
NaCl	3–10		4	3	4		
PO_4	1.0–5.0		5	2	3		
Na_2SO_4	5–25		8	13	14		
SiO_2	0.12–0.20	0.005 max	0.14	0.13	0.15	0	0
NH_3		1.0 max				0.153	0.180
Cl		0.5 max					
Conductivity, μm		2.2–4.5				4.5	4.0
Total dissolved solids, ppm	30–50	0.5–1.0				0.7	0.7

[a]Sampled on random dates.

allowable ranges of impurities and the results of random chemical analyses on the water and steam. Chemicals are added to the demineralizer and boiler to control the O content, pH, and general chemistry of the water and steam. Chemical analyses of the saturated steam consistently show chloride below the minimum chemically detectable amount (0.5 ppm) and < 1 ppm O in the boiler water.

Corrosion is being determined both from the weight gain and from the thickness of the scale that forms on the transverse, strip specimens, which are 2 7/8 in. long × 1/2 in. wide × 1/16 in. thick. These specimens were machined from 1/2-in.-thick weldments made by the gas tungsten-arc process with 5/32-in. filler wire. The machined specimens are given a final 100-mesh grind to assure a consistent surface finish from specimen to specimen. The alloy combinations we are now investigating are listed in Table 25.2. These combinations of materials are being considered for advanced steam generators for gas-cooled reactors in which part of the unit may operate at high temperatures (705 to 760°C), another part may operate at intermediate temperatures (595 to 650°C), and still another part may operate at lower temperatures.

Table 25.2. Alloy Combinations for Steam Corrosion Studies at 595 and 650°C

Identification Code	Base Metal	Base Metal	Filler Metal
A9	Inconel 625	Inconel 625	Inconel 625
A13	Inconel 625	Incoloy 800	Inconel 625
A12	Inconel 625	Incoloy 800	Inconel 82
A18	IN 102	IN 102	IN 102
A19	IN 102	Incoloy 800	IN 102
A20	IN 102	Incoloy 800	Inconel 82
A5	Hastelloy X	Hastelloy X	Hastelloy X
A6	Hastelloy X	Incoloy 800	Hastelloy X
A8	Hastelloy X	Incoloy 800	Hastelloy W
A7	Hastelloy X	Incoloy 800	Inconel 82
A2	Incoloy 800	Incoloy 800	Inconel 82
A3	Inconel 600	Inconel 600	Inconel 82
A16	2.25% Cr–1% Mo	Incoloy 800	Inconel 82
A4	Type 304 stainless steel	Type 304 stainless steel	Type 308 stainless steel

General Corrosion at 595 and 650°C and Weldability

Corrosion Studies (J. P. Hammond)

At 595°C, the corrosion on weldments of 2.25% Cr–1% Mo low-alloy steel joined to Incoloy 800 with Inconel 82 filler metal was 100 times that on other weldments of dissimilar metals. We recognized this as a marginal temperature for the low-alloy steel and discontinued the tests.

The weldments consisting of Incoloy 800 welded to Inconel 625, Hastelloy X, and IN 102 (materials for use at high temperatures) with Inconel 82 filler metal, showed very good corrosion behavior at both 595 and 650°C, though we observed some spallation in welds of the IN 102 alloy at 650°C. After exposure for 6000 hr at 650°C, the weight gains for these weldments were very low (≤ 3.5 mg/cm^2). The scales that formed on Inconel 625 and Hastelloy X wrought plate and filler metal and on the Inconel 82 filler metal were uniform, tenacious, and only 2 to 6 μm thick. Figure 25.3 shows the scales on weldments A13 and A7.

The corrosion of the weldments between similar metals as a function of time at 595 and 650°C is indicated by the weight-gain curves in Fig. 25.4. The anomaly of a greater weight gain in the IN 102 weldment at 595°C than at 650°C can probably be explained by the tendency of this alloy to spall at the higher temperature.

Measurements of the weight gained by weldments on both similar and dissimilar metals correlated well with metallographic observations of the characteristics and thickness of the scale that was formed.

Preferential Corrosion

Stress-Corrosion Cracking (J. P. Hammond)

Stress-corrosion cracking tests on statically stressed U-bend specimens 3 1/4 in. long × 5/16 in. wide × 1/16 in. thick were conducted in the 595°C autoclave at the same time that the specimens for study of the general corrosion were being exposed. Duplicate tests were conducted on the weldments of similar and dissimilar metals and on the unwelded

PHOTO 96679

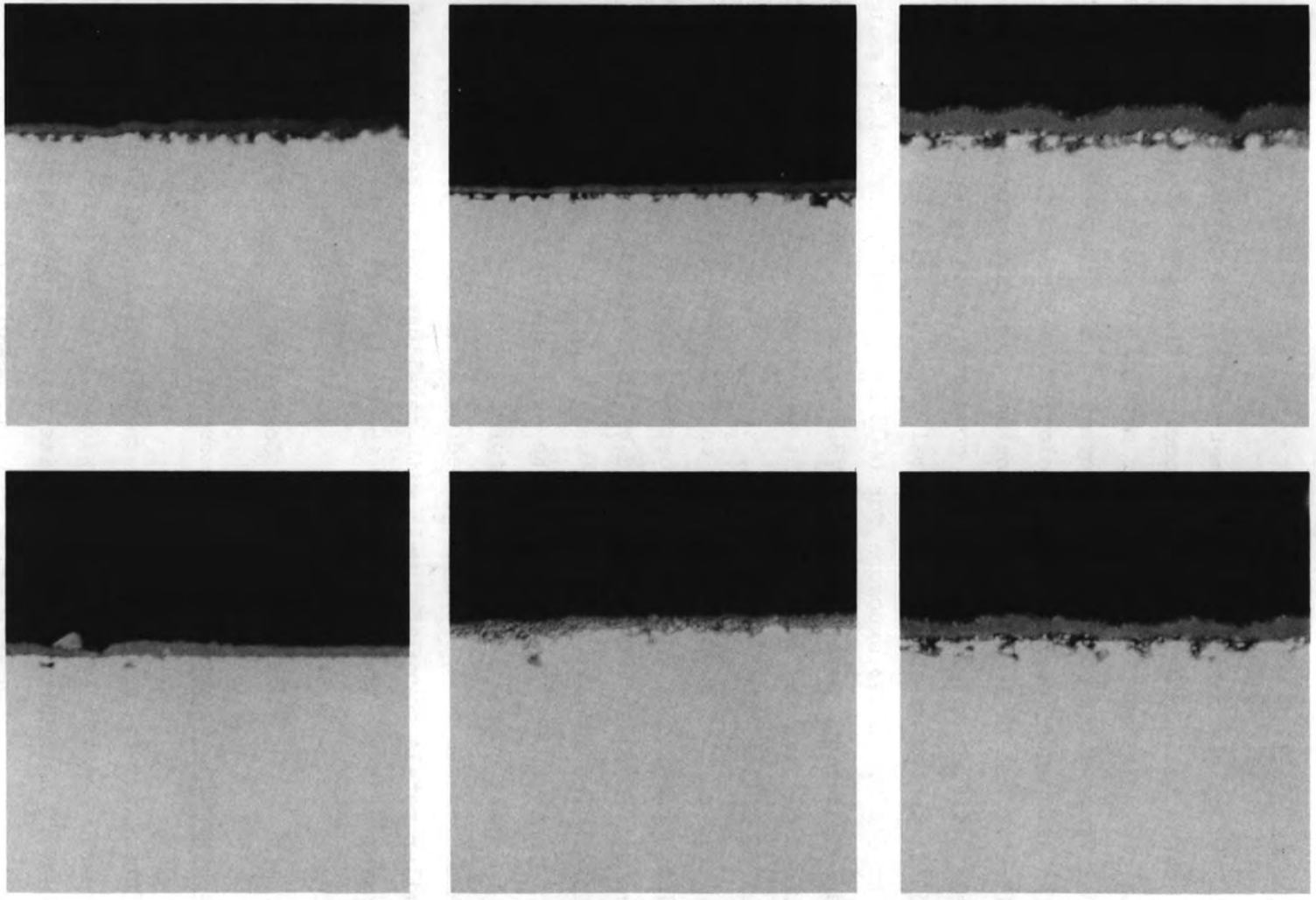

Fig. 25.3. Typical Scales Formed on Two Weldments in Steam at 650°C in 4000 hr. Top sequence shows (left to right) scale on Inconel 625 plate, Inconel 625 filler metal, and Incoloy 800 plate. Bottom sequence similarly shows Hastelloy X plate, Inconel 82 filler metal, and Incoloy 800 plate. As polished. 2000×. Reduced 15%.

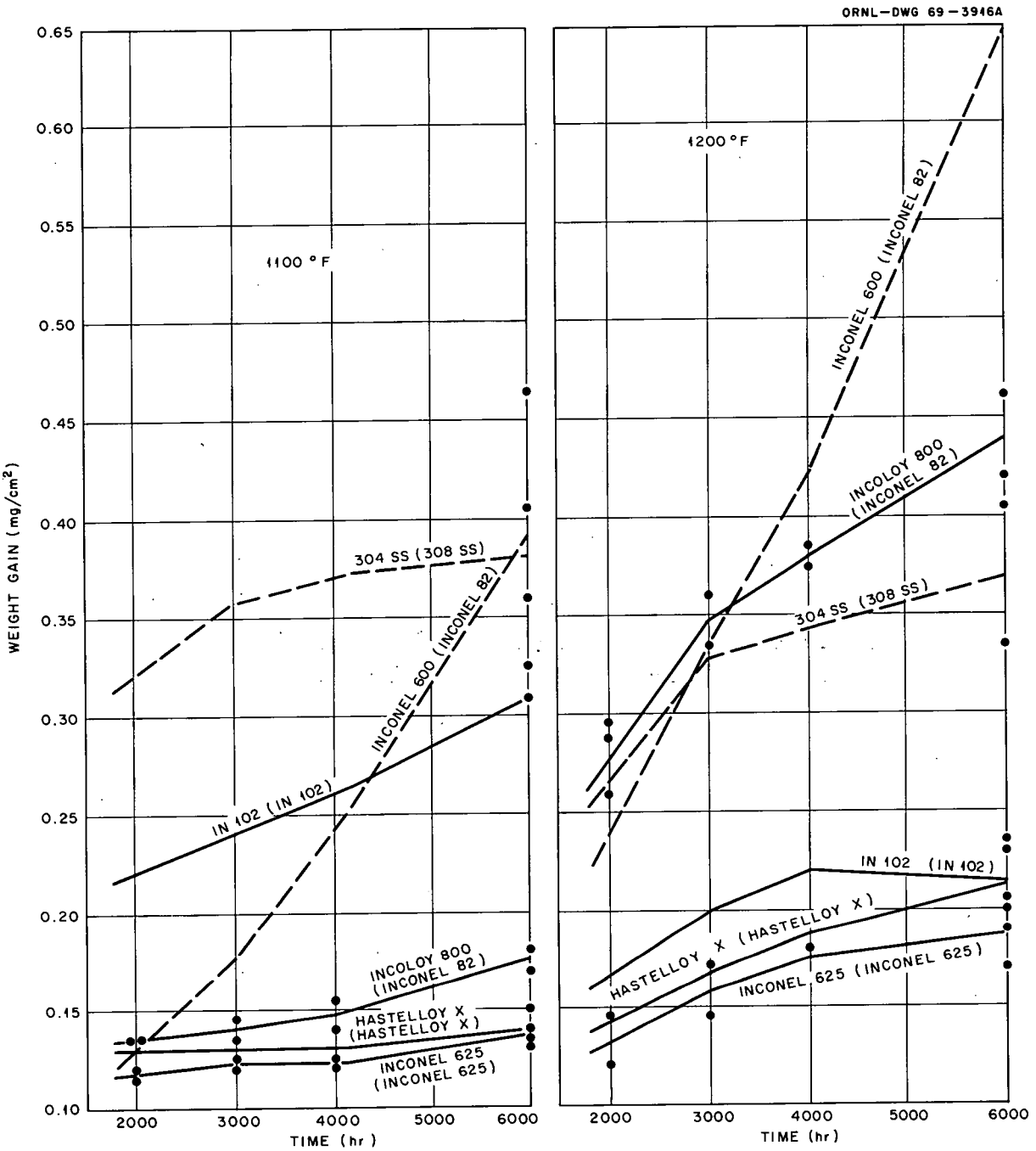

Fig. 25.4. Weight-Gain Curves of Weldments Between Similar Metals. Materials in parentheses represent filler metals.

base metals. Small microfissures in ten of the weldment specimens acted as ideal corrosion crevices. One of the duplicate A2, A8, A9, A13, A16, and A19 specimens and both A18 and A20 specimens contained one or more of these flaws. Visual examination after 1000, 2000, and 3000 hr and a final metallographic examination at 4000 hr revealed no cracks or evidence of crack propagation that could be attributed to stress corrosion.

We are developing a high-pressure corrosion loop that will enable us to inject chloride and O_2 to levels of 20 ppm so that we may study stress-corrosion cracking of these weldments under the influence of contaminants. This loop should be available for use by July 1970.

References

1. This program was initiated by the Gas-Cooled Reactors Branch of RDT and is currently funded by the Fuels and Materials Branch.
2. F. Eberle and J. H. Kitterman, "Scale Formations on Superheater Alloys Exposed to High Temperature Steam," pp. 67–113 in Behavior of Superheater Alloys in High Temperature, High Pressure Steam, American Society of Mechanical Engineers, New York, 1968.
3. G. P. Wozaldo and W. L. Pearl, Corrosion 21, 355–369 (1965).

Previous reports in this series:

ORNL-4330	Period Ending June 30, 1968
ORNL-4350	Period Ending September 30, 1968
ORNL-4390	Period Ending December 31, 1968
ORNL-4420	Period Ending March 31, 1969
ORNL-4440	Period Ending June 30, 1969

ORNL-4480
UC-25 — Metals, Ceramics, and Materials

INTERNAL DISTRIBUTION

1–3. Central Research Library
4–5. ORNL — Y-12 Technical Library
Document Reference Section
6–20. Laboratory Records Department
21. Laboratory Records, ORNL RC
22. ORNL Patent Office
23. R. E. Adams
24. G. M. Adamson, Jr.
25. S. E. Beall
26. R. L. Beatty
27. R. J. Beaver
28. M. Bender
29. R. G. Berggren
30. D. S. Billington
31. E. E. Bloom
32. A. L. Boch
33. E. S. Bomar
34. C. D. Bopp
35. B. S. Borie
36. D. T. Bourgette
37. G. E. Boyd
38. R. A. Bradley
39. R. J. Breeding
40. R. B. Briggs
41. R. E. Brooksbank
42. D. A. Canonico
43. R. W. Carpenter
44. R. M. Carroll
45. J. V. Cathcart
46. A. K. Chakraborty
47. D. L. Clark
48. G. W. Clark
49. N. C. Cole
50. K. V. Cook
51. W. H. Cook
52. G. L. Copeland
53. W. B. Cottrell
54. C. M. Cox
55. F. L. Culler
56. C. W. Cunningham
57. J. E. Cunningham
58. V. A. DeCarlo
59. W. E. Deeds
60. J. DeLuca
61. J. H. DeVan
62. J. R. DiStefano
63. C. V. Dodd
64. R. G. Donnelly
65. D. A. Dyslin
66. T. Eck
67. J. H. Erwin
68. R. B. Evans III
69. K. Farrell
70. J. I. Federer
71. D. E. Ferguson
72. R. B. Fitts
73. B. Fleischer
74. B. E. Foster
75. A. P. Fraas
76. J. H Frye, Jr.
77. W. Fulkerson
78. L. C. Fuller
79. R. E. Gehlbach
80. T. G. Godfrey, Jr.
81. G. M. Goodwin
82. J. M. Googan (Y-12)
83. R. J. Gray
84. W. R. Grimes
85. A. G. Grindell
86. H. D. Guberman
87. L. L. Hall
88. D. G. Harman
89. W. O. Harms
90–93. M. R. Hill
94. D. O. Hobson
95. H. W. Hoffman
96. F. J. Homan
97. R. W. Horton
98. W. R. Huntley
99. H. Inouye
100. D. H. Jansen
101. J. D. Jenkins
102. W. H. Jordan
103. G. W. Keilholtz
104. R. T. King
105. R. L. Klueh
106. R. W. Knight
107. W. J. Lackey

108. J. A. Lane
109. J. M. Leitnaker
110. B. C. Leslie
111. C. S. Lever
112. T. B. Lindemer
113. C. T. Liu
114. H. R. Livesey
115. B. T. Loh
116. E. L. Long, Jr.
117. A. L. Lotts
118. C. D. Lundin
119. J. W. Luquire
120. R. N. Lyon
121. H. G. MacPherson
122. R. E. MacPherson
123. M. M. Martin
124. W. R. Martin
125. R. W. McClung
126. H. E. McCoy, Jr.
127. H. C. McCurdy
128. R. E. McDonald
129. W. T. McDuffee
130. D. L. McElroy
131. C. J. McHargue
132. A. J. Miller
133. E. C. Miller
134. J. P. Moore
135. R. E. Moore
136. C. S. Morgan
137. J. G. Morgan
138. F. H. Neill
139. T. A. Nolan (K-25)
140. K. Notz
141. A. R. Olsen
142. M. F. Osborne
143. P. Patriarca
144. W. H. Pechin
145. R. B. Perez
146. A. M. Perry
147. S. Peterson
148. L. E. Poteat
149. R. A. Potter
150. R. B. Pratt
151. M. K. Preston
152. W. W. Proaps
153. R. E. Reed
154. C. R. Reese
155. G. A. Reimann
156. A. E. Richt
157. P. L. Rittenhouse
158. H. E. Robertson
159. M. W. Rosenthal
160. D. J. Rucker
161. C. F. Sanders
162. G. Samuels
163. A. W. Savolainen
164. J. E. Savolainen
165. A. C. Schaffhauser
166. J. L. Scott
167. J. D. Sease
168. C. E. Sessions
169. O. Sisman
170. G. M. Slaughter
171. S. D. Snyder
172. K. E. Spear
173. I. Spiewak
174. J. E. Spruiell
175. W. J. Stelzman
176. R. L. Stephenson
177. J. O. Stiegler
178. D. A. Sundberg
179. R. W. Swindeman
180. E. J. Tenckhoff
181. V. J. Tennery
182. K. R. Thoms
183. D. B. Trauger
184. G. M. Watson
185. S. C. Weaver
186. M. S. Wechsler
187. A. M. Weinberg
188. J. R. Weir, Jr.
189. W. J. Werner
190. H. L. Whaley, Jr.
191. G. D. Whitman
192. F. W. Wiffen
193. J. M. Williams
194. L. C. Williams
195. R. K. Williams
196. R. O. Williams
197. J. C. Wilson
198. R. G. Wymer
199. F. W. Young, Jr.
200. C. S. Yust
201. C. M. Adams, Jr. (Consultant)
202. Leo Brewer (Consultant)
203. L. S. Darken (Consultant)
204. Walter Kohn (Consultant)

EXTERNAL DISTRIBUTION

AIR FORCE MATERIALS LABORATORY, Wright-Patterson Air Force Base

205. C. H. Armbruster
206. H. M. Burte
207. G. Glenn
208. Technical Director

AIR FORCE WEAPONS LABORATORY, Kirtland Air Force Base

209. D. Brooks

AMES LABORATORY

210. O. N. Carlson
211. W. L. Larsen
212. M. Smutz
213. F. H. Spedding

ARGONNE NATIONAL LABORATORY

214. L. Baker
215. J. H. Kittel
216. M. V. Nevitt
217. P. G. Shewmon
218. R. C. Vogel

LMFBR PROGRAM OFFICE, Argonne National Laboratory

219. A. Amorosi
220. L. Burris
221. L. Kelman
222. J. M. McKee

AEC-RDT SITE REPRESENTATIVES

223. M. E. Jackson, Argonne National Laboratory
224. D. J. Wille, Atomic Power Development Associates
225. R. L. Morgan, Atomics International
226. J. V. Levy, General Electric, Sunnyvale
227. R. H. Ball, Gulf General Atomic
228. J. E. Hebert, Idaho
229. D. A. Moss, Idaho
230. K. A. Trickett, Idaho
231. D. F. Cope, Oak Ridge National Laboratory
232. C. L. Matthews, Oak Ridge National Laboratory
233. P. G. Holsted, Battelle-Northwest
234. J. Sako, Battelle-Northwest
235. Atomic Energy Commission Library, Washington

DIVISION OF NAVAL REACTORS, AEC, Washington

236. R. H. Steele

DIVISION OF REACTOR DEVELOPMENT AND TECHNOLOGY, AEC, Washington

237. J. C. Crawford, Jr.
238. G. W. Cunningham
239. A. Giambusso
240. H. G. Hembree
241. K. E. Horton
242. J. R. Hunter
243. E. E. Kintner
244. W. H. Layman
245. W. H. McVey
246. J. J. Morabito
247. R. E. Pahler
248. A. J. Pressesky
249. M. A. Rosen
250. J. M. Simmons
251. E. E. Sinclair
252. B. Singer
253. A. Taboada
254. A. N. Tardiff
255. A. Van Echo
256. C. E. Weber
257. M. J. Whitman

DIVISION OF RESEARCH, AEC, Washington

258. P. W. McDaniel
259. D. K. Stevens

DIVISION OF SPACE NUCLEAR SYSTEMS, AEC, Washington

260. R. E. Anderson
261. D. Beard
262. J. F. Griffo
263. F. D. Haines
264. C. E. Johnson
265. J. A. Powers
266. F. C. Schwenk

OAK RIDGE OPERATIONS OFFICE

267. W. J. Larkin
268. Laboratory and University Division

ATOMIC POWER DEVELOPMENT ASSOCIATES

269. E. C. Kovacic
270. A. A. Shoudy

ATOMICS INTERNATIONAL

271. H. Pearlman
272. J. G. Asquith

BABCOCK AND WILCOX COMPANY, Lynchburg, Virginia 24505

273. C. Baroch
274. S. P. Grant
275. C. Johnson
276. L. Weissert

BATTELLE MEMORIAL INSTITUTE, Columbus, Ohio

277. W. Berry
278. D. Keller
279. S. J. Paprocki
280. Defense Materials Information Center

BATTELLE-NORTHWEST, Richland, Washington

281. A. L. Bement
282. J. J. Cadwell
283. T. T. Claudson
284. D. L. Condotta
285. E. Evans
286. J. E. Hanson
287. B. R. Hayward
288. B. M. Johnson
289. W. E. Roake
290. D. W. Shannon
291. J. C. Tobin
292. R. G. Wheeler
293. Technical Information File

FAST FLUX TEST FACILITY, Battelle-Northwest

294. E. R. Astley

BROOKHAVEN NATIONAL LABORATORY

295. D. H. Gurinsky
296. C. Klamut

BUREAU OF MINES

297. Haruo Kato, Albany Metallurgy Research Center, P.O. Box 70, Albany, Oregon 97321
298. T. Sullivan, Bureau of Mines, Boulder City, Nevada 89005

COMBUSTION ENGINEERING

299. W. P. Chernock
300. S. S. Christopher

GENERAL ELECTRIC, Cincinnati

301. D. H. Ahmann
302. H. C. Brassfield
303. V. P. Calkins
304. E. Hoffman
305. J. McGurty
306. J. Moteff

GENERAL ELECTRIC, Nuclear Systems Programs, Cincinnati

307. E. E. Hoffman

GENERAL ELECTRIC, San Jose

308. R. Duncan
309. H. Klepfer

GENERAL ELECTRIC, Pleasanton

310. H. W. Alter

GENERAL ELECTRIC, Sunnyvale

311. K. P. Cohen
312. F. Comprelli
313. R. Skavdahl
314. C. Spalaris
315. E. L. Zebroski

GULF GENERAL ATOMIC

316. D. B. Coburn
317. A. J. Goodjohn
318. J. P. Howe
319. S. Jaye
320. J. F. Watson

IDAHO NUCLEAR CORPORATION

321. W. C. Francis
322. William Yuill

ILLINOIS INSTITUTE OF TECHNOLOGY RESEARCH INSTITUTE

323. D. J. McPherson

JET PROPULSION LABORATORY (NASA)

324. J. Davis

KNOLLS ATOMIC POWER LABORATORY

325. R. F. Wojciescak
326. Document Library

LOS ALAMOS SCIENTIFIC LABORATORY

327. R. D. Baker
328. D. B. Hall
329. J. A. Leary
330. R. Perkins
331. R. E. Peterson
332. Reports Library

MOUND LABORATORY

333. R. G. Grove

NASA HEADQUARTERS

334. J. J. Lynch

NASA, LEWIS RESEARCH CENTER

335. M. Ault
336. J.W.R. Creagh
337. J. J. Lombardo
338. T. P. Moffitt
339. T. A. Moss
340. F. E. Rom
341. L. Rosenblum
342. N. D. Sanders
343. N. Saunders
344. C. M. Scheuermann
345. H. Schwartz

NAVAL RESEARCH LABORATORY

346. J. R. Hawthorne
347. C. Serpan
348. L. E. Steele

NORTH CAROLINA UNIVERSITY, Raleigh, North Carolina 27607

349. J. Beeler
350. R. E. Dahl

NUCLEAR MATERIALS AND EQUIPMENT CORPORATION

351. C. Caldwell
352. K. Puechl

OHIO STATE UNIVERSITY, Columbus, Ohio 43212

353. M. G. Fontana
354. R. W. Staehle

RENSSELAER POLYTECHNIC INSTITUTE

355. W. Dickinson
356. W. F. Savage
357. C. B. Willingham, Jr.

SANDIA CORPORATION

358. J. Read Holland
359. J. Jacobs
360. D. R. Johnson

SAVANNAH RIVER LABORATORY

361. P. H. Permar
362. S. P. Rideout

TRW SYSTEMS (NASA), Redondo Beach, California 90278

363. H. Lurie

UNION CARBIDE CORPORATION, New York

364. J. A. Swartout

UNION CARBIDE CORPORATION, Materials Systems Division, Indianapolis

365. C. F. Leitten, Jr.

UNITED NUCLEAR CORPORATION

366. A. Strasser

UNIVERSITY OF CALIFORNIA, Lawrence Radiation Laboratory, Livermore

367. W. R. Holman
368. J. S. Kane
369. L. W. Roberts
370. A. J. Rothman
371. B. Rubin

U.S. NAVAL AIR SYSTEM COMMAND (AIR-52031B)

372. T. Kearns
373. I. Machlin

USAEC Scientific Representative, American Embassy, Box 40 FPO, N.Y. 09510

374. W.L.R. Rice

WESTINGHOUSE, Advanced Reactor Division, Waltz Mill Site

375. E. C. Bishop
376. J.C.R. Kelly
377. P. J. Levine
378. P. Murray
379. W. E. Ray
380. G. A. Whitlow

WESTINGHOUSE, Astronuclear Laboratory

381. R. T. Begley
382. D. C. Goldberg

WESTINGHOUSE, Atomic Power Division

383. T. Stern

WESTINGHOUSE, Bettis

384. R. H. Fillnow
385. P. N. Gustafson
386. Westinghouse Bettis Laboratory Library

387–594. Given distribution as shown in TID-4500 under Metals, Ceramics, and Materials category (25 copies – CFSTI)